The Institute of Paper Science and Technology

Atlanta, Georgia

Doctor's Dissertation

The Stability and Disintegration of Radially Thinning Liquid Sheets

Thomas M. Spielbauer

June, 1992

THE STABILITY AND DISINTEGRATION OF RADIALLY THINNING LIQUID SHEETS

A thesis submitted by

Thomas M. Spielbauer

B.S. 1986, University of Wisconsin - Madison

M.S. 1988, Lawrence University - the Institute of Paper Chemistry

in partial fulfillment of the requirements
for the degree of Doctor of Philosophy
from the Institute of Paper Science and Technology
Atlanta, Georgia

June 1992

TABLE OF CONTENTS

LIST OF FIGURES

LIST OF TABLES

ABSTRACT

The purpose of performing this study is to determine the mechanisms which cause a thin liquid sheet to break up into drops. A simple splash plate nozzle is used to produce radially thinning liquid sheets which are then imaged with both high-speed 16 mm and video cameras. The physical processes captured in these images are used as a basis for developing a description of the stages of sheet breakup. Key steps in the proposed mechanism are examined experimentally and analytically.

The dominant mechanism of disintegration for the radially thinning sheets observed involves the formation, growth, and interaction of holes. Each hole collects liquid into a thick, circular rim as surface tension forces drive its growth. The rims of neighboring holes interact to form clumps and strands which are unstable and will break into a distribution of drop sizes. The mean drop size and the range of drop sizes produced are determined by the spatial distribution of the holes, their growth rates, and the way in which neighboring rims interact.

An equation for predicting the thickness and mean velocity of a liquid sheet formed by a splash plate nozzle is obtained from a correlation of experimental data. The growth rates of perforations are measured from high-speed images of the sheet. As these growth rates are inversely proportional to the sheet thickness, they can be used as an indirect method for measuring the downstream thickness of a free sheet. These thicknesses are significantly less than that accounted for by radial thinning alone.

The effects of wave disturbances on the downstream sheet thickness are investigated. Wave growth is shown to contribute significantly to the thinning of the sheet, and to facilitate the subsequent perforation and breakup. Existing analyses of wave growth on viscous, radially thinning liquid sheets are used to predict trends in the downstream wave-thinned sheet

thickness. These trends are compared to experimentally measured perforation formation rates, and good qualitative agreement is obtained.

The physical processes which can cause the sheet to rupture, including suspended solid particles, entrained air bubbles, drop impingement, and wave interactions, are evaluated. Relying on both experimental and analytical results, the importance of hydrodynamic mechanisms and rupture initiated by external effects are discussed. The influence of external vibrations on the wave disturbances and sheet breakup is also presented.

Based on the results of this study, the production of a distribution of drop sizes from the breakup of liquid sheets is a direct consequence of the random distribution of perforations in the region of breakup. The downstream location of breakup is a function of the initial sheet thickness and velocity, the rate of downstream thinning, and the wavelength and growth rate of the dominant waves. Adjusting the rate of sheet thinning and the dominant wavelength may provide some degree of control on the mean drop size produced, but a distribution of drop sizes about this mean is still expected because the precise location of each perforation is determined by the random positions of the air bubbles or particles causing rupture.

INTRODUCTION

Spraying converts a bulk quantity of liquid into a large number of small drops. Such a transformation is useful in many operations including liquid fuel injection, spray drying, pesticide application, spray painting, and metal powder manufacture.[1]

A wide variety of mechanical devices, called nozzles, have been developed to produce drops. Nozzles can be grouped into two categories, jet producing and sheet producing. Jet producing nozzles eject the liquid as a cylindrical strand, which, under the influence of aerodynamic and surface tension forces, breaks up into drops. Sheet producing nozzles form a thin layer of liquid which may disintegrate into drops directly, or may produce cylindrical strands as an intermediate step.

This study focuses on the formation of drops from a simple, sheet producing nozzle. The device, called a splash plate nozzle, forms a liquid sheet by impinging a circular jet on a small, flat plate. The fluid spreads out on the plate and, when it reaches the edge, continues to expand radially forming a free thin sheet. Although experiments were conducted using this single design, the qualitative and analytical descriptions of sheet breakup developed are expected to apply to a variety of sheet producing devices.

The remainder of this introduction is used to discuss the importance of spray research. First, a general review of the influence of drop size on the performance of liquid fuel combusters will be presented. Second, the range of drop sizes produced by typical industrial nozzles will be discussed.

Following this background material, the literature pertaining to the formation and disintegration of thin liquid sheets will be reviewed. The discussion of sheet formation processes will be limited to splash plate nozzles. This description of sheet breakup will include the three commonly ascribed processes for the formation of drops from sheets, the wave, perforation, and rim mechanisms.

The remainder of the document is divided into three sections: first, a description of the objectives and the experimental approach; second, a discussion of the key findings, including experimental and analytical results; and finally, a summary of the importance of these results and their practical implications.

IMPORTANCE OF DROP SIZE

Depending on the particular application, the use of a nozzle to disperse a liquid as a large number of small drops achieves different objectives. In processes such as fuel injection and spray drying, the formation of drops increases the surface area per unit volume and thus enhances energy and mass transfer rates.[2,3] The surface area per unit volume for a range of drop sizes is given in Table 1.

Table 1. Total surface area and number of drops per unit volume as a function of drop diameter.

drop diameter (μm)	number of drops per liter of liquid	area per unit volume (m^2 / liter)
5000	1.52×10^4	1.2
1000	1.91×10^6	6.0
500	1.52×10^8	12
100	1.91×10^9	60
10	1.91×10^{12}	600
1	1.91×10^{15}	6,000

Liquid Fuel Combustion

One specific application of spraying is the introduction of liquid fuels into the combustion zone of diesel engines, gas turbines, and furnaces. In this case, the objective is to produce small drops of fuel which will rapidly evaporate, allowing the fuel to mix with the air and burn.[2,4]

The liquid fuel is sprayed into the combuster using a mechanical device called a nozzle or atomizer. The performance of liquid fuel combusters is dominated by the drop sizes produced by the nozzle and the mixing patterns of the fuel and air.[2,3] As will be discussed, these parameters affect the physical mechanisms of combustion, the ignition and stability of the flame, and the production of pollutants.

Mechanisms of Combustion

Two mechanisms of liquid fuel combustion have been described, homogeneous and heterogeneous.[1,3] In both cases, as a liquid fuel drop evaporates, the gas-phase fuel mixes with the oxidizer (usually air), and the mixture burns producing combustion products. Homogeneous spray combustion occurs when the evaporation of the fuel drop is complete prior to ignition of the fuel/oxidizer mixture. In heterogeneous spray combustion, ignition occurs while a portion of the fuel is still in liquid drop form. This liquid continues to evaporate providing fuel to sustain combustion.

In his review of spray combustion behavior, Lefebvre[1] discussed the relationship between evaporation time and drop size for single component liquid fuels. He reported that the rate of fuel volatilization was proportional to the surface area of the drop. This "D^2 - law," given as

$$\frac{d(D(t)^2)}{dt} = - K_{sst}, \qquad (1)$$

where: $D(t)$ = drop diameter at time, t [m*];
t = time [s]; and
K_{sst} = steady-state evaporation constant [m^2/s],

has been derived analytically and correlates well with available experimental data.[1,2,3,4] If the initial drop diameter is known, then Eq. 1 can be integrated to obtain an expression for the diameter of the drop as a function of time,

$$D(t)^2 = D(0)^2 - t \cdot K_{sst}. \qquad (2)$$

By setting D(t) equal to zero, the time required for complete evaporation, given by

$$t_e = \frac{D(0)^2}{K_{sst}}, \qquad (3)$$

is shown to be proportional to the square of the initial drop diameter.

Equations 1-3 apply when the time required to raise the drop temperature to its boiling point is negligible. For large drop diameters or high ambient temperatures, this unsteady heat-up period cannot be neglected.[1] Lefebvre[1] investigated the role of drop size on the duration of the heat-up period and found it could be approximated by a D^2 - law. The form of the expression is similar to Eq. 1, with the steady-state evaporation constant, K_{sst}, being replaced by a new constant valid during the heat-up period, K_{hu}. The lifetime of a drop is then given by the sum of the heat-up and evaporation times.

* The MKS system will be used to define the units for each term in the equations presented in this thesis.

Two heterogeneous combustion configurations have been described. If the drop is in a stagnant environment or moves slowly relative to the gas phase, then the drop will be surrounded by a thin, approximately spherical "envelope flame." The flame will be centered on the drop, but will exist some distance away from its surface.[2,4,5] When the drop velocity is high relative to the gas phase velocity, a "wake flame" occurs, and combustion is confined to a region downstream of the drop. The velocity at which the transition from envelope to wake flame occurs increases with the square root of the drop diameter.[3]

In heterogeneous combustion, the drop lifetime is related to the time required for the initial evaporation to occur prior to ignition and the time elapsed during the subsequent evaporation and combustion of the remaining fuel. For most single component fuels, the kinetics of combustion are sufficiently rapid such that the overall rate of combustion is limited by the rate of fuel evaporation;[1,2,3] thus, even after ignition, a D^2 - law dependance for the lifetime of single drops has been predicted analytically and observed experimentally.[2,3,5]

A more complicated process occurs in the combustion of heavy fuel oil and coal-water slurry fuels. In these cases, heterogeneous combustion occurs, and the burning of the individual drops proceeds in a series of overlapping steps. The procedure described by Williams[3] for coal-water slurry fuels will be presented, but similar steps occur in the combustion of heavy fuel oil[2] and bitumen-water slurries,[3] as well.

When the fuel drop enters the combustion chamber, energy transfer to the drop begins, and the drop temperature is raised to its boiling point. The drop temperature is then assumed to remain constant as water is evaporated. After most of the water is driven off, the drop temperature begins to rise again; volatile components in the coal vaporize; and the drop swells as gases expand from the drop center. During this volatilization step, the fuel/oxidizer mixture ignites, and a visible flame appears. The end of this stage is marked by the disappearance of

the flame and the simultaneous end of drop swelling. At this point, a solid, porous char carbon particle remains. The final step is the combustion of this carbon matrix. The time required for each stage of combustion (heat up, drying, volatiles burning, and char burning), as well as the time to ignition, increase with increasing drop size.[6]

Ignition and Flame Stability

Williams[3] discussed three mechanisms for the ignition of liquid fuels: thermal or spontaneous, network, and spark. In each case, the drop size influences the ease of ignition and the stability of the combustion process.

In thermal ignition, drops evaporate, and the fuel diffuses into the surrounding oxidizing environment. As the concentration and temperature of this mixture of fuel and oxidizer change, they enter into the inflammability limits for the system, and spontaneous ignition occurs. The ignition delay time is defined as the sum of a physical delay time associated with the processes of fuel evaporation and mixing, and a chemical delay time related to the kinetics of the combustion reactions for the particular fuel/oxidizer system.[3] A number of parameters including the chemical composition of the fuel, the local concentrations of fuel and oxidizer, the temperature, and the pressure influence the delay time for thermal ignition.[3,4] Drop size, by way of its influence on the evaporation rate, also affects the delay time.[3]

In homogeneous, spontaneously ignited combustion systems, the stability of the flame is related to the time and energy required to evaporate and raise the temperature of the incoming fuel drops. The energy required to evaporate the fuel entering the combustion zone is provided by the combustion of the fuel which proceeded it. If the average drop size is excessive, the energy available for evaporation may be insufficient, and the flame will be extinguished.[2]

Network ignition occurs when a relatively cool drop enters into the combustion zone and is ignited by the flame surrounding a second burning drop. In this case, the ignition delay depends upon both the size of the drops and the spacing between them.[3]

The use of an electrical spark is an important technique for igniting liquid fuel sprays, particularly in gasoline engines[2,4] and gas turbines.[2] The electric spark raises the temperature of a ball or kernel of air which then passes through the spray evaporating fuel and producing an ignitable fuel/oxidizer mixture. The minimum energy of the spark required to evaporate the fuel and ignite the spray increases with the cube of the initial fuel drop diameter.[2,3]

Pollutant Formation

In addition to influencing the processes of combustion, initial drop size affects the formation of various pollutants including unburnt fuel, carbon monoxide, nitrous oxides, soot, and smoke. In each of these cases, a decrease in the initial fuel drop diameter results in a decrease in the quantity of the pollutant formed.[2,3]

As previously discussed, the rate of fuel evaporation decreases, and the time to ignition increases as fuel drop size increases. Both of these factors result in the less rapid combustion of the fuel drop and thus an increase in the probability of unburnt fuel remaining after the combustion zone of the burner.[3]

Combustion in a fuel rich environment promotes nitrous oxide formation, soot and particulate production, and stack emissions.[3] Both the drop size and velocity affect the composition of the local combustion environment. During heterogeneous combustion, fuel rich conditions exist for all drops surrounded by an envelope flame. If wake flame conditions can be achieved, better air/fuel mixing conditions will result, and pollutant formation rates will be

decreased. As previously stated, the relative drop velocity at which the transition from envelope to wake flame conditions occurs increases with the square root of the drop diameter;[3] thus, larger drops are more likely to burn in fuel rich conditions and produce pollutants.

Gonzalez and Reitz[7] reported that initial drop size affected the penetration of the liquid fuel into the combustion zone of a diesel engine, and this would affect local fuel/oxidizer compositions. If fuel rich zones result, pollution production rates will increase. In addition, large, high momentum drops may pass through the combustion zone unburnt and strike relatively cool surfaces of the combustor. Here, this material may react to form carbon deposits.[2]

Choudhury and Gerstein[8] investigated the combustion of heavy fuel oils. They developed an expression for predicting the rate of decomposition of components in the fuel to nonvolatile, hard-to-burn particles. This rate increased relative to the rate of fuel evaporation with the square of the initial drop diameter. Thus, the combustion of larger drops results in an increase in the rate of particulate pollution formation.

Black Liquor Sprays

The introduction of black liquor into the combustion zone of a recovery boiler is a spray application of direct importance to the pulp and paper industry. This process will be discussed, beginning with a brief description of black liquor and the geometry of recovery boilers. The role of drop size will be presented with an emphasis placed on the similarities with the previously discussed combustion applications.

Wood consists primarily of cellulose fibers bound together by a matrix of organic material called lignin. Pulping is the process by which wood is separated into individual fibers. In the kraft pulping process, an aqueous solution of sodium sulfide and sodium

hydroxide is combined with wood chips in a reaction vessel called a digester. The inorganic pulping chemicals react primarily with the lignin breaking it into smaller molecular weight units, thus releasing the fibers. The resulting solubilized lignin fragments and the reacted inorganic compounds are washed from the fibers. The fibers are sent on for further processing, while the aqueous solution of organic and inorganic material, called weak black liquor (because of its color) is concentrated to 65-75% solids (strong black liquor) in a multiple-effect evaporator.

The economic feasibility of the kraft process is dependent upon the effective recovery of the inorganic pulping chemicals and the efficient use of the chemical energy contained in the organic fraction of the black liquor.[9,10] To achieve these objectives, the black liquor is burned in an industrial, water-walled furnace called a recovery boiler. The energy released during the combustion of the organic material is used to produce high pressure steam, while the inorganic chemicals are recovered from the lower portion of the furnace as molten salts. A sketch showing the major unit operations in the recovery cycle is shown in Fig. 1.

In order to facilitate the discussion of black liquor combustion, the general layout of a recovery boiler will be described. The single drop combustion behavior of black liquor will be presented next, followed by a discussion of the unique problems associated with the processing of the inorganic compounds.

Recovery Boiler Characteristics

A sketch of a typical black liquor recovery boiler is shown in Fig. 2. Although it is similar to other large industrial boilers, it must serve the additional function of processing the inorganic chemicals which comprise approximately one-third of the dry mass of the liquor.[9,10] For the purposes of this discussion, the furnace will be considered in three sections, as labeled in Fig. 2, the char bed, the in-flight combustion zone, and the pendant heat transfer section.

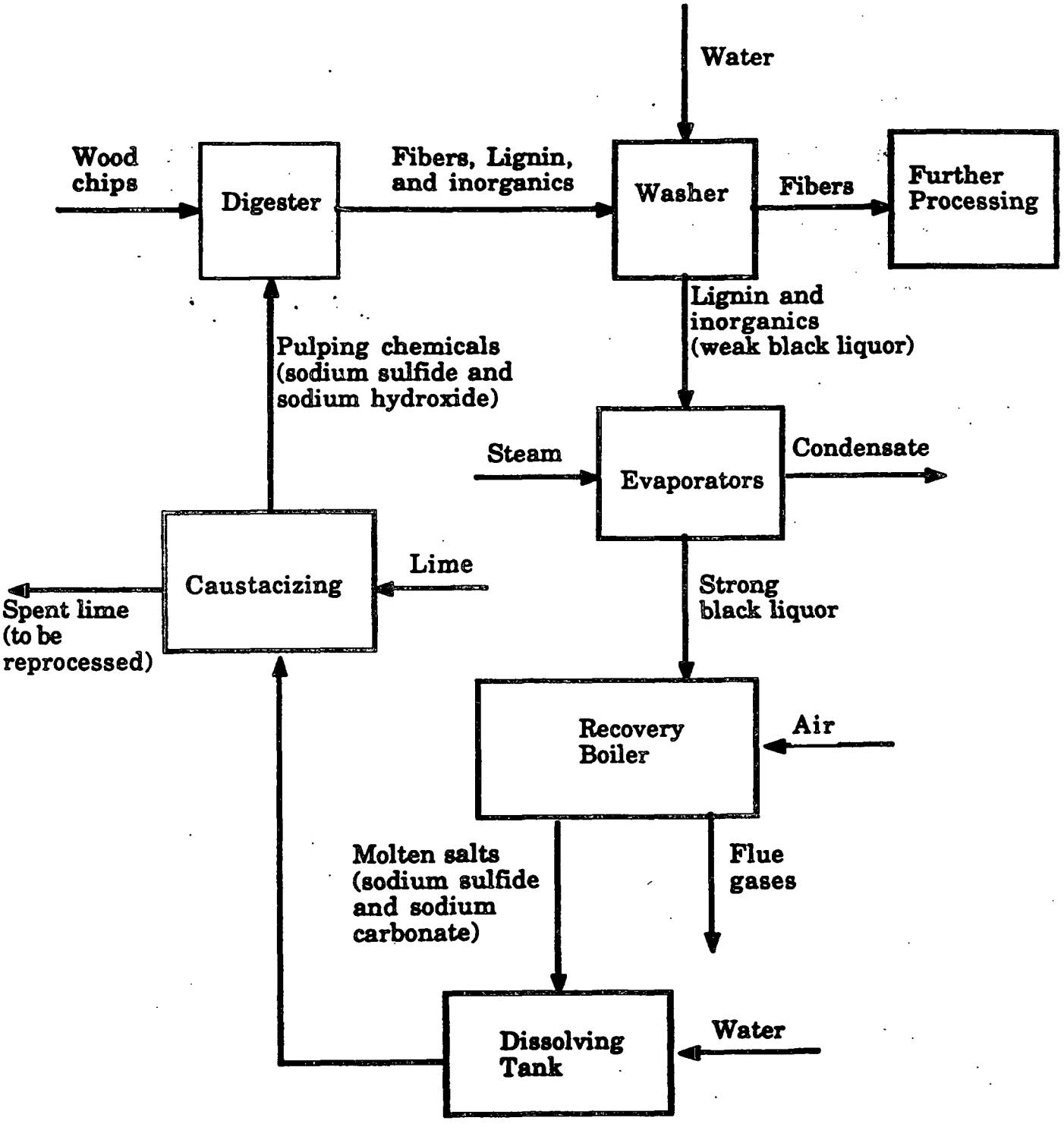

Figure 1. Sketch of the unit operations in the kraft recovery process.

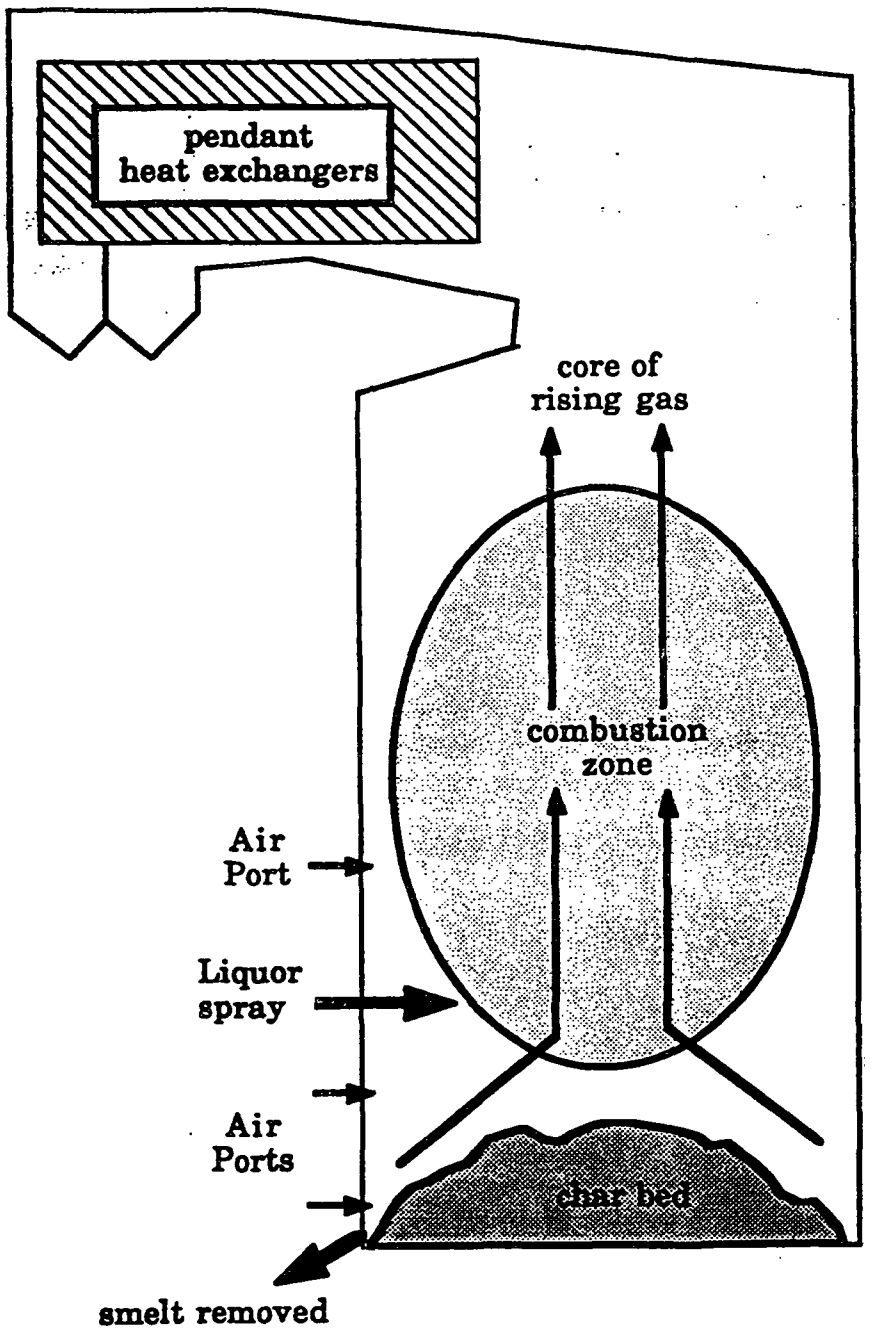

Figure 2. A sketch of a typical black liquor recovery boiler.

These divisions are somewhat arbitrary, as certain phenomena may occur in more than one section.

Nozzles are used to spray the black liquor into the combustion zone, at a level approximately five meters above the floor of the furnace.[10] Air is introduced into the boiler at two, or more commonly, three levels, one of which is located above the elevation at which the liquor is introduced.[9,10] Computational models of the air flow patterns in recovery boilers have been used to predict the existence of a core of rising gases with recirculation zones near the furnace walls.[10,16,17]

Like coal-water slurry and heavy fuel oil, black liquor is expected to undergo several stages of combustion during flight in the recovery boiler. These stages are commonly referred to as drying, volatilization, and char combustion.[10] At the completion of these steps, a drop of molten, inorganic salts remains. Ideally, this material collects in the char bed at the bottom of the furnace, where further inorganic reactions occur.

All of the drying should occur in the in-flight combustion zone of the furnace, as contact between water and the molten salts in the char bed can result in a powerful explosion.[9,10] The extent to which the volatilization and char combustion stages occur in flight will depend on the drop diameter, the air flow patterns, and the operating characteristics of the boiler.

Volatilization and char combustion are completed in the char bed section of the furnace. The conversion of sodium sulfate to sodium sulfide also occurs in this region by way of a reduction reaction with the char carbon.[9,10] The molten inorganic compounds which collect in the char bed, mainly sodium sulfide and sodium carbonate, are continuously drained from the bottom of the boiler. These salts are dissolved in water. The resulting aqueous

solution (green liquor) is sent to a unit operation called causticizing where the sodium carbonate is converted to sodium hydroxide (see Fig. 1). This completes the regeneration of the inorganic pulping chemicals.[9]

A portion of the energy released by the combustion of the volatile organic compounds and the char carbon is recovered by energy transfer to the water wall tubes encasing the combustion cavity.[10] More energy is recovered as the combustion gases rise through the furnace and enter the pendant heat transfer section. Here, the gases are cooled by convective and radiative energy transfer to heat exchangers, similar to what occurs in conventional boilers. The entrainment of drops in the rising combustion gases must be minimized to avoid the excessive buildup of deposits on the heat exchanger surfaces, as these deposits decrease the efficiency of energy removal and corrode tube surfaces.

Drop Combustion

The combustion of black liquor has been investigated by burning single drops suspended in flowing-gas[12] and stagnant[13] environments. The role of drop size on each stage of combustion has been reported.

Water accounts for 20-40% of the black liquor mass as sprayed into the boiler.[10] This water is evaporated in the first, or drying, stage of black liquor combustion. During this step, the drop is an energy sink as the temperature of the liquor is raised to its elevated boiling point and the latent heat of vaporization is provided. Frederick[13] reported that the time required for drying increases linearly with the initial drop diameter.

In the second phase, the volatilization and combustion of the organic material, a significant amount of recoverable energy is released. During this stage, the drop swells,[12,13,14]

and its density is reduced. The time required for devolatilization increases with initial drop size to the five-thirds power.[13]

Vapor phase sulfur compounds can be evolved during the volatilization stage. This loss of sulfur can result in both an environmental problem in the form of malodorous emissions from the recovery boiler and an economic loss resulting from a decrease in the fraction of sodium sulfide recovered in the boiler. Harper[15] reported that the mass of sulfur released per unit mass of liquor increases with increasing initial drop size to the first power.

The third process a black liquor drop undergoes is char combustion. In this phase, the carbon remaining after pyrolysis reacts to form carbon monoxide and carbon dioxide. It is reported that the time required for char combustion increases with initial drop diameter to the five-thirds power.[13]

Recovery of Inorganic Compounds

Inorganic materials are contained in the fuel used in coal fired boilers[3,4,11] and, to a lesser extent, in oil fired boilers.[3] In these operations the inorganic materials represent an undesirable component which contributes to the fouling and corrosion of energy transfer surfaces, and the formation of sulfur-containing pollutants.[3,4] Although the inorganic materials in black liquor can cause the fouling and subsequent corrosion of the energy transfer surfaces in recovery furnaces, their presence in the fuel is desired, as inorganic reactions essential to the recycle of the pulping chemicals occur in the boiler.

As is shown in Table 1, smaller drops have a higher surface-to-volume ratio and thus provide favorable conditions for the mass and energy transfer needed for evaporation and combustion. However, the column of gas rising through the furnace can entrain drops and carry them into the upper furnace if the drag force is larger than the gravitational force. The

desire to collect the inorganic materials in the bottom of the boiler therefore places a lower limit on the acceptable drop size produced in black liquor sprays.

The relative magnitudes of the drag and gravitational forces are not constant because the mass of the drop decreases as water and organic material are lost during the various combustion stages. Also, swelling occurs during these processes,[12,13,14] resulting in an increase in the cross-sectional area of the drop and thus the drag force acting on it. Adams and Frederick[10] examined the range of drop sizes expected to be entrained during typical recovery boiler operation. They found both a lower diameter limit, below which all drops would be carried over regardless of their initial trajectory, and an upper diameter limit, above which no larger drops would be carried over. The carry-over probability of a drop having a diameter between these limits was reported to be a function of the initial drop trajectory.

In summary, in order to control the performance of a black liquor recovery boiler, both the maximum and minimum drop size produced by the nozzle must be controlled. The presence of an upper limit of acceptable drop size is consistent with the requirements for the combustion of traditional fuels such as oil. The additional constraint on the minimum drop size is a direct result of the desire to collect the inorganic fraction of the black liquor in the lower furnace. The precise range of acceptable drop sizes will be a function of the fuel, the furnace geometry, and the air flow patterns.

DROP SIZE DISTRIBUTIONS

Most industrial atomizers produce a distribution of drop sizes rather than monosized drops.[3] These distributions can be characterized by splitting the range of drop sizes produced into J separate bins, where J is the total number of bins. For each bin, j, where $1 \leq j \leq J$, both a characteristic diameter, D_j, and the range of drop sizes in that bin, ΔD_j, are defined. A number-weighted frequency distribution, $d(N)/d(D)$, is obtained by measuring the number

fraction of drops that occurs within each size range. Similarly, a volume-weighted frequency distribution can be developed if the incremental volume fraction of the spray which occurs in each size range is known. Alternatively, cumulative number and volume distributions can be obtained if the total number fraction (or volume fraction) of drops having a diameter less than or equal to D_j is known. These cumulative distribution functions can also be derived by integrating the appropriate frequency distribution function. These four drop size distributions are plotted for an idealized spray in Fig. 3.

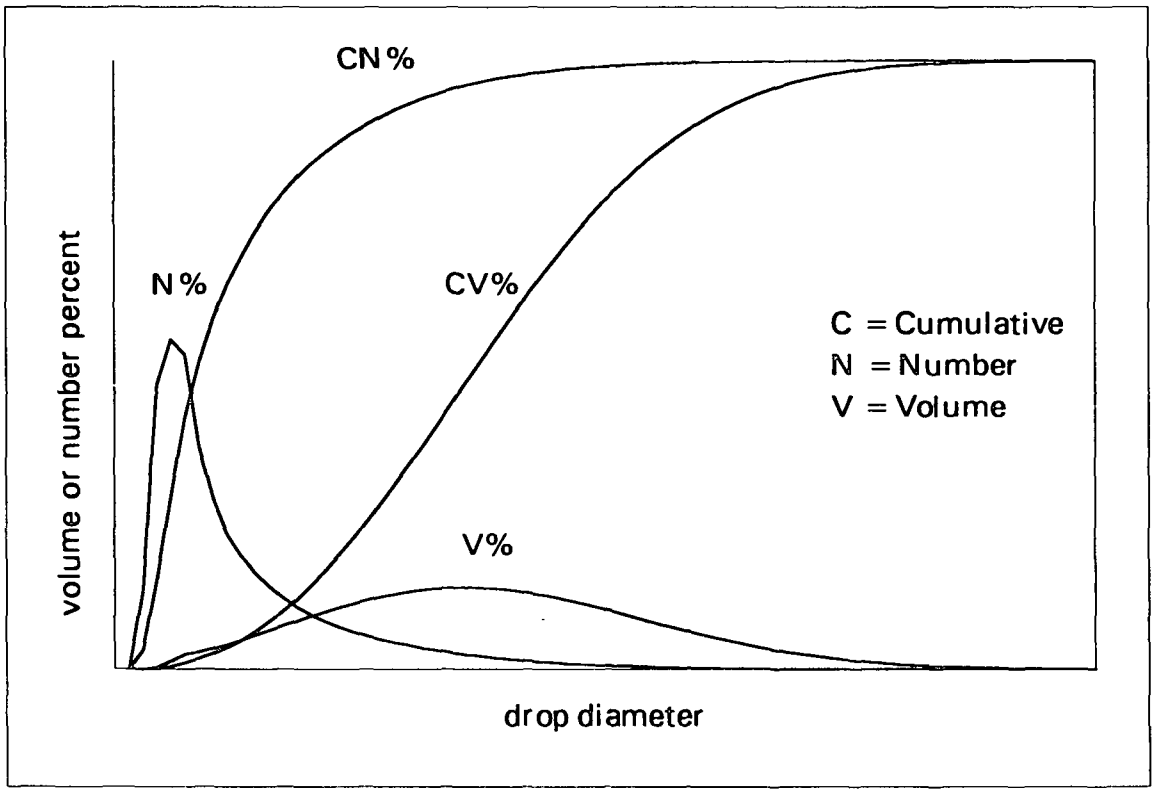

Figure 3. Number and volume drop size distributions.

These graphical representations of the drop size distribution are obtained from experimental measurements of the spray. In order to facilitate analyses and comparisons of drop size distributions, an equation is often fit to the experimental data. Empirical expressions must be used, as no theoretical basis is available for predicting drop size distributions *a priori*.[1,3]

The simplest mathematical description of a drop size distribution is a single parameter characteristic of some property of the spray as a whole. This could be either a mean or a representative diameter. Mugele and Evans[18] presented a generalized expression for defining a set of representative diameters, D_{ab},

$$(D_{ab})^{a-b} = \frac{\int_{D_{min}}^{D_{max}} D^{a}(dN/dD)dD}{\int_{D_{min}}^{D_{max}} D^{b}(dN/dD)dD}, \qquad (4)$$

where: D_{ab} = representative diameter [m];
a,b = integers;
D_{max} = maximum drop size observed;
D_{min} = minimum drop size observed; and
dN = number of drops observed in the diameter range dD.

Sowa[19] related a number of these diameters to the moments of the number-, area-, and volume-weighted normal distribution functions. He showed that the strict statistical interpretation of some of the representative diameters differed from the interpretation inferred from their commonly used names. For example, D_{20} ($a = 2$ and $b = 0$ in Eq. 4) is often referred to as the surface mean diameter.[1] Sowa's analysis showed that D_{32} is the actual mean of the surface area weighted drop diameter distribution, while D_{20} is related to the variance of the number-weighted distribution.

While a mean or representative diameter may be useful in correlating particular physical processes,[1,18] a single parameter provides only limited information about the drop size distribution of a spray; thus, a second parameter is required to indicate the range of drop sizes present. The normal distribution function has been used to model drop size distribution data. This expression,

$$\frac{d(N)}{d(D)} = \frac{1}{std\sqrt{2p}} \exp\left(-\frac{(D - D_{mean})^2}{2\ std^2}\right), \tag{5}$$

contains two adjustable parameters, a mean diameter, D_{mean}, and a standard deviation, std. The value of the standard deviation is a measure of the spread of the distribution about the mean. For the normal distribution function, the standard deviation is defined such that approximately 95% of the drops will lie within three standard deviations on either side of the mean. Thus, a larger value of the standard deviation indicates a broader spread of drop sizes.

Limited success has been achieved using the standard normal distribution to fit drop size distribution data.[1,20] This function has been modified to use a root of the drop diameter as the independent parameter, thus obtaining square root-normal, cube root-normal, etc., distribution functions.[20] The log of the drop diameter has also been used to obtain a log-normal distribution function.[1] In all cases, the distribution is described by a characteristic mean diameter, the standard deviation, and the mathematical properties of the normal distribution function.

In addition to the functions based upon the normal distribution, empirical expressions have been developed including the: Nukiyama-Tanasawa,[21] Rosin-Rammler,[22] upper-limit,[18] and three-term log-hyperbolic[23] equations. Each of these expressions has been used successfully to fit experimental data.

The Rosin-Rammler distribution is given by

$$Q = 1 - \exp\left(\frac{-D}{D_{RR}}\right)^q, \tag{6}$$

where: Q = fraction of the volume contained in drops of diameter less than D;
D_{RR} = characteristic diameter defined such that 63.2% of the mass is carried by drops of diameter less than D_{RR} ($D_{RR} = D_{0.632}$); and
q = dispersion parameter (higher values of q indicate a narrower drop size distribution).

Chin and Lefebvre[28] have advocated using the Rosin-Rammler function because it is simple; it is readily attainable from commercial drop size measuring devices; and the various mean drop diameters are uniquely related to the dispersion parameter, q.

In addition to a standard deviation or a dispersion parameter, the relative span factor (RSF), defined by

$$RSF = \frac{D_{0.9} - D_{0.1}}{D_{0.5}}, \tag{7}$$

can be used to indicate the spread of drop sizes produced. In this expression, D_n is defined as the drop diameter such that (100·n)% of the volume of fluid sprayed is contained in smaller diameter drops. Also, of interest is the ratio of the largest to the smallest drop size produced. Chin and Lefebvre[28] presented expressions which can be used to obtain these ratios if the drop size distribution is assumed to be described by the Rosin-Rammler equation. The ratio of the drop size below which 90% of the mass is carried to the drop diameter below which 10% of the mass is carried, is given by

$$\frac{D_{0.9}}{D_{0.1}} = \frac{(3.32)^{1/q}}{(0.152)^{1/q}}. \tag{8}$$

A similar expression is obtained when the drop size below which 99.9% of the mass is contained is used,

$$\frac{D_{0.999}}{D_{0.1}} = \frac{(9.968)^{1/q}}{(0.152)^{1/q}}. \tag{9}$$

The drop size distribution data presented by Dietrich[26] can be used to estimate RSF values and drop diameter ratios for the hollow cone, full cone, and flat spray nozzles he investigated. Likewise, Andreussi *et al.*[27] presented drop size data for annular-mist nozzles which can be used to calculate these parameters, as well. Table 2 contains the values for the RSF and drop size ratios calculated from the data of Dietrich[26] and Andreussi *et al.*[27] These values are only intended to demonstrate the range of these parameters which might be expected to occur in practice, as a Rosin-Rammler drop size distribution had to be assumed.

Table 2. Expected range for the Relative Span Factor and maximum to minimum drop size ratios.

Nozzle	# of trials		RSF	$\frac{D_{0.9}}{D_{0.1}}$	$\frac{D_{0.999}}{D_{0.1}}$
hollow cone[a]	9	maximum	1.18	3.4	5.3
		minimum	0.82	2.4	3.2
		average	1.0	2.8	4.1
full cone[a]	8	maximum	1.25	3.6	5.8
		minimum	1.04	2.9	4.3
		average	1.1	3.3	5.0
flat spray[a]	13	maximum	1.22	3.5	5.5
		minimum	0.91	2.6	3.6
		average	1.0	2.9	4.3
annular mist[b]	57	maximum	-	10.1	23.0
		minimum	-	2.2	2.9
		average	-	4.3	7.4

a based on data presented by Dietrich[26]
b based on data presented by Andreussi *et al.*[27]

Based on the values presented in Table 2, the range of maximum to minimum drop size can be as high as about 23 to 1 and is typically about 5 to 1. These ranges may be considered conservative, as $D_{0.1}$ was used as the minimum drop diameter, while smaller drops are presented, and in fact contain 10% of the mass. It is this broad range of drop sizes which is of concern to recovery boiler operation, as both an upper and lower limit to drop size exists. The

range of drop sizes produced by a given nozzle may be so large that staying within both limits may not be possible.

Drop size distribution functions have been discussed in greater detail in a variety of sources,[1,3,18,20,24] and are the subject of ASTM standard E 799.[25] The major point of this discussion is that at least two independent variables are required to describe a drop size distribution: some characteristic diameter, and a parameter which is indicative of the spread of drop sizes about this diameter. Additional parameters can be included to improve the fit to experimental data.

LITERATURE REVIEW

Drop size is an important parameter in numerous unit operations including: diesel and gas turbine combusters, black liquor recovery boilers, and spray dryers. The nozzles used to produce these drops generate a range of drop sizes.[1,20] The cause of this distribution of drop sizes is not well understood. Some attribute it to the random nature of the physical processes involved in converting the bulk liquid into individual drops.[1]

As mentioned before, spray systems form drops from either a sheet or a jet. In this study, we focus on the disintegration of sheets. In this section, it is convenient to separate the description of the spraying process into three stages: (1) the formation of a thin sheet of liquid, (2) the breakup of this sheet into cylindrical strands, and (3) the disintegration of these strands into drops. The potential variability of the fundamental processes occurring in each of these steps may contribute to the production of the distribution of drop sizes observed experimentally, and each stage will be examined in turn.

SHEET FORMATION

A vast array of nozzle designs are available for the production of liquid sheets. Masters[20] has presented an overview of the nozzles commonly used in spray drying applications. Lefebvre[1,2] has reviewed the mechanisms of atomization, the flow characteristics, and the performance of a variety of nozzle designs, focussing on those used in combustion applications. In the study to be discussed here, a simple splash plate nozzle was analyzed in some detail.

A splash plate nozzle is shown in Fig. 4. In this nozzle, the liquid is accelerated through a short entrance length tube and exits from a circular orifice. The resulting free jet

travels a short distance before striking a flat plate. The forces developed in the region of impact drive the liquid out radially, nearly parallel to the plate surface.[29]

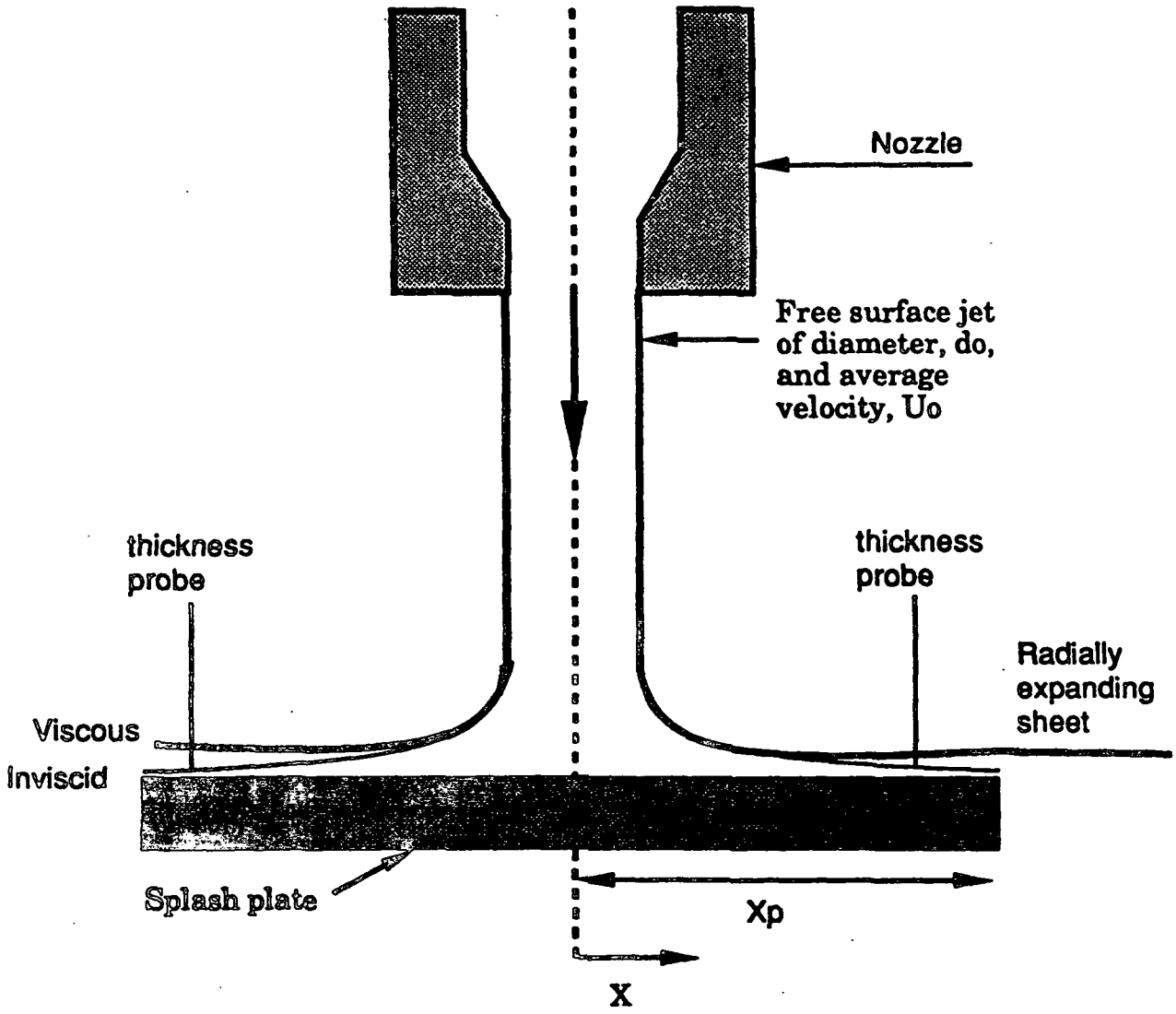

Figure 4. A splash plate nozzle.

Taylor performed several studies on the formation of sheets either by the impingement of two opposing jets[31] or by the impingement of a single jet on a plate.[29,32,33] For the case of a jet impinging on a plate at a 90° angle, a mass balance can be used to predict the sheet

thickness as a function of the distance downstream. Such an expression was reported by Taylor[33] and, after a change of variables, is given here as

$$2h(x) = \left(\frac{d_0^2}{8x}\right) \cdot \left[\frac{U_0}{U_{s,avg}(x)}\right], \tag{10}$$

where:
- d_0 = nozzle orifice diameter [m];
- h = sheet half-thickness ($2h$ = full thickness of the sheet) [m];
- U_0 = jet velocity [m/s];
- $U_{s,avg}$ = average sheet velocity [m/s]; and
- x = radial position downstream from the point of jet impact [m].

In this expression, 2h rather than h is used to represent the sheet thickness in order to be consistent with the nomenclature used in derivations to be presented later in this document.

It can be seen from Eq. 10 that the downstream sheet thickness is affected by two independent processes. First, the sheet thins due to the radial spreading of the fluid. This is a purely geometrical effect and is expressed as $d_0^2/8x$. If there were no momentum losses in the region of jet impact, and the fluid was inviscid such that no momentum loss occurred due to viscous shear at the plate surface, then the sheet thickness as a function of radial position would be described by this term alone. The inviscid sheet thickness is shown as a dashed line in Fig. 4.

Losses are expected to occur in all real spray systems. The resulting decrease in fluid momentum is accounted for by the second term in Eq. 10, $U_0/U_{s,avg}(x)$, since any loss in momentum of the fluid will result in a decrease in the average sheet velocity relative to the jet velocity. The average sheet velocity is expressed as a function of x because viscous shear forces at the plate surface are expected to decrease the fluid momentum continuously as the

fluid expands radially on the plate. The thickness of viscous fluid spreading on a plate is shown as a solid line in Fig. 4.

Although Taylor[33] did not identify the nature of the momentum losses he observed, he estimated them to be approximately 20%, so that he reported a constant value for $U_0/U_{s,avg}$ of 1/0.8. Obuskovic and Adams[34] assumed that the loss in momentum was caused solely by viscous shear at the plate surface. They performed mass and momentum balances between the nozzle orifice and an arbitrary position downstream on the plate. In their momentum balance, a linear velocity profile given by

$$U(x,z) = U_{max}(x)\left(\frac{z}{2h(x)}\right) \tag{11}$$

was assumed for the radially spreading liquid. The expression they obtained for the ratio of jet to sheet velocity is given as

$$\frac{U_0}{U_{max}(x)} = 1 + \frac{16}{Re_{jet}}\left[\left(\frac{x}{d_0}\right)^3 - \left(\frac{x_v}{d_0}\right)^3\right], \tag{12}$$

where: U_{max} = maximum velocity assumed to occur at the top surface of the sheet[34] [m/s];

x_v = an empirical constant [m];

z = distance measured perpendicular to the plate surface [m]; and

Re_{jet} = jet Reynolds number $Re = \frac{\rho_{liq} U_0 d_0}{\mu_{liq}}$.

In the original derivation by Obuskovic and Adams,[34] an algebraic error was made in the expression of the continuity equation (their Eq. 4). The velocity of the top surface of the sheet, rather than the average velocity of the sheet was used to calculate the mass flow rate as a function of downstream position. This correction was made, and the expression for the downstream sheet velocity was rederived. The form of the expression is identical to that

obtained by Obuskovic and Adams,[34] but the values of the constants have changed. The corrected values are reported in Eqs. 12 and 13.

The velocity profile assumed by Obuskovic and Adams[34] is linear; therefore, the average velocity of the sheet is equal to one-half the maximum, or top surface, velocity. Upon making this substitution and combining the resulting expression with Eq. 10, the downstream sheet thickness is predicted to be

$$2h(x) = \left(2 + \frac{32}{Re_{jet}} \left[\left(\frac{x}{d_0} \right)^3 - \left(\frac{x_x}{d_0} \right)^3 \right] \right) \cdot \left(\frac{d_0^2}{8x} \right). \tag{13}$$

Watson[35] also derived an expression relating the thickness to the downstream position for a liquid expanding radially on a solid surface. Again, only viscous shear losses were considered in the calculation of the sheet velocity. In this analysis, a similarity solution based on either a developing or fully developed boundary layer was used. The radial component of velocity was expressed as

$$U(x,z) = U_{max}(x) \cdot f(z/2h). \tag{14}$$

In this expression, $U_{max}(x)$ is the maximum sheet velocity and is a function of the radial position measured downstream from the point of jet impact, only. The similarity function, f(z/2h), was determined as part of Watson's analysis.

The location of the transition from the developing boundary layer region to the fully developed boundary layer region, x_t, is defined by

$$x_t = 0.1834 \, d_0 \cdot Re_{jet}^{1/3}. \tag{15}$$

As the radial location increases from x to x_t, the boundary layer thickness, δ, increases from 0 to 2h(x). The fluid above the boundary layer ($\delta \leq z \leq 2h[x]$) is assumed to be unaffected by the shear forces and maintains a velocity equal to that of the incident jet. The boundary layer thickness increases with x until the fluid passes into the region $x > x_t$. At this point the boundary layer thickness is equal to the sheet thickness; the unaffected fluid region no longer exists; and the top surface velocity begins to decrease. These regions and the corresponding velocity profiles are sketched in Fig. 5.

The expressions derived by Watson[35] for the sheet thickness and top surface velocity in the two regions are given as

$$2h(x) = \frac{d_0^2}{8x} + \left(1 - \frac{2p}{3\sqrt{3}c^2}\right)\delta, \tag{16}$$

where,

$$\delta^2 = \left(\frac{\pi\sqrt{3}c^3}{\pi - c\sqrt{3}}\right)\cdot\left(\frac{\nu\, x d_0^2}{4\, Q}\right) \tag{17}$$

and

$$U_{max}(x) = U_0 = \text{jet velocity} \tag{18}$$

for $x \leq x_t$, and by

$$2h(x) = \left(\frac{2\,\pi^2}{3\,\sqrt{3}}\right)\cdot\left(\frac{\nu(x^3 + \Gamma^3)}{Q\,x}\right) \tag{19}$$

and

$$U_{max}(x) = \left(\frac{27c^2}{8\,\pi^4}\right)\left(\frac{Q^2}{\nu(x^3 + \Gamma^3)}\right) \tag{20}$$

for $x > x_t$,

where:
- x_t = location of transition to fully developed boundary layer flow [m];
- c = constant = 1.402;
- Q = volumetric flow rate [m^3/s];
- δ = boundary layer thickness [m];
- ν = kinematic viscosity ($\nu = \mu_{liq}/\rho_{liq}$) [$m^2/s$]; and
- Γ = characteristic length scale [m].

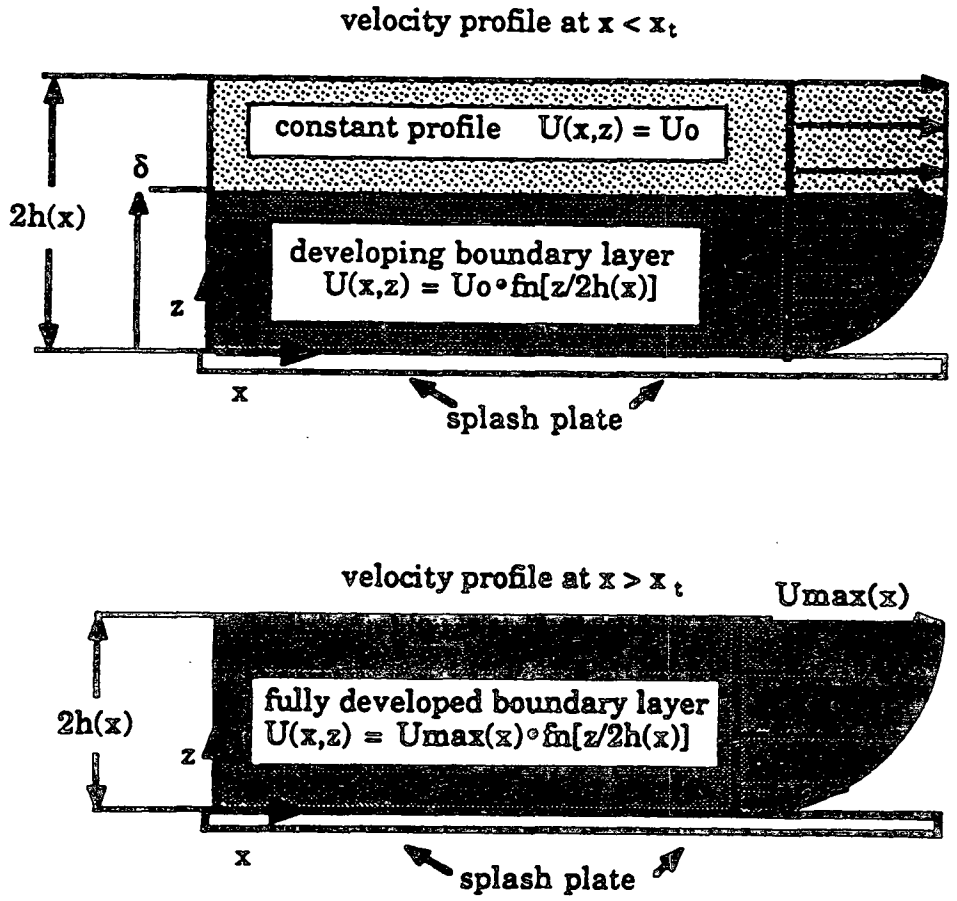

Figure 5. Boundary layer velocity profiles for $x < x_t$ and $x > x_t$.

It is important to note that the variable h in these expressions is the sheet half-thickness, while the same symbol was used for the full sheet thickness in the original work by Watson.

In these expressions, Γ is a characteristic length scale given here as

$$\Gamma = 0.330\, d_0 Re_{jet}^{1/3}. \qquad (21)$$

The analysis by Watson will be applied to the splash plate nozzle in a later section.

STRAND FORMATION

Dombrowski and Fraser[36] performed a comprehensive photographic study on the breakup of sheets produced by fan spray nozzles. A wide variety of liquids were sprayed, and the effects of varying liquid physical properties over several orders of magnitude were investigated. A representative list of the fluids investigated is given in Table 3 in order to demonstrate the range of liquid properties they examined.

Table 3. A representative list of the liquids investigated by Dombrowski and Fraser.[36]

liquid sprayed	temperature (°C)	density (gm/cc)	surface tension (dyne/cm)	viscosity (cp)
mercury	20	13.60 [a]	476 [a]	1.55
sodium	148	0.92	187	0.55
distilled water	20	1.00	73	1.00
84 % glycerine/water	20	1.22	66	99.60 [a]
98% ethyl alcohol	20	0.80	23 [b]	1.28
acetone	20	0.79 [b]	24	0.32 [b]

a Maximum value for liquids investigated
b Minimum value for liquids investigated

Dombrowski and Fraser[36] identified several mechanisms of liquid sheet breakup. The dominant mechanism varied with the liquid properties and the nozzle operating conditions, specifically the discharge pressure and the sheet velocity.

Rim Disintegration

The liquid sheet produced by a fan spray nozzle spreads out from the orifice as the sector of a circle. The two side edges of this sheet are drawn in by surface tension forces

producing rims. Liquid drops are formed both from antennae extending from these edges and from the breakup of the rims themselves.[36] An image of drop formation via the rim mechanism is shown in Fig. 6. The diameter of the rims and the size and frequency of drop formation depend on the surface tension and the viscosity of the liquid. With low-viscosity fluids, the rims break into drops near the nozzle, leaving a thin sheet edge. Surface tension forces rapidly contract this new edge forming another rim, and the process is repeated. When higher viscosity liquids are sprayed, the original rims persist further downstream, and fewer drops are formed from rim breakup.[37]

When a jet impinges on a plate at a 90° angle, the liquid will spread out in all directions forming a circular sheet. The only free rim in this case will be the leading edge of the sheet. The equilibrium location of this edge was investigated by Huang,[38] who formed sheets by the impingement of two axially opposed jets. For the case of low jet Weber numbers ($We_{jet} < 800$), where the Weber number is defined by

$$We_{jet} = \frac{U_0^2 d_0 \rho_{liq}}{\sigma}, \tag{22}$$

with σ representing the surface tension, the equilibrium location of the leading rim could be predicted by assuming a balance between the momentum force of the fluid to the opposing surface tension force.

The resulting expression is

$$x_b = \left(\frac{C_c d_0}{8}\right) \cdot We_{jet}, \tag{23}$$

where C_c is the contraction coefficient (a function of the nozzle geometry), and x_b is the downstream location of the leading edge (breakup distance). Huang reported good agreement between the predicted and measured location of the leading edge of the sheet.

Huang[38] investigated the breakup length of sheets at higher Weber numbers as well ($800 < We_{jet} < 30{,}000$). In this regime, the breakup distance was no longer determined by the balance of surface tension and inertial forces. Rather, the presence of large amplitude antisymmetric waves resulted in the destruction of the sheet before the equilibrium position could be attained. Thus, for circular sheets produced in this range of Weber numbers, the rim disintegration mechanism is not expected to contribute to the formation of drops.

Wave Mechanism

The waves observed by Huang[38] were described qualitatively by Dombrowski and Fraser.[36] They noted that a wave mechanism of liquid sheet breakup occurred at conditions of low viscosity and low surface tension. The waves were induced by aerodynamic forces acting on the air/liquid interface. As the amplitude of the waves increased, strands were torn from the crests, and holes were blown through the sheet. The holes formed in this manner were characterized by the shedding of drops from their expanding rims.

Fraser et al.[39] described an idealized wave disintegration mechanism which is summarized here. A single, optimally growing wave increases in amplitude with position downstream. When this wave reaches its critical amplitude, sheet segments are torn off at half-wavelength intervals to form bands of liquid. Surface tension forces rapidly contract these bands into cylindrical strands which ultimately break up into drops.

Analyses of the wave breakup mechanism have focused on the temporal or spatial growth of disturbances to the air/liquid interface. When this boundary is perturbed, aerodynamic, inertial, surface tension and viscous forces will be active. The stability of the sheet and the growth rate of unstable disturbances are determined by the relative magnitudes of these forces.

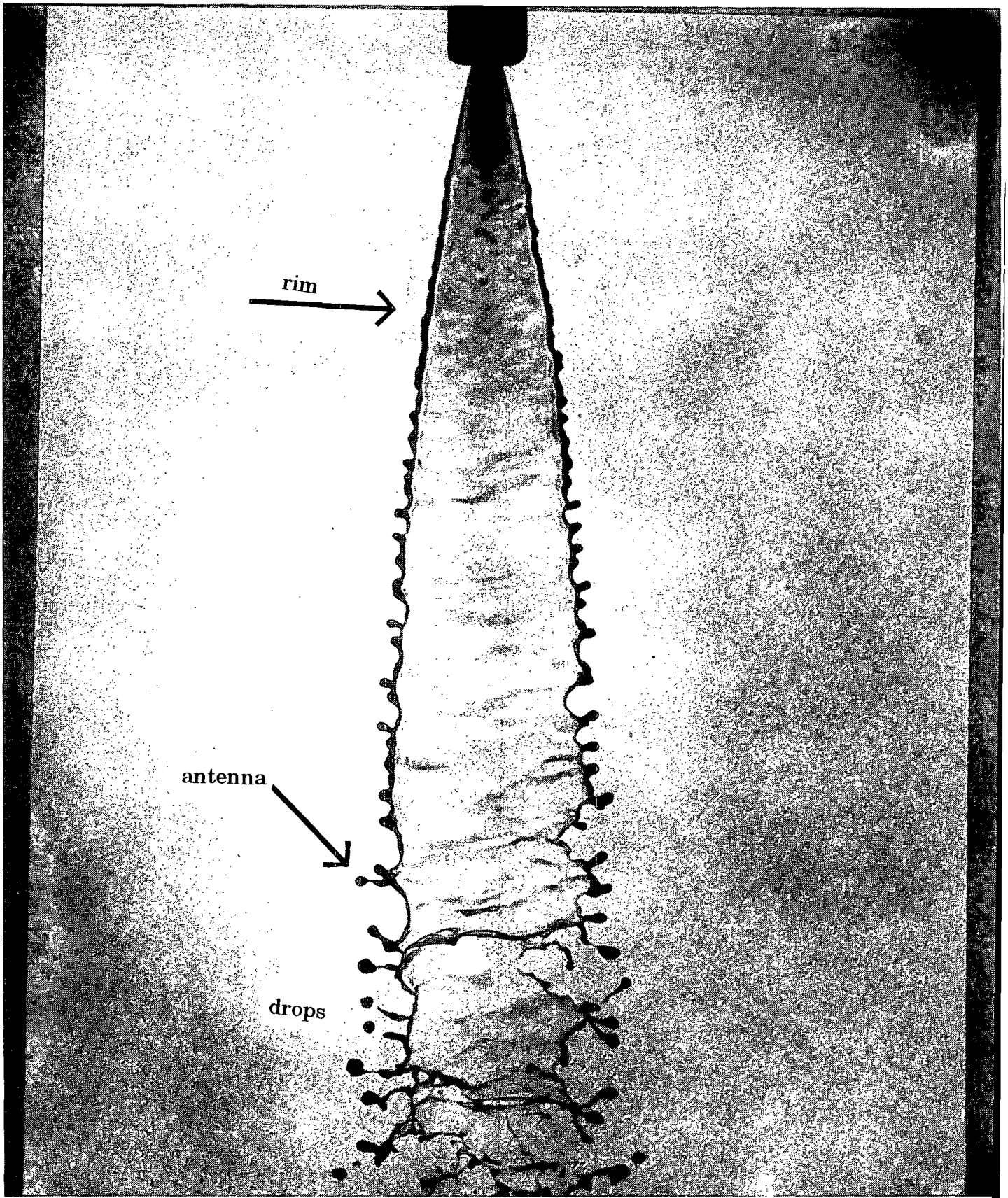

Figure 6. The rim disintegration mechanism.

Description of the Relevant Forces

A planar liquid sheet is shown in Fig. 7. The same sheet is also shown perturbed by a sinuous wave. The crest and trough of the wave are labeled "1" and "2," respectively. Once initiated, the disturbance will continue to grow unless other forces in the system overcome the inertia of the liquid.

The wave perturbation causes an increase in interfacial area, δA. The work required to create this additional area, W_s, is given by

$$W_s = \sigma \delta A. \tag{24}$$

If this perturbation is to grow, additional energy would be required to continue increasing the surface area. Thus, the surface tension force is stabilizing as it retards the growth of all disturbances to the air/liquid boundary.[1]

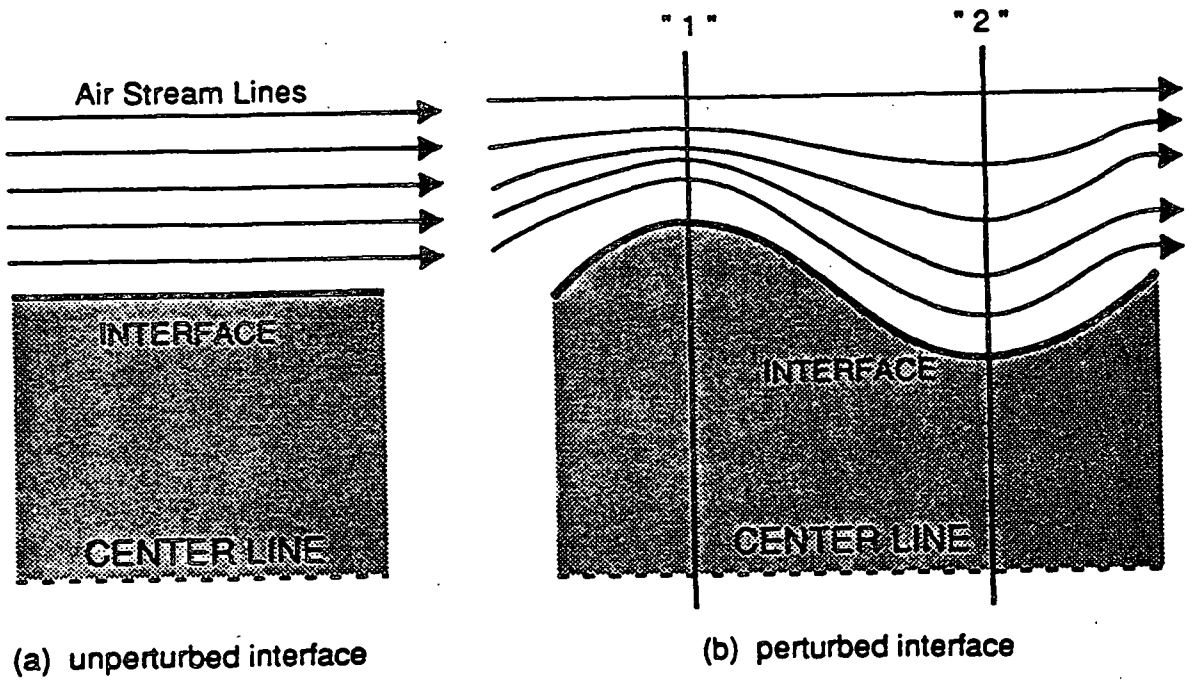

Figure 7. A planar and a perturbed liquid sheet.

In contrast, aerodynamic forces are destabilizing.[1] At point "1," the air moving relative to the liquid sheet surface will be accelerated. This increase in velocity is depicted by a decrease in the spacing between stream lines. As the gas velocity increases, the gas phase pressure will decrease according to Bernoulli's Equation,

$$\frac{P}{\rho_{gas}} + \frac{U_{gas}^2}{2} = \text{constant}, \tag{25}$$

where: P = gas phase pressure [kg/ms^2];
U_{gas} = velocity of the gas phase relative to the liquid phase [m/s]; and
ρ_{gas} = gas phase density [kg/m^3].

Similarly, at point "2," the air velocity will be lower, and the gas phase pressure will be higher. The result is a destabilizing pressure gradient which drives the growth of disturbances.

A growing disturbance in the position of the sheet surface will produce velocity gradients in the liquid and air. Viscous forces will act to dampen these gradients and retard growth; thus, like the surface tension force, viscous forces are expected to stabilize a planar sheet.[40] However, Li and Tankin[41] have reported a viscosity-enhanced mode of instability in addition to the aerodynamic instability discussed here.

Theory for Planar Inviscid Sheets

Numerous analytical studies on the growth of disturbances have been performed using the ideal flow assumption (inviscid, incompressible, irrotational flow).[39,42,43,44] In these studies, the stability of a planar liquid sheet was modeled in Cartesian coordinates using a first-order perturbation scheme. A discussion of the key steps in these analyses and the important results obtained are presented below.

A semi-infinite liquid sheet of thickness $2h_o$ travels at a uniform velocity, U_s, relative to the surrounding air. The positions of the upper and lower interfaces are perturbed from their equilibrium positions, $+h_o$,

$$h_+ = +h_o + \hat{h} \cdot e^{i(kx - st)}, \tag{26}$$

and $-h_o$,

$$h_- = -h_o + \hat{h} \cdot e^{i(kx - st + \zeta)}, \tag{27}$$

where: h_+ = position of the sheet top surface relative to the center line [m];
h_- = position of the sheet bottom surface relative to the center line [m];
h_0 = undisturbed sheet half-thickness [m];
$\hat{h}$ = disturbance magnitude [m];
k = radial perturbation wave number [m^{-1}];
s = temporal growth rate parameter [s^{-1}]; and
ζ = phase angle between upper and lower sheet surface disturbances.

In these expressions, both k and s are continuous variables. The nature of the radial perturbation wave number, k, governs the spatial behavior of the disturbance. If k is real only, the disturbance will oscillate sinusoidally with position downstream. If k has a positive (negative) imaginary component, the magnitude of the disturbance will decay (grow) exponentially with position downstream. A disturbance which grows exponentially and has zero group velocity is said to be unstable in an absolute sense.

Similarly, the growth rate parameter, s, governs the temporal behavior of the disturbance. A value of s that is real only indicates a perturbation which oscillates in time. Because of the negative sign in front of the temporal exponents in Eqs. 26 and 27, the

imaginary part of s must be positive for exponential growth and absolute temporal instability to occur.

An expression relating the growth rate parameter to the wave number as a function of the liquid physical properties and the operating conditions is obtained by simultaneously solving the gas and liquid phase continuity and momentum equations. The boundary conditions applied are: (a) the liquid and gas velocities at each interface must equal the velocity of that interface (fluid cannot cross the boundaries); (b) the upper and lower gas-phase velocities must remain finite as z approaches $+\infty$ and $-\infty$, respectively; and (c) the pressure on the liquid side of an interface must equal the sum of the gas phase pressure at that location and the LaPlace contribution resulting from the presence of a curved interface. The gas phase pressure is determined from the unsteady Bernoulli Equation, and the magnitude of the LaPlace contribution is given by the Young-LaPlace Equation,

$$P_{surf} = \sigma(\nabla \cdot \tilde{n}), \tag{28}$$

where: P_{surf} = LaPlace contribution to the liquid phase pressure [kg/ms^2];

$\tilde{n}$ = unit outward normal vector;

∇ = gradient operator [m^{-1}] $\frac{\partial}{\partial x} + \frac{\partial}{x\partial\theta} + \frac{\partial}{\partial z}$ (in polar coordinates);

x = radial polar coordinate; and

z = axial polar coordinate.

In this expression, $\tilde{n}$ is the unit outward normal vector, and thus, $(\nabla \cdot \tilde{n})$ defines the local radius of curvature.

Using this procedure, Hagerty and Shea[44] demonstrated that only two wave forms could exist in the sheet, antisymmetric (sinuous) waves for which the disturbances to the upper and lower interfaces are in phase ($\zeta = 0$), and symmetric (dilational or varicose) waves for which the disturbances are 180° out of phase ($\zeta = \pi$). These wave forms are sketched in

Fig. 8. At all conditions where these disturbances were temporally unstable, the calculated growth rate of the sinuous wave was greater than that of the corresponding dilational wave.[44] This analytical result has been supported by experimental observations.[44,45]

For the case of sinuous waves, the temporal growth rate of a disturbance is given by[44]

$$s_{sine} = \frac{-2kU_s\tanh(kh_o) \pm \sqrt{[2kU_s\tanh(kh_o)]^2 - 4(\tanh(kh_o)+\gamma)(k^2U_s^2\tanh(kh_o) - \sigma k^3/\rho_{liq})}}{2(\tanh(kh_o)+\gamma)}. \quad (29)$$

In this expression, γ is the ratio of gas density to liquid density. This ratio is usually much less than $\tanh(kh_o)$ and can be neglected in comparison; thus, the full temporal growth rate expression can be reduced to

$$s_{sine} = -kU_s \pm \sqrt{\frac{\sigma k^3/\rho_{liq} - \gamma k^2U_s^2}{\tanh(kh_o)}}, \quad (30)$$

where γ is the density ratio ($\gamma = \rho_{gas}/\rho_{liq}$). A similar expression was derived for dilational waves,[44]

$$s_{dil} = -kU_s \pm \sqrt{\frac{\sigma k^3/\rho_{liq} - \gamma k^2U_s^2}{\coth(kh_o)}}. \quad (31)$$

In Eqs. 30 and 31, the temporal growth rate parameter can be expressed as the sum of a real and an imaginary part,

$$s = s_{real} + i \cdot s_{imag}. \quad (32)$$

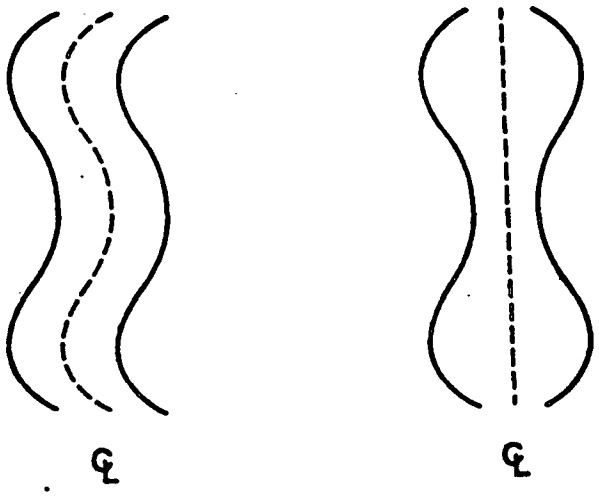

(a) sinuous (b) dilational

Figure 8. Sinuous and dilational wave disturbances.

As previously stated, the imaginary part of s must exist for absolute temporal instability to occur. This can only occur when the inequality,

$$k < \frac{\rho_{gas} U_s^2}{\sigma}, \tag{33}$$

holds. This result was presented by both Fraser et al.,[39] and Hagerty and Shea[44] as the minimum or critical wavelength for instability, λ_{crit}. Their result,

$$\lambda_{crit} = \frac{2\pi\sigma}{\rho_{gas} U_s^2}, \tag{34}$$

can be obtained by substituting the definition of the wave number ($k = 2\pi/\lambda$) into Eq. 33 and rearranging for the wavelength. The wavelength of the sinuous disturbance with the maximum temporal growth rate was predicted by Squire[42] and Fraser et al.[39] and is given as

$$(\lambda_{opt})_{sine} = \frac{4\pi\sigma}{\rho_{gas} U_s^2}, \qquad We >> 1. \tag{35}$$

This expression is only valid when the liquid sheet Weber number defined as $\left(We_{sheet} = \frac{\rho_{liq} U_s^2 h}{\sigma} \right)$ is much greater than one. (Note that this definition of the Weber number differs from Eq. 22 in that the sheet half-thickness, rather than the jet diameter, is used as the characteristic length scale.) Squire[42] defined the Weber number as the reciprocal of We_{sheet} and, thus, required his Weber number to be much less than one.

Because first-order perturbation techniques were used to obtain these results, the expressions are valid only when the disturbance magnitudes are small compared to the sheet thickness. However, it is generally assumed that the wave of optimum growth at this condition will also dominate at breakup when the disturbance amplitudes are large.[43]

Theory for Viscous Sheets

The results obtained for inviscid sheets have been extended by Dombrowski and Johns[40] to include the effects of a finite liquid-phase viscosity and a decreasing sheet thickness. The growth rate of a disturbance was found to be a function of both the wavelength and the sheet thickness; thus, the wave of maximum growth rate at one distance from the nozzle may not be the optimal wave further downstream. However, the results of this analysis were used to demonstrate the existence of a single wave of maximum amplitude at all positions downstream;[40] therefore, the breakup of the sheet is expected to be dominated by a disturbance of a particular wavelength. Dombrowski and Johns[40] also predicted that viscous forces would retard the growth of waves; therefore, the growth rate of a disturbance in a viscous sheet is less than the growth rate of the same disturbance in an inviscid sheet.

Li and Tankin[41] analyzed the stability of viscous sheets over a wide range of Weber numbers. In agreement with Dombrowski and Johns,[40] they found that an increase in liquid

viscosity reduced the growth rate of aerodynamic instabilities and increased the wavelength of maximum growth rate. In addition to the aerodynamic instability, they reported the existence of a viscosity-enhanced instability. However, this mechanism was only important when the gas phase Weber number was less than the ratio of gas density to liquid density.

Radially Expanding Sheets

Dombrowski and Johns[40] considered the stability of a sheet that decreased in thickness with position downstream; however, they assumed that the rate of change of sheet thickness was small enough that the sheet could be modeled as planar at any given location. Weihs[46] also examined the behavior of radially thinning, viscous sheets, but did not apply the local planar sheet assumption in his initial analysis. Both Weihs[46] and Dombrowski and Johns[40] determined that the temporal instability limit was identical to that predicted by Fraser et al.[39] and Hagerty and Shea,[44] and that the wave of maximum growth rate was a function of sheet velocity and thickness. The magnitude of the change in the wavelength of maximum growth rate per unit change in sheet thickness was predicted to increase with increasing liquid viscosity.

In addition to the temporal instability reported by others, Weihs[46] predicted a form of spatial instability resulting from a sinusoidal disturbance with increasing successive maxima. This form of instability could occur even when the sheet was temporally stable.

Perforation Mechanism

In their study of fan spray nozzles, Fraser and Dombrowski[36] observed a third mechanism of sheet disintegration. Unlike the wave mechanism, the perforation mechanism involves the formation of holes in the sheet near the nozzle orifice. Liquid is collected in the thick rim formed around each expanding hole. As neighboring rims intersect, a web of strands

is formed. No drops are formed during the growth of the rims, but the web itself is unstable and breaks up into drops.

Sources of Perforations

The perforation mechanism has been investigated by numerous researchers. The source of the holes has been attributed to a variety of causes, many of which are particular to the specific operating conditions employed.

Dissolved air

Fraser et al.[39] investigated the role of dissolved air in the formation of perforations. They obtained photographs of a water sheet produced by a fan spray nozzle. The sheet was formed in a vacuum in order to suppress aerodynamically-induced waves. Both aerated and deaerated distilled water sheets were examined. The air content was reported to have no effect on the formation of holes nor on the breakup length of the sheet.

Clark and Dombrowski[37] also investigated the role of the release of dissolved air on hole formation. They sprayed tap water, which was found to be supersaturated with air, and distilled water with the air content reduced to 1 p.p.m. At conditions when perforations were formed, no difference in the breakup of the sheets could be detected.

Suspended particles

Dombrowski and Fraser[36] studied the breakup of water and alcohol sheets containing 3-60 micron suspended solid particles. Regardless of their size, particles wetted by the liquid did not lead to the formation of holes. Particles which were not wetted, however, initiated a perforation when the thickness of the sheet was on the order of the characteristic particle dimension.

Similarly, a water/oil emulsion spray was observed to break up via the perforation mechanism.[36] As the oil globule size was increased, the sheet ruptured closer to the nozzle where the sheet was thicker, and the breakup length of the sheet decreased.

Particle impingement

Fraser et al.[39] observed local disturbances on liquid sheets. They reported that, while not all such disturbances developed into perforations, all perforations resulted from this source. The local disturbances were attributed to the impingement of particles on the sheet surface. These particles were assumed to be drops of the sprayed liquid, and their source was investigated.

Fraser et al.[39] reported that the number of perforations was not reduced when the position of baffles in the spray chamber were adjusted to protect the sheet from drops deflected from the walls nor were perforations eliminated by the placement of parallel glass plates close to, and on opposite sides of the sheet. It was concluded that the drops must form at the nozzle tip and follow a trajectory close to the sheet before striking it. The entrainment of ambient air by the high velocity liquid sheet was suggested as the mechanism causing drops to follow such a path.

Wave interactions

Clark and Dombrowski[37] investigated the breakup of liquid sheets formed in a high temperature environment. They observed two distinct wave disturbances on the sheet. The first type, observed at low ambient temperatures, was simply the aerodynamic waves discussed previously. The second type was only observed at high ambient gas temperatures. The wavelengths of these disturbances were much shorter than the lower cutoff limit predicted for

aerodynamically-induced waves. These second waves, reported to be electrohydrodynamic in origin, were symmetric, suggesting that local thin spots led to the formation of perforations.

Thin film rupture

The fluid contained in a thin liquid film possesses different thermodynamic properties than does the same fluid in a bulk phase.[47] Short-range forces such as electric double layer interaction and London dispersion forces affect the stability of such films.

Patzer and Homsey[48] performed a theoretical analysis on the stability of spherically concentric, draining, fluid sheets. They predicted a critical film thickness for rupture on the order of one micron. This value is expected to be an upper bound, as the stabilizing effects of electric double layer repulsion were neglected.

Pandit and Davidson[49] studied the rupture of thin, draining spherical films experimentally. They found a critical rupture thickness of 0.05-0.09 microns. High ionic strength salts were added to the liquids in sufficient concentration to suppress the effects of the electric double layer; thus, these values may be considered an upper bound for the spontaneous rupture thickness, as well.

Point disturbances were observed by Dombrowski and Fraser.[36] These disturbances were shown to have originated at the nozzle orifice and were believed to be the result of turbulence. However, spontaneous rupture was ruled out as the source of perforations. Dombrowski and Fraser[36] reported an assumed critical sheet thickness of 10^{-7} μm based on work by Fisher,[50] while the minimum sheet thickness they obtained experimentally was reported to be 10^{-4} μm. These values for sheet thickness appear to be excessively small. It seems likely that a typographical error occurred as values of 10^{-7} cm (10^{-3} μm) and 10^{-4} cm (1 μm) are consistent with other data presented in the article. For instance, Dombrowski and

Fraser[36] report that sheet thickness in microns is approximately equal to 14 divided by the distance downstream in centimeters. If the reported minimum observed sheet thickness value of 10^{-4} μm is correct, the corresponding downstream distance would be 1.4×10^{5} cm. If, however, the value 10^{-4} cm is used, the corresponding downstream distance would be 14 cm.

Perforation Growth Rates

Once a hole is formed in a liquid sheet, its stability will be determined by the balance of forces acting upon it. Taylor and Michael[51] calculated, that for a planar sheet in equilibrium, any hole with a radius greater than the thickness of the liquid sheet would grow, while smaller holes would close. This conclusion was based on minimizing the surface area. Experiments in which a hole was formed in a sheet of mercury suspended in water demonstrated the existence of a minimum initial hole size for growth to occur.

Fraser et al.[39] calculated the growth rate of perforations in a flat sheet by balancing surface tension and inertial forces. The resulting expression is given as

$$e = \frac{\partial R_p}{\partial t} = \sqrt{\frac{\sigma}{h\rho_{liq}}}, \tag{36}$$

where: e = growth rate of a perforation [m/s]; and
R_P = radius of a perforation [m].

In order to maintain a nomenclature consistent with that used to describe the wave mechanism, the symbol h is used to designate the half-thickness of the sheet. For the case of a radially thinning liquid sheet, the half-thickness is inversely proportional to the downstream position. (See Eq. 10) The proportionality constant, K_N, is a function of the nozzle geometry and the flow characteristics of the sheet.

If the rate of change in sheet thickness is small, as it is far from the nozzle orifice, then the value of h in Eq. 36 can be taken as the half-thickness of the sheet at the center of the perforation as given by

$$h = \frac{K_N}{x}. \tag{37}$$

The expression for perforation growth rate in a thinning sheet is then

$$e = \sqrt{\frac{\sigma x}{\rho_{liq} K_N}}. \tag{38}$$

Fraser et al.[39] found good agreement between perforation growth rates predicted with this expression to those measured experimentally.

DROP FORMATION

Both the wave and the perforation mechanisms produce strands as an intermediate step in the formation of drops. In wave breakup, free strands are formed from the collapse of half-wavelength sheet segments, while a web of strands, resulting from the growth and merging of neighboring rims, is expected in the perforation mechanism. Usually, the formation of drops from these cylindrical structures is analyzed using traditional jet breakup theories.

Rayleigh's Analysis

One of the first theoretical treatments of the stability of capillary jets was performed by Lord Rayleigh.[52] In his analysis, Rayleigh examined the stability of a stationary, infinitely long, inviscid liquid cylinder with a circular cross section. In addition to these simplifications, the interactions of the liquid with the surrounding air were neglected. Thus, the stability of the

liquid cylinder was determined by perturbing the circular cross section and comparing the resulting inertial and surface tension forces.

Rayleigh's idealized jet was subjected to a radial perturbation of the form

$$r = r_o + A_n \cdot \exp(st) \cos(n\theta) \cos(kz). \tag{39}$$

In this expression, the axial wave number k, defined as $2\pi/\lambda$, can take on any positive value. Because the radius of the strand is 2π periodic, the tangential wave number, n, is restricted to positive integer values.

Rayleigh demonstrated that a liquid cylinder subjected to such a disturbance would be stable to all perturbations for which $n > 0$; thus, only axisymmetric disturbances ($n = 0$) were examined. Rayleigh studied the growth of axisymmetric disturbances and derived the classic equation

$$s^2 = \left(\frac{\sigma}{\rho_{liq} r_0^3} \right) \cdot \left(\frac{I_1(kr_0)}{I_0(kr_0)} \right) \cdot [kr_o - (kr_o)^3], \tag{40}$$

which relates the temporal growth rate parameter, s, to the axial wave number, k. In this expression, I_0 and I_1 are the modified Bessel functions of the first kind, of order zero and one, respectively. The growth rate parameter is made dimensionless with respect to $(\sigma/\rho_{liq} r_o^3)$ and is defined as Ψ. The dimensionless axial wave number, defined as ξ, is $k \cdot r_o$. Thus, Eq. 40 can be rewritten in dimensionless form as

$$\Psi^2 = \left(\frac{I_1(x)}{I_0(x)} \right) \cdot [x - x^3]. \tag{41}$$

In all physically real situations, ξ must be greater than or equal to zero. Thus, because $I_0(\xi)$ and $I_1(\xi)$ are always real and greater than or equal to zero when ξ is greater than zero,[53]

it can be shown that the condition for instability ($\Psi^2 > 0$) is met only when $\xi < 1$. This occurs when the axial wavelength of the disturbance is greater than the circumference of the undisturbed jet. It should also be noted that the solution to Eq. 41 exhibits a maximum; thus, a wavelength of optimum growth rate is predicted to exist. This behavior can be seen in the plot of the dimensionless growth rate versus the dimensionless axial wave number shown as Fig. 9. The peak in the growth rate curve occurs at $\xi = 0.697$. This corresponds to a wavelength of approximately nine times the radius of undisturbed jet.

The drop size which would result from Rayleigh's breakup can be determined from a simple mass balance if the liquid contained in a cylindrical section one wavelength long is assumed to collect into a single drop,

$$\rho_l(\pi r_0^2 \lambda) = \rho_l\left(\frac{\pi D^3}{6}\right) \tag{42}$$

This expression can be rearranged for the drop diameter,

$$D = \sqrt[3]{6\lambda r_0^2}. \tag{43}$$

Viscous and Aerodynamic Forces

Weber[54] incorporated liquid viscosity and air/liquid interactions into a theory of jet breakup. His analysis resulted in a quadratic equation for growth rate as a function of wave number. This expression,

$$\Psi^2 + \Psi\left(\frac{3\xi^2\sqrt{We_{str}}}{Re_{str}}\right) = \frac{(1-\xi^2)\xi^2}{2} + \left(\frac{\rho_g}{\rho_l}\right)\left(\frac{We_{str}\xi^3 K_0(\xi)}{2\,K_1(\xi)}\right) \tag{44}$$

has been made dimensionless using the same definitions as were applied to Rayleigh's equation. In this expression, K_0 and K_1 are modified Bessel functions of the second kind, of order zero and one, respectively.

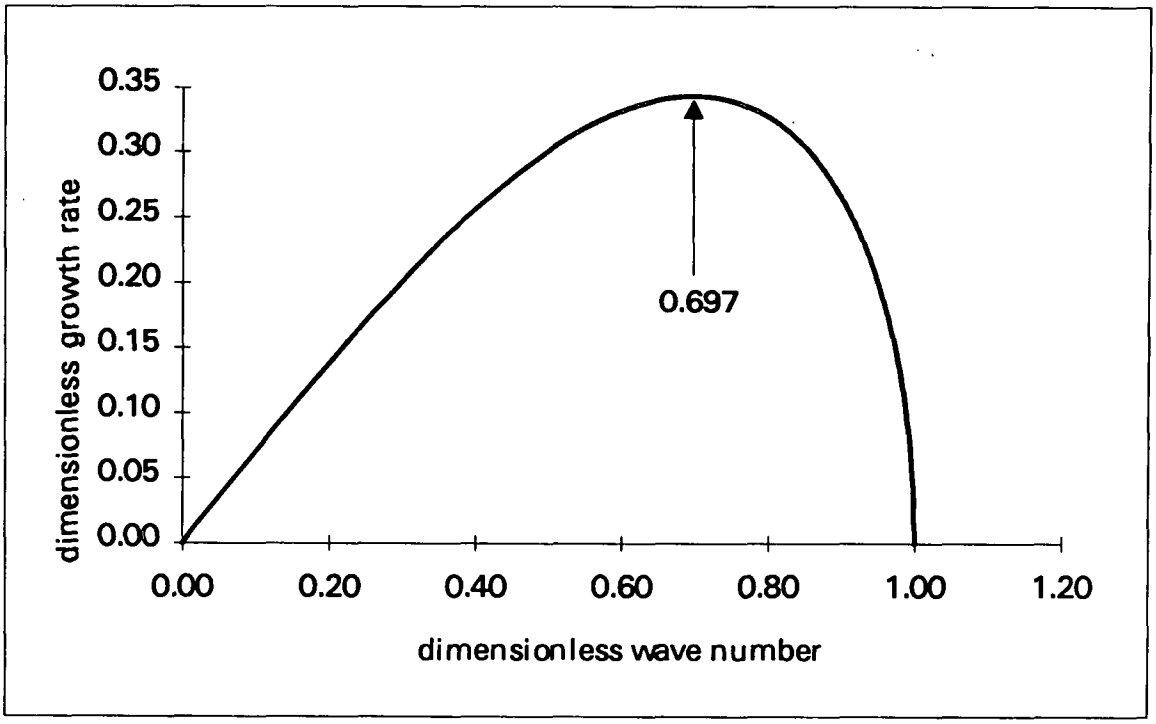

Figure 9. Dimensionless growth rate versus wave number based on Rayleigh's analysis.

In Eq. 44, the Reynold's and Weber numbers are based on the liquid phase properties and use the strand radius as the characteristic length scale. The addition of viscous and aerodynamic forces has led to a modified growth rate relation;

however, a wavelength of maximum growth rate is still predicted. Therefore, a single drop size is expected to be produced from a strand of a given diameter.

Nonlinear Analyses

The previous studies have relied on linear perturbation techniques to analyze the breakup of jets. These results are expected to be valid only when the magnitude of the disturbance is sufficiently small so that nonlinear interactions can be neglected. As the disturbances grow toward the point of breakup, these nonlinearities can no longer be neglected, and their influence on the drop sizes produced must be determined.

Yuen[55] derived a third-order perturbation solution for the capillary instability of an inviscid jet, neglecting aerodynamic interactions and found a wave of optimum growth at $\xi = 0.7$, in excellent agreement with linear theory. Rutland and Jameson[56] used Yuen's[55] results to numerically predict the shape of the jet near breakup. From this shape, both main drops and satellite drops were expected to form, where satellites are drops formed between main drops. The diameters of the main and satellite drops were calculated from the shape of the strand and compared to experimentally determined values. While the drop sizes were predicted with good accuracy, satellite drops were only predicted for $\xi < 0.7$, while experimentally satellite drops were observed for all wave number disturbances.

Yuen[55] reported that his solution contained secular terms at third order. Secular terms grow with time and cause the perturbation solution to become invalid at large times. Lafrance[57] performed a third-order perturbation analysis on an inviscid, circular jet which he claimed was free of secular terms. Like Yuen,[55] Lafrance[57] did not include aerodynamic interactions in his analysis. The two key results from this work were: (1) the third-order accurate solution still led to the prediction of a single wavelength of optimum growth rate, and (2) at certain conditions ($\xi < 0.8$), the existence of a satellite drop is predicted in addition to the main drop.

In all cases, the diameter of the satellite drop is predicted to be smaller or equal to the diameter of the main drop. Lafrance[57] compared the predicted drop sizes to experimental data reported by Rutland and Jameson,[56] as well as to data he had obtained. Good agreement was obtained in both cases. Despite the apparent success of Lafrance's[57] predictions, it has been reported that the solution is invalid at third-order as the boundary conditions were not satisfied to equal order.[58]

Despite the limitations of the nonlinear analyses discussed, the results are in good agreement with the available experimental data. Thus, it appears that the nonlinear interactions which arise as the disturbance amplitude increases lead to the formation of a satellite drop in addition to the main drop predicted by linear theory, but not to the broad distribution of drop sizes observed in industrial spray applications.

Velocity Profiles Around a Strand

The literature on strand breakup deal almost exclusively with stationary cylinders or jets travelling parallel to their axes. Yet, a significant percentage of the strands formed from sheet breakup may have the dominant component of velocity perpendicular to the z-axis. This cross flow of air is expected to interact with the liquid jet differently than would a coaxial flow.

Weihs and Frankel[59] studied the effects of a cross flowing air stream on an initially circular liquid cylinder. An analytical perturbation approach was used. The equilibrium cross-sectional shape of the strand was calculated as a second-order perturbation using the Weber number (based on gas properties) as the perturbation parameter. The analysis was stated to be valid up to $We_{str,g} = 0.5$, where

$$We_{str,g} = \frac{\rho_{gas} U_{str}^2 r_{str}}{\sigma}$$

with: ρ_{gas} = density of the gas phase [kg/m^3];
U_{str} = velocity of the strand relative to the gas phase; and
r_{str} = radius of the strand [m].

The calculated cross section was subjected to a radial disturbance similar to that employed by Rayleigh[52] and Weber.[54] The form of this disturbance is given by

$$r = r_o(\theta)\cdot(1 + \eta), \tag{45}$$

and

$$\eta = \eta_o\left(B_o + \sum_{n=0}^{\infty}\left[A_n\cdot\sin(n\theta) + B_n\cdot\cos(n\theta)\right]\right)\exp(st + ikz). \tag{46}$$

In their solution for growth rate versus wave number, Weihs and Frankel[59] showed that a perturbation with a tangential wave number of n would be unstable only if $We_{str,g} \geq \frac{n+1}{2}$, for n ≥ 1. Since the results of this analysis were restricted to conditions when $We_{str,g} \leq 0.5$, these disturbance modes could be neglected, and thus, only axisymmetric modes (n=0) were considered in the stability analysis.

Weihs and Frankel[59] solved for the growth rate as a function of wave number, and as with the previous studies, a wavelength of maximum growth rate was predicted. The wavelength of optimum growth rate was found to increase with decreasing Weber number. Although incorporating the effects of cross flow has modified the growth rate expression, only a few discrete drop sizes are expected to form, rather than a broad distribution of drop sizes.

PROBLEM ANALYSIS AND OBJECTIVES

The purpose of performing this thesis is to investigate the breakup mechanisms which dominate the disintegration of thin liquid sheets. Because of the complex flow characteristics of industrial nozzles, a simple spray configuration will be used. The particular geometry and flow characteristics were selected to be similar to those of a common black liquor spray device, the splash plate nozzle. It is expected that the results obtained using this nozzle will apply in varying degrees to other sheet forming devices as well.

Sprays can be analyzed in two independent, yet complementary ways. Liquid can be sprayed through a particular nozzle over its useful range of operating conditions and the resulting drop size and trajectory distributions measured. The effects of the adjusted parameters could then be determined and correlations developed. Alternatively, the basic mechanisms of drop formation could be investigated. This fundamental understanding of the nozzle operation could then be used to predict the effects of various operating conditions. While both approaches provide useful information, the later offers the greatest opportunity for understanding and thus optimizing the process.

The objectives of this thesis are:

- to identify the dominant mechanism(s) of sheet breakup and strand formation for splash plate sheets;
- to investigate the mechanism(s) in terms of the controlling parameters;
- to develop a description of the sheet breakup mechanism which is consistent with the experimental observations and the existing literature; and
- to derive analytical expressions for predicting characteristics of the breakup process.

EXPERIMENTAL APPROACH

The main objective of this thesis is to determine the dominant mechanisms of breakup for splash plate sprays. The mechanisms of sheet disintegration can only be identified by observing the spraying process; therefore, a facility was constructed to produce and allow the imaging of splash plate sprays. The process equipment used to produce the liquid sheet and to monitor the relevant parameters will be described.

Because of the high liquid velocities, neither direct observation nor standard photographic procedures can be used to examine sheet behavior; therefore, a variety of alternative imaging techniques were employed. The imaging methods used were short duration, intensified video imaging' and high-speed 16 mm photography. The optics and lighting arrangements for these systems will be discussed.

THE SPRAY FACILITY

A sketch of the spray facility used in this study is shown in Fig. 10. A 1.2 m x 1.2 m (4 ft. x 4 ft.) galvanized steel tank acts as a reservoir for the test fluid. The bottom of the tank slopes toward a drain located in the center of the base, providing 380 liters (100 gallons) of storage capacity. Plexiglass walls extend upward on all four sides to constrain the spray. These transparent walls provide flexibility in locating the lighting sources needed to image the sprays. A 0.5 m x 0.5 m (20 in. x 20 in.) Plexiglass window installed in the bottom of the tank allows the spray to be illuminated from below, as well. The piping and data acquisition devices are mounted on a rigid support structure surrounding the tank.

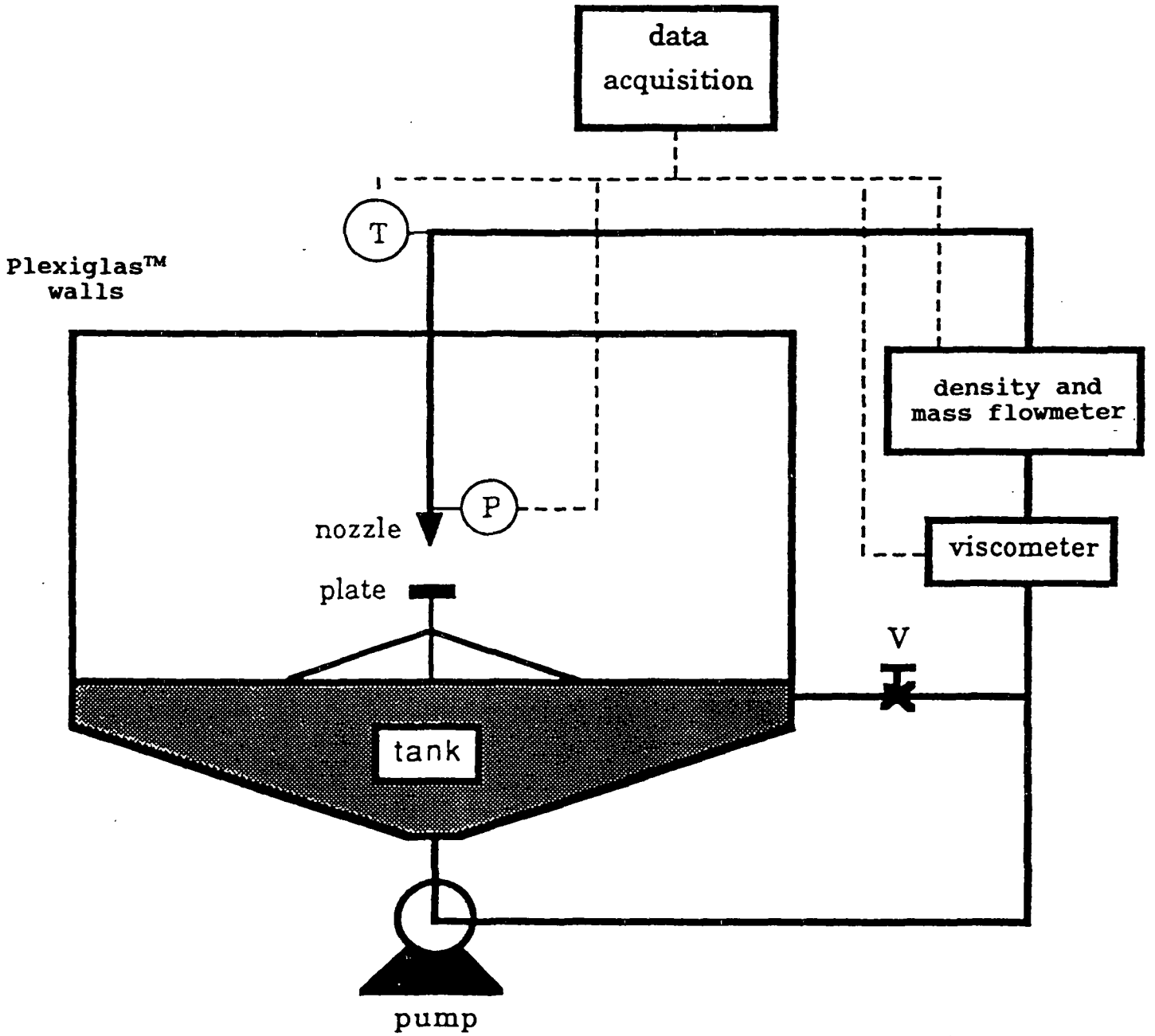

Figure 10. Sketch of the experimental spray apparatus.

The outlet of the tank discharges to the inlet of a Roper 2AM06 rotary gear pump. This pump is rated to deliver 0.023 liters (0.006 gallons) per revolution with a maximum discharge pressure of 890 kPa (100 psi). A 3.0 hp, 1725 RPM motor drives the pump, thus delivering a constant flow rate of approximately 40 liters/min (10 gallons/minute).

The discharge from the pump splits into two 1½ inch internal diameter (I.D.) lines. One line, a short recirculation loop, discharges back into the reservoir. A ball valve located in this loop controls the relative flow rates through the two lines. The main line reduces to a one inch nominal I.D. pipe before connecting to a viscometer and a flowmeter in series. The pipe reduces to one-half inch before entering a flexible tube installed to dampen any vibrations in the system. The flexible line connects to a 90° elbow, and the liquid then flows through a 56 cm (22 inch) one-half inch schedule 40 pipe (1.58 cm, 0.655 inch I.D.). A collar, located at the discharge end of this straight length of pipe, connects the nozzle to the main flow loop.

The in-line viscometer is a Brookfield TT100 coaxial cylinder rotational viscometer. The rotational speed of the sensing element is 72 RPM. The viscometer was field calibrated to achieve a reported accuracy of 1% of full scale. The full-scale range used was 0-200 cp, leading to a bias error of $\pm$ 2 cp.

A Smith Meter Inc. S100 S-mass meter was used to obtain mass flow rate and density information. For the flow rate, a rated accuracy of $\pm$0.15% of full scale was calculated for the operating conditions employed. This corresponds to a bias error of $\pm$0.3 kilograms per minute ($\pm$0.6 pounds per minute). The reported accuracy of the density output of the S-mass meter was $\pm$0.005 g/cm^3.

An Omega type J thermocouple was installed through the elbow upstream of the nozzle. The thermocouple tip was centered in the vertical pipe length about 2 cm (1 inch)

downstream of the elbow. The analog output from the thermocouple was processed by an Omega model #650J-A digital thermometer. Accounting for the uncertainty in the thermocouple and the digital thermometer, the bias error in the temperature measurements is $\pm 2°C$.

The flush mounted pressure transducer (Sensotec model #Z/5541-07) is connected to a Sensotec Model GM signal condition-indicator. The bias error in the pressure measurements resulting from this combination is ± 0.3 psia.

A threaded support rod, welded to the base of the tank directly below the discharge orifice of the nozzle, provides support for a stainless steel plate 4.99 cm (1.96 inches) in diameter. Positioning rods connected the support rod to four equally spaced locations on the base of the reservoir. Using these positioning rods, the support rod can be adjusted to ensure that the plate's surface is horizontal. Because the plate was mounted in the center of the reservoir, the liquid sheet formed from the impact of the jet on the plate will travel a minimum distance of 0.6 m (2 ft.) before striking the Plexiglass walls encompassing the spray chamber.

The top and side surfaces of the plate were polished with progressively finer grades of sandpaper. Following the polishing procedure, the surfaces of the plate were treated with a silicone release agent. The procedure for polishing and coating the plates is included in Appendix A.

Seven nozzles were used to produce straight jets. The orifice diameter of each nozzle was measured using a telescope gage. The reported diameter is the average of four measurements made at equally spaced locations around the orifice. All of the nozzles were selected to mate with a 1/2" nominal female pipe connection. The entrance region, where the flow area decreased from the 1/2" pipe to the final orifice dimension, varied with nozzle design, as sketched in Fig. 11.

Table 4. Straight jet nozzle descriptions.

nozzle	nominal diameter	measured diameter
[a]Bete Fog NF-6000	3/16 inch (4.76 mm)	4.83 ± 0.01 mm
Bete Fog NF-8000	7/32 inch (5.56 mm)	5.56 ± 0.02 mm
Bete Fog NF-10000	1/4 inch (6.35 mm)	6.07 ± 0.01 mm
[b]S.S. Co. QU-00100	15/64 inch (5.95 mm)	5.94 ± 0.01 mm
S.S. Co. QU-00120	1/4 inch (6.35 mm)	6.56 ± 0.01 mm
S.S. Co. QU-00200	21/64 inch (8.33 mm)	8.45 ± 0.01 mm
Sharp Edge	1/4 inch (6.35 mm)	6.36 ± 0.02 mm

a Bete Fog Inc., Greenfield, MA 01302

b Spraying Systems Co., Wheaton, IL 60188

The location of the nozzle relative to the plate was controlled by four positioners used to connect the movable vertical pipe, to which the nozzle was attached, to the rigid support structure mounted around the spray tank. A Newport TSV-9 vertical positioner was used to raise and lower the nozzle relative to the fixed plate surface. A Newport 460-XZ positioner was used to locate the nozzle in the plane perpendicular to the vertical axis such that the jet impacted at the center of the plate. Finally, two Newport 481-S rotary stages were used to ensure that the angle of jet impact relative to the plate surface was 90°.

Sheet thickness probes, in the form of three extended micrometers, were installed around the nozzle, 120° apart. The location of each micrometer tip was 2.14 ± 0.04 cm (0.84 ±0.03 inch) downstream from the center of jet impact and, thus, 0.36 ± 0.04 cm upstream from the edge of the plate. These probes are sketched in Fig. 4.

The in-line data acquisition devices (viscometer, flow and density meter, thermocouple, and pressure transducer) were connected to the Metrabyte DAS-8PGA analog to digital data

conversion system. The data were collected using LABTECH NOTEBOOK installed on a PC's Limited 286 personal computer.

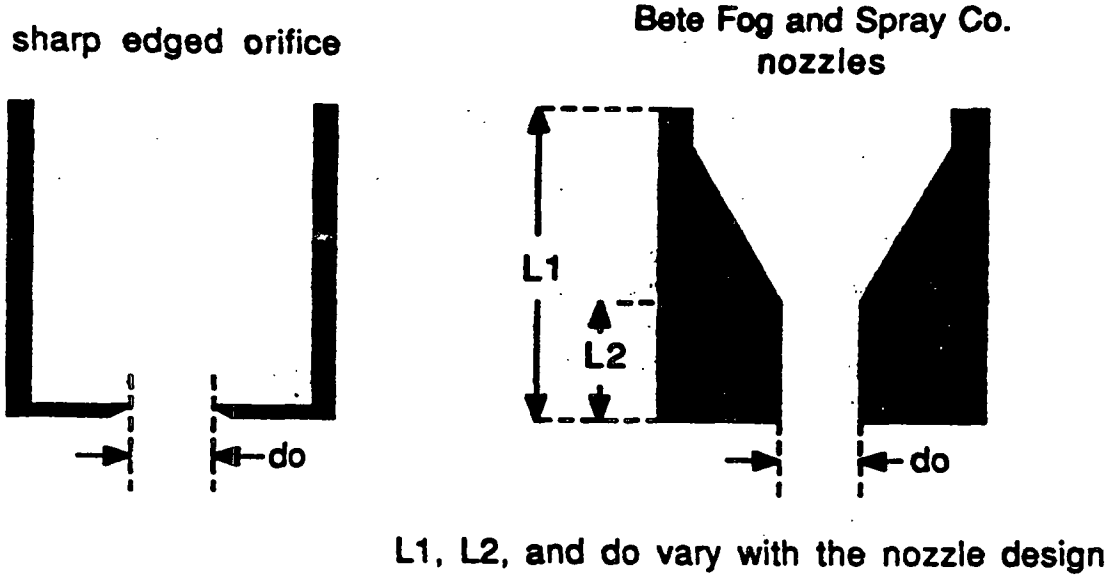

Figure 11. Sketch of the nozzle geometries.

The test fluid used was a 96% glycerol in water solution obtained from Dial Corporation. This solution was diluted with sufficient water to obtain the desired viscosity. A summary of the density, viscosity, and surface tension of glycerol/water solutions is given in Table 5.

Table 5. Physical properties of glycerol in water solutions.

glycerol	density (kg/m^3)		viscosity ($kg/m \cdot s$)			surf. tens. (kg/s^2)
weight %	@ 20°C	@ 25°C	@ 20°C	@ 25°C	@ 30°C	@ 18°C
100	1261 [a]	1258.3 [b]	1.495 [b]	0.942 [b]	0.622 [b]	0.0630 [c]
98	-	1253.2 [b]	0.971 [b]	0.627 [b]	0.423 [b]	-
95	-	1245.4 [b]	0.5435 [b]	0.365 [b]	0.248 [b]	-
88	1229.9 [a]	-	0.1472 [a]	-	-	-
84	1219.2 [a]	-	0.0842 [a]	-	-	0.0660 [c]
80	1208.5 [a]	1205.7 [b]	0.0618 [b]	0.0457 [b]	0.0348 [b]	-

a CRC Handbook - 61st Edition.[60]

b CRC Handbook - 72nd Edition.[61]

c Lange's Handbook of Chemistry - 13th Edition.[62]

The surface tension of the glycerol/water solution was measured off-line using a DuNouy ring tensiometer. A summary of the operating procedures, the experimental data, and the calculations is given in Appendix B.

THE IMAGING EQUIPMENT

In order to examine the mechanisms of breakup, the images obtained must effectively freeze the motion of the spray. Motion blur is defined as the distance an object moves during the time it is being imaged (the exposure time). Depending on the field of view and the intended end-use of the images, a motion blur of less than 0.1 to 1.0 mm was desired. Sheet velocities on the order of 10 m/s were expected; therefore, the maximum imaging time allowable was 10-100 μsec.

A Xybion ISG-500 intensified gated camera was used to obtain images of the spray stored directly on super VHS videotape for later analysis. This camera had a fixed imaging

rate of 30 frames per second; however, the exposure time for each image can be adjusted continuously between 25 nanoseconds and 30 milliseconds ($25 \times 10^{-9} \leq t \leq 30 \times 10^{-3}$ seconds).

A Redlake Hycam 16 mm high-speed camera was also used to obtain spray images. This rotating prism camera is capable of shuttering rates up to 10,000 frames per second. The exposure time for each frame is equal to (1/2.5) divided by the framing rate. Kodak 3-X and 4-X reversal film was used to collect the images. When processed, this film yields positive prints of the subject, directly.

The imaging rate of the Hycam is not constant throughout a given run, but rather, an acceleration period is followed by a constant imaging rate period. In order to determine the framing rate at each position on the exposed film, a built-in timing light generator (TLG) was used. This device placed marks on the periphery of the film at a user selected rate of 100, 1000, or 5000 hertz with a reported accuracy of 0.01%. After exposing the film, the number of marks per frame could be counted. Then, using the known TLG rate, the framing rate could be determined.

OPERATING PROCEDURES

The general procedure for operating the spray system is outlined here. The key details for each set of experiments will be presented in the results section.

Inspect the splash plate for defects and repolish and coat if necessary
Install the desired test nozzle
    Connect the nozzle to the collar
    Adjust the position of the nozzle
        Ensure that the jet impacts the plate surface at a 90° angle
        Ensure that the jet impacts at the center of the plate
    Turn on the pump (low flow) and observe the jet impact and the resulting sheet
        The fluid sheet should form a symmetric bell around the plate
        Make fine adjustments to the nozzle position based on the shape of the bell
        Check agreement of sheet thickness measurements from three probes
        Turn off the pump
Modify the data acquisition program
    Apply the appropriate scaling factors for the nozzle selected
    Adjust the data acquisition rate and duration
Turn on the data acquisition devices and allow them to warm up
Position the imaging equipment as desired
    Adjust the lighting
    Locate the camera
        Check the field of view and light levels
        Obtain an image of a length scale for subsequent measurements
Run the data acquisition program to obtain a zero flow reference pressure
Turn on the pump
Adjust the flow rate to the desired value
Run the data acquisition program and collect the additional data desired
Adjust the flow rate and repeat
Monitor the fluid in the reservoir between runs, when entrained air bubbles are visible, stop the experiments and allow them to rise out of the fluid

RESULTS

MECHANISM OF SHEET BREAKUP

The photographs shown as Figs. 12-15 represent only a small fraction of the high-speed 16 mm and video images obtained in this study. After reviewing the full set of films obtained, a qualitative description of the breakup process was developed with the aid of theoretical analyses.

The formation and interaction of holes in the sheet clearly dominate the first stage of sheet breakup. The majority of these holes form in a narrow region of the downstream position. These holes grow rapidly, interact to form clumps and strands of liquid which ultimately break up into drops.

The formation and growth of a perforation is shown in Figs. 12a-l. The rim of the perforation is first visible in Fig. 12c. If the hole is present in the prior images, the resolution of the images is not sufficient to detect it. In subsequent images (12d-l), the perforation grows, and its rim becomes thicker. In Figs. 12j-l, the perforation rim approaches and ultimately merges with the rims of other perforations, forming a small network of strands.

The interaction of two adjacent perforations is also shown in Figs. 13a-f. In Fig 13b, a section of the sheet is seen inside the perimeter of the lower perforation. This indicates that the sheet is folding over upon itself, as the visible sheet segment is below the region containing the perforation.

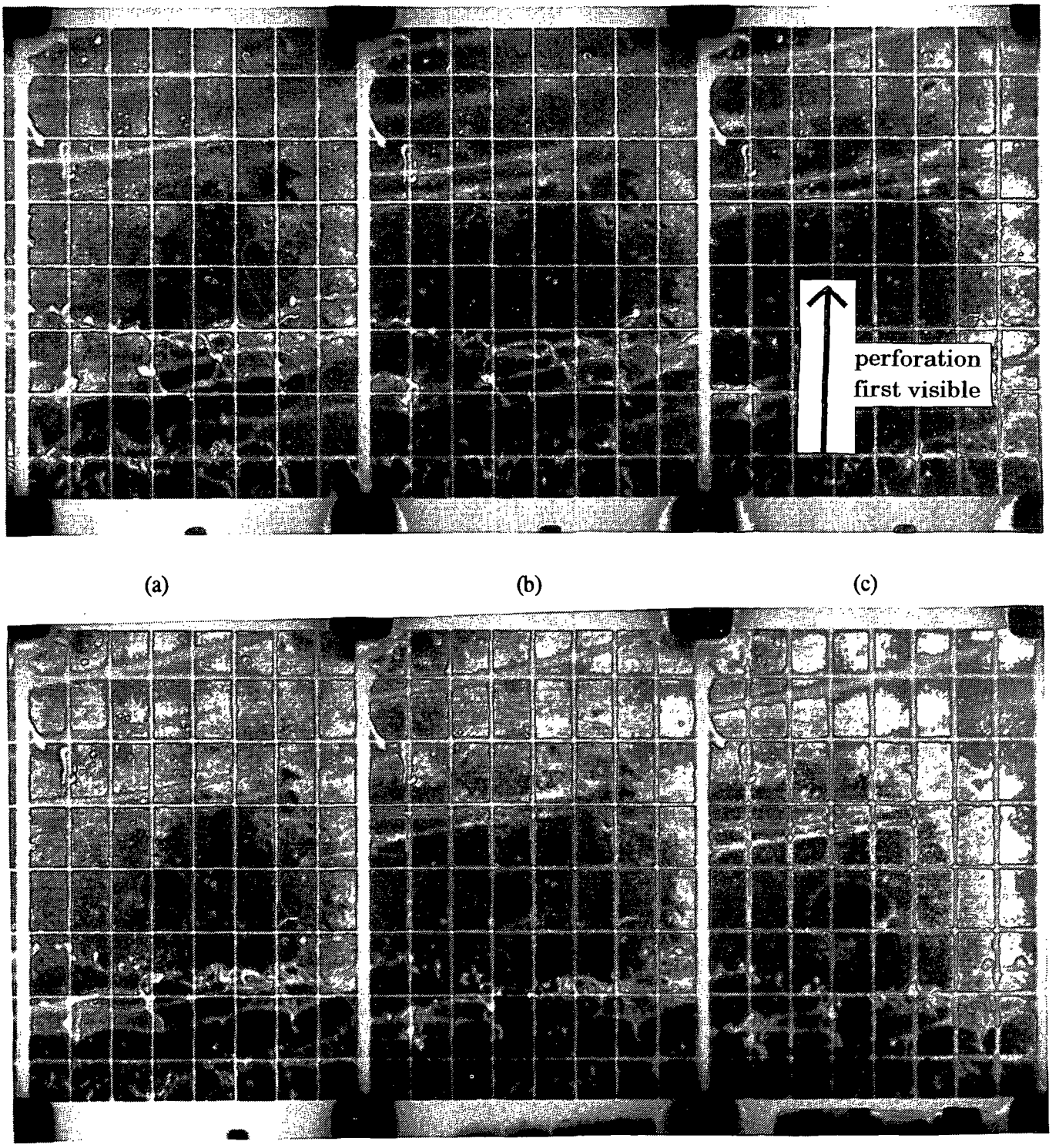

Figure 12. Formation, growth, and interaction of perforations.

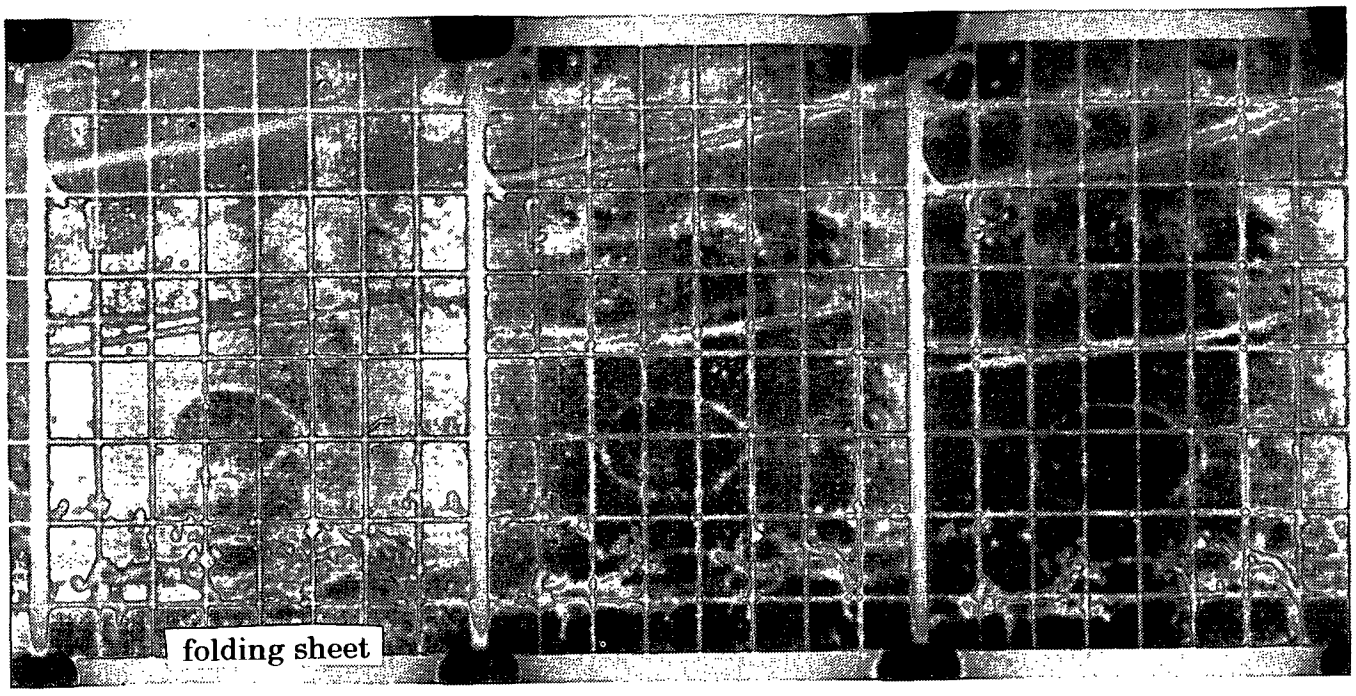

(g) (h) (i)

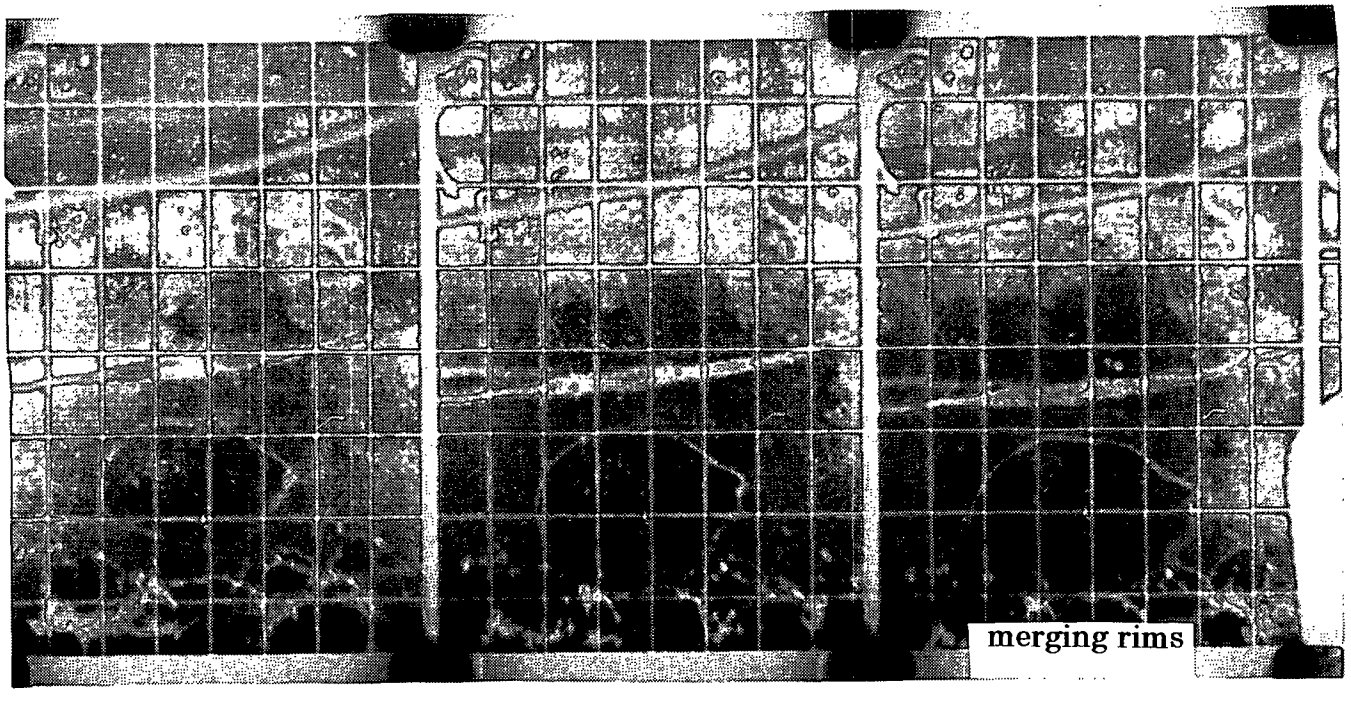

(j) (k) (l)

Figure 12. Formation, growth, and interaction of perforations (continued).

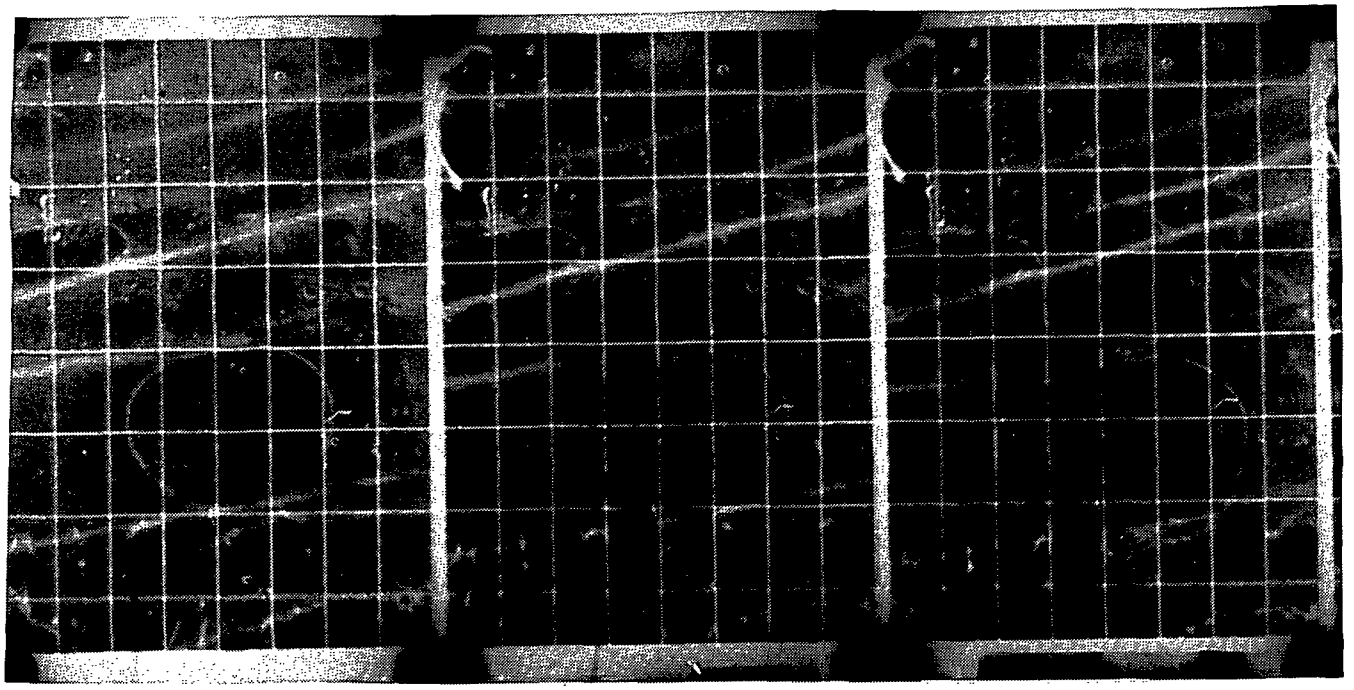

(a) (b) (c)

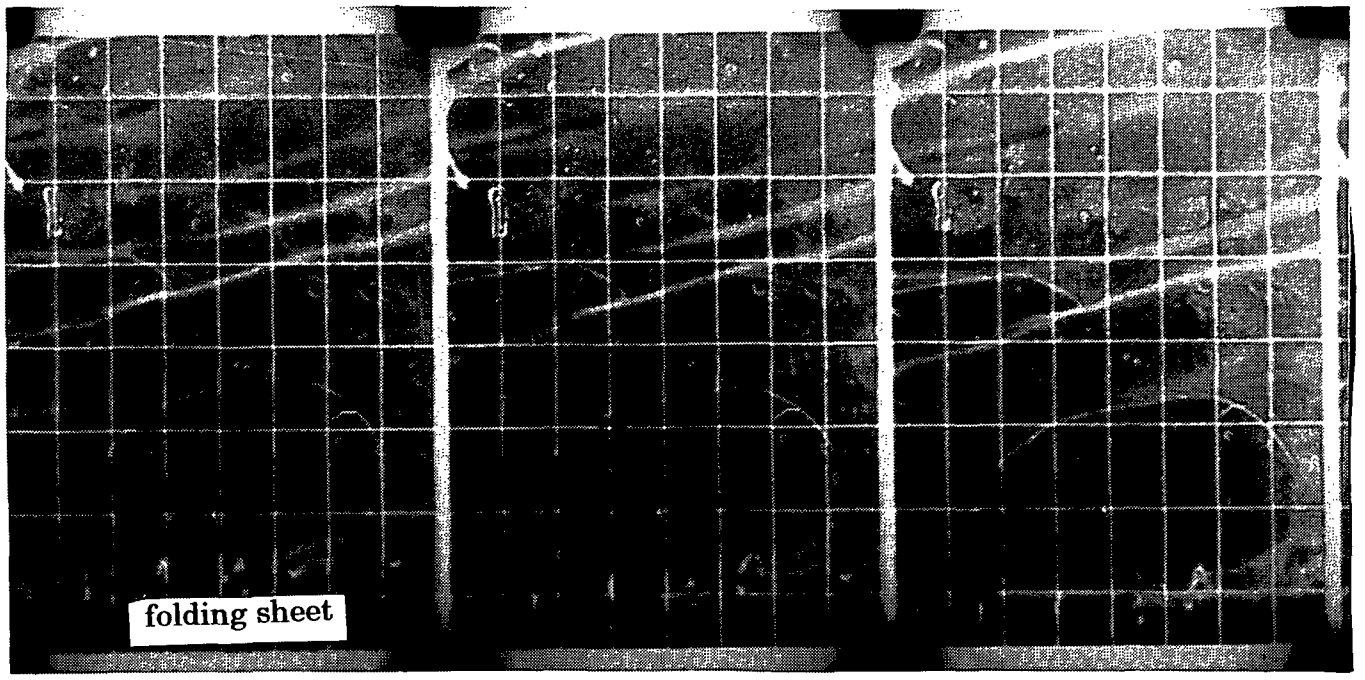

(d) (e) (f)

Figure 13. Perforation growth and sheet folding.

Figure 14 shows a section of the sheet in the region of breakup. The light streaks in the upper right-hand corner are associated with the sinuous waves in the sheet. A spray of droplets can be seen in the lower left-hand corner of the image. The transition from the sinuously disturbed sheet to the droplets is seen to occur in a narrow band, approximately 2-3 cm wide. In this region, the merging of several perforations and the resulting formation of clumps and strands can be seen.

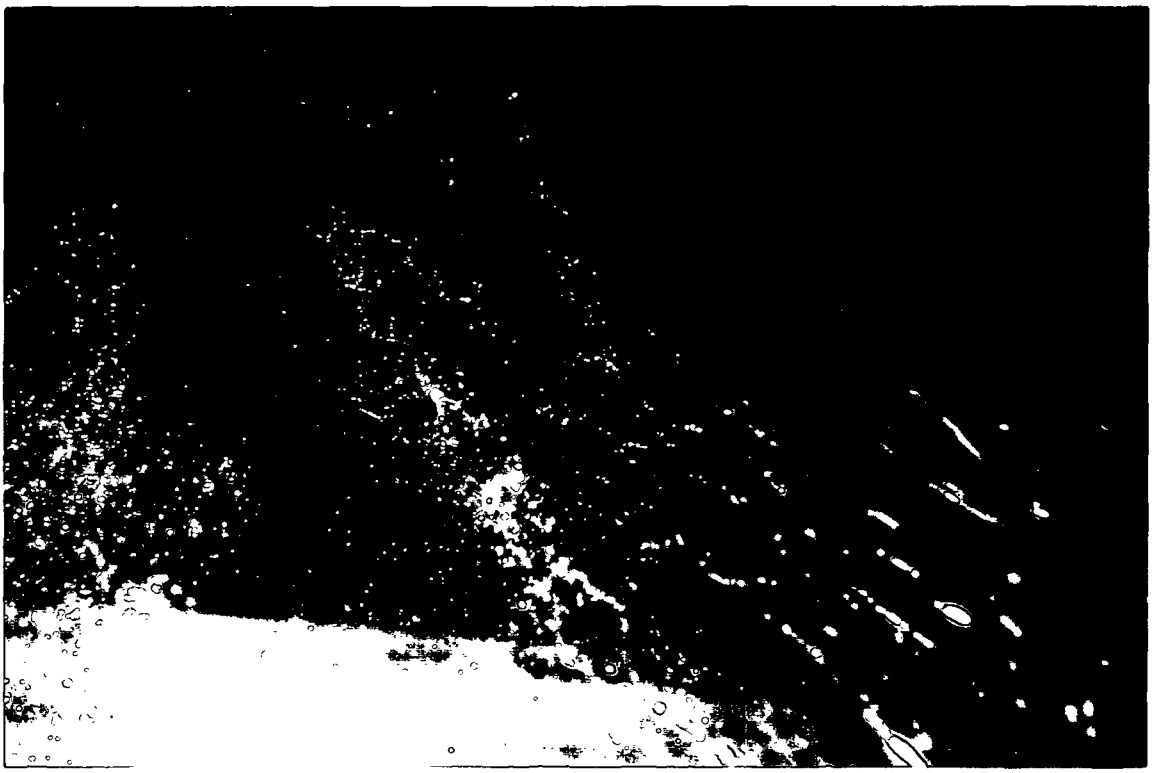

Figure 14. Liquid sheet in the region of breakup.

Using a procedure to be described in detail in a later section, the radially expanding sheet was split with a thin wire. Downstream from the split, surface tension forces contract the fluid into rims as described previously. These rims were illuminated with a strobe light and imaged. One such image is shown in Fig. 15a. A sinuous wave disturbance is clearly visible from the point at which the sheet is split (near the right-hand side of the image) out to the region of breakup (near the left-hand side of the image). The narrow range over which the

liquid progresses from a sinuously disturbed sheet to a spray of drops should be noted in this picture as well.

A second image of the rims formed by splitting the sheet is shown in Fig. 15b. Again, sinuous waves are visible. This wave is seen to grow with position downstream (from right to left) and becomes distorted from a pure sine wave.

These images, showing the growing sinuous waves, the distortion of the waves as their amplitude increases, the folding over of the sheet, the formation and growth of perforations, the interaction of neighboring perforation rims to form clumps and strands, and the breakup of these clumps to form drops, demonstrate the complexity of the overall drop formation process. In order to increase our understanding of this process, certain aspects of the breakup of liquid sheets were investigated in greater detail.

Figure 15a. Sinuous wave disturbance in a radially thinning sheet.

Figure 15b. Growing sinuous wave on a radially thinning sheet.

LOCATION OF SHEET RUPTURE

As discussed in the previous section, although perforations were observed throughout the length of the sheet, the majority of the holes appeared in a narrow region near the point of breakup. Experiments were performed to quantify the radial distribution of perforations as a function of the nozzle diameter and the jet velocity.

Liquid sheets were formed by the perpendicular impingement of a circular jet on a polished disc. The jet diameter was varied by using three nozzles with different orifice sizes. Each nozzle was operated over its practical range of jet velocities using a glycerol/water solution as the test liquid. The Xybion high-speed video camera was focused on a small area of the sheet, downstream from the plate edge. Images were collected for approximately one minute; thus, as the Xybion operates at a rate of 30 frames per second, about 2000 images were obtained during each trial. This process was repeated at a series of downstream

positions. One thousand images were viewed for each combination of nozzle diameter, jet velocity, and downstream location. The perforations observed in these images were counted, and the size and scale of the images were recorded.

Because the imaging area was independent of the downstream location, the fraction of the total circumferential area of the spray observed varied with the radial position. Therefore, to provide a uniform basis for comparison, the observed perforation counts were normalized. The area corrected perforation count, $(Np)_{area}$, was obtained by first multiplying the number of perforations observed, $(Np)_{obs}$, by the ratio of the circumference of the spray sheet at the imaging position, x, to the width of the imaging area, W. This value was then divided by the radial span of the imaging area, S, to obtain

$$(Np)_{area} = (Np)_{obs} \cdot \left(\frac{2\pi x}{W S}\right), \tag{47}$$

where:
- x = radial position of the center of the imaging area [m];
- $(Np)_{obs}$ = number of perforations observed at downstream position, x;
- $(Np)_{area}$ = area corrected number of perforations at downstream position per centimeter of radial span [Np/cm];
- W = lateral width of the imaging area [m]; and
- S = radial span of the imaging area [cm].

The width and span are defined in Fig. 16 for two representative locations.

In order to estimate the number of <u>new</u> perforations formed in a given range of downstream position, the area corrected perforation count at each location was modified to exclude the perforations accounted for at positions upstream of that location. Thus, if the sheet is imaged at some number of radial positions, M, then the number of perforations reported for the m^{th} position (where $2 \leq m \leq M$) is given by

$$(Np)_{rep,m} = (Np)_{area,m} - \sum_{j=1}^{m-1} (Np)_{rep,j}, \quad (\text{for } m \geq 2). \tag{48}$$

The reported number of perforations is equal to the area corrected number of perforations for the first radial location, m = 1,

$$(Np)_{rep,1} = (Np)_{area,1}. \tag{49}$$

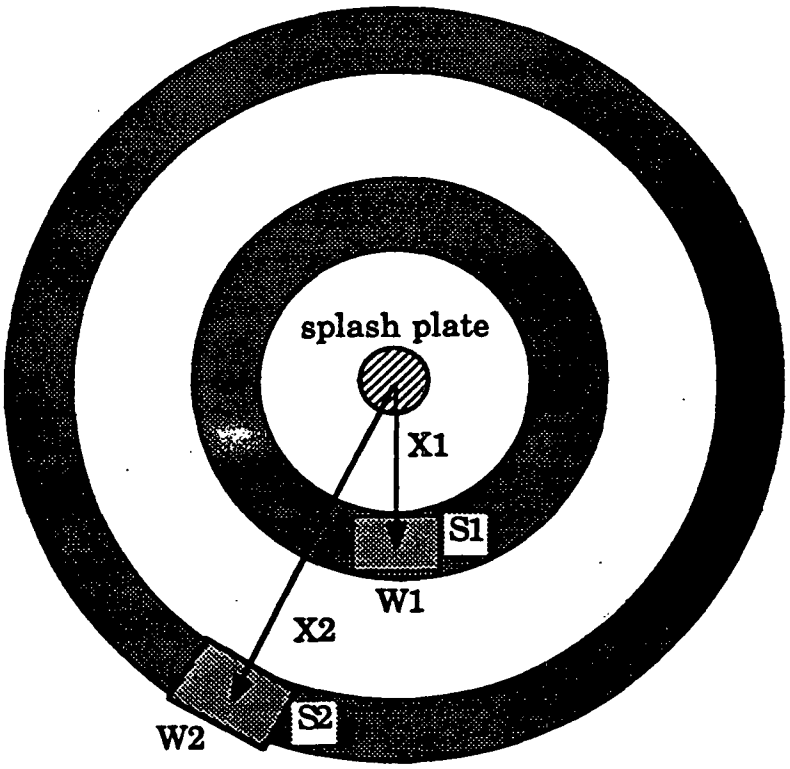

Figure 16. Representative imaging areas for the perforation count experiments.

The range of parameters investigated in this set of experiments is summarized in Table 6. A complete list of the operating conditions, including the observed and the normalized perforation counts, is included in Appendix C.

Table 6. Operating conditions for the radial perforation distribution experiments.

nozzle	number of trials	number of locations	range of locations (cm)	range of jet velocities (m/s)
NF-6000	22	5	13-21	15-20
NF-8000	38	7	8-21	12.5-22.5
NF-10000	16	3	10-20	12.5-22.5

The radial perforation distribution as a function of the jet velocity is shown for the three nozzle orifice diameters in Figs. 17-19. The reproducibility of these experiments can be estimated by comparing the data presented for duplicate runs performed at 19 cm downstream with the NF-6000 nozzle (labeled as 19a and 19b in Fig. 17) and duplicate runs at 16 cm downstream for the NF-8000 nozzle (labeled 16a and 16b in Fig. 18). As can be seen in these plots, only a small percentage of the total number of perforations observed occurred in the region near the splash plate ($x < \approx 16$ cm). This relatively undisturbed portion of the spray was followed by a narrow band of downstream positions in which a rapid increase in the number of observed perforations was recorded. The downstream location at which this transition occurred varied with the orifice diameter and the jet velocity. In general, the downstream location at which the rapid increase in observed perforations occurred decreased with increasing jet velocity.

In each of the three plots showing the number of perforations recorded, no data are plotted for the trials corresponding to the highest jet velocities and furthest positions downstream. These trials were run, and the high-speed video images were reviewed; however, in these cases the sheet had already broken up into clumps and strands, and a numeric value for the number of perforations could not be determined accurately.

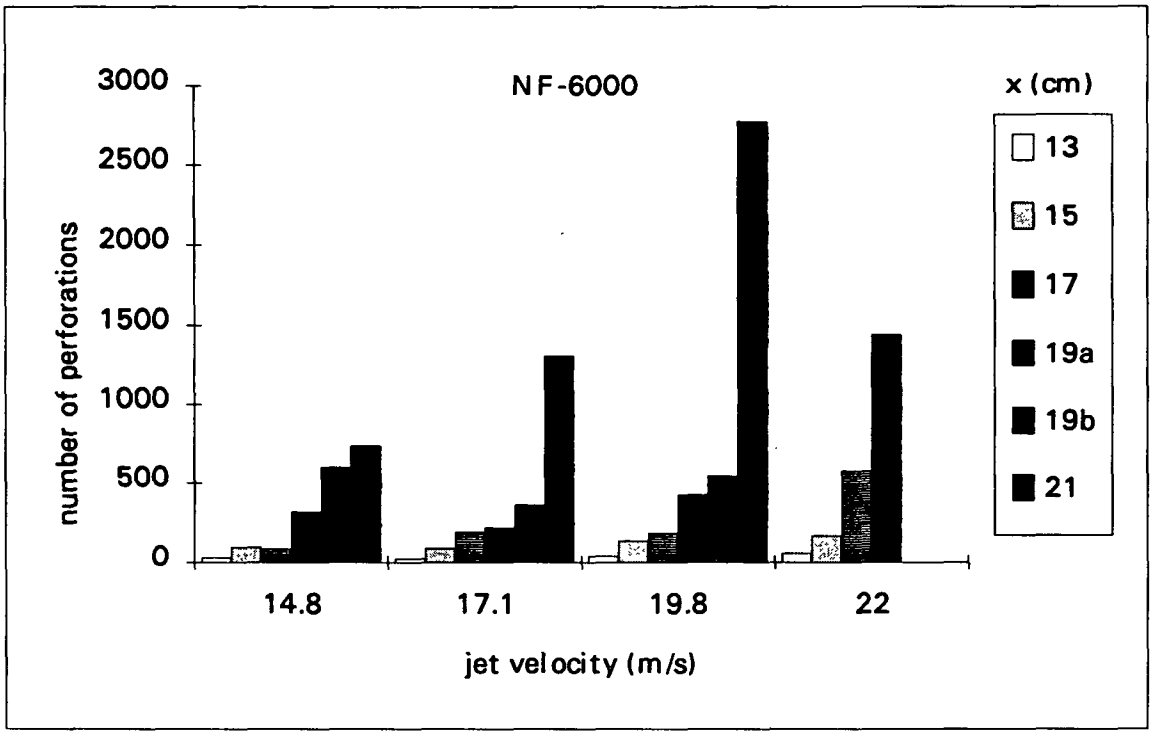

Figure 17. Reported perforation count versus downstream location: NF-6000 nozzle.

SHEET THICKNESS AND VELOCITY

Derivation of the Predictive Equations

The thickness and the velocity of a free sheet affect both the wave and perforation mechanisms of breakup; thus, it would be advantageous to be able to predict these parameters as functions of the operating conditions and fluid properties, particularly in the region of rapid perforation. First, analytical methods for predicting the sheet thickness and velocity of a viscous liquid spreading radially on a plate will be presented. Next, the equations for estimating the sheet velocity after it leaves the splash plate will be derived. Finally, experimental sheet thickness and downstream velocity data collected in this study will be compared to predicted values in order to assess the applicability of these equations for the spray system being investigated.

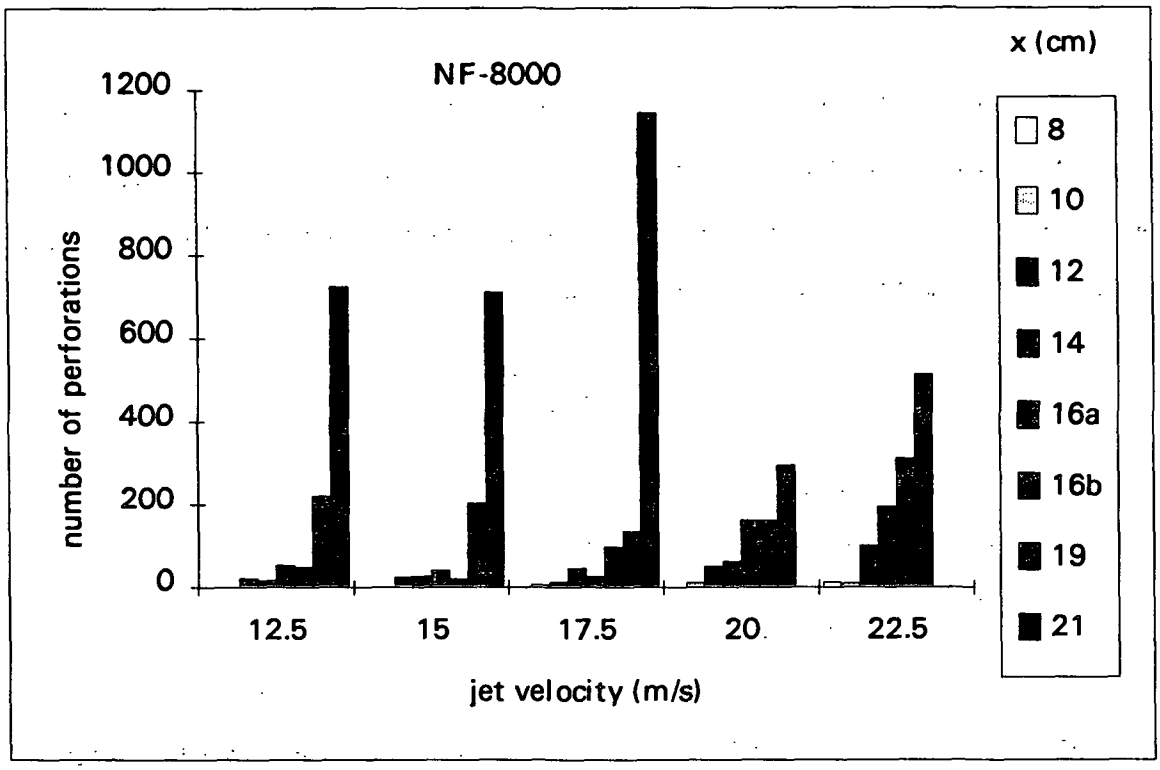

Figure 18. Reported perforation count versus downstream location: NF-8000 nozzle.

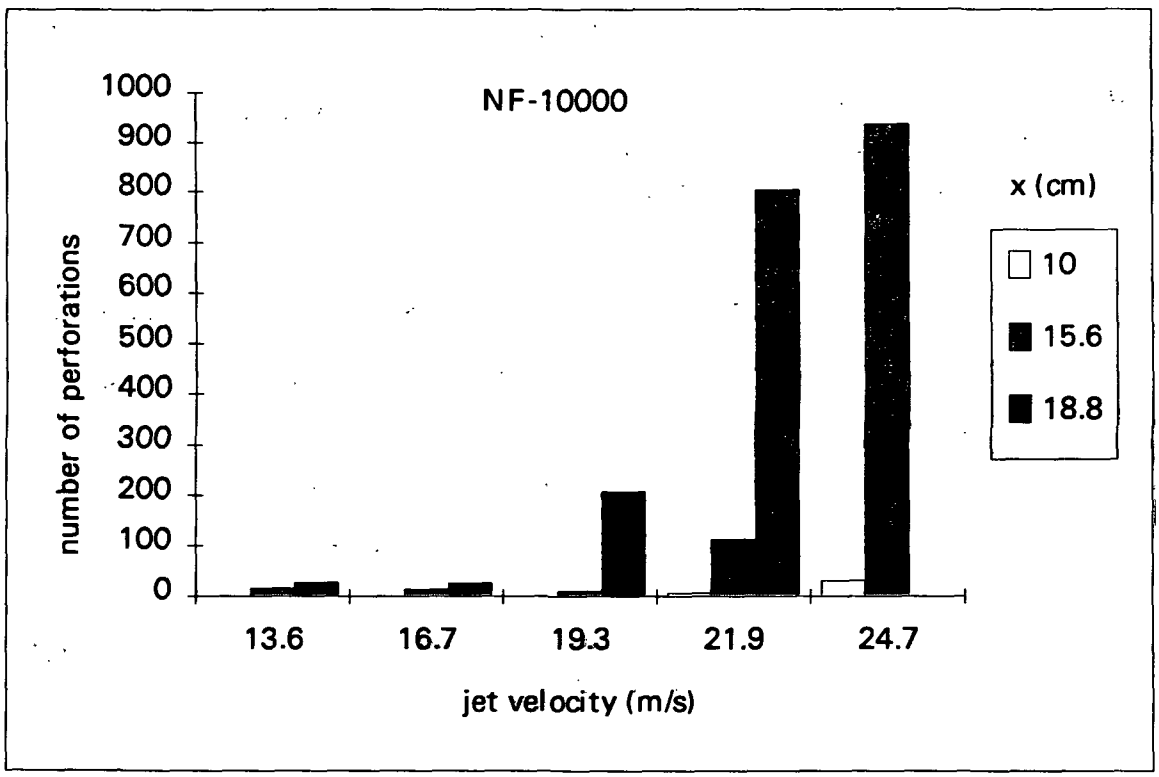

Figure 19. Reported perforation count versus downstream location: NF-10000 nozzle.

For the case of a sheet formed by the impingement of a jet on a plate at a 90° angle, the thickness and velocity can be determined from a mass balance. The mass flow rate through the nozzle is given by the product of the cross-sectional area of the nozzle orifice, the average velocity of the jet and the density of the fluid, that is

$$\dot{m} = \frac{\pi d_0^2 U_0 \rho_{liq}}{4}, \tag{50}$$

where: d_0 = jet diameter;
$\dot{m}$ = mass flow rate;
U_0 = average jet velocity; and
ρ_{liq} = liquid density.

Likewise, the mass flow rate at an arbitrary position on the plate, x, can be calculated from

$$\dot{m} = 2\pi x \cdot 2h(x) \cdot U_{s,avg}(x)\, \rho_{liq}, \tag{51}$$

where: x = position downstream from the center of jet impact [m];
$2h(x)$ = sheet thickness at x; and
$U_{s,avg}(x)$ = arithmetic mean sheet velocity at x.

Although both the sheet thickness and the arithmetic mean sheet velocity are functions of the downstream position, this explicit dependence will not be noted in succeeding equations.

By the principle of the conservation of mass, the mass flow rate equations can be set equal to one another and the resulting expression rearranged to obtain

$$2h = \frac{U_0 d_0^2}{U_{s,avg}\, 8x}. \tag{52}$$

Equation 52 is identical to that given previously as Eq. 10. If the sheet is inviscid and no momentum loss occurs in the region of jet impact, then the sheet velocity will equal the jet

velocity. Equation 52 can then be simplified to obtain an expression for the theoretical, inviscid, downstream sheet thickness, 2h*,

$$2h^* = \frac{d_0^2}{8x}. \tag{53}$$

This thickness is independent of the fluid properties and the jet velocity. Equations 52 and 53 can be combined to show that the ratio of the jet velocity to the average sheet velocity is equal to the ratio of the downstream sheet half-thickness to the theoretical inviscid sheet half-thickness, that is

$$\frac{U_0}{U_{s,avg}} = \frac{h}{h^*}. \tag{54}$$

The expressions for the downstream sheet thickness in the developing and fully-developed boundary layer regions were given as Eqs. 16 and 19. These expressions can be divided through by the theoretical inviscid half-sheet thickness in order to obtain an equation for predicting the velocity or sheet thickness ratio. The expression obtained for the developing boundary layer region ($x \leq x_t$) is

$$\frac{h}{h^*} = \frac{U_0}{U_{s,avg}} = 1.0 + \frac{7.96}{(Re_{jet})^{1/2}}\left(\frac{x}{d_0}\right)^{3/2}, \tag{55}$$

and the equation for the fully-developed boundary layer region ($x > x_t$) is

$$\frac{h}{h^*} = \frac{U_0}{U_{s,avg}} = 1.39 + \frac{38.7}{Re_{jet}}\left(\frac{x}{d_0}\right)^3. \tag{56}$$

These expressions are derived in Appendix D.

Likewise, the expression for the downstream sheet thickness obtained by Obuskovic and Adams,[34] presented here as Eq. 13, can be rearranged to obtain an equation for the downstream sheet thickness or velocity ratio,

$$\frac{h}{h^*} = \frac{U_0}{U_{s,avg}} = 2 + \frac{32}{Re_{jet}} \left[\left(\frac{x}{d_0}\right)^3 - \left(\frac{x_v}{d_0}\right)^3 \right]. \tag{57}$$

The empirical constant, x_v,[34] is expected to be on the order of the jet diameter; thus, for $x >> d_0$, Eq. 57 can be reduced to

$$\frac{h}{h^*} = \frac{U_0}{U_{s,avg}} \approx 2 + \frac{32}{Re_{jet}} \left(\frac{x}{d_0}\right)^3. \tag{58}$$

Equations 56 and 58 are of the linear form,

$$\frac{h}{h^*} = \frac{U_0}{U_s} = C_0 + \frac{C_1}{Re_{jet}} \left(\frac{x}{d_0}\right)^3; \tag{59}$$

therefore, a plot of $\frac{h}{h^*}$ versus $\frac{1}{Re_{jet}} \left(\frac{x}{d_0}\right)^3$ should yield a straight line with a slope of C_1 and an intercept of C_0.

These sheet thickness and velocity expressions are expected to be valid only while the liquid is spreading across the splash plate. Once the fluid sheet leaves the surface of the plate, viscous shear forces will no longer be active, and the velocity of the sheet should then be constant and equal to some average velocity of the sheet at the edge of the plate. Two representative sheet velocities can be defined, the arithmetic mean velocity and the root mean square velocity. Although both the arithmetic mean and the root mean square velocities are average velocities, the subscript "avg" will be used to denote the arithmetic mean value, while

"rms" will be used for the root mean square velocity. As will be shown, the appropriate choice of average velocity will depend on the behavior of the sheet as it leaves the plate.

The liquid leaving the edge of the plate flows through an area defined by the lateral distance $2\pi x_p$ and the sheet thickness $2h_p$, where the subscript p denotes the value of a variable at the edge of the splash plate. The arithmetic mean velocity, $U_{s,avg}$, is defined such that the mass flow through the area defined by $2\pi x_p \cdot 2h_p$ is the same as the mass flow rate through this area for a sheet with the true velocity profile,

$$\int_{z=0}^{z=2h} 2\pi\rho_{liq}x_p U(x_p,z)dz = 2\pi\rho_{liq}x_p U_{s,avg}\int_{z=0}^{z=2h} dz. \tag{60}$$

This expression can be rearranged to give

$$U_{s,avg} = \frac{\int_{z=0}^{z=2h} U(x_p,z)dz}{\int_{z=0}^{z=2h} dz}. \tag{61}$$

This expression is simply the definition of the arithmetic mean for the variable $U(x_p,z)$ over the thickness, 2h.

Likewise, the root mean square velocity, $U_{s,rms}$, is defined such that the momentum flux through the area defined by $2\pi x_p \cdot 2h_p$ is the same as the momentum flux through this area for a sheet with the true velocity profile,

$$2\pi\rho_{liq}x_p\int_{z=0}^{z=2h} U^2(x_p,z)dz = 2\pi\rho_{liq}x_p U^2_{s,rms}\int_{z=0}^{z=2h} dz. \tag{62}$$

This expression can be rearranged to obtain

$$U_{s,rms}(x_p) = \sqrt{\frac{\int_{z=0}^{z=2h} U^2(x_p,z)dz}{\int_{z=0}^{z=2h} dz}}. \qquad (63)$$

The right-hand side of this expression is the definition of the root mean square velocity, denoted on the left-hand side by the subscript, rms.

The linear or the boundary layer velocity profile, defined by Eqs. 11 and 14, respectively, can be substituted into Eqs. 61 and 63 to calculate the ratios of the arithmetic mean and root mean square velocities to the maximum velocity at the plate edge. As the maximum velocity at the plate edge can be predicted with either Eq. 12 for the linear profile or Eq. 20 for the boundary layer profile, this set of equations can be used to estimate an average velocity of the sheet downstream from the plate edge. A summary of the results obtained is given in Table 7. The integrations needed to derive the velocity ratios from the boundary layer equation are presented in Appendix D.

Table 7. Predicted ratios of the maximum, linear average, and root mean square sheet velocities.

velocity profile	$\frac{U_0}{U_{s,avg}}$	$\frac{U_{s,avg}}{U_{max}}$	$\frac{U_{s,rms}}{U_{max}}$	$\frac{U_{s,rms}}{U_{s,avg}}$
linear (Obuskovic and Adams[34])	$2 + \frac{32}{Re_{jet}}\left(\frac{x}{d_0}\right)^3$	0.500	0.577	1.15
fully-developed boundary layer (Watson[35])	$1.39 + \frac{38.7}{Re_{jet}}\left(\frac{x}{d_0}\right)^3$	0.615	0.690	1.12

Experimental and Predicted Sheet Thicknesses

The jet velocity, fluid properties, and downstream sheet thickness were measured using the experimental apparatus previously described. For all of the tests, the thickness probes

were located 2.14 $\pm$ 0.04 centimeters downstream from the center of jet impact. An electrical circuit connects each micrometer tip to the base of the reservoir. The circuit includes an ohm meter, and when the micrometer tip touches the surface of the splash plate, the circuit is completed; thus, a reference position could be obtained. The micrometer tips are retracted until they just touch the top surface of the liquid flowing across the plate. The location of the top sheet surface relative to the reference position (the top surface of the plate) is then taken to be the thickness of the sheet.

A summary of the range of operating conditions investigated is given in Table 8. Included in this table is the maximum value of x_t calculated for each nozzle, where x_t is the downstream position at which Watson[35] predicted the flow would change from a developing boundary layer to a fully-developed boundary layer. (See Eq. 15) In all cases, the thickness probes were in the fully-developed boundary layer region; thus, Eq. 19 should apply.

Flow rate and physical property data were collected twice per second for the duration of each 60 second trial. A complete list of the operating conditions is given in Appendix E.

The micrometer readings and the sheet thicknesses determined from each probe are listed in Appendix E. The standard deviation in the thicknesses measured by the three micrometers is also listed. The normalized standard deviation (the standard deviation divided by the average sheet thickness) varied from 1 to 20 percent, with an average value of 6 percent.

For each trial, the sheet thickness was determined by averaging the measurements made with the three probes. This average sheet thickness was divided by the theoretical inviscid sheet thickness calculated from Eq. 53. The resulting experimental sheet thickness ratio is plotted versus $\frac{1}{Re_{jet}}\left(\frac{x}{d_0}\right)^3$ in Fig. 20.

Table 8. Range of operating conditions investigated in the sheet thickness studies.

nozzle style	diameter (mm)	number of trials	velocity (m/s)	viscosity (cp)	density (kg/m^3)	Reynolds number	maximum x_t (cm)
sharp edge	6.36	21	5.9-17.2	51-67	1210	1300-4400	1.6
QU-00120	6.556	14	5.6-18.3	79-102	1220	700-2500	1.4
NF-6000	4.66	18	8.6-24.9	69-85	1220	900-3200	1.1
QU-00200	8.448	17	3.0-12.6	85-96	1220	500-2400	1.8

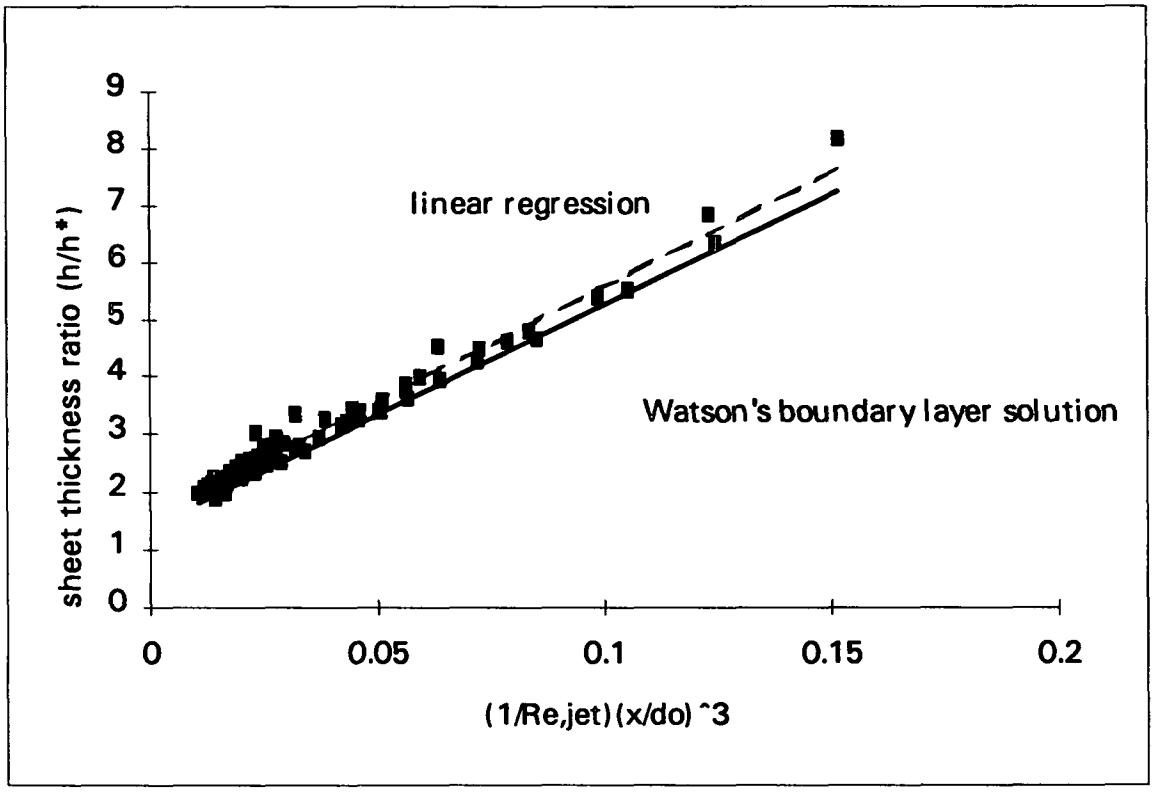

Figure 20. Dimensionless sheet thickness correlation.

The theoretical curve based upon the boundary layer velocity profile is shown as a solid line. The best fit regression line, shown as a dashed line, has a slope of 40 and an intercept of 1.55,

with a coefficient of determination of 0.978. A comparison of these values with those predicted using the techniques of Watson[35] and Obuskovic and Adams[34] is shown in Table 9.

Table 9. Comparison of predicted and measured values of the slope and intercept of the sheet thickness correlating equation.

variable	experimental	boundary layer Watson[35]	linear profile Obuskovic and Adams[34]
intercept (A)	1.55 ± 0.08	1.39	2.00
slope (B)	40.2 ± 1.4	38.7	32.0

The method of successive regression was used to determine if the sheet thickness ratio was a function of the jet velocity or of the orifice diameter, apart from their contribution to $\left(\frac{1}{Re_{jet}}\right)\left(\frac{x}{d_0}\right)^3$. Analysis of variance was used to determine the significance of the added terms. Neither the addition of a term proportional to the jet velocity nor a term proportional to the orifice diameter significantly improved the correlation at the 95% confidence level. The regression and F-test statistics used to make these determinations are presented in Appendix E.

The residuals for the two-term linear regression equation were calculated as the difference between the measured sheet thickness ratio and the sheet thickness ratio predicted with the linear regression model,

$$\text{residual} = \left(\frac{h}{h^*}\right)_{\text{measured}} - \left(\frac{h}{h^*}\right)_{\text{predicted}} \tag{64}$$

Plots of these residuals versus the predicted sheet thickness ratio, the measured sheet thickness ratio, the jet Reynolds number, and the nozzle orifice diameter are included in Appendix E. In all cases, the residuals appeared to be distributed equally about zero, with no apparent trend in the data.

In summary, the results of both Obuskovic and Adams[34] and Watson[35] can be used to predict that the ratio of the viscous to inviscid thickness of a liquid spreading on a plate will increase with $(1/Re_{jet})(x/d_0)^3$. This general behavior was confirmed by measuring the thickness of a sheet over a range of jet Reynold's numbers and nozzle orifice diameters.

The measured slope agrees, within the uncertainty limits at the 95% confidence level, to the value predicted using the fully-developed boundary layer velocity profile. However, the intercepts do not agree, and the reduction in sheet velocity and the corresponding increase in sheet thickness are underpredicted at all jet velocities. The magnitude of this difference varied form 5% to 9%, decreasing with increasing values of $(1/Re_{jet})(x/d_0)^3$. This error could be the result of neglecting the momentum losses which may occur in the region of jet impact.

Neither the slope nor the intercept predicted using the linear velocity profile agrees with the experimental values. Because of the low value of the slope, the rate of momentum loss with position downstream will be underpredicted. This error is a result of assuming a linear velocity profile at the plate surface. Viscous momentum loss is proportional to the rate of change in radial velocity with vertical position at the plate surface. As the change in velocity is expected to be greater than linear near the plate, a linear profile will result in an underprediction of these momentum losses and, thus, an underprediction of the corresponding decrease in average sheet velocity.

The behavior of both the boundary layer and linear profile methods can be examined in the limiting case of zero viscosity. Both solutions should predict a sheet thickness ratio of one, that is, the true sheet thickness should equal the ideal, inviscid sheet thickness.

In the case of Watson's[35] approach, the transition distance, x_t, is found to approach infinity as the liquid viscosity goes to zero; therefore Eq. 56, the expression for predicting the

thickness ratio in the developing boundary layer region should apply. In the limit as viscosity goes to zero, the Reynold's number approaches infinity, and the second term in Eq. 56 goes to zero; thus, the sheet thickness ratio is indeed predicted to be one. It is important to note that, although the limiting behavior of the developing boundary layer equation is consistent with the expected behavior, the expression has not been compared to experimental data for the case of small, but finite viscosity flows.

The limiting behavior of Obuskovic and Adams'[34] analysis is determined from Eq. 57. In this case, as the viscosity goes to zero, the jet Reynold's number approaches infinity, and the second term in Eq. 57 goes to zero. This leads to the prediction that the sheet thickness ratio is two, inconsistent with the expected physical behavior.

Experimental Sheet Velocities

In a limited number of experiments, relatively large air bubbles became entrained in the glycerol/water solution. When this fluid was sprayed, air bubbles were visible in the images of the fluid sheet obtained with the high-speed 16 mm camera. Frames from these films were projected onto sheets of paper; the positions of selected air bubbles were tracked for successive frames; and the distances traveled by the air bubbles were measured. Timing light generator (TLG) marks on the film were used to determine the time elapsed per frame; thus, knowing both the distance the bubbles traveled per frame and the framing rate, a measure of the sheet velocity could be obtained.

All of the sheets in which air bubbles were observed were formed using the QU-00120 nozzle (d_0 = 0.656 cm = 0.258 inch). The operating conditions for each trial are summarized in Table 10. The operating conditions, including the velocity determined from each measurement, are listed in Appendix F. The velocity for each trial was taken as the average velocity of all of the bubbles tracked for that trial, with the exception of film #61491.2, as

explained below. The uncertainty in the calculated sheet velocity was less than 5% at the 95% confidence level.

Three of the 21 measurements made for film #61491.2 were examined as outliers. Following the recommendation in ASTM standard E 178-80[63] for dealing with potential outliers located on both sides of the mean, the method presented by Tietjen and Moore[64] was used. All three points could be rejected at the 95% confidence level. These data and the statistical analysis for evaluating outliers are presented in Appendix F.

Table 10. Summary of the sheet velocity experiments.

trial number	density (kg/m^3)	viscosity ($kg/m \cdot s$)	jet velocity (m/s)	number of measurements
61491.1	1215	0.067	11.6	16
61491.2	1213	0.060	15.33	21*
61491.4	1213	0.056	15.50	17
61491.5	1212	0.055	11.58	20

* Only 18 of the 21 points were used, as three measurements were eliminated as outliers.

The measured sheet velocities are compared to the predicted linear average and root mean square velocities based on the linear and boundary layer profiles. Predicted values based on the linear regression equation are included as well. These velocities were calculated assuming a boundary layer velocity profile was accurate, but the initial velocity was reduced by losses in the region of impact. Thus, the ratios between the average and maximum velocities derived from Watson's[35] analysis could be used. These results are shown in Table 11.

Although only a limited amount of data is available, there appears to be good agreement between the measured downstream velocity and the average velocities predicted

using the constants given by Watson.[35] The root mean square sheet velocity determined using the constants calculated in the sheet thickness study also shows good agreement with the measured values.

Table 11. Comparison of predicted and measured sheet velocities.

		boundary layer		linear profile		regression	
trial number	measured U_s (m/s)	U_{rms}	U_{avg}	U_{rms}	U_{avg}	U_{rms}	U_{avg}
61491.1	4.0 ± 0.2	4.3	3.9	4.0	3.5	4.0	3.6
61491.2	6.2 ± 0.3	6.7	6.0	6.0	5.9	6.2	5.5
61491.4	6.8 ± 0.3	6.9	6.1	6.1	5.3	6.3	5.7
61491.5	4.5 ± 0.2	4.3	3.8	3.9	3.4	4.0	3.5

DOWNSTREAM SHEET THICKNESS

Once the liquid leaves the plate surface at x_p, a simple mass balance can be used to predict the decrease in the sheet thickness with downstream position. The mass balance can then be written as

$$[2px][2h(x)]U_{s,avg}(x) = [2px_p][2h(x_p)]U_{s,avg}(x_p).$$

If the downstream sheet velocity is assumed to be equal to the average sheet velocity at the plate edge ($U_{s,avg}[x] = U_{s,avg}[x_p]$), then this expression can be reduced to

$$h(x) = h(x_p)\cdot\left(\frac{x_p}{x}\right) \tag{65}$$

Using the linear regression equation obtained in the previous section, the thickness of the liquid sheet at the edge of the splash plate can be estimated, and Eq. 65 can then be used to estimate the sheet thickness at any position, $x > x_p$.

In the perforation distribution experiments, the sheet thickness on the plate edge was found to vary from 400 to 700 microns. Using Eq. 65 and the measured radius of the plate (x_p = 2.54 cm), the decrease in sheet thickness with downstream position was determined. These calculated results are plotted in Fig. 21 for the range of sheet thicknesses at the plate edge observed experimentally. The region where the perforation rate increased significantly (17-21 cm downstream) is shown in greater detail in Fig. 22.

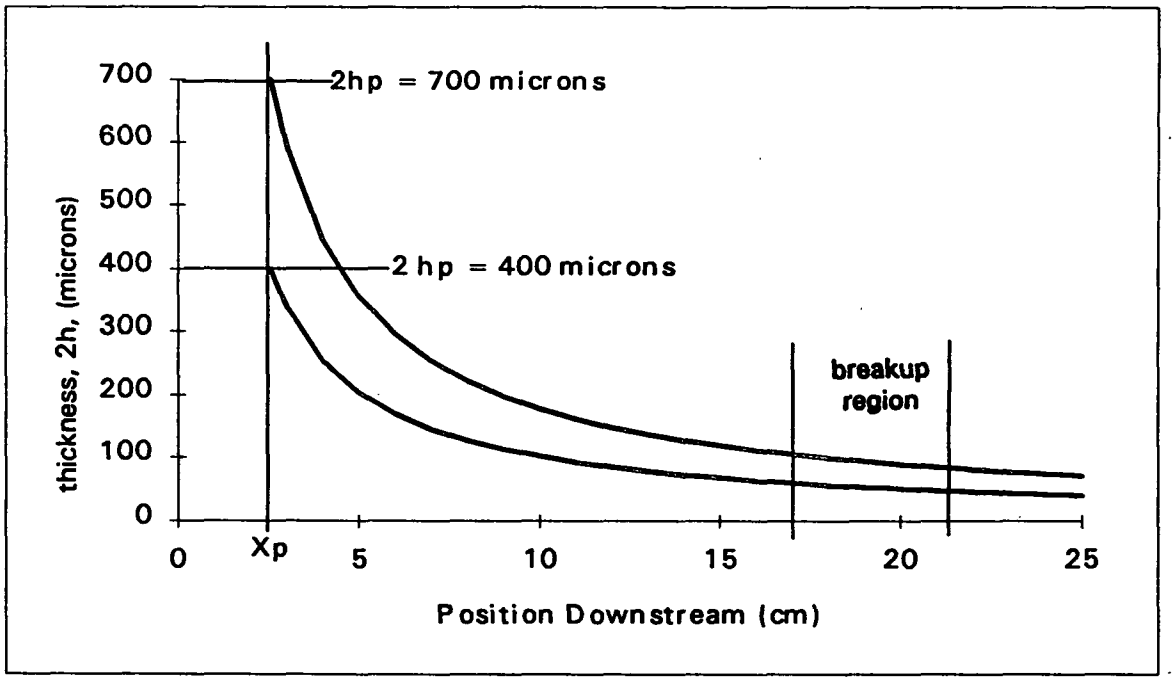

Figure 21. Predicted downstream sheet thickness.

Because the sheet thickness at the plate edge varies with the jet velocity, the fluid properties, and the orifice diameter the sheet thickness variation with downstream location was calculated for each individual perforation count experiment. The number of perforations observed for each trail, previously plotted versus downstream location in Figs. 17-19, is now plotted versus the predicted sheet thickness in Fig. 23. Although there is significant scatter in the data, there appears to be a critical range for sheet thicknesses in which the majority of the perforations occur.

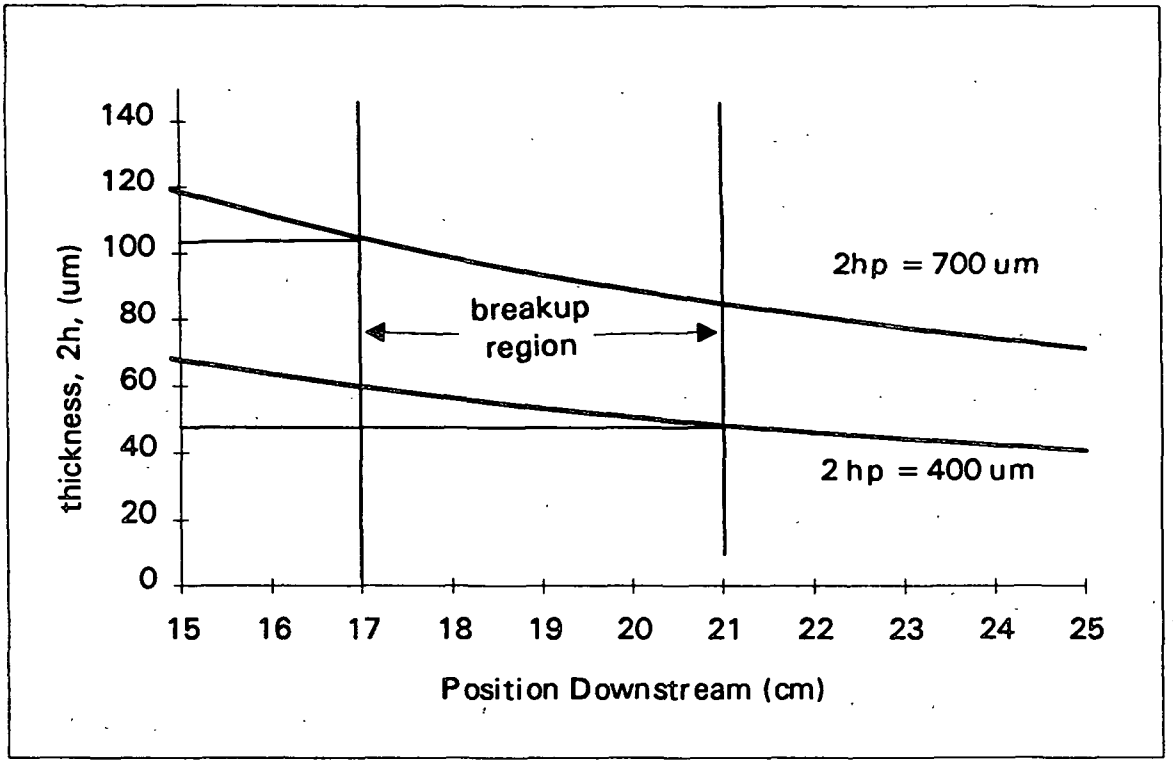

Figure 22. Predicted downstream sheet thickness in the region of breakup.

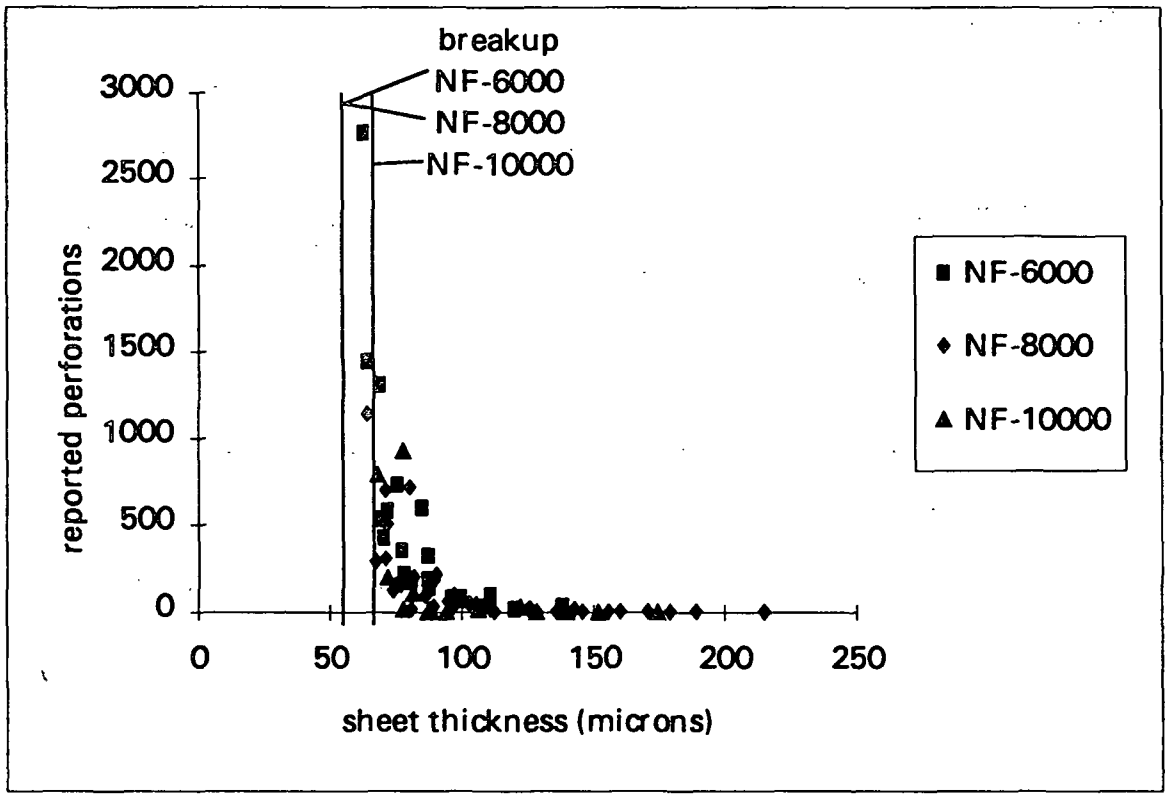

Figure 23. Number of perforations as a function of downstream sheet thickness.

Several trends in the breakup behavior can be inferred from the qualitative features observed in Figs. 17-19 and Fig. 23. First, from Fig. 23, the sheet thickness at breakup is greater for the larger orifice diameter nozzle than for the smaller nozzles. This trend is also noted in Figs. 17-19, where for a fixed velocity, the number of perforations is seen to increase rapidly closer to the plate as the orifice diameter is increased. Also, the number of perforations observed at a fixed position downstream increased with increasing velocity. These trends noted in the experimental data will be compared to results predicted from additional analyses of the breakup process.

WAVE THINNING

Although the perforation count versus sheet thickness data can be used to infer that a critical thickness for sheet rupture exists, as can be seen in Fig. 22, the sheet thickness is 50-65 microns in the breakup region. This is two to three orders of magnitude larger than the predicted critical sheet thickness for spontaneous rupture.[48,49] Also, as determined from analysis of variance, the critical sheet thickness may be affected by the orifice diameter and jet velocity. In order to address these issues, the investigation of the relationship between the downstream position, the sheet thickness, and the number of observed perforations was extended.

The sheet thickness values plotted in Fig. 22 were determined for systems free from external disturbances and will be referred to as the undisturbed sheet thicknesses. Sinuous and dilational waves are expected to disturb the planar geometry of the liquid sheet and, as will be shown, can reduce the thickness of the sheet.

A sheet segment is shown in the figure below. This same segment is also shown perturbed from its initially planar configuration by a sinuous and a dilational disturbance, each

of wavelength, λ. In both cases, the minimum thickness of the sheet is affected by the presence of the wave.

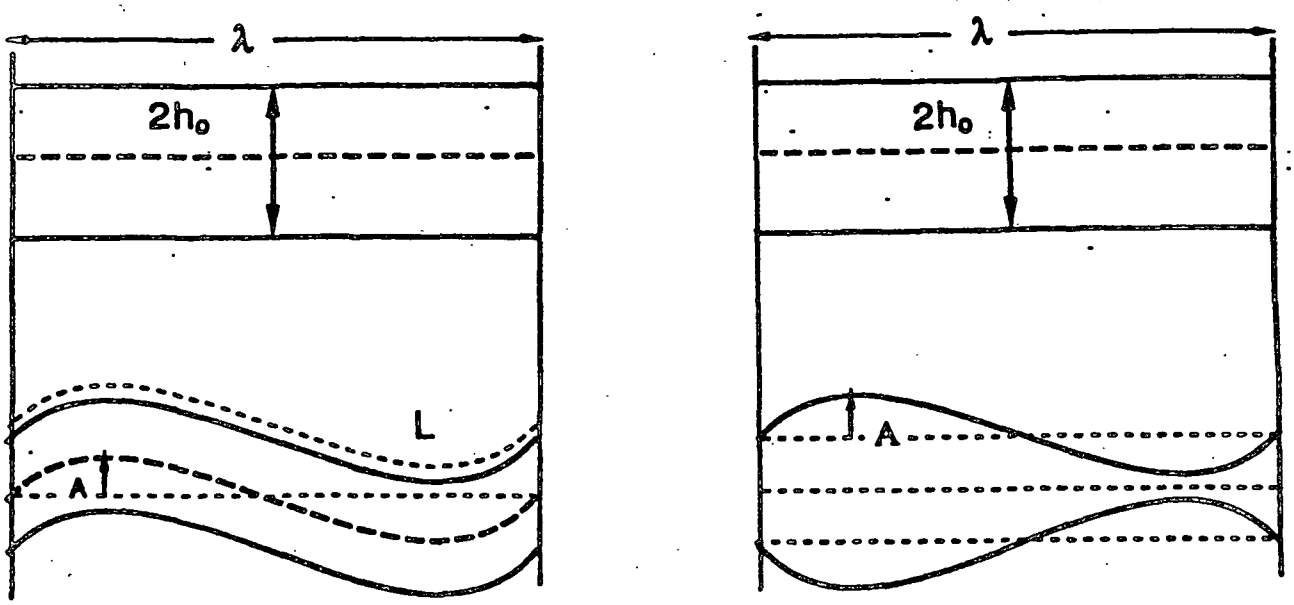

Figure 24. Sinuous and dilational wave thinning.

From Fig. 24, it can be seen that the minimum thickness of the sheet perturbed by the dilational wave is

$$h_{dil} = h_0 - A, \tag{66}$$

where: A = amplitude of the wave disturbance [m]; and
h_{dil} = half-thickness of a sheet disturbed by a dilational wave [m].

If rupture occurs in a sheet prethinned by dilational waves, then the wave-thinned sheet thickness, $2h_{dil}$, will equal the critical thickness, $2h_{crit}$. The amplitude of the dilational disturbance at breakup, determined from Eq. 66, is then

$$A_{b,dil} = h_0 - h_{crit}, \tag{67}$$

where the subscript b is used to denote the value of a variable at breakup.

The thinning caused by a sinuous wave can be estimated from a mass balance performed on the undisturbed and the disturbed sheet. In this analysis, it is assumed that a sheet segment of width, W, with an initial thickness, $2h_0$, thins uniformly along one wavelength, λ.

The mass contained in the unperturbed sheet segment, m_u, is

$$m_u = 2h_0 \cdot W \cdot \lambda \cdot \rho_{liq}. \tag{68}$$

The mass contained in the sinuously perturbed sheet segment, m_{sine}, is

$$m_{sine} = 2h_{sine} \cdot W \cdot L \cdot \rho_{liq}, \tag{69}$$

where L is the length of sheet segment measured along the surface, as shown in Fig. 24.

These masses can be equated and the resulting expression rearranged to obtain

$$h_{sine} = h_0 \left(\frac{\lambda}{L} \right), \tag{70}$$

an equation for the sinuously perturbed sheet half-thickness.

If sheet rupture occurs in regions prethinned by sinuous waves, then at the breakup length, the disturbed sheet thickness, $2h_{sine}$, will equal the critical sheet thickness, $2h_{crit}$. After making this substitution in Eq. 70 and rearranging, an expression for the ratio of sheet length to disturbance wavelength at the breakup distance

$$\frac{L_b}{\lambda} = \frac{h_0}{h_{crit}}, \tag{71}$$

is obtained.

In order to estimate the length of the sinuously disturbed sheet segment at breakup, L_b, the sheet is assumed to be perturbed by a single wave given by

$$z = A \cdot \sin\left(\frac{2\pi x}{\lambda}\right). \tag{72}$$

The length of a sine wave can be calculated from

$$L = \frac{\lambda_{opt}\sqrt{1 + p^2}}{2\pi} \int_{\hat{x}(init)}^{\hat{x}(final)} [1 - \hat{p}^2 \sin^2 \hat{x}]^{1/2}\, d\hat{x}, \tag{73}$$

where: $\hat{x} = 2\pi x/\lambda$

$\hat{p} = \sqrt{\frac{1 + p^2}{p}}$, and

$p = 2\pi A/\lambda$.

This expression is derived in Appendix G. Since x(init) is zero and x(final) is the wavelength of the disturbance, λ, $\hat{x}$(init) is zero, and $\hat{x}$(final) is 2π. Using these limits of integration, the length of the sine wave can be written as

$$L = \frac{\lambda_{opt}\sqrt{1 + p^2}}{2\pi} \int_{0}^{2\pi} [1 - \hat{p}^2 \sin^2 \hat{x}]^{1/2}\, d\hat{x}.$$

Using the periodic properties of the integral, this reduces to

$$L = \frac{\lambda_{opt}\sqrt{1 + p^2}}{2\pi}\left(4 \int_{0}^{\pi/2} [1 - \hat{p}^2 \sin^2 \hat{x}]^{1/2}\, d\hat{x}\right) \tag{74}$$

The integral appearing in this expression is the complete elliptic integral of the second kind, denoted by $E(\hat{p};\pi/2)$.[65]

Using this notation and the definition of p, Eq. 74 can be rearranged to give

$$A_{b,sine} = \left(\frac{\lambda_{opt}}{4\,E(\hat{p};\pi/2)}\right)\left[\left(\frac{L_b}{\lambda_{opt}}\right)^2 - \left(\frac{2\,E(\hat{p};\pi/2)}{\pi}\right)^2\right]^{1/2}, \tag{75}$$

an expression for the amplitude of the sinuous wave at breakup.

As previously stated, the minimum bulk thickness of the sheet in the region of rapid perforation was approximately 50 microns, while the thickness at rupture is expected to be less than one micron. Using these values in Eq. 71, a minimum value of 50 is calculated for the ratio of the disturbed to undisturbed sheet length. For this high a value of (L_b/λ), $\hat{p}$ can be taken to be 1.0, and $E(1;\pi/2) = 1.^{65}$. Making use of this limiting behavior, Eq. 75 can be simplified to

$$A_{b,sine} \approx \left(\frac{L_b}{4}\right) \tag{76}$$

This expression can be rewritten using Eq. 71 and the definition for the optimum sinuous wave, thus, obtaining

$$A_{b,sine} \approx \lambda_{opt}\left(\frac{L_b}{4\,\lambda_{opt}}\right) = \left(\frac{\pi\,h_0}{We}\right)\left(\frac{h_0}{h_{crit}}\right) \tag{77}$$

For the temporally growing disturbances discussed previously, the amplitude of either a dilational or a sinuous wave disturbance can be written as

$$A(t) = A_0 \cdot \exp(s_{imag}\,t), \tag{78}$$

where: $A(t)$ = amplitude of the wave disturbance at time t [m];
A_0 = initial amplitude of the disturbance at t = 0 [m]; and
s_{imag} = temporal growth rate parameter [sec^{-1}].

This expression was obtained from linear theory; therefore, it is only valid for small values of the disturbance amplitude, A. However, results obtained using this expression for large amplitude disturbances may be useful in predicting trends in sheet breakup behavior.

If the wave speed is assumed to be equal to the velocity of the sheet, then the amplitude at each position x can be determined by substituting $t = x/U_s$ into Eq. 78,

$$A(x) = A_0 \cdot \exp\left(\frac{S_{imag}\, x}{U_s}\right). \tag{79}$$

Using results presented by Gaster,[66] Asare *et al.*[67] showed that this transformation between the temporal growth rate and a spatial growth rate is valid provided the wave velocity is equal to the sheet velocity. In a note appended to Asare *et al*'s[67] paper, Morris[68] showed that these velocities are approximately equal provided the density ratio (ρ_{gas}/ρ_{liq}) is much less than tanh(kh), and kh/tanh(kh) is of order unity. As will be discussed in the next section, both conditions are met for the sheets investigated in this work; thus, Eq. 79 can be used to investigate the spatial development of waves. It should be noted that this transformation was necessary in order to analyze the behavior of the waves, as the temporal growth rate parameter can be obtained analytically, while the spatial growth rate parameter must be determined numerically.[67,69]

Equation 79 can be rearranged with the use of the natural log function and the definition that the amplitude of the disturbance reaches the breakup amplitude, A_b, at the downstream breakup position, x_b, to obtain

$$x_b = \left(\frac{U_s}{S_{imag}}\right) \ln\left(\frac{A_b}{A_0}\right). \tag{80}$$

The temporal growth rate of the disturbances, s_{imag}, has been determined analytically for a number of physical systems.

Planar Inviscid Sheets

Hagerty and Shea[44] investigated the growth rates of sinuous and dilational waves in inviscid, planar fluid sheets. These results were discussed in the Literature Review section. The temporal growth rate parameter can be obtained as the imaginary part of Eq. 30,

$$(s_{imag})_{sine} = \left(\frac{k^2 U_s^2 \gamma - k^3 \sigma / \rho_{liq}}{\tanh(kh)} \right)^{1/2}, \tag{81}$$

for a sinuous wave and Eq. 31,

$$(s_{imag})_{dil} = \left(\frac{k^2 U_s^2 \gamma - k^3 \sigma / \rho_{liq}}{\coth(kh)} \right)^{1/2}, \tag{82}$$

for a dilational wave. The wave number of optimum growth, k_{opt}, can be determined by differentiating Eqs. 81 and 82 with respect to the wave number, k, and setting the result equal to zero. It is generally assumed that the product of the wave number and the sheet half-thickness, kh, is much less than one, so that tanh(kh) and coth(kh) can be replaced by kh and 1/kh, respectively. Using these substitutions, the expression obtained for sinuous waves is

$$(k_{opt})_{sine} = \frac{U_s^2 \rho_{gas}}{2\sigma}. \tag{83}$$

The corresponding equation for dilational waves is

$$(k_{opt})_{dil} = \frac{3 U_s^2 \rho_{gas}}{4\sigma}. \tag{84}$$

Using these expressions for the wave number, the data presented in Appendix E could be used to calculate values of kh for each of the perforation count experiments. The condition $1.02 \geq kh/\tanh(kh) \geq 1.0$ is met, provided that kh is less than 0.25. Using the sinuous wave number, the predicted value of kh is less than 0.25 in every case. Basing the kh value on the dilational wave number, two of the 79 trials have a kh value greater than 0.25 at the plate edge; however, because the sheet thickness decreases rapidly just downstream of the plate edge (See Fig. 21), $(k_{dil}h)_{max}$ is less than 0.25 before the sheet travels 0.5 cm from the plate edge. Thus, the simplifications that $\tanh(kh) = kh$ and $\coth(kh) = 1/kh$ can be used, and the second condition required for the wave speed to equal the sheet speed ($kh/\tanh(kh)$ is of order one) is met.

The first condition imposed by Morris[68] was that $\rho_{gas}/\rho_{liq} << \tanh(kh)$. The minimum value of kh and, thus, $\tanh(kh)$, calculated for the sinuous wave was 0.019. Using the dilational wave number, the minimum value of $\tanh(kh)$ is 0.029. Both these values are an order of magnitude greater than the gas-to-liquid density ratio of approximately 0.001 (1.2/1220) encountered in this study. Based on these calculations, the transformation between the temporal and spatial growth rates was determined to be acceptable.

Examining sinuous disturbances first, Eq. 83 can be substituted into Eq. 81, and the resulting expression rearranged to obtain an equation for the growth rate of the optimum disturbance,

$$[(s_{imag})_{sine}]_{opt} = \left(\frac{U_s^2}{h_0^{1/2}}\right)\sqrt{\frac{\rho_{gas}^2}{4\sigma\,\rho_{liq}}}. \tag{85}$$

This expression can be substituted into Eq. 80 to obtain an expression for the breakup distance, $x_{b,sine}$, for a planar, inviscid sheet, perturbed by the optimum sinuous disturbance,

$$x_{b,sine} = \left(\frac{h_0^{1/2}}{U_s}\right)\sqrt{\frac{4\sigma\,\rho_{liq}}{\rho_{gas}^{\,2}}}\cdot\ln\left(\frac{A_{b,sine}}{A_0}\right) \tag{86}$$

The corresponding expressions for dilational waves, based on Eqs. 67, 82, and 84, are

$$[(s_{imag})_{dil}]_{opt} = (h_0^{1/2}\,U_s^{\,4})\sqrt{\frac{27\,\rho_{gas}^{\,4}}{256\sigma^3\,\rho_{liq}}}, \tag{87}$$

and

$$x_{b,dil} = \left(\frac{1}{h_0^{1/2}\,U_s^{\,3}}\right)\sqrt{\frac{256\sigma^3\,\rho_{liq}}{27\,\rho_{gas}^{\,4}}}\cdot\ln\left(\frac{A_{b,dil}}{A_0}\right). \tag{88}$$

The relative importance of sinuous and dilational waves can be estimated from the ratio of the breakup lengths calculated with Eqs. 86 and 88,

$$\frac{(x_b)_{sine}}{(x_b)_{dil}} = \frac{\ln[A_{b,sine}/A_0]}{\ln[A_{b,dil}/A_0]}\left(\frac{3\sqrt{3}}{8}\right)\left(\frac{\rho_{gas}\,h_0U_s^{\,2}}{\sigma}\right). \tag{89}$$

The term $A_{b,sine}$ is defined by Eq. 77, and $A_{b,dil}$ was given as Eq. 67. Using these expressions, the ratio of breakup lengths is found to be a function of the sheet Weber number,

$$We_{sheet,g} = \frac{\rho_{gas}\,h_0U_s^{\,2}}{\sigma}, \tag{90}$$

the undisturbed sheet thickness, the critical sheet thickness, and the initial disturbance amplitude, that is

$$\frac{(x_b)_{sine}}{(x_b)_{dil}} \approx \frac{\ln[\pi\,h_0^2/We_{sheet,g}h_{crit}\,A_0]}{\ln[(h_0 - h_{crit})/A_0]}\left(\frac{3\sqrt{3}}{8}\right)We_{sheet,g}. \tag{91}$$

If h_{crit} and A_0 are made dimensionless using h_0 as the length scale, then the ratio of breakup lengths is a function of three parameters, the Weber number, (h_{crit}/h_0), and (A_0/h_0). A transition Weber number is defined as the Weber number at which the ratio of breakup lengths exceeds one. This is the point where the optimum dilational wave results in breakup rather than the optimum sinuous wave.

The transition Weber number is plotted versus (A_0/h_0) for three values of (h_0/h_{crit}) in Fig. 25. Because the maximum Weber number in the perforation count experiments was 0.58, and in most cases was less than 0.1, the sinuous wave is expected to dominate the sheet thinning process. Based on this result, only sinuous waves were considered in succeeding analyses.

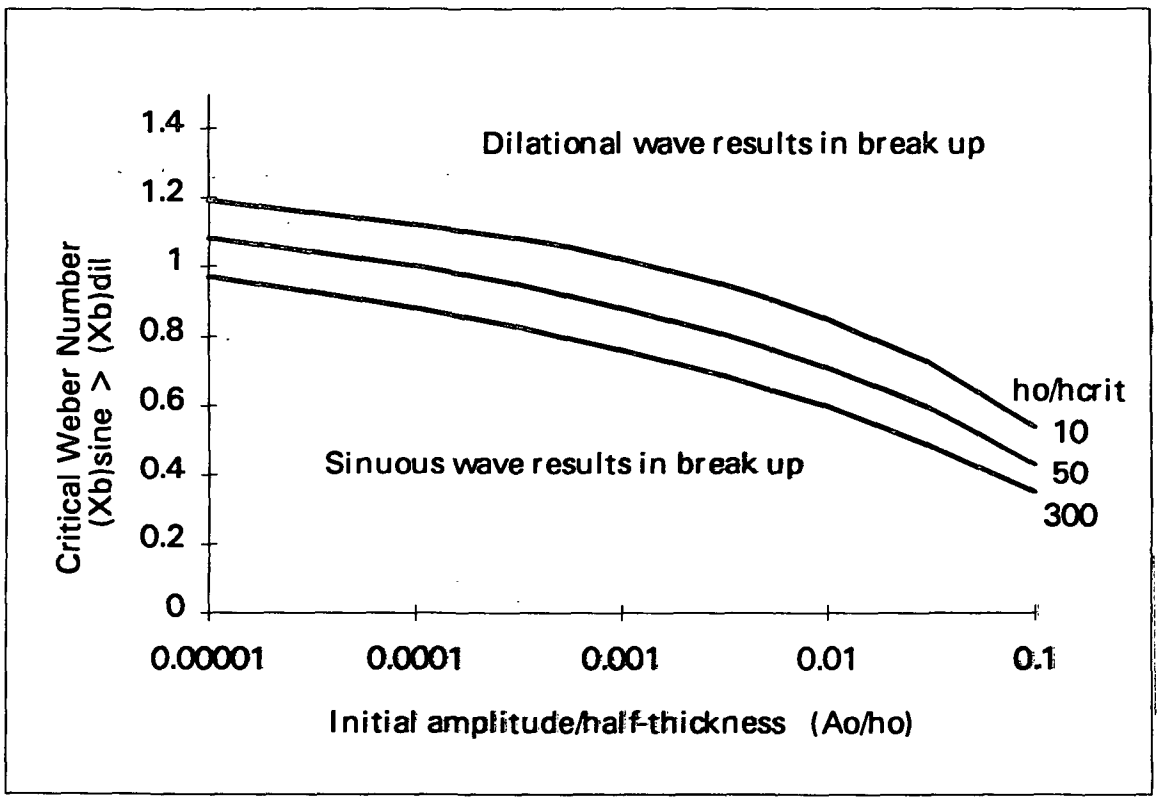

Figure 25. Comparison of sinuous and dilational wave breakup lengths.

Planar Viscous Sheets

Weihs[46] derived the relationship between the temporal growth rate parameter and the wave number of a sinuous disturbance in a viscous planar sheet. The expression he obtained is given here as

$$s_{imag} = \frac{\nu k^2}{2}\left[-1 + \left(1 + \frac{8(\rho_{gas} U_s^2 k - \sigma k^2)}{2h \rho_{liq} \nu^2 k^4}\right)^{1/2} \right]. \quad (92)$$

In order to determine the optimally growing wave (the wave number, k, for which the maximum value of s_{imag} is obtained), this expression is first rearranged to give

$$s_{imag} = \frac{\nu}{2}\left[-k^2 + \left(k^4 + \frac{8(\rho_{gas} U_s^2 k - \sigma k^2)}{2h \rho_{liq} \nu^2}\right)^{1/2} \right]. \quad (93)$$

An expression for the optimum wave number is obtained by differentiating this expression with respect to the k and setting the result equal to zero, that is

$$\frac{d(s_{imag})}{dk} = 0 = \frac{\nu}{2}\left[-2k + \frac{1}{2}\left(k^4 + \frac{8(\rho_{gas} U_s^2 k - \sigma k^2)}{2h \rho_{liq} \nu^2}\right)^{-1/2} \cdot \left(4k^3 + \frac{8[\rho_{gas} U_s^2 - 2\sigma k]}{2h \rho_{liq} \nu^2}\right)\right]. \quad (94)$$

This expression can be rearranged to obtain

$$k^3 - \left(\frac{4\sigma^2}{2h\rho_{liq} \nu^2 \rho_{gas} U_s^2}\right) k^2 + \left(\frac{4\sigma}{2h\rho_{liq} \nu^2}\right) k - \left(\frac{4\rho_{gas} U_s^2}{8h\rho_{liq} \nu^2}\right) = 0, \quad (95)$$

a cubic equation in k. A dimensionless wave number, k*, is defined as the ratio of the wave number to the wave number of optimum growth in an inviscid sheet.

$$k^* = \frac{k}{k_{opt,inv}} = \frac{2\sigma k}{\rho_{liq} U_s^2} \quad (96)$$

Upon substituting this definition into Eq. 95 and rearranging, a dimensionless expression for the optimum wave number is obtained,

$$k^{*3} - 4\Omega k^{*2} + 8\Omega k^{*} - 4\Omega = 0, \tag{97}$$

where the second dimensionless parameter is defined by

$$\Omega = \frac{\sigma^3 \rho_{liq}}{\mu_{liq}^2 \, h \, \rho_{gas}^2 \, U_s^4}. \tag{98}$$

The operating conditions and fluid properties encountered in spray applications vary such that Ω can range over several orders of magnitude. The variation of k^* with the log of Ω is shown in Fig. 26. Two regions can be distinguished in this plot. At high values of Ω ($\Omega > 400$), k^* is relatively insensitive to changes in Ω, while for intermediate values of Ω ($0.01 < \Omega < 400$), k^* is seen to decrease with a decrease in the log of Ω.

Once the sheet is formed, the only parameter in Ω which varies is the sheet thickness. The geometry of the nozzle can be used to determine the rate of change of sheet thickness with position downstream. This information can be used with the definition of Ω and its influence on k^* to determine the expected variation in the wave number of optimum growth with position downstream.

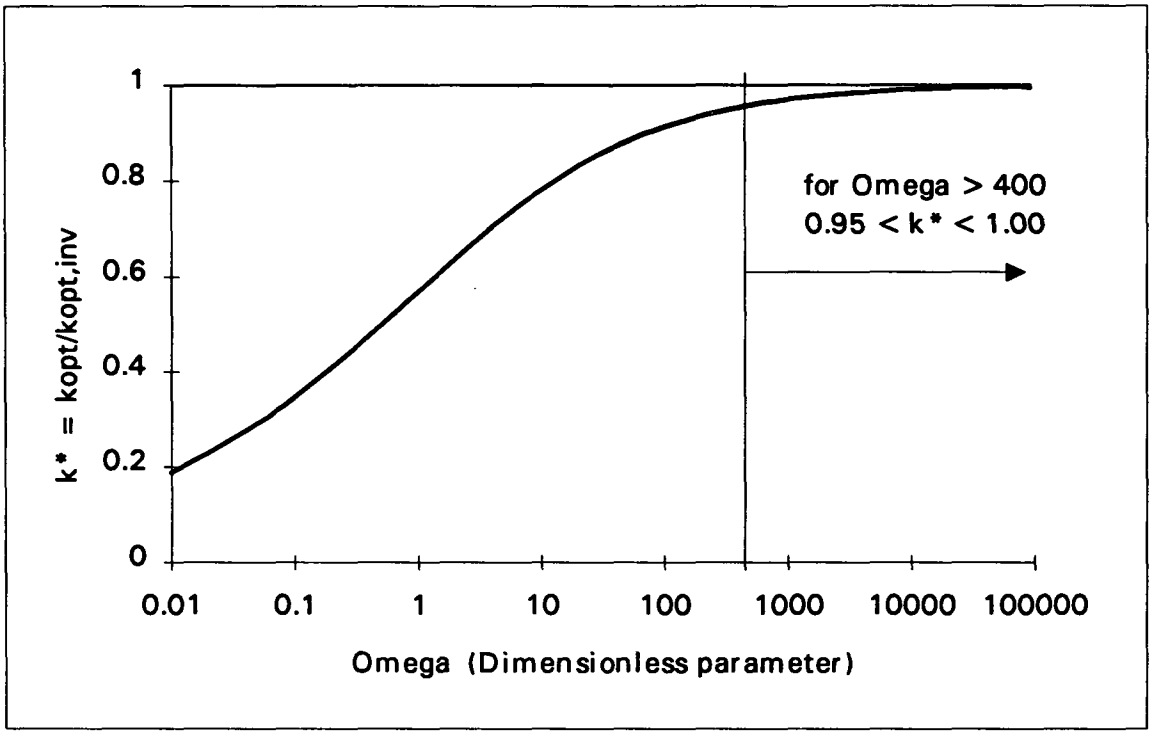

Figure 26. Dimensionless wave of optimum growth versus Ω.

Effects of the Nozzle Orifice Diameter and Jet Velocity

Before proceeding, it will be useful to examine the effects of the nozzle orifice diameter and jet velocity on each parameter which affects the wave-thinned sheet thickness, that is the undisturbed sheet thickness, the sheet velocity, the optimum wavelength, and the disturbance growth rate. A more complete picture will be developed by examining the effects of the orifice diameter and jet velocity on the calculated wave-thinned sheet thicknesses for a model system. Finally, this understanding will be used to explain the more complicated breakup behavior observed experimentally. The values plotted in the figures in this section are based on a liquid density of 1220 kg/m^3, a gas density of 1.2 kg/m^3, a liquid viscosity of 0.065 kg/m·s, and a surface tension of 0.063 kg/s^2. These values are typical of the fluid properties encountered in this study.

The expression for the sheet thickness ratio can be rewritten as

$$2h(x) = 2h^*(x)\cdot\left(C_0 + \frac{C_1 \mu_{liq}}{\rho_{liq} d_0 U_0}\left(\frac{x}{d_0}\right)^3\right). \tag{99}$$

Using the definition of the ideal sheet thickness, the sheet thickness is given by

$$2h(x) = \left(\frac{C_0}{8}\right)\left(\frac{d_0^2}{x}\right) + \left(\frac{C_1 \mu_{liq}}{8 \rho_{liq}}\right)\left(\frac{x^2}{d_0^2 U_0}\right). \tag{100}$$

Taking the derivative of the predicted sheet thickness with respect to the jet velocity,

$$\frac{\partial[2h(x)]}{\partial U_0} = \left(\frac{-C_1 \mu_{liq} x^2}{8 \rho_{liq} d_0^2}\right)\left(\frac{1}{U_0^2}\right), \tag{101}$$

it can be shown that, all other parameters being fixed, the sheet thickness at x will decrease with increasing jet velocity.

The effect of the orifice diameter on the sheet thickness is more complicated. The ratio of the viscous to inviscid sheet thickness decreases with increasing orifice diameter, but the inviscid sheet thickness itself increases with the square of the orifice diameter; thus, the viscous sheet thickness may increase or decrease with changes in the orifice diameter. For each orifice diameter, there is a downstream position at which the sheet thickness is minimized. This value of x is determined by setting the derivative of the predicted sheet thickness with respect to downstream position equal to zero,

$$\frac{\partial[2h(x)]}{\partial x} = \frac{-C_0 d_0^2}{8x^2} + \frac{C_1 \mu_{liq} x}{4 \rho_{liq} d_0^2 U_0} = 0. \tag{102}$$

This expression can be rearranged to obtain an equation for the dimensionless location of minimum sheet thickness (x/d_0), that is

$$\frac{x}{d_0} = \left(\frac{C_0\, Re_{jet}}{2\, C_1}\right)^{1/3}. \tag{103}$$

The effects of both the orifice diameter and the jet velocity on the sheet thickness at the plate edge are shown in Fig. 27. As can be seen, at low jet velocities, the predicted sheet thickness for the 6.0 mm nozzle is greater than that for the 7.0 mm nozzle, but at higher jet velocities, this trend is reversed.

The expression for the average sheet velocity can be written as

$$U_{s,avg}(x) = \frac{U_0}{C_1 + C_4\left(\frac{x^3}{d_0{}^4 U_0}\right)} = \frac{d_0{}^4\, U_0{}^2}{C_1 d_0{}^4 U_0 + C_4 x^3}. \tag{104}$$

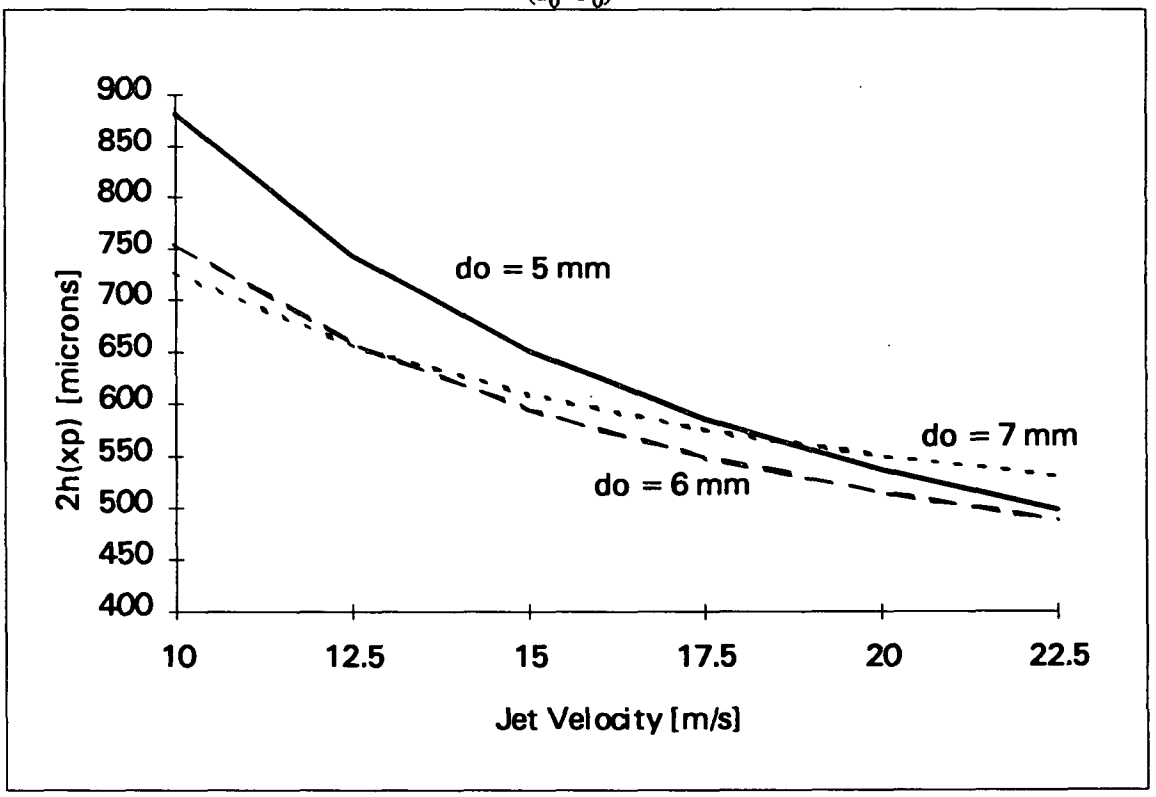

Figure 27. Predicted sheet thickness on the plate edge.

The effects of the orifice diameter and jet velocity on the predicted average sheet velocity are shown in Fig. 28. In this case, it is apparent from Eq. 104 that increasing either parameter (d_0 or U_0) leads to an increase in the average velocity of the sheet.

Once the sheet thickness and velocity at the plate edge are known, the wave-length of optimum growth can be calculated. The optimum wavelength for an inviscid sheet is plotted as a function of the orifice diameter and jet velocity in Fig. 29. As shown, increasing either parameter decreases the wavelength of optimum growth rate. The effect is most pronounced at low jet velocities (U_0 < 15 m/s).

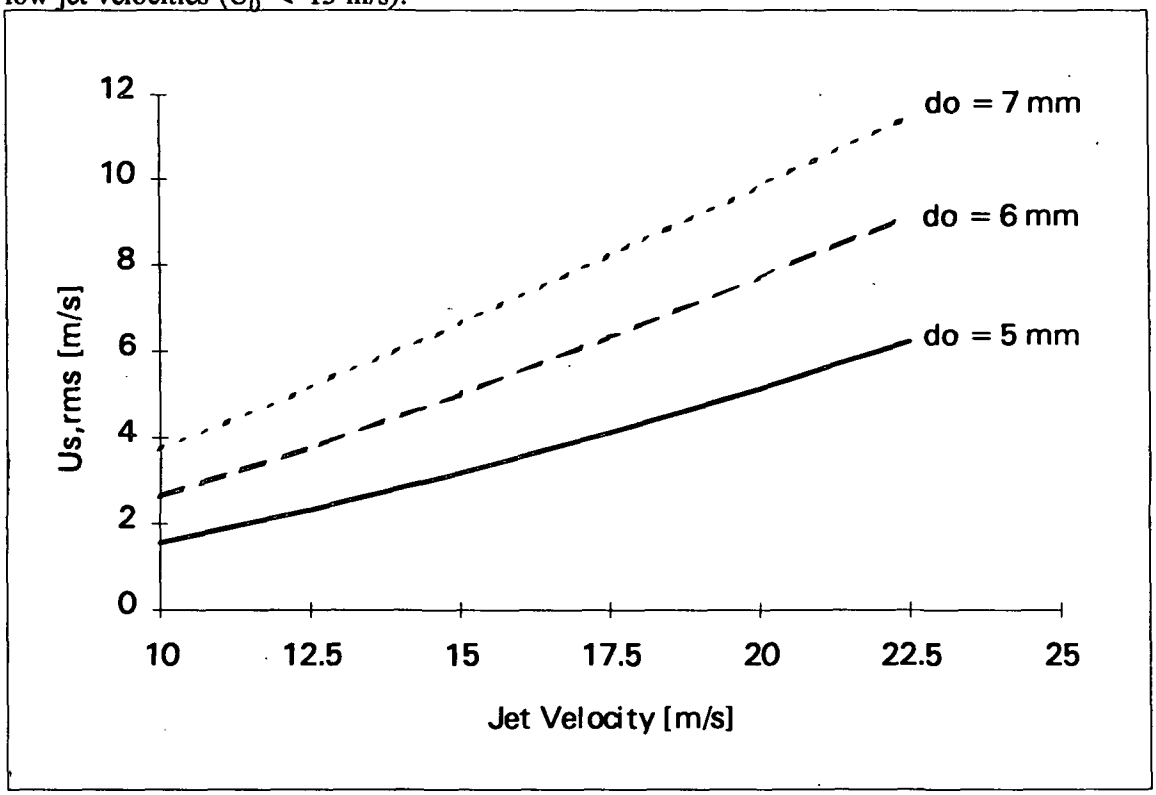

Figure 28. Predicted sheet velocity on the plate edge.

It is important to note that the influence of the jet diameter on the wavelength of optimum growth at a fixed jet velocity is due to the previously described variations in the sheet velocity at the plate edge. For instance, referring to Fig. 28, using the 5 mm nozzle to

produce a 20 m/s jet will result in a sheet with a velocity of approximately 5 m/s, while at the same jet velocity, the sheet produced using the 7 mm nozzle will have a velocity of about 10 m/s. Because the optimum wavelength is inversely proportional to the square of the sheet velocity, this difference in sheet velocity for a fixed jet velocity results in a difference in the optimum wavelength as well.

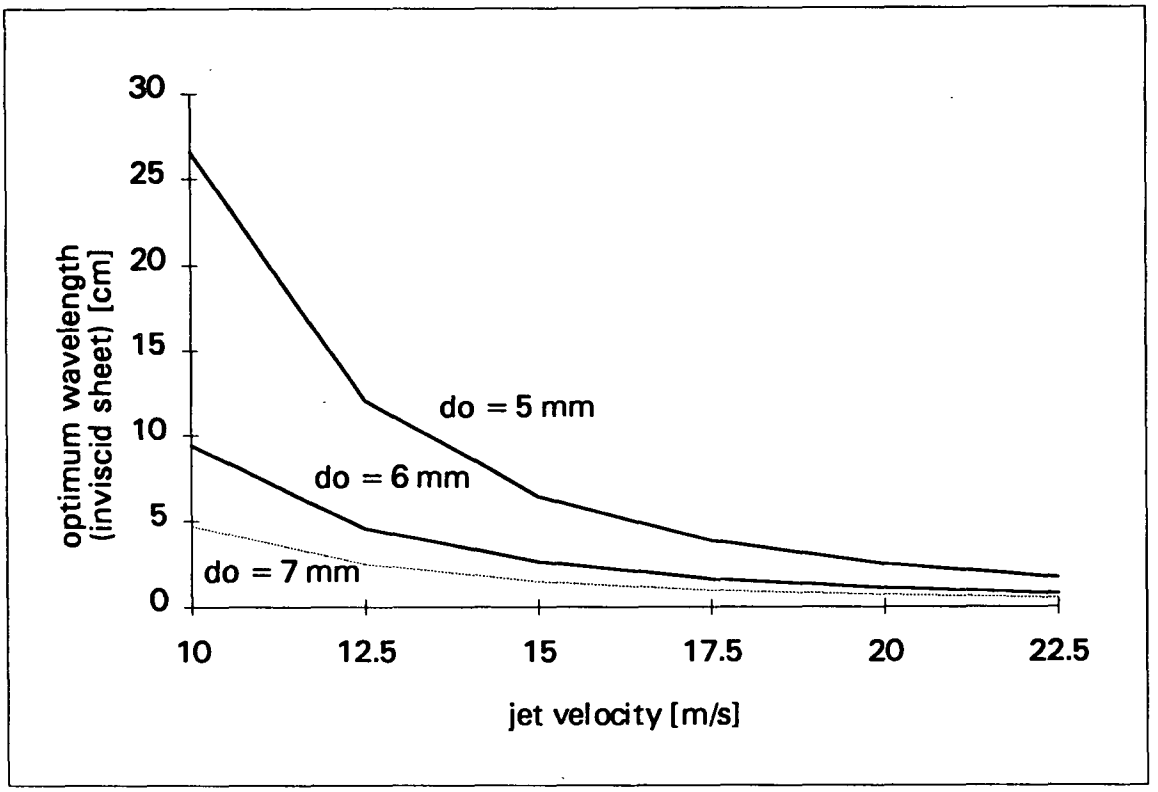

Figure 29. Predicted optimum wavelength at the plate edge.

As shown in Fig. 26, the wave number of optimum growth in a viscous sheet is a function of the dimensionless parameter, Ω. Based on Eq. 98, Ω varies with one over the sheet velocity to the fourth power. The sheet velocity and nozzle diameter also affect Ω through their influence on the sheet thickness, as Ω is a function of one over h.

The change in the wavelength of optimum growth in a viscous sheet relative to the optimum inviscid wave is shown in Figs. 30 and 31 for the 5.0 and 6.0 mm nozzles. In both cases, an increase in the jet velocity results in an increase in the wavelength of optimum

growth relative to the inviscid wave of optimum growth. Comparing the two figures, it can be seen that this effect is greater for the larger orifice diameter nozzle.

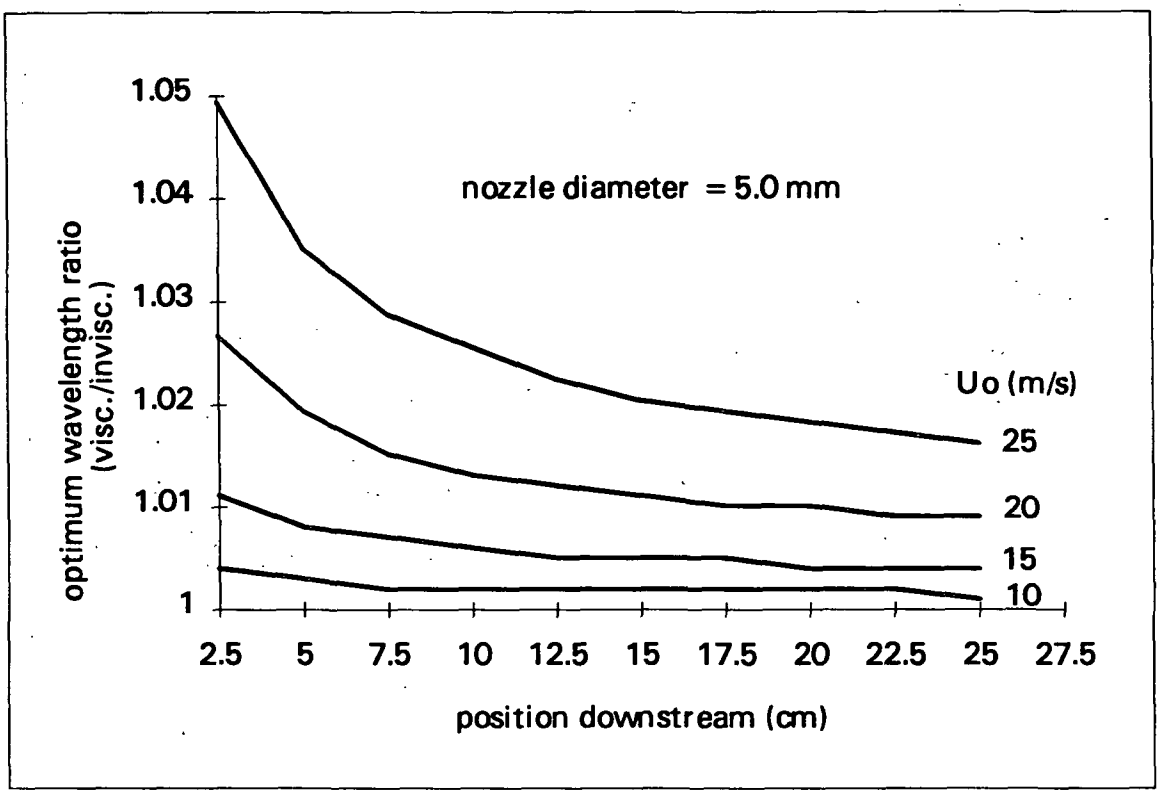

Figure 30. Predicted optimum wavelength ratio (viscous/inviscid) for d_0 = 5 mm.

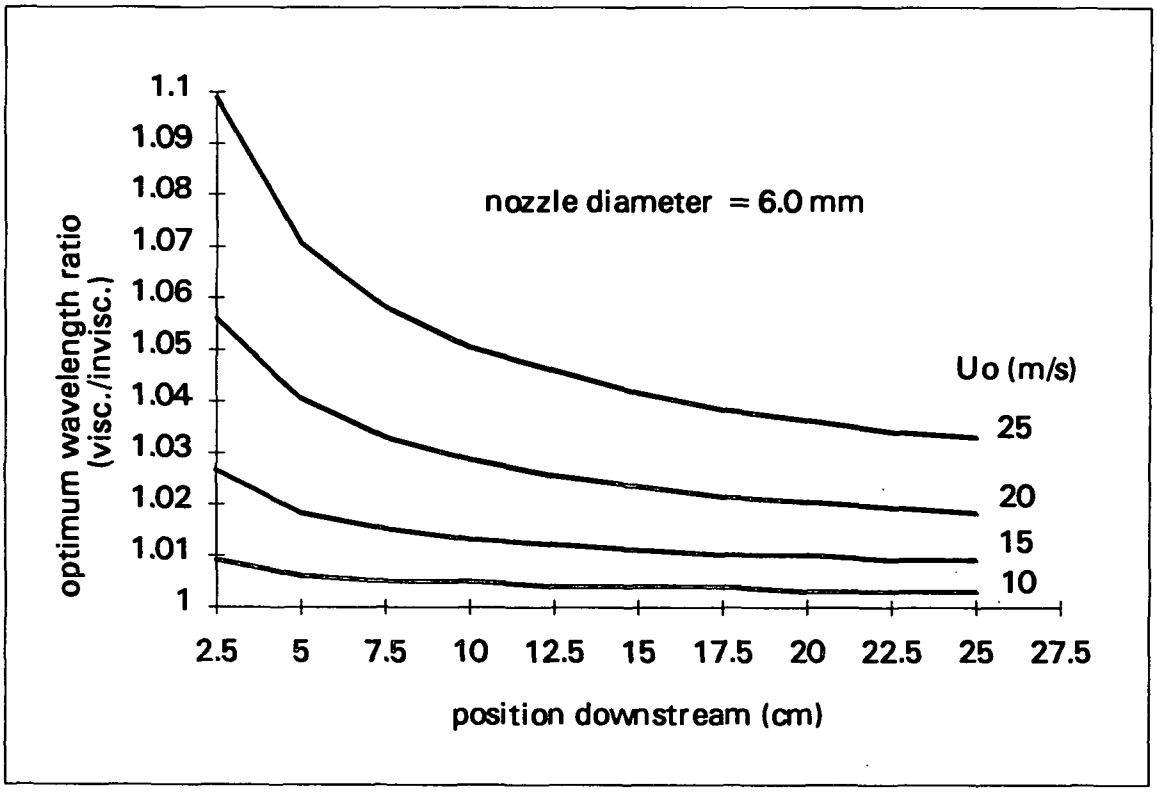

Figure 31. Predicted optimum wavelength ratio (viscous/inviscid) for d_0 = 6 mm.

Finally, the effects of the orifice diameter and jet velocity on the growth rate of the optimum disturbance mode are shown in Fig. 32.

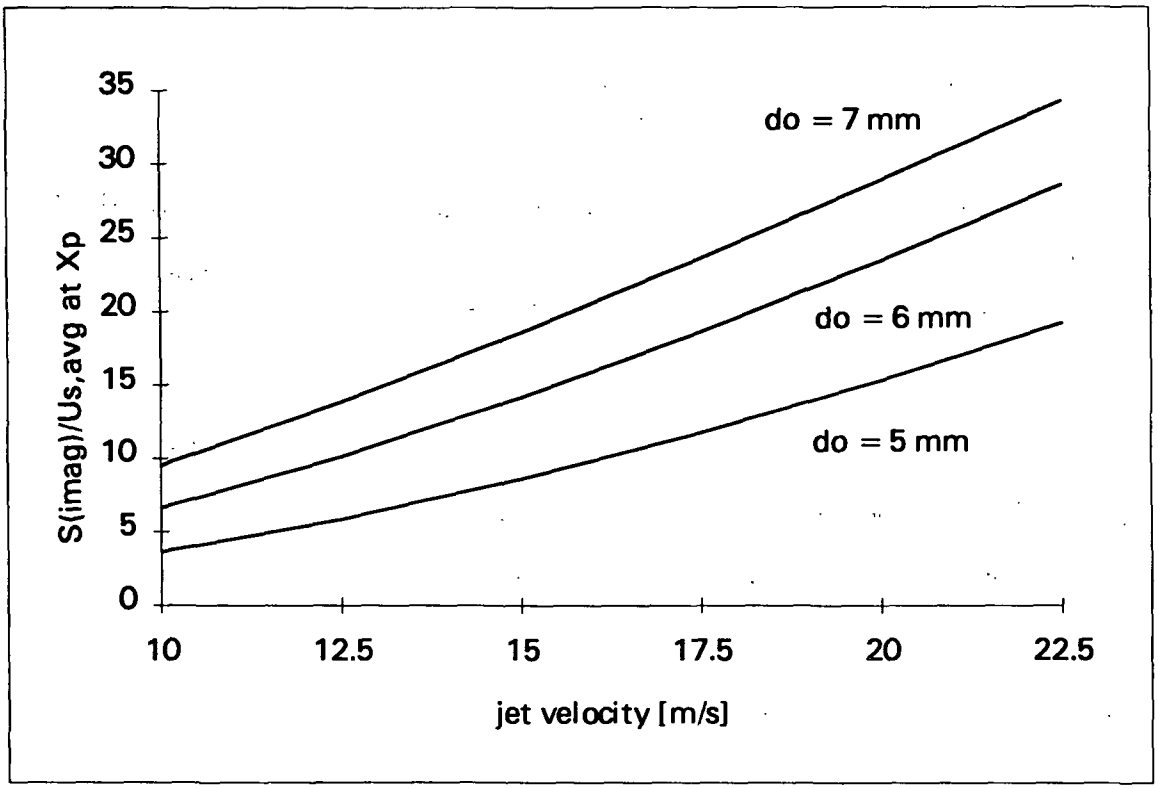

Figure 32. Predicted wave growth rate at the plate edge.

The temporal growth rate parameter, s_{imag}, is divided by the sheet velocity to give a measure of the expected rate of increase in the amplitude of the disturbance with position downstream, as shown in Eq. 79. Increasing either the jet velocity or the orifice diameter is seen to lead to a more rapidly growing wave and, thus, should result in the breakup of the sheet closer to the plate edge.

The predicted effects of the orifice diameter and jet velocity on the downstream behavior of the sheet are summarized in Table 12.

Table 12. The predicted effects of the nozzle orifice diameter and jet velocity on the downstream behavior of a liquid sheet.

parameter	effect of increasing d_0	effect of increasing U_0
downstream sheet thickness, 2h(x)	may increase or decrease	decreases
downstream sheet velocity, $U_{s,avg}$	increases	increases
optimum inviscid wavelength, λ_{opt}	decreases	decreases
viscous/inviscid wavelength	increases	increases
spatial growth rate, $s_{imag}/U_{s,avg}$	increases	increases

General trends in the wave-thinned sheet thickness

In this computational study, the physical properties of the fluid were fixed in order to determine the effects of the nozzle orifice diameter, the jet velocity, and the downstream position on the predicted wave-thinned sheet thickness. The values used were typical of the glycerol/water solutions used experimentally and are summarized in Table 13.

Table 13. Parameter range investigated in the numerical study of wave-thinned sheet thicknesses.

parameter	values investigated
nozzle diameter	5.0 and 6.0 mm
jet velocity	10-25 m/s
downstream position	2.5-27 cm
liquid density	1220 kg/m^3
gas density	1.2 kg/m^3
liquid viscosity	0.065 kg/ms
surface tension	0.063 kg/s^2

The FORTRAN program written to perform the necessary calculations is included in Appendix H. The procedure used is summarized here.

Set the operating conditions
- the physical properties of the fluid
- the nozzle diameter
- the jet velocity

Calculate the base conditions
- sheet thickness at the plate edge (Eq. 59)
- sheet velocity at the plate edge (Eq. 59)
- minimum value for Ω (Eq. 98)
- optimum wave number for an inviscid sheet (Eq. 83)
  - using Ω_{min} and k_{inv}, determine the minimum k_{opt} (Eq. 95)
  - investigate growth of 20 disturbances with $k_{opt,min} < k < k_{inv,opt}$

Step from the plate edge (x_p = 2.5 cm) out to 27 cm in increments of 0.1 cm
- assume an initial disturbance amplitude of $A_0 = 1 \times 10^{-6}$ m at $x = x_p$
- calculate the undisturbed sheet thickness (Eq. 65)
- calculate the local growth rate of each disturbance (Eq. 92)
- calculate the amplitude of each disturbance (Eq. 79)
  - determine the wave number which yields the greatest amplitude
  - determine the wave-thinned sheet thickness for this disturbance (Eq. 70)

Plot the wave-thinned sheet thickness versus the downstream position

Repeat these steps for a range of jet velocities

Repeat these steps for each nozzle orifice diameter

The estimated thicknesses at 0.5 cm intervals from 2.5 to 25 cm downstream are plotted in Figs. 33 and 34 for the 5.0 and 6.0 mm nozzles, respectively.

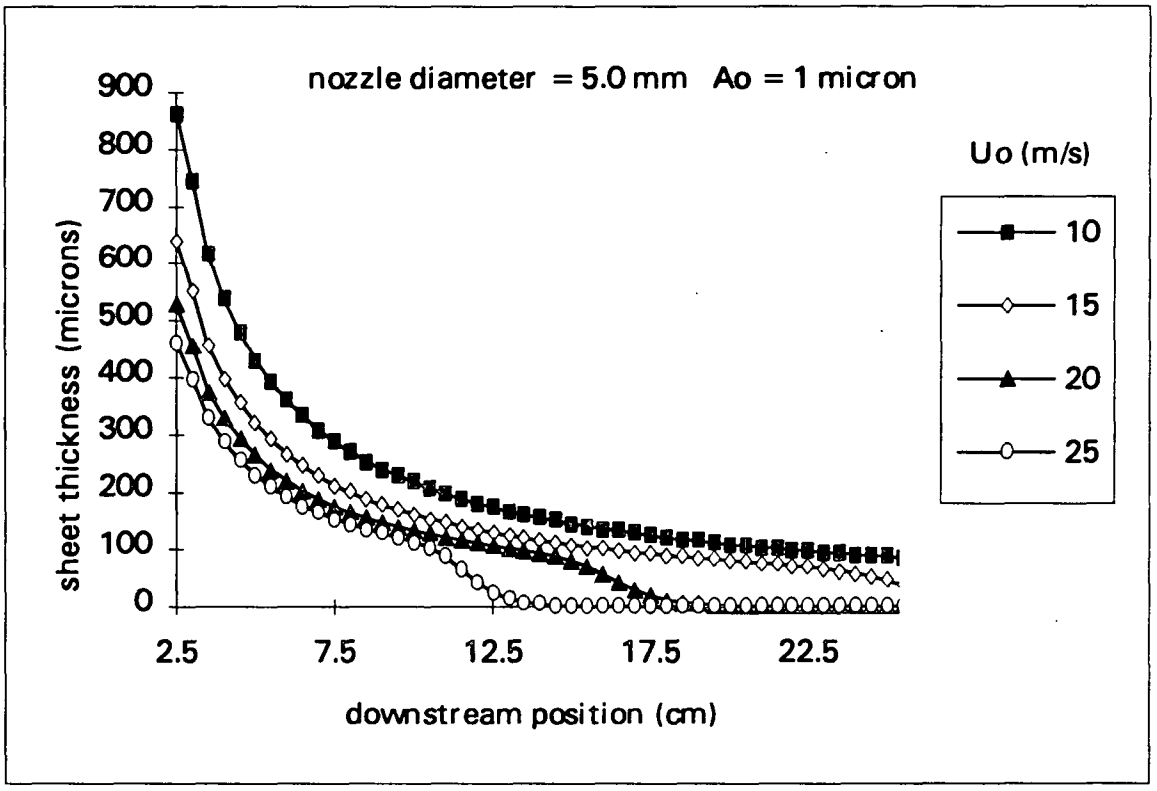

Figure 33. Predicted downstream sheet thickness (d_0 = 5.0 mm).

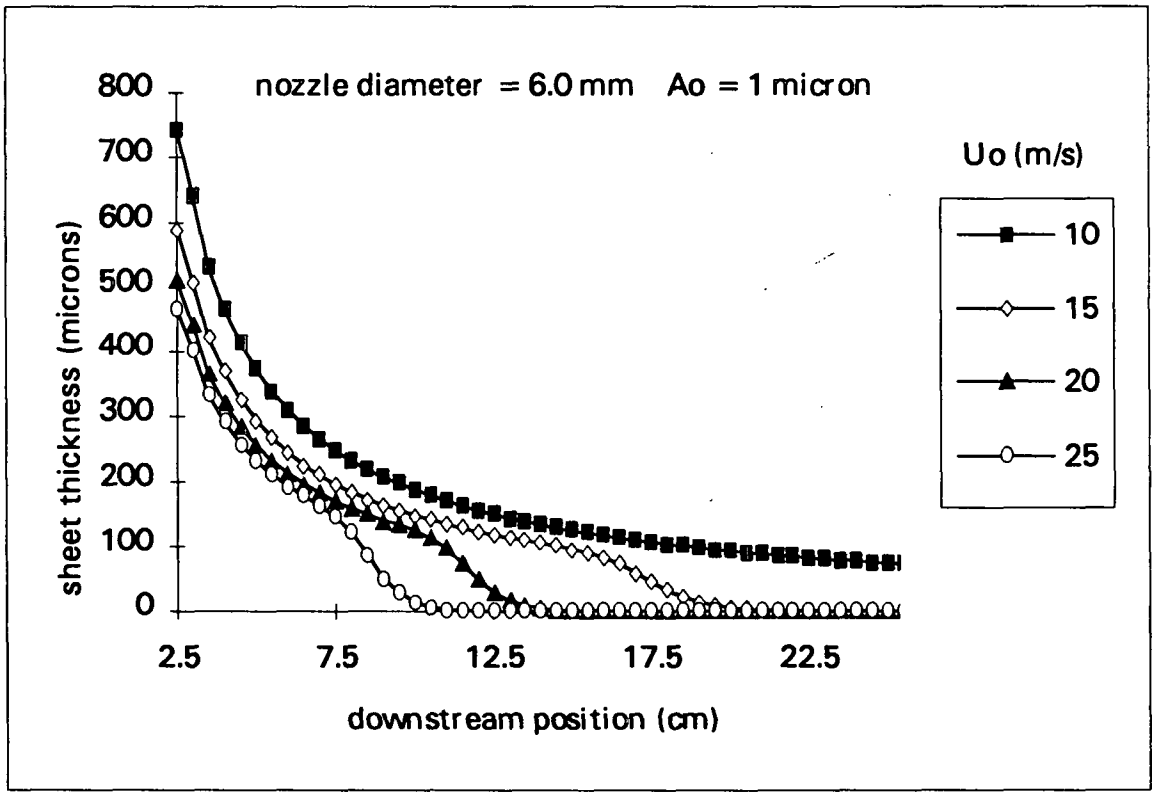

Figure 34. Predicted downstream sheet thickness (d_0 = 6.0 mm).

Upon examining Fig. 33, several trends are apparent. First, at the plate edge, the sheet thickness decreases with increasing velocity. This is a direct result of the viscous drag on the plate. The reduction in the sheet velocity will be a function of the magnitude of the shear forces at the plate surface relative to the inertia of the liquid. Schlichting[70] showed that for a Newtonian fluid, the shear stress at the plate surface would be proportional to $U_{max}^{3/2}$. As the inertial force is proportional to U_{max}^{2}, the ratio of the shear force to the inertial force is seen to be proportional to $\frac{1}{\sqrt{U}}$, and higher initial velocity sheets will be affected less by the shear stress at the plate. This result can be seen in Fig. 27, where the higher velocity (higher Reynold's number) flow is seen to be slowed less by the shear forces at the plate surface, and thus, the sheet is thinner at the plate edge than a sheet formed by a lower velocity jet. As the undisturbed downstream sheet thickness is proportional to the sheet thickness at the plate edge, the difference in sheet thickness with jet velocity persists downstream.

The sheet thickness curve for the 10 m/s sheet is seen to decrease smoothly with position downstream out to 25 cm. The unstable disturbance mode in this sheet does not grow large enough to significantly affect the sheet thickness in this range of downstream location. The thinning observed up to this position (25 cm downstream) is due solely to the radial expansion of the liquid.

The higher jet velocity sheets show this same smooth decrease in sheet thickness near the plate edge, but then a rapid drop, caused by wave-thinning, is observed. The radial position at which substantial wave-thinning is observed decreases with increasing jet velocity. This is consistent with the behavior shown in Figs. 27 and 28. At higher jet velocities, the disturbance wavelength will be shorter; thus, the amplitude required to thin the sheet to any given value is decreased relative to a longer wavelength disturbance. Also, since the rate of

amplitude increase with position downstream is greater at higher jet velocities, significant thinning will occur closer to the plate.

Comparing Figs. 33 and 34, the same general trends are observed; however, both the initial sheet thickness and the downstream location of rapid wave-thinning are seen to decrease with increasing orifice diameter for a fixed jet velocity. The decrease in the initial sheet thickness is a result of the effects of viscous drag on the plate, as previously discussed. The decrease in the breakup length with an increase in the orifice diameter is a result of the shorter disturbance wavelength and higher growth rate expected when the orifice diameter is increased for a fixed jet velocity, as shown in Figs. 29 and 32.

Calculated wave-thinned sheet thicknesses for the perforation count experiments

The wave-thinned sheet thickness for each of the perforation count experiments could be predicted using the procedure outlined in the previous section if the initial disturbance amplitude at the plate were known; however, this amplitude is unknown. An arbitrary amplitude of $A_0 = 1 \times 10^{-6}$ m was chosen to investigate trends in the predicted behavior. The results are plotted in Figs. 35, 36, and 37, for the NF-6000, NF-8000, and NF-10000 trails, respectively.

These estimated sheet thicknesses plotted in these figures can be compared qualitatively to the perforation counts shown in Figs. 17-19. The number of new perforations is seen to increase rapidly in the region where the sheet thickness decreases rapidly. This correspondence implies that the sheet ruptures when the wave-thinned sheet thickness reaches a critical value.

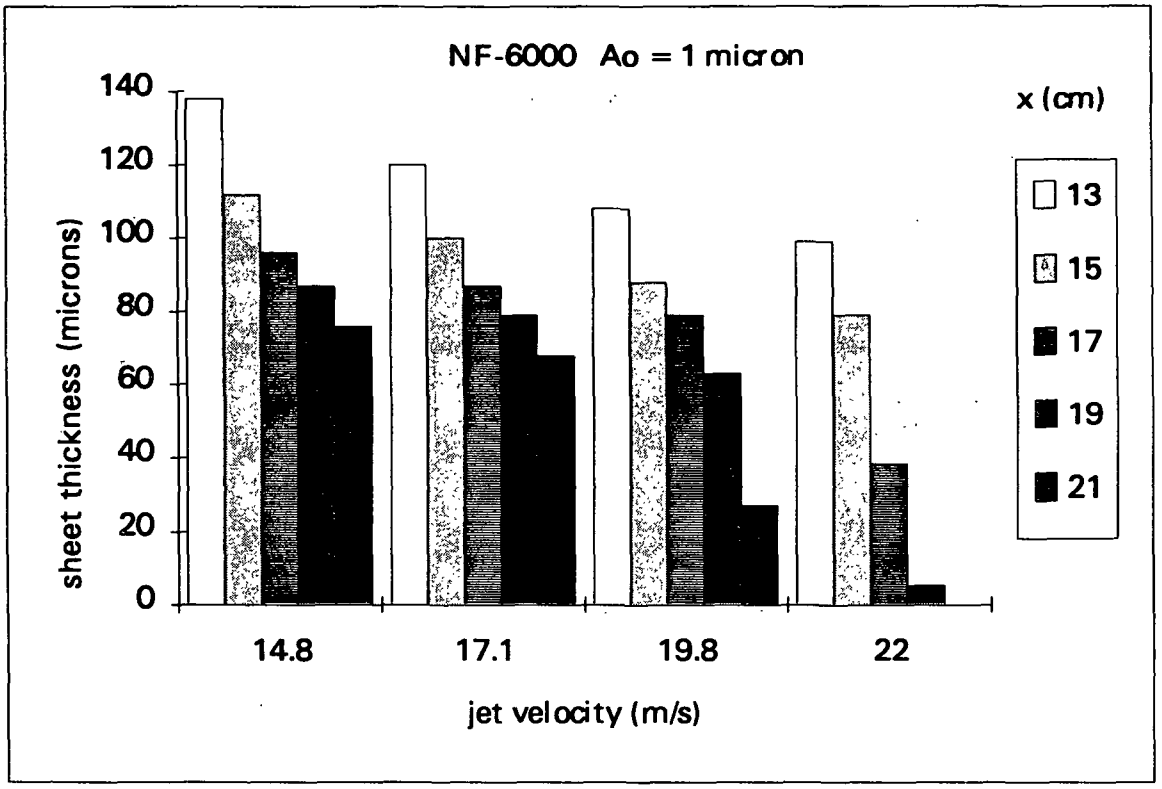

Figure 35. Calculated wave-thinned sheet thickness for the NF-6000 nozzle.

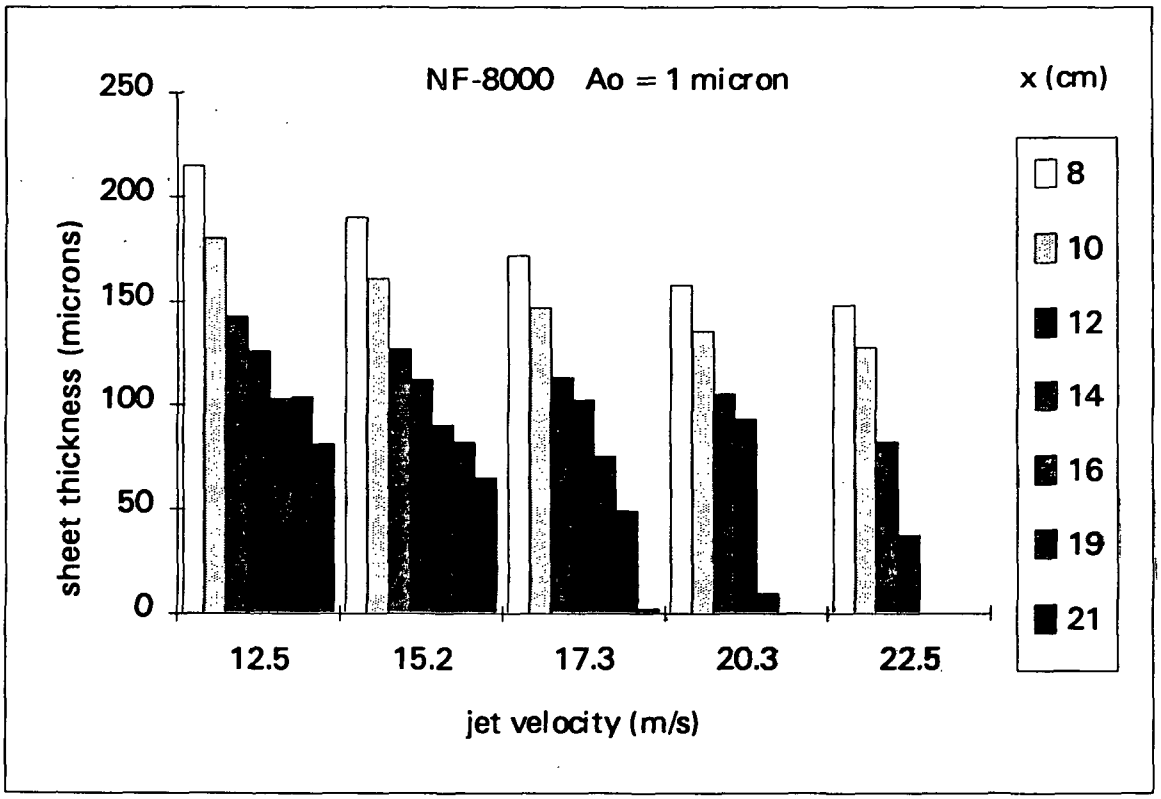

Figure 36. Calculated wave-thinned sheet thickness for the NF-8000 nozzle.

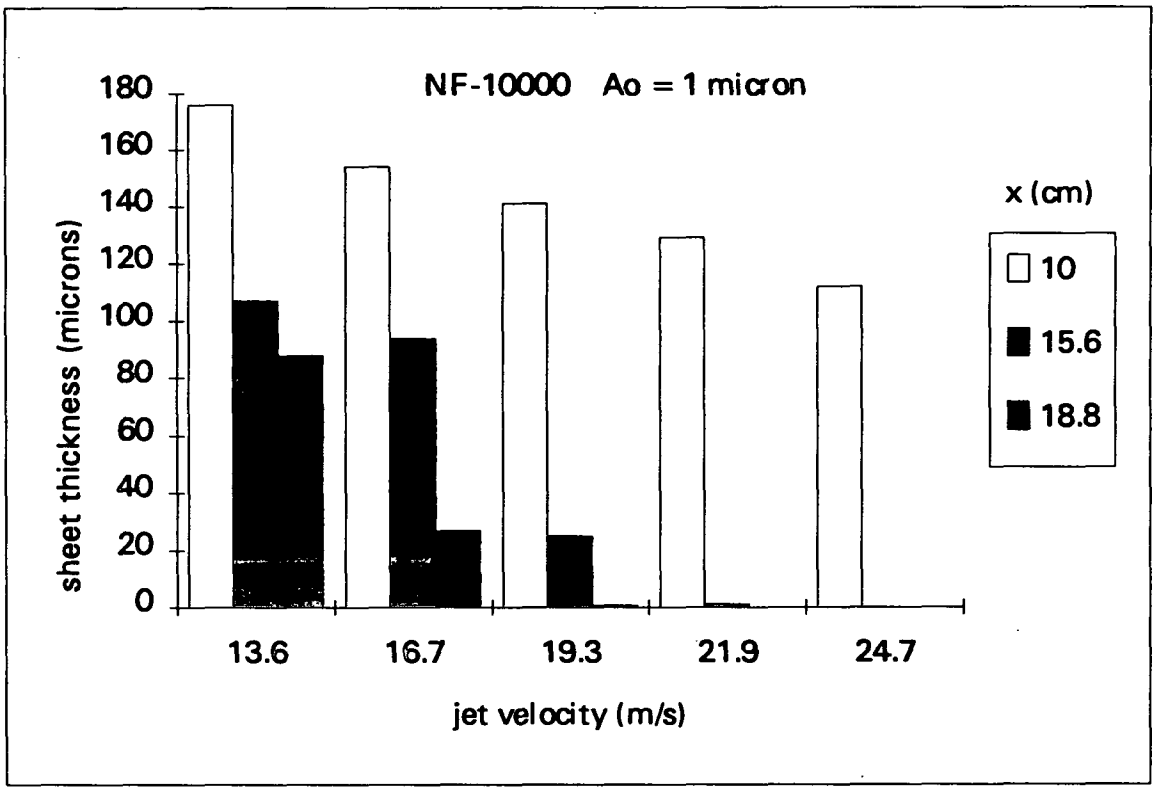

Figure 37. Calculated wave-thinned sheet thickness for the NF-10000 nozzle.

Although the wave-thinned sheet thickness is related to the undisturbed sheet thickness, the nozzle orifice diameter and jet velocity, through their effects on the wave disturbances, also play a role. Of particular importance is the predicted trend in the location of rapid thinning as a function of the nozzle orifice diameter. Despite the possibility of producing a sheet which is initially thicker at the plate edge, the sheets produced by larger orifice diameter nozzles will reach the point of rapid wave-thinning closer to the plate edge than will sheets produced by smaller orifice diameter nozzles. This occurs because the sheet velocity is higher, and thus, the disturbance wavelength is shorter, and the disturbance growth rate is higher. This predicted decrease in the breakup length with increasing orifice diameter is consistent with the trend expected from the perforation count data.

Based on the results of the perforation count experiments, the breakup length (or location of rapid thinning) should decrease as a function of the sheet velocity. This is

consistent with the results of the wave-thinning analysis; however, only a limited range of sheet velocities were investigated. Additional effects of waves on the breakup length as a function of the sheet velocity will be investigated in a later section. The role of externally-induced disturbances and their growth rates relative to the wave of optimum growth is of particular importance.

Experimental Measurement of Perforation Growth Rates

The wave-thinning analysis and numerical calculations were used to predict a significant decrease in the downstream sheet thickness relative to the undisturbed sheet thickness. In order to confirm these predictions, experiments were performed to determine the downstream sheet thickness.

The thickness of the sheet spreading on the fluid plate could be measured directly using extended micrometer probes. For the free sheet spreading radially from the plate edge, this method cannot be used as the location of both the top and bottom surfaces is expected to vary as sinuous and dilational waves perturb the sheet. In this section an indirect method for measuring the sheet thickness is described.

As reported in the background section, Fraser *et al.*[39] derived an expression for predicting the growth rates of perforations in a thin sheet based on a balance of surface tension and inertial forces. Based on this equation, the growth rate is expected to be inversely proportional to the square root of the sheet thickness; thus, if the fluid properties and the growth rate of the perforations are known, then the sheet thickness can be estimated as

$$h = \frac{\sigma}{e^2 \rho_{liq}} = \frac{\sigma}{\left(\frac{\partial R_P}{\partial t}\right)^2 \rho_{liq}} . \qquad (36)$$

High-speed films obtained with the Hycam 16 mm camera were projected onto a sheet of paper. The outline of a perforation was traced for consecutive frames from the point at which it was first observed until it left the field of view or interacted with a second perforation. These tracings were used to measure the axis of the perforation both radially (in the direction of flow) and laterally (perpendicular to the direction of flow). These data were divided by two in order to obtain values of the radial semiaxis and the lateral semiaxis of the perforation. The rate of change with time of either of these values could then be used as $\partial R_P/\partial t$ in Eq. 36 to estimate the sheet thickness.

In order to use this data to obtain perforation growth rates, the framing rate and the sheet velocity must be known. The framing rate was calculated from the TLG marks on the films. The sheet velocity was taken to be the root mean square velocity based on the linear regression equation obtained previously. The spray operating conditions for which perforation growth rate data were collected are included in Appendix I.

The geometry of the spray is such that the apparent growth rate in the lateral direction is expected to be greater than that in the radial direction. This increase in measured growth is a result of the lateral spread of the fluid sheet as it proceeds downstream. The stretching of the perforations can be estimated from the geometry of the system as shown in Fig. 38. In this figure, a perforation at position x with a lateral semiaxis length of $R_{P,L}(x)$ moves downstream with the sheet velocity, U_s. After a time, Δt, the perforation is located at $x + \Delta x$, and the length of the lateral semiaxis is $R_{P,L}(x+\Delta x)$. This increase in length is caused by both the surface tension driven temporal growth and the spatial growth or stretching of the perforation, that is

$$R_{P,L}(x+\Delta x) = R_{P,L}(x) + \frac{\partial R_{P,L}}{\partial t}\Delta t + \frac{\partial R_{P,L}}{\partial x}\Delta x. \qquad (105)$$

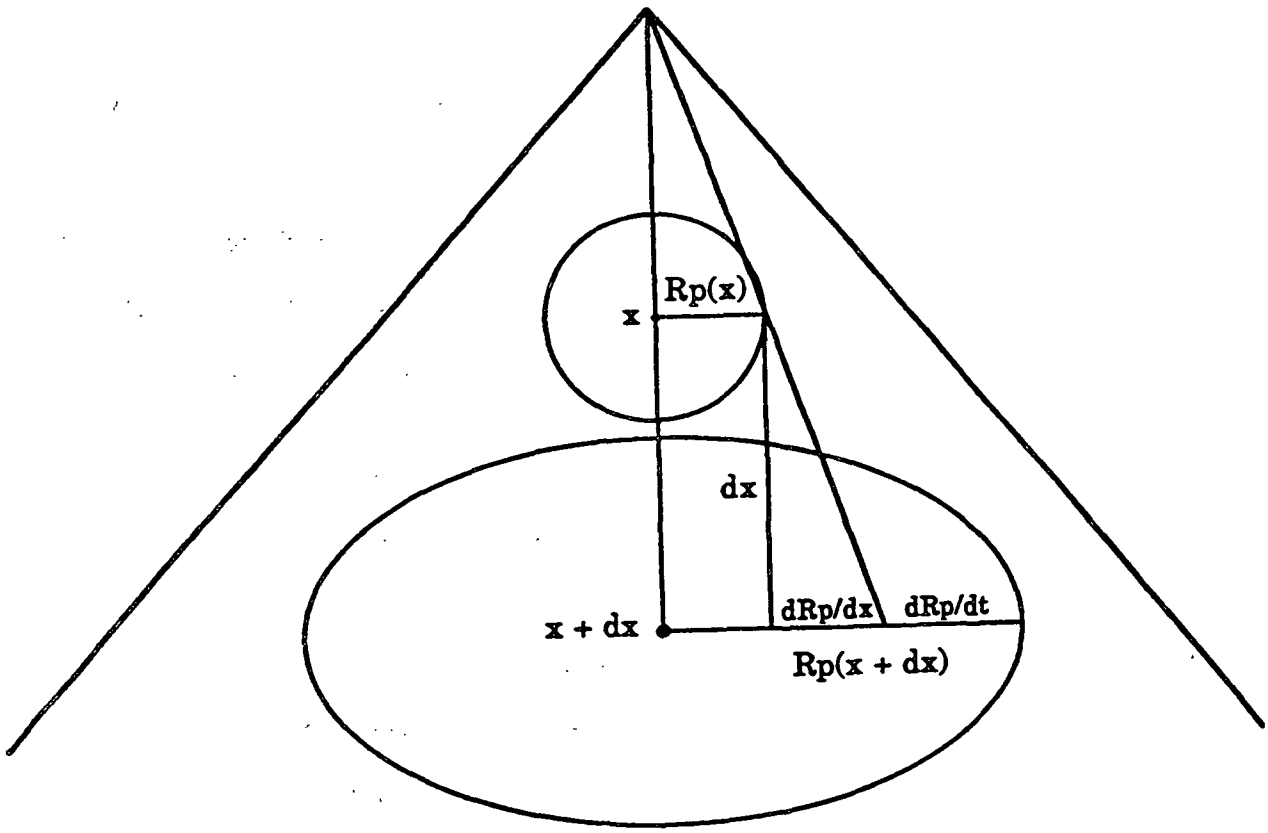

Figure 38. Lateral stretching of a perforation in a radially thinning sheet.

From the geometry of the perforation, the stretching of the perforation is given by

$$\frac{\partial R_{P,L}}{\partial x} \approx \frac{R_{P,L}(x)}{x}, \tag{106}$$

The differential increase in downstream position, Δx, can be written as $U_s \Delta t$. These expressions can be combined and the result rearranged to obtain an equation for the temporal growth of the perforation,

$$\left(\frac{\partial R_{P,L}}{\partial t}\right)\Delta t = R_{P,L}(x+\Delta x) - R_{P,L}(x) - \left(\frac{U_s R_{P,L}(x)}{x}\right)\Delta t \qquad (107)$$

This expression was used to correct the lateral semiaxis growth data in order to obtain the true value for the surface tension driven growth of the perforations. Because the ratio of the lateral semiaxis length to downstream position was small, this correction was less than 5% for all of the perforations investigated.

Plots of the radial and lateral semiaxes as a function of time are shown in Figs. 39 and 40 for two representative perforations. Plots of the lateral and radial perforation growth as a function of time are included in Appendix I for each perforation measured. In both cases, the lateral perforation semiaxis increases linearly with time, in agreement with the prediction of Fraser *et al.*[39] The radial perforation semiaxis appears to increase linearly with time in the early stages of growth, but at a rate which is significantly less than that of the lateral semiaxis.

Linear regression was used to determine the best fit straight line to the semiaxis length versus time data. The slope of this line could then be used to estimate the perforation growth rate. This value was used with the measured values for the liquid density and surface tension to estimate the sheet thickness in the region of rupture.

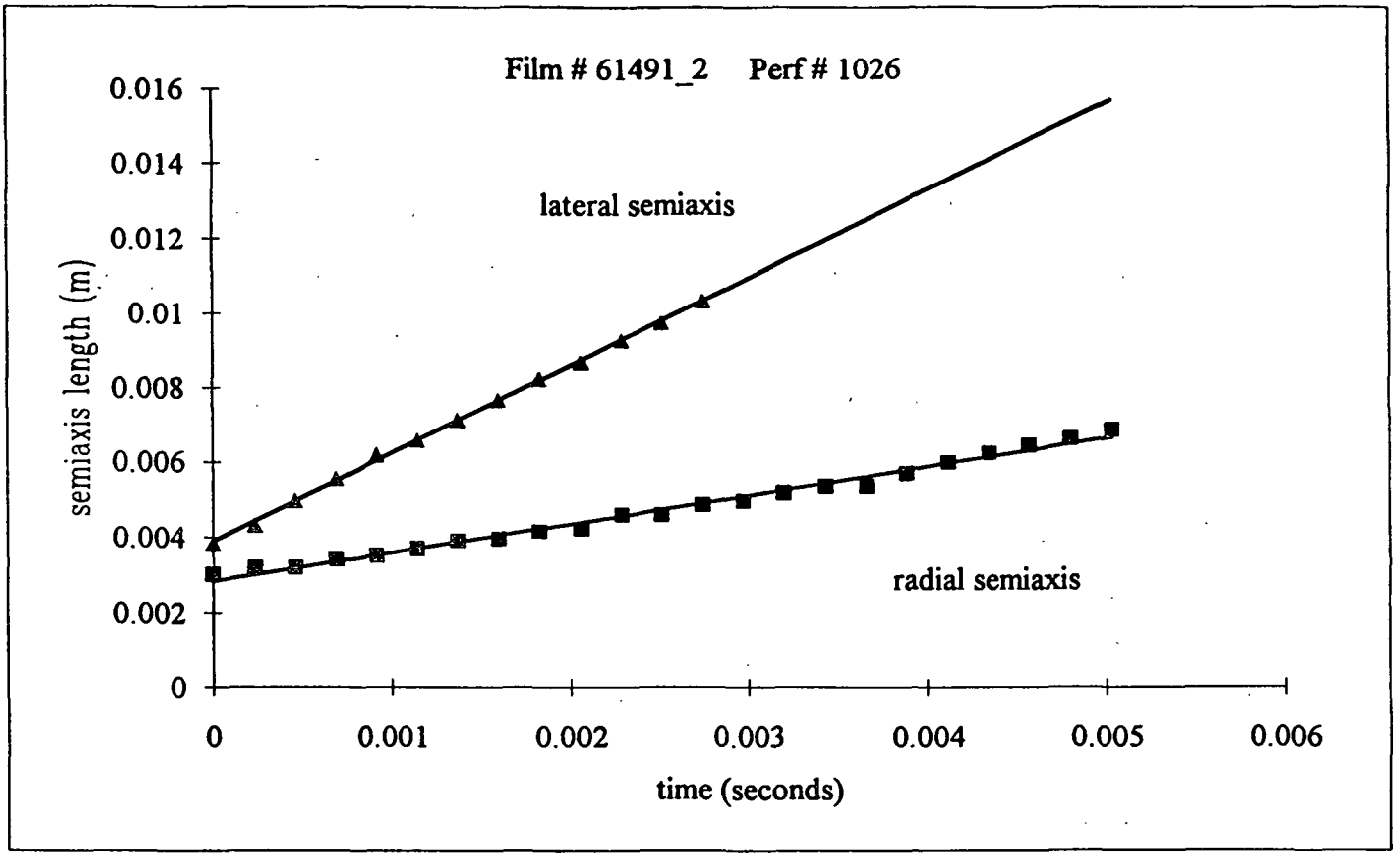

Figure 39. Lateral and radial perforation growth rates: Film #61491_2, #1026.

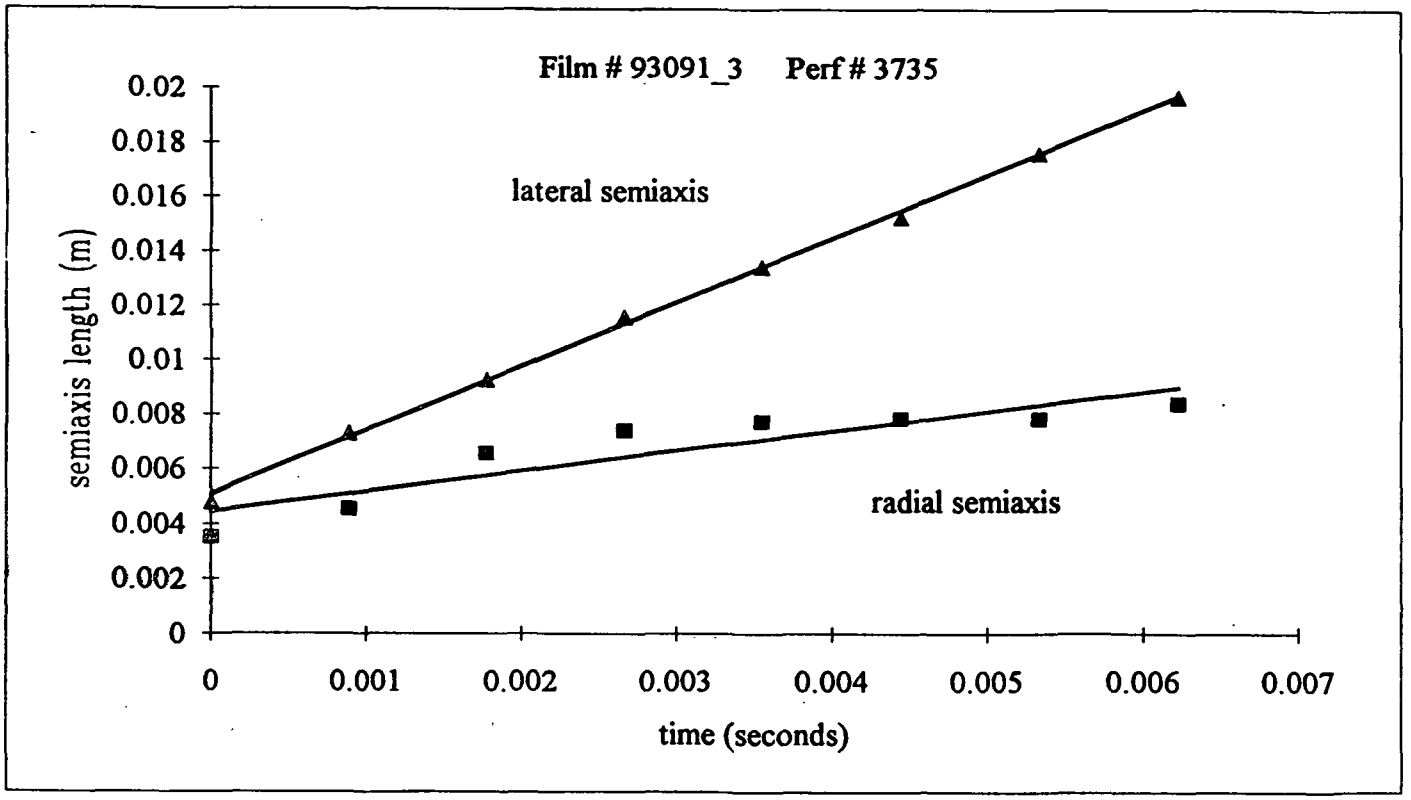

Figure 40. Lateral and radial perforation growth rates: Film #93091_3, #3735.

The operating conditions for each trial are summarized in Table 14. The radial and lateral perforation growth rates, the coefficient of determination for the linear regression, and the sheet thicknesses calculated from these values are listed in Table 15. In these tables, the Film number refers to the particular 16 mm film from which the perforation growth rates were measured. The I.D. number refers to the frame number at which the perforation was first seen.

Table 14. Operating conditions for the perforation growth rate experiments.

Film number	U_0 (m/s)	viscosity (kg/m·s)	downstream position (cm)	2h[a] (microns)
61491-2	15.3	0.060	16	45
61491-4	15.5	0.056	20	35
93091-2	16.1	0.128	39	50
93091-3	17.7	0.126	39	50
93091-4	19.1	0.123	39	48

a predicted thickness based on radial expansion only

Table 15. Measured perforation rim velocities and calculated sheet thicknesses.

film #	ID #	$dR_{P,R}/dt$	r^2	2h (μm)	$dR_{P,L}/dt$	r^2	2h (μm)
61491-2	908	1.1 ± 0.3	0.993	80 ± 50	-	-	-
	920	1.7 ± 0.2	0.995	30 ± 10	-	-	-
	927	2.3 ± 1.7	0.941	20 ± 10	4. ± 4.	0.883	6 ± 2
	962	1.7 ± 0.3	0.992	40 ± 10	4.6 ± 0.2	0.999	4.9 ± 0.4
	976	1.2 ± 0.1	0.978	70 ± 20	5.1 ± 0.1	0.999	4.0 ± 0.2
	1026	0.83 ± 0.05	0.989	150 ± 60	2.35 ± 0.05	0.999	19 ± 2

Table 15. Continued

film #	ID #	$dR_{P,R}/dt$	r^2	2h (μm)	$dR_{P,L}/dt$	r^2	2h (μm)
61491-4	580	2.4 ± 0.8	0.981	18 ± 6	-	-	-
	612	1.2 ± 0.5	0.906	60 ± 50	4.0 ± 0.3	0.986	6.4 ± 0.6
	655	3.5 ± 0.8	0.994	8 ± 2	7. ± 10	0.980	2.1 ± 0.5
	665	3.6 ± 1.1	0.989	8 ± 2	5.8 ± 0.4	0.997	3.0 ± 0.2
	716	1.20 ± 0.08	0.993	70 ± 20	-	-	-
	726	2.4 ± 0.5	0.953	17 ± 8	9. ± 3.	0.988	1.2 ± 0.1
	746	0.21 ± 0.07	0.785	2000 ± 9000	-	-	-
	752	0.88 ± 0.06	0.981	130 ± 50	-	-	-
93091-2	9536	0.9 ± 0.3	0.984	100 ± 90	1.7 ± 0.3	0.999	40 ± 10
	9570	1.46 ± 0.05	0.999	48 ± 9	2.17 ± 0.05	0.979	22 ± 2
	9584	1.3 ± 0.2	0.971	60 ± 30	2.2 ± 0.2	0.986	22 ± 4
	9593	1.8 ± 0.2	0.996	29 ± 8	3.2 ± 0.3	0.997	10 ± 1
	9699	1.3 ± 0.2	0.992	60 ± 30	2.3 ± 0.9	0.925	20 ± 8
	9704	1.2 ± 0.1	0.992	70 ± 20	3.4 ± 0.3	0.994	9 ± 1
	9562	1.06 ± 0.06	0.890	100 ± 30	-	-	-
	9669	1.57 ± 0.07	0.997	40 ± 10	-	-	-
	9704	1.18 ± 0.06	0.992	70 ± 20	-	-	-

Table 15. Continued

film #	ID #	$dR_{P,R}/dt$	r^2	2h (μm)	$dR_{P,L}/dt$	r^2	2h (μm)
93091-3	3735	0.7 ± 0.3	0.825	200±300	2.35 ± 0.07	0.999	19 ± 12
	3736	1.2 ± 0.3	0.961	60 ± 40	3.0 ± 0.3	0.992	12 ± 2
	3747	0.6 ± 0.4	0.685	300±600	2.5 ± 0.3	0.988	16 ± 3
	3755	1.3 ± 0.2	0.979	50 ± 20	2.4 ± 0.1	0.996	18 ± 2
	3758	1.9 ± 0.1	0.993	27 ± 5	2.6 ± 0.1	0.997	15 ± 2
	3777	1.3 ± 0.1	0.991	60 ± 20	2.22 ± 0.09	0.998	21 ± 3
	3779	2. ± 1.	0.934	20 ± 10	2.9 ± 0.4	0.992	12 ± 2
	3782	2.4 ± 0.2	0.998	17 ± 3	2.82 ± 0.06	0.9999	13 ± 1
	3785	1.6 ± 0.1	0.992	39 ± 9	2.6 ± 0.1	0.997	15 ± 2
	3804	1.4 ± 0.2	0.948	50 ± 20	2.47 ± 0.04	0.999	17 ± 1
	3834	1.6 ± 0.2	0.994	40 ± 10	3.2 ± 0.1	0.9995	10.1 ± 0.8
	3848	2.1 ± 0.3	0.984	23 ± 6	2.5 ± 0.1	0.997	16 ± 2
	3851	3.8 ± 0.5	0.994	7 ± 1	3.6 ± 0.5	0.995	8 ± 3
	3855	3. ± 30.	0.626	10 ± 10	3. ± 2.	0.999	8 ± 3
	3902	2.4 ± 0.3	0.994	18 ± 4	4.0 ± 0.4	0.998	6.4 ± 0.7
	3911	1.5 ± 0.3	0.971	40 ± 20	3.3 ± 0.5	0.978	9 ± 2
	3912	1.3 ± 0.3	0.985	60 ± 30	1.9 ± 0.3	0.987	29 ± 9

Table 15. Continued

film #	ID #	$dR_{P,R}/dt$	r^2	2h (μm)	$dR_{P,L}/dt$	r^2	2h (μm)
93091-4	1379	1.8 ± 0.4	0.962	30 ± 10	3.1 ± 0.1	0.998	11 ± 1
	1382	4	-	6	4	-	6
	1388	2.9 ± 0.9	0.990	12 ± 3	4.4 ± 0.9	0.996	5.3 ± 0.7
	1396	1.8 ± 0.2	0.992	31 ± 8	2.9 ± 0.4	0.992	12 ± 2
	1407	4. ± 2.	0.976	8 ± 2	4. ± 2.	0.981	6 ± 2
	1421	2.2 ± 0.2	0.985	21 ± 4	2.2 ± 0.3	0.971	22 ± 5
	1423-A	3. ± 1.	0.950	11 ± 3	2.5 ± 0.7	0.978	17 ± 5
	1423-B	3.7 ± 0.2	0.986	7.5 ± 0.7	2.1 ± 0.1	0.997	23 ± 3

As can be seen in the plots of the perforation semiaxis growth and the data presented in Table 15, the rate of increase in the length of the radial semiaxis with time is less than that of the lateral semiaxis. Also, the growth rate of the radial semiaxis is not constant, but rather decreases as the perforation grows. Two potential causes for this phenomenon will be examined. First, geometric distortion may result from the two-dimensional nature of the imaging process. Second, local sheet thickness nonuniformities may affect the rate of rim expansion.

Image distortion

The high-speed camera was positioned such that the imaging plane was approximately parallel to the plate surface. As the liquid spreads out from the plate, it is in this plane as well; however, as wave disturbances perturb the sheet, the surfaces will be curved in and out of this plane. The growing perforation must follow the contours of the perturbed sheet

surface; thus, as the perforation grows radially, the rim of the hole will move not only in the imaging plane, but also perpendicular to it. Because only motion in the imaging plane of the camera can be observed on the resulting films, the motion of the perforation out of the plane will be unaccounted for. This process is sketched in Fig. 41, where the true motion of a rim on a sinuously disturbed sheet is shown, along with the apparent distance measured by an observer looking at a plane located at the centerline of the sine curve.

The lateral semiaxis grows parallel to a wave front and is assumed to remain in a plane parallel to the imaging plane; therefore, the lateral growth rate should equal the true growth rate of the perforation. If the sheet is assumed to be disturbed by a single wave, and the hole is assumed to grow uniformly in all directions at the rate calculated from the lateral semiaxis growth data, then the apparent radial growth of the perforation can be predicted as a function of the disturbance amplitude. The perforation is assumed to be initiated at the crest of a wave. This wave is assumed to be the sinuous wave of optimum growth. The distance measured along the sinuous surface of the sheet, L, is projected onto the x-axis using

$$L = \frac{\lambda_{opt}\sqrt{1 + p^2}}{2\pi} \int_{\hat{x}(init)}^{\hat{x}(final)} [1 - \hat{p}^2 \sin^2 \hat{x}]^{1/2} \, d\hat{x}. \qquad (108)$$

The derivation of this expression is given in Appendix G.

Because the perforation was assumed to originate at the crest of a wave, x(init) = $\lambda_{opt}/4$, and thus, $\hat{x}(init) = \pi/2$. An iterative technique was used to determine the upper limit of the integral such that the length as measured along the sine wave was equal to the lateral semiaxis length. The upper limit minus the lower limit was taken to be the projected length and was compared to the measured radial semiaxis length. If the difference in the measured lateral and radial semiaxis lengths was due solely to the curvature of the sheet, these values would be equal. A sample of this comparison is shown in Figs. 42 and 43, corresponding to

the perforations shown in Figs. 39 and 40. The FORTRAN program written to solve for L as a function of R_p, A and λ is given in Appendix H.

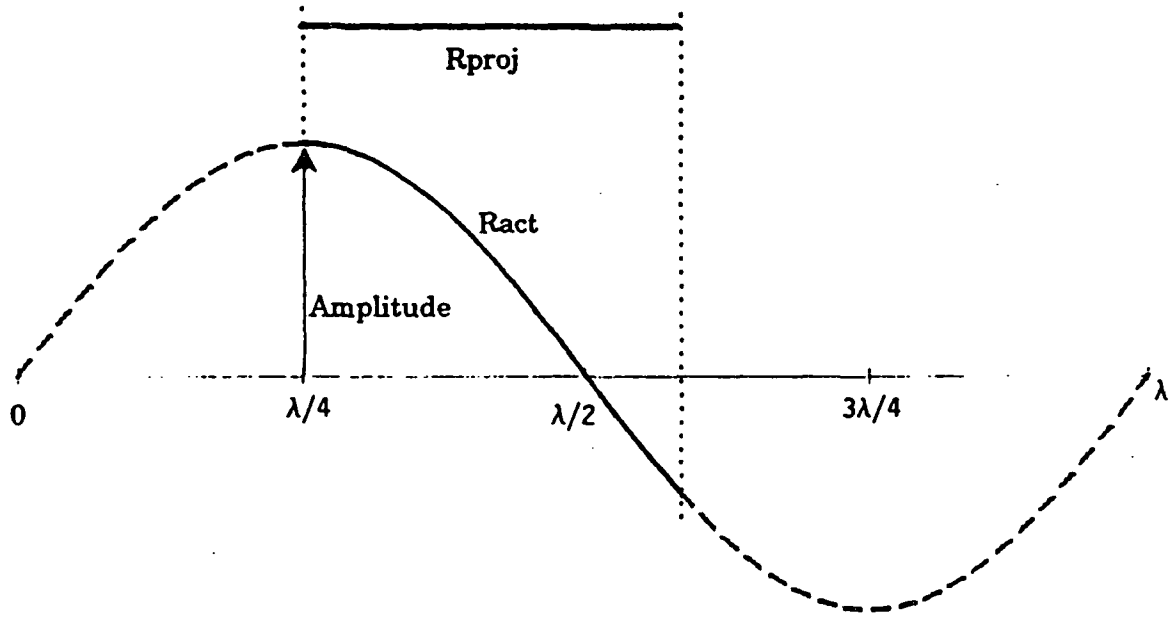

Figure 41. Projection of growth along a sine wave onto the x-axis.

Sheet thickness nonuniformity

The decrease in the measured radial growth rate compared to the lateral growth rate may also be the result of local variations in the sheet thickness. As the perforation rim enters a thicker area, the velocity of the rim decreases as shown in Eq. 36. In the previous analysis, the sheet thickness was assumed to be constant around the periphery of the perforation; however, because the sheet is thinning radially, the thickness of the sheet on the downstream edge of the perforation will be less than that on the upstream edge. The magnitude of this variation and its affect on the perforation growth rate measurements were investigated analytically.

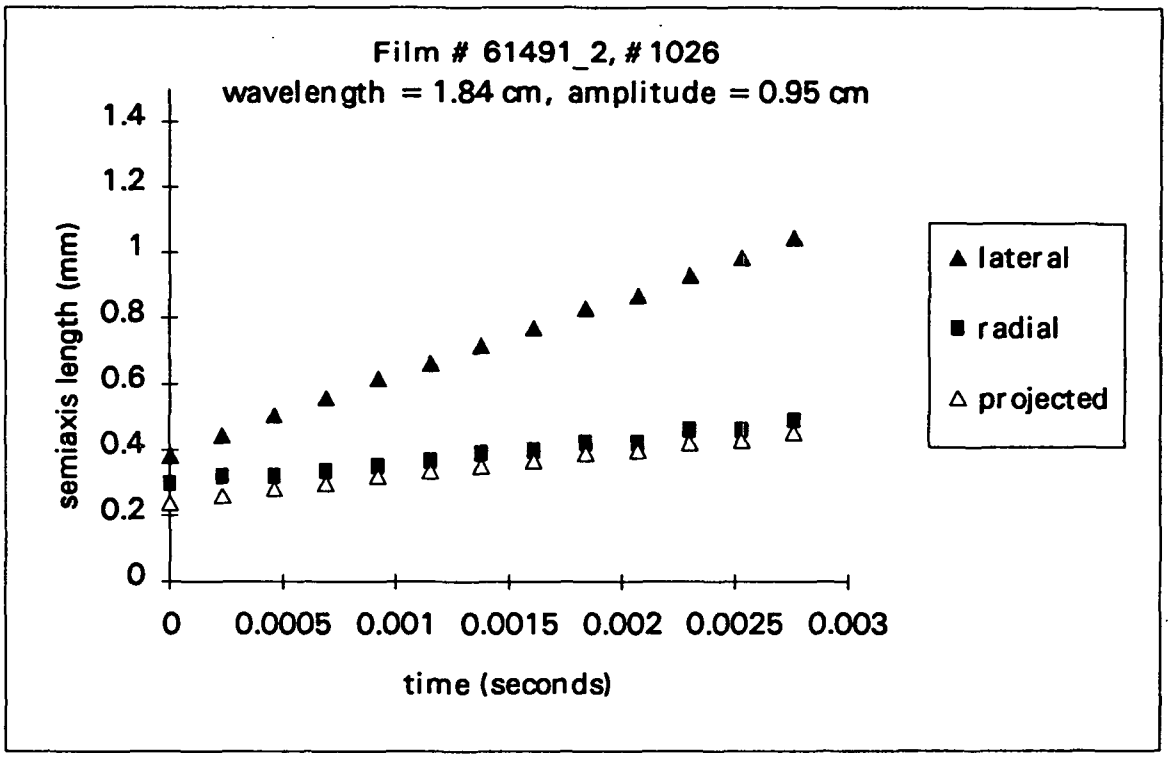

Figure 42. Radial perforation growth corrected for sine wave distortion: Film #61491_2, #1026.

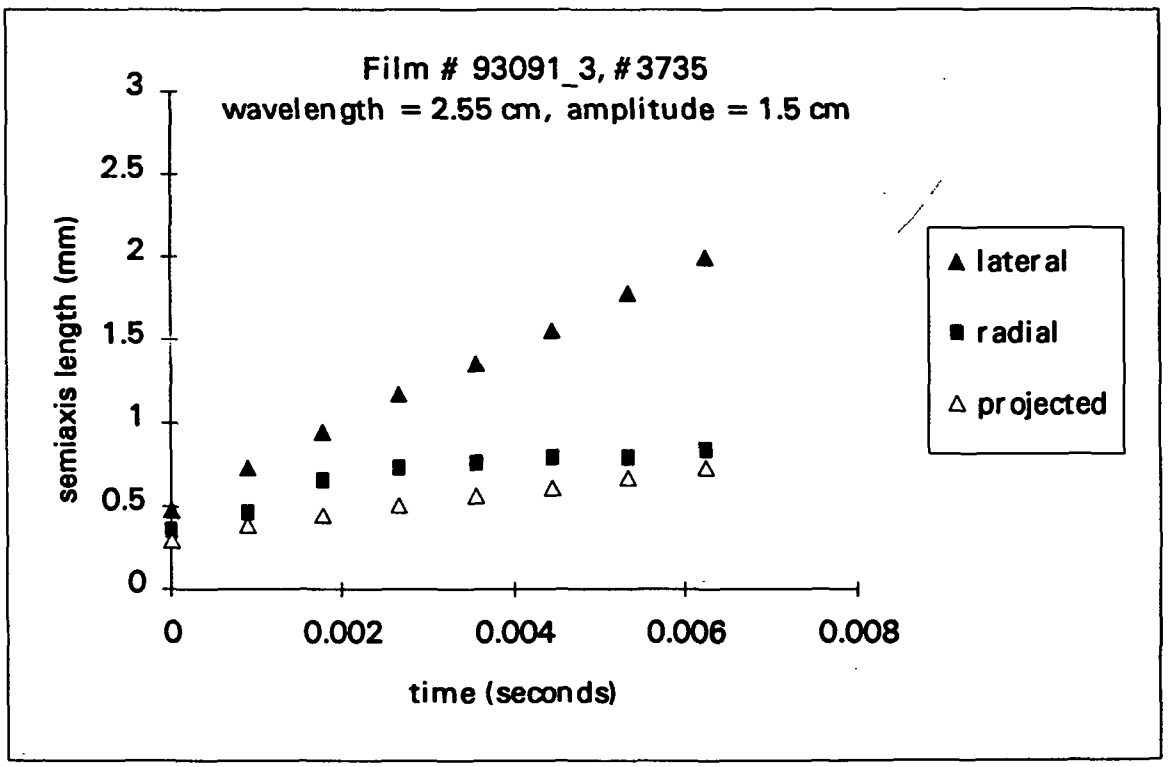

Figure 43. Radial perforation growth corrected for sine wave distortion: Film #93091_3, #3735.

A perforation with a uniform radius, R_P, centered at a position, x_0, is shown in Fig. 44. From geometry, the downstream position of any point on the rim is given by

$$x(\theta) = x_0\left[1 - 2\cos(\theta)\left(\frac{R_P}{x_0}\right) + \left(\frac{R_P}{x_0}\right)^2\right]^{1/2}, \tag{109}$$

where:
- θ = angular position of a point on the rim ($\theta = 0$ is upstream);
- $x(\theta)$ = downstream position of a point on the rim [m];
- x_0 = downstream position of the center of the perforation [m]; and
- R_P = radius of the perforation [m].

The angular position on the rim is defined such that $\theta = 0$ is the upstream direction, and $\theta = \pi$ is the downstream direction.

Because the ratio of the perforation radius to the position downstream of the perforation center is generally much less than one, Eq. 109 can be evaluated by expanding it in powers of R_P/x_0. Solutions accurate to zeroeth order in R_P/x_0,

$$x(\theta) \approx x_0, \tag{110}$$

and to first order in R_P/x_0,

$$x(\theta) \approx x_0\left[1 - \cos(\theta)\left(\frac{R_P}{x_0}\right)\right], \tag{111}$$

have been derived.

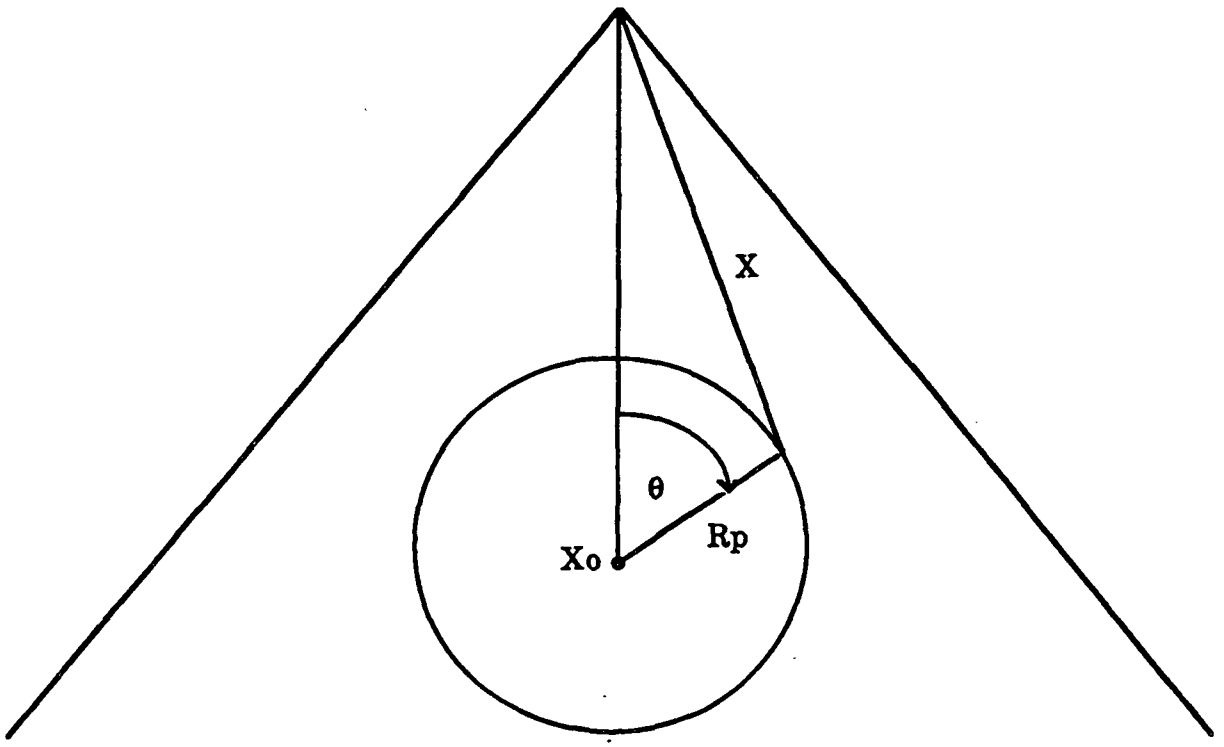

Figure 44. Geometry of a perforation in a radially thinning sheet.

An expression for predicting the downstream sheet thickness was given as Eq. 65. Substituting in the zeroeth-order equation for the downstream location, the sheet thickness can be calculated, and is predicted to be independent of theta.

$$2h(x) = \frac{2h(x_p)x_p}{x_0} = \frac{2K_N}{x_0}, \tag{112}$$

where: $2h(x_p)$ = sheet thickness at the plate edge [m];
x_p = downstream location of the plate edge [m]; and
K_N = $2h(x_p)\cdot x_p$ = sheet thinning parameter [m^2]
(constant for fixed operating conditions).

Likewise, the first-order accurate expression for the sheet thickness can be obtained,

$$2h(x,\theta) = \frac{2h(x_p)\cdot x_p}{x_0 - R_P\cos(\theta)} = \frac{2K_N}{x_0 - R_P\cos(\theta)}. \tag{113}$$

In this case, the sheet thickness is a function of theta.

If Eq. 112 is used, the growth rate for perforations in a planar sheet derived by Fraser *et al.*[39] will be obtained. The first-order accurate solution can be derived by following the analysis presented by Fraser *et al.*,[39] but using Eq. 113 to define the local sheet thickness.

The growth of a differential element of the perforation, defined by $d\theta$, is determined by balancing the surface tension force,

$$F_{surf} = 2\sigma R_P d\theta, \tag{114}$$

with the rate of change in momentum of the rim,

$$\frac{d(\text{momentum})}{dt} = \frac{d(\text{mass}\cdot\text{velocity})}{dt},$$

where: mass = rim mass = $[2h(x,\theta)\rho_{liq}][\frac{1}{2}R_P^2 d\theta]$ [kg]; and
velocity = rim velocity = $\frac{dR_P}{dt}$ [m/s].

Upon making these substitutions, the rate of change in momentum is given by

$$\frac{d(\text{momentum})}{dt} = 2hR_P\rho_{liq}\left(\left(\frac{\partial R_P(\theta)}{\partial t}\right)^2 + \frac{R_P}{2}\left(\frac{\partial^2 R_P(\theta)}{\partial^2 t}\right)\right). \tag{115}$$

After substituting the first-order accurate expression for the sheet thickness and rearranging, a differential equation describing the growth rate of a perforation in a radially thinning liquid sheet is obtained,

$$\left(\frac{2\sigma}{K_N \rho_{liq}}\right)\left(\frac{x_0}{R_P} - \cos(\theta)\right) = \frac{2}{R_P}\left(\frac{\partial R_P}{\partial t}\right)^2 + \left(\frac{\partial^2 R_P}{\partial^2 t}\right) \tag{116}$$

Using the mathematical substitutions presented by Fraser *et al.*,[39] this expression can be integrated to yield an equation for the growth rate of the perforation as a function of θ,

$$e_1(\theta) = \frac{dR_P(\theta)}{dt} = \left[\left(\frac{\sigma}{K_N \rho_{liq}}\right)^{1/2}\cdot\left(x_0 - \frac{4R_P\cos(\theta)}{5} + \frac{4C_1}{R_P^4}\right)\right]^{1/2}. \tag{117}$$

Fraser et al.[39] showed that the constant of integration, C_1, could be neglected when the fourth power of the ratio of the initial perforation radius to the current perforation radius was much less than one $\left(\left(\frac{R_P(0)}{R_P(x)}\right)^4 << 1\right)$. The initial perforation radius is expected to be on the order of the sheet thickness, which in this study was 10-100 μm, while the minimum perforation radius observed was on the order of 1 mm (1000 μm); thus, this condition is met; C_1 can be neglected. The growth rate for a perforation in a radially thinning sheet, accurate to first order in the perforation radius, can then be written as

$$e_1(\theta) = \frac{dR_P(\theta)}{dt} = \left[\left(\frac{\sigma}{K_N \rho_{liq}}\right)^{1/2}\left(x_0 - \frac{4R_P\cos(\theta)}{5}\right)\right]^{1/2}. \tag{118}$$

The zeroeth-order expression for the growth rate of perforations was obtained by Fraser *et al.*[39] and was presented as Eq. 38. These growth rate expressions can be compared to determine the relative effect of the first-order correction on the predicted perforation growth rate,

$$\frac{\text{first order}}{\text{zeroeth order}} = \frac{e_1(\theta)}{e_0} = \left(1 - \frac{4R_P\cos(\theta)}{5\,x_0}\right)^{1/2} \qquad (119)$$

The growth rate ratio is plotted versus theta for various values of R_P/x_0. Because this expression is symmetric about $\theta = 0$, only values of θ between 0 and π are shown.

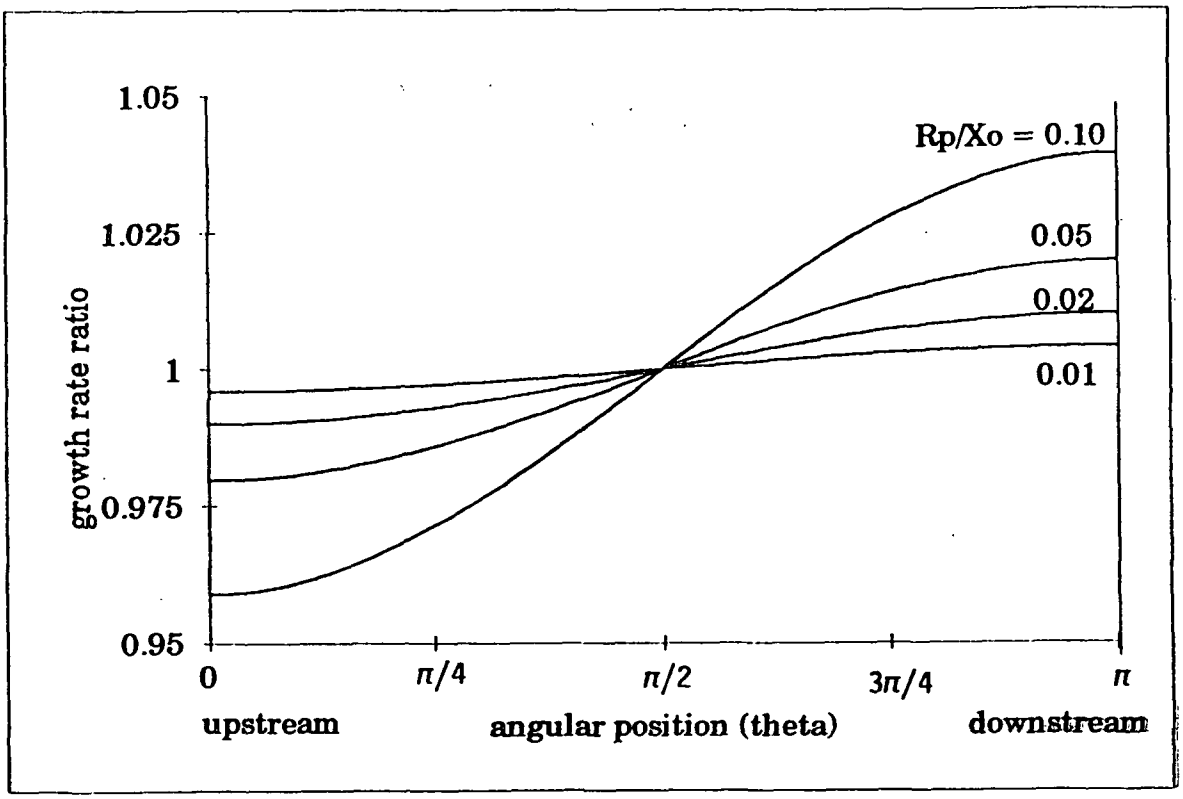

Figure 45. Comparison of zeroeth- and first-order perforation growth rate expressions.

The results of this analysis can be used to infer that the upstream growth rate may be as much as 10% less than the downstream growth rate, depending on the ratio of the perforation radius to mean distance downstream. However, upstream and downstream radii were not measured independently; rather, the sum of these radii were measured; this value was divided by two; and the result was called the radial semiaxis. To determine the effect of sheet thickness variations around the perforation rim on these measured quantities, this predicted

value for this definition of the radial semiaxis should be compared to the predicted lateral semiaxis length.

The expected value for the measured length of the lateral perforation semi-axis is one-half the sum of Eq. 118 evaluated at $\theta = \pi/2$ and $\theta = 3\pi/2$,

$$R_{P,L} = \frac{1}{2}\left(\frac{\sigma}{K_N \rho_{liq}}\right)^{1/2} [x_0^{1/2} + x_0^{1/2}].$$

This expression can be rearranged to obtain

$$R_{P,L} = \left(\frac{\sigma x_0}{K_N \rho_{liq}}\right)^{1/2}. \tag{120}$$

The expression derived is identical to that predicted for the zeroeth-order case evaluated by Fraser *et al.*[39] This result is obtained because the first-order correction to the sheet thickness and growth rate expressions is zero in the directions defined by $\theta = \pi/2$ and $\theta = 3\pi/2$.

The length of the radial semiaxis is given by one-half the sum of Eq. 118 evaluated at $\theta = 0$ (upstream) and $\theta = \pi$ (downstream),

$$R_{P,R} = \frac{1}{2}\left(\frac{\sigma}{K_N \rho_{liq}}\right)^{1/2} \left[\left(x_0 - \frac{4R_P}{5}\right)^{1/2} + \left(x_0 + \frac{4R_P}{5}\right)^{1/2}\right]. \tag{121}$$

If x_0 is factored from the terms inside the square brackets, the resulting expression can be evaluated by expansion in terms of R_P/x_0, a small parameter. Keeping terms to first order in this parameter, consistent with the previous expansion, the predicted length of the radial perforation semiaxis is found to be equal to both the predicted length of the lateral perforation semiaxis and the length predicted from the zeroeth-order solution,

This result is obtained because the first-order correction term in the downstream direction is equal in magnitude, but opposite in sign to the first-order correction in the upstream direction.

In summary, sheet thickness variations around the perforation rim are predicted to result from the radial thinning of the sheet and the finite size of the hole. This variation is expected to affect the local growth rate of the perforation such that it grows faster in the downstream direction where the sheet is thinner and slower in the upstream direction where the sheet is thicker. The magnitude of the effect decreases with the square root of the ratio of the perforation radius to the downstream location of the center of the perforation. Although rim velocity non-uniformities are predicted to exist, the measured lengths of the radial and lateral perforation axis should be equal if the second-order terms in the expansion for the local sheet thickness are negligible. Finally, both growth rates are predicted to match the growth rate expression derived by Fraser *et al.*,[39] and thus, both growth rates are predicted to be proportional to the square root of the sheet thickness.

Limitations of the sheet thickness measurements

Because the downstream sheet thickness of a sheet disturbed by waves could not be measured directly, the indirect method of measuring perforation growth rates and relating them to the sheet thickness was used. While the results obtained clearly demonstrate the effect of wave-thinning, several limitations exist in this process.

First, in order to obtain accurate measurements of the perforation growth rates, only isolated perforations (perforations which were not interacting or merging with other perforations) could be examined. Thus, the sheet was imaged in the region where perforations were first observed, rather than in the region of rapid perforation. Because the waves are expected to continue to grow and further thin the sheet as it moves downstream, the calculated

sheet thickness in the region of few perforations can be considered an upper bound at which perforations can be expected to occur.

Second, perforations could be detected in the high-speed images because the rims refract the light differently than does the surrounding sheet; therefore, the perforations could only be detected once they reached a finite size. Because of this, the initial growth rate of the perforations could not be determined, and the sheet thickness at the immediate point of rupture could not be determined.

CHARACTERIZATION OF WAVES

The preceding analysis of the wave-thinned sheet thickness relied on the results of linear theory to predict the wavelength of the optimum disturbance. When the wave amplitude is large, as must occur for sheet thinning to be significant, linear theory is no longer valid, and the wavelength of optimum growth may be affected. Also, investigations by Crapper and Dombrowski[71] and Weihs[46] have shown that the dominant wave in a spray may be related to external disturbances to the system. These issues were investigated experimentally and analytically.

Measured Wavelengths

The dominant wavelength has been measured from images of the side edges of sheets.[39,44,67] Because the sheet formed in this study had no side edges, the spray was split in order to form them. When the sheet was split, the fluid near the newly formed edges contracted to form thick, visible rims. When the spray was then illuminated, the waves in the sheet could be examined by imaging the motion of the rims. Although splitting the sheet and the resultant formation of rims will alter the wave characteristics, this technique is expected to yield an estimate of the disturbance wavelengths.

The sheet was split by inserting a 0.030 inch diameter wire through the sheet, perpendicular to the direction of flow and the plane of the sheet. Provided the wire intersected the sheet far enough downstream, the sheet would split, and two rims would form. If the wire split the sheet too far upstream, the sheet would separate at the wire, but reconnect a short distance downstream. The position downstream at which the wire could be located and the sheet would stay separated increased with decreasing sheet velocity.

The spray was illuminated from below using a General Radio Company Strobtac 1531-A strobe light. The stobe frequency was adjusted for each trial in an attempt to freeze the motion of the waves. If the strobe frequency was too high, the waves appeared to move upstream, while if the strobe frequency was too low, they appeared to travel downstream. Images of the rims were collected using a 35 mm camera with ASA 1600 color slide film. Two examples of the images obtained were shown as Figs. 15a and 15b. In addition to the rim images, several images of a ruler, positioned next to the rim, were collected. These images were used as a reference scale for determining the disturbance wavelengths.

The slides were projected onto a sheet of paper, the rims were traced, and the wavelengths measured. The measured wavelengths are plotted versus the optimum inviscid wavelength in Fig. 46. The sheet velocity used to calculate the optimum disturbance wavelength was the arithmetic average velocity based on the two-term linear regression equation. The line of 1:1 correspondence between the predicted and measured wavelengths is shown as a solid line. A second line shows the predicted wavelengths if the root mean square velocity based on the two-term linear regression equation is used. Although there is considerable scatter in measured wavelength data, good agreement between the predicted and measured wavelengths is shown.

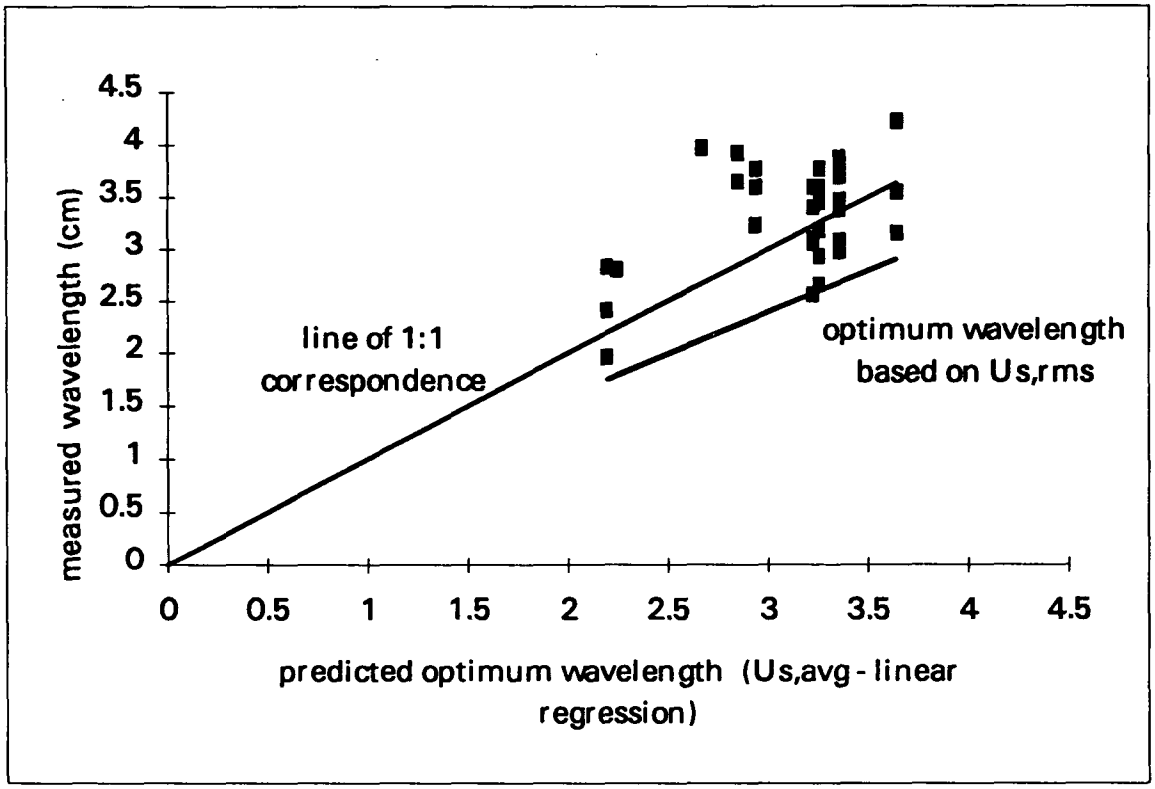

Figure 46. Comparison of measured and predicted disturbance wavelengths.

External Disturbances

Experimental Measurements

Because the dominant wave may be related to vibrations in the spray system, these disturbances were investigated. An Endevco Model # 2217 accelerometer was used in conjunction with a Columbia Research Laboratories Inc., Model 4101 charge follower to monitor the vibrations in the system. The signal from the charge follower was collected with a LeCroy 7200 Precision Digital Oscilloscope. A fast Fourier transform (FFT) was used to convert the signal from the time domain into the frequency domain. The resulting FFT spectra were used to determine the dominant disturbance frequencies in the system.

Spectra were collected for the flowmeter, the viscometer, the pump, and the motor. In these trials, the accelerometer was held against the device being monitored by hand. The accelerometer was then mounted beneath the plate perpendicular to the plate surface. For these tests, a threaded hole was drilled in the base of the plate, 1/32" from the outer edge. The accelerometer could then be attached firmly to the plate using the screw provided with it.

A spectrum was obtained with all of the equipment associated with the spray apparatus turned off. Next, a spectrum was collected with the pump on, recirculating flow back to the reservoir (that is, no flow through the nozzle). FFT spectra were then collected while a jet of glycerol/ water was impinging on the plate. The jets were formed over a range of flow rates (11.7-21.9 m/s) using a QU-00120 nozzle. Finally, the disturbances to the nozzle at flow rates of 7.9 and 17.3 m/s were monitored. The accelerometer was held against the nozzle by hand during these tests. These spectra are included in Appendix J.

There was a dominant peak at about 354 hertz in the FFT spectra for both the plate and the nozzle, independent of the jet velocity. The plate spectra had additional peaks, corresponding to several harmonics of the 354 hertz peak. These peaks can be seen in the plate spectrum for the 21.9 m/s flow rate shown in Fig. 47.

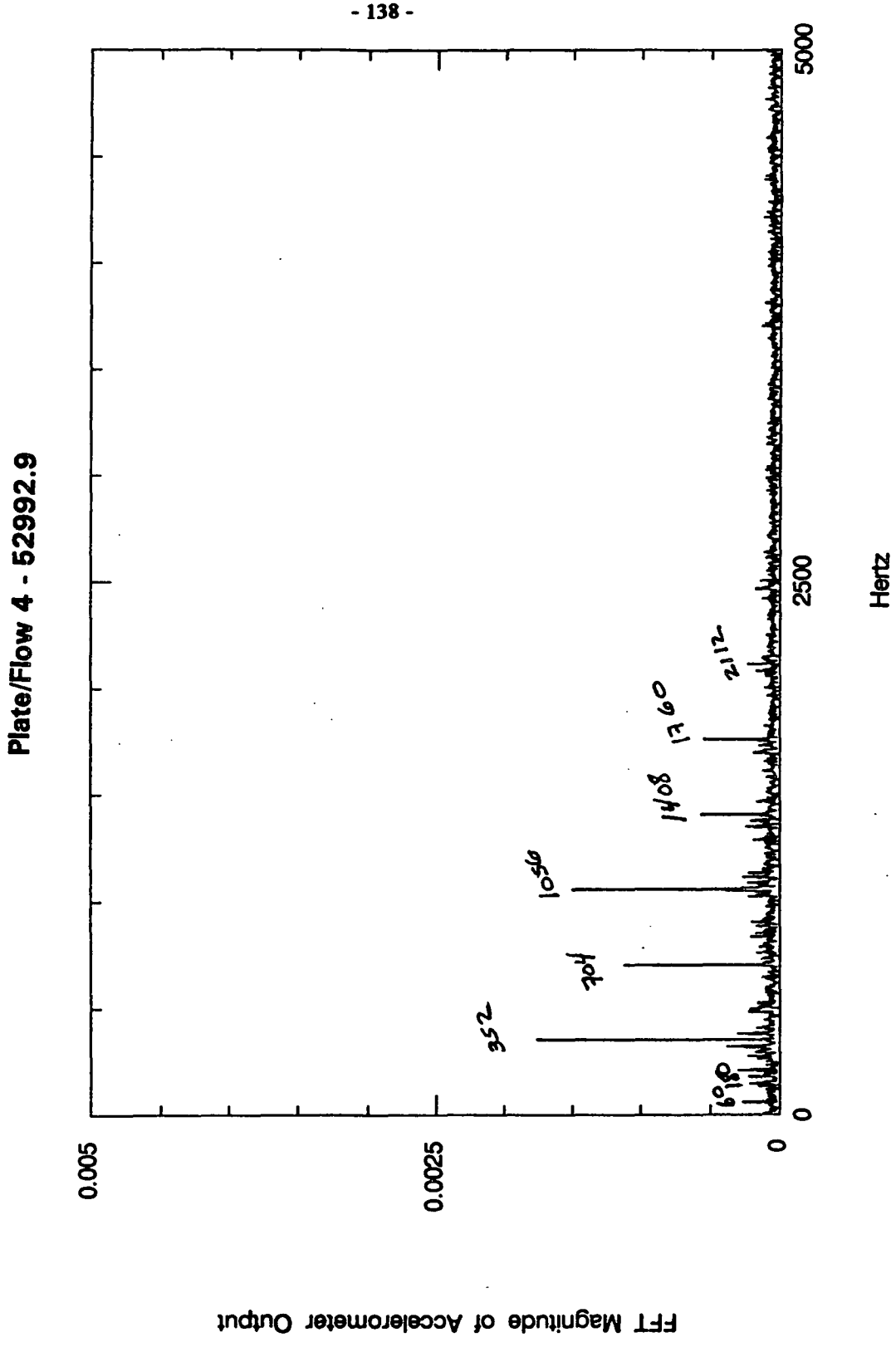

Figure 47. FFT spectra of the vibrations at the splash plate (U_0 = 21.9 m/s).

The 354 hertz peak may be related to a corresponding peak in the spectrum obtained for the motor driving the pump. Other frequencies associated with the pump, motor, or the data acquisition devices did not appear to affect the nozzle nor the plate.

In order to investigate the vibrations in the plane of the plate surface, a second mounting hole was drilled in the plate. This hole was located on the side of the plate, at the midpoint of the plate height. Four spectra were collected with the accelerometer mounted in the first hole (beneath the plate) in order to determine if the presence of the second hole altered the dominant frequencies. In all cases, a jet of glycerol/water was impinging on the plate. Seven spectra were then collected during jet impingement with the accelerometer mounted in the second hole, thus measuring vibrations parallel to the plate surface.

The dominant frequencies measured perpendicular to the plate surface were 355 Hz and its harmonics (710 and approximately 1060 Hz). These values are similar to the dominant peaks detected without the presence of the second mounting hole in the plate. The 355 and 710 Hz peaks were the only frequencies detected when the accelerometer was mounted in the plane of the plate surface. The intensity of the disturbances was significantly less relative to the magnitude measured perpendicular to the plate surface, and they decreased as the jet velocity increased.

The potential effects of the plate and nozzle vibrations on the sheet were investigated analytically. The wavelength of a disturbance, λ, is related to its frequency, f, and speed, U, that is

$$\lambda = U/f. \tag{123}$$

If the wave speed of the disturbances induced by the plate vibrations is assumed to be equal to the sheet velocity, then the wavelength can be calculated and compared to both the experimentally measured wavelengths and the wavelength of optimum growth predicted by linear theory. This comparison is shown in Fig. 48. For fixed fluid properties, there is a one-to-one correspondence between the sheet veolcity and the optimum wavelength. These sheet velocities are shown on the top axis.

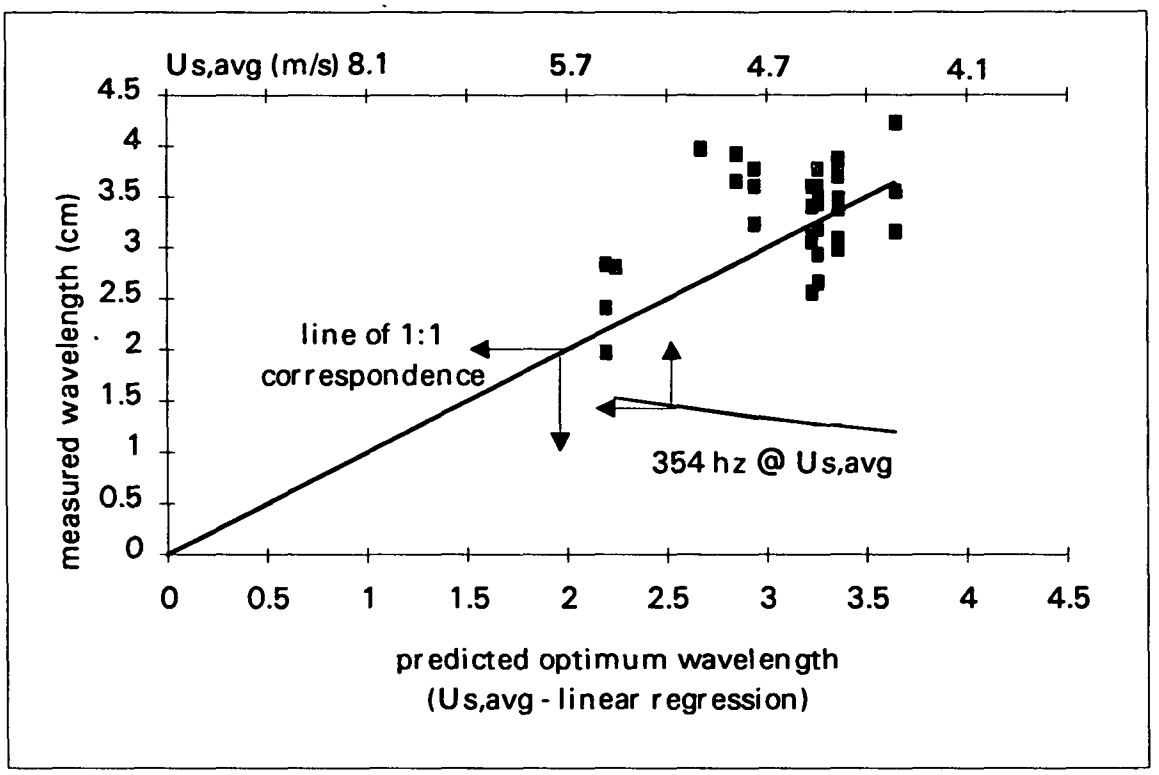

Figure 48. Comparison of the vibration-induced disturbance wavelengths.

Predicted Effects

Because the range of operating conditions for which disturbance wavelengths were measured was only a fraction of the total range investigated in this study, further assessment of the role of external disturbances on sheet stability was performed analytically. The influence of induced waves relative to the wave of optimum growth can be estimated from the relationship between the wavelength of a sinuous disturbance and its predicted growth rate in

an inviscid sheet. This expression given as Eq. 81 can be made dimensionless with respect to the wave number of optimum growth , k_{opt}, and its corresponding growth rate, s_{opt}. Expressions for k_{opt} and s_{opt} were given as Eqs. 83 and 85, respectively. The resulting dimensionless equation,

$$\frac{k}{k_{opt}} = 1 \pm \sqrt{1 - \left(\frac{s}{s_{opt}}\right)^2} \qquad (124)$$

is plotted in Fig. 49. Using the relationship between the wave number of a disturbance and its wavelength ($\lambda = 2\pi/k$), these data are replotted in Fig. 50 as the growth rate versus the wavelength, where both values have been made dimensionless with respect to the optimum values predicted from linear theory. As can be seen in Fig. 49, the maximum unstable wave number ratio is predicted to be two. Based on linear theory for inviscid sheets, disturbances of higher wave number are expected to be stable. This maximum wave number of two corresponds to a minimum wave length ratio of 0.5, indicating that disturbances with a wavelength of less than half the optimum disturbance wavelength will not grow.

Both the minimum and optimum disturbance wavelengths are functions of the sheet velocity, as was shown in Eqs. 34 and 35, respectively. These wavelengths were calculated for the range of sheet velocities encountered in this study (2-10 m/s) and are plotted in Fig. 51. The line corresponding to the predicted wavelength of a disturbance induced by the 354 Hz vibration discussed earlier is also shown. As can be seen in this plot, below approximately 5 m/s, the 354 Hz disturbance is predicted to be stable and, thus, should have no effect on the breakup of the sheet.

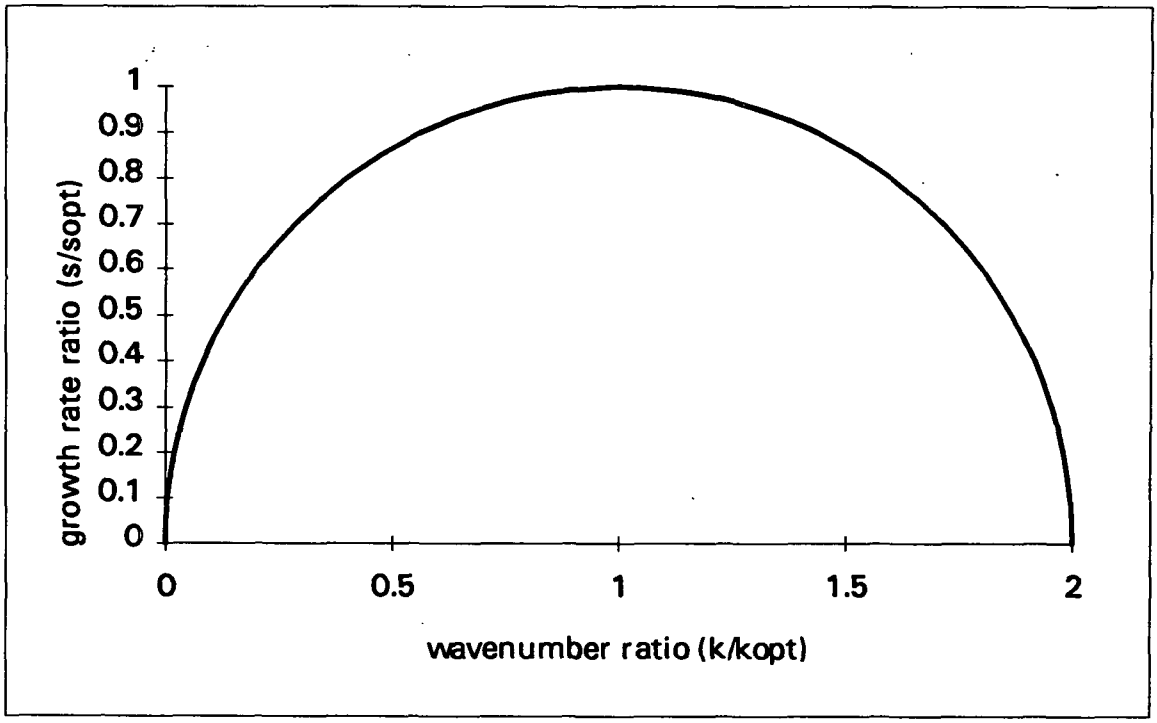

Figure 49. Dimensionless growth rate versus dimensionless wave number.

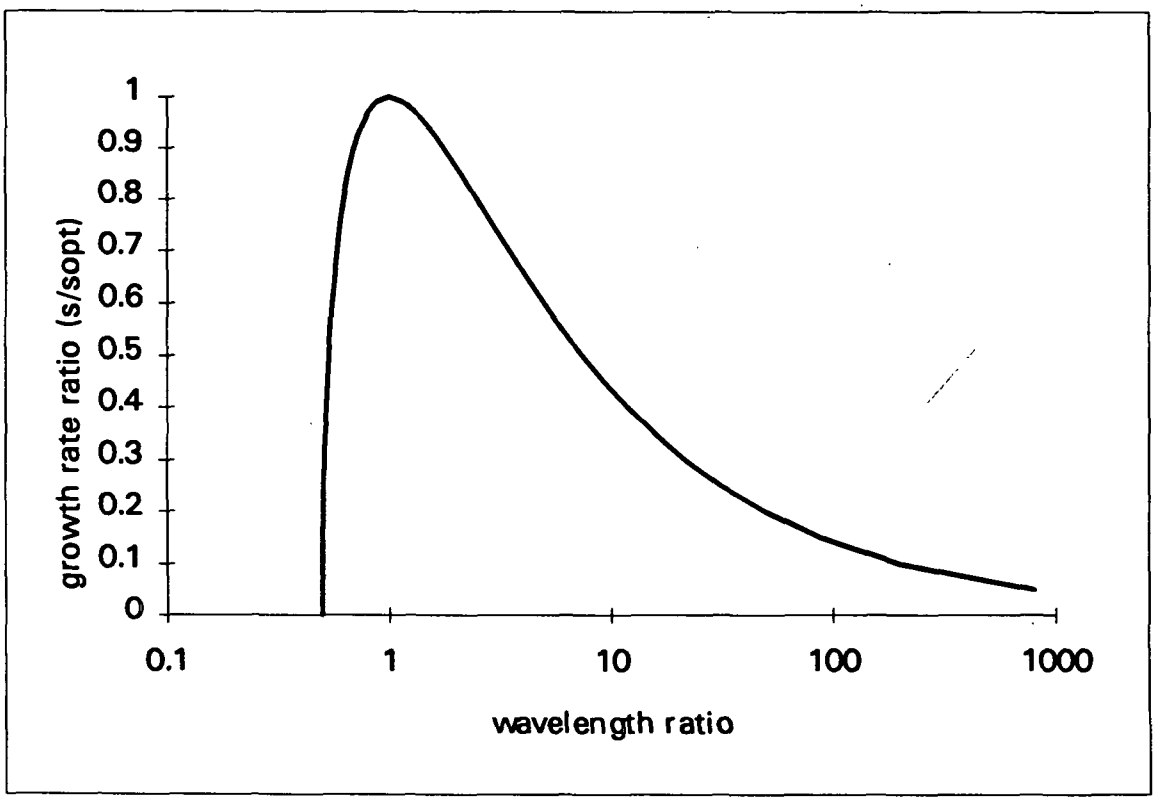

Figure 50. Dimensionless growth rate versus dimensionless wavelength.

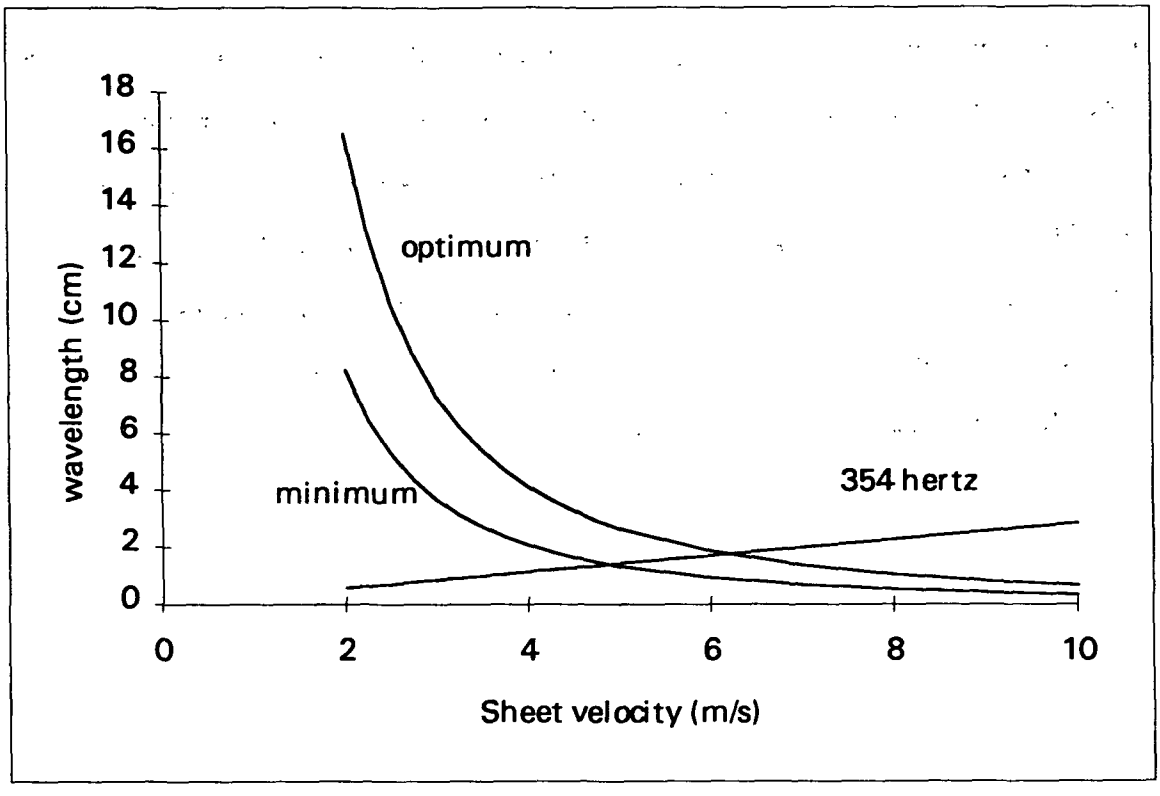

Figure 51. Optimum and minimum wavelength as a function of the sheet velocity - based on linear, inviscid theory.

Above 5 m/s, the wavelength of the externally-induced disturbance is unstable. The 354 Hz vibration is predicted to result in a disturbance with a wavelength less than the optimum wavelength for sheet velocities less than about 6 m/s, while above 6 m/s, the induced wavelength will be greater than the optimum wavelength. Based on these results, the following behavior is expected.

The breakup length is expected to decrease with decreasing wavelength and increasing initial amplitude and growth rate. As the sheet velocity increases, the wavelength of the optimum disturbance decreases while its growth rate increases, and the sheet is expected to reach a given level of thinning closer to the plate edge. This effect is enhanced by the external driving of a disturbance near the optimum wavelength, corresponding to an increase in the initial disturbance amplitude. When the sheet velocity is approximately 6 m/s, the external

disturbance corresponds to the wavelength of optimum growth, and the greatest decrease in the breakup distance is expected. As the sheet velocity is further increased, the optimum disturbance wavelength is still predicted to decrease while its growth rate increases, thus suggesting that the breakup length should continue to decrease. This would be true for a system free from external disturbances; however, because the 354 Hz disturbance is no longer the optimally growing disturbance, the initial amplitude of this disturbance is no longer enhanced, and the breakup length is expected to increase.

DISCUSSION

THE MECHANISM OF LIQUID SHEET BREAKUP

The formation and disintegration of a radially thinning liquid sheet formed by a splash plate nozzle was investigated. Based upon the high-speed video and 16 mm images obtained, the experimental sheet thickness and perforation count data collected, and the results of the additional analytical investigations, the following description of the breakup process was developed.

A radially thinning free sheet is formed by a splash plate nozzle. This sheet thins due to both the radial expansion of the sheet and the growth of sinuous waves resulting from the hydrodynamic instability of disturbances. When the sheet thickness is sufficiently reduced, local rupture occurs. The resulting holes grow rapidly, and the rims surrounding them interact to form clumps and strands of liquid. These clumps and strands break up into the observed drop size distribution. Several steps in this processes were examined in greater detail, as summarized below.

The sheet is formed by the perpendicular impingement of a circular jet on a flat plate. As the fluid spreads out radially, viscous shear at the plate surface slows the sheet and increases its thickness relative to an inviscid sheet. This increase in the relative sheet thickness is proportional to $\frac{1}{Re_{jet}}\left(\frac{x}{d_0}\right)^3$; thus, for fixed fluid properties, the relative sheet thickness at the plate edge will increase with a decrease in the jet velocity or nozzle diameter. Because the inviscid sheet thickness is proportional to d_0^2, the sheet thickness may decrease with a decrease in the orifice diameter, even though the ratio of the viscous to inviscid sheet thickness increases.

As the liquid releases from the edge of the plate, a radially thinning free sheet is formed. In this free sheet, shear forces will no longer be significant, and the velocity of the sheet is related to an average velocity of the sheet at the edge of the plate. As the sheet travels downstream, it continues to thin due to the geometric expansion of the liquid. This thinning is enhanced by the presence of waves.

Previous investigations of wave mechanism of breakup have focused on sinuous waves, as their growth rate is larger than that of dilational waves. However, as was shown in this study, the amplitude of a dilational wave needed to provide a fixed degree of wave-thinning is also significantly less than the amplitude of a sinuous wave. The relative importance of the two waves was shown to be a function of the sheet thickness, the critical thickness at rupture, the initial disturbance amplitudes, and the sheet Weber number.

In this study, sinuous waves were predicted to result in breakup before dilational waves. Based on linear theory, the optimally growing sine wave in an inviscid sheet is independent of the sheet thickness; however, in a viscous sheet, the wavelength increases with an increase in either the sheet thickness or the liquid viscosity. Using a growth rate expression available in the literature, a cubic equation was derived which relates the wave number of optimum growth in a viscous sheet to the wave number of optimum growth in an inviscid sheet. This ratio was found to be a function of a single dimensionless parameter, Ω. Examination of this equation showed that the rate of increase in the wavelength of the optimum sinuous wave with the liquid viscosity is a function of the gas and liquid phase densities, the surface tension, the sheet thickness, and the sheet velocity.

The viscous growth rate equations were used to predict the wave-thinned downstream thickness of the sheet. When the amplitude of the wave was small, the presence of the disturbance did not enhance the radial thinning of the sheet appreciably; however, as the wave

grew, the sheet thickness decreased significantly over a narrow range of downstream position. The downstream position of this rapid decrease in sheet thickness is predicted to decrease with increasing jet velocity and nozzle orifice diameter.

The radially thinning free sheet was imaged using a high shutter speed video camera. These images were used to count the number of perforations formed in the sheet as a function of the nozzle orifice diameter, the jet velocity, and the radial position downstream. The number of perforations formed was found to increase rapidly at a critical position downstream which varied with the orifice diameter and jet velocity.

The predicted effects of the jet velocity and orifice diameter on the sheet thickness correspond qualitatively to their observed effects on the number of perforations formed. It was concluded that the combination of the radial and wave thinning reduces the sheet thickness to a critical value, at which point rupture occurs.

Images obtained with a high-speed 16 mm camera were used to measure the growth rates of perforations in the sheet. These growth rates were used to calculate the thickness of the sheet. These calculated thicknesses were significantly less than the thickness predicted in the absence of waves. This provides support for a wave-thinning induced sheet rupture mechanism; however, the measured thickness was still one to two orders of magnitude larger than the maximum sheet thickness predicted for spontaneous rupture; thus, other mechanisms of rupture may be important.

The formation of perforations has been attributed to a number of causes. These mechanisms were described previously and will be evaluated here, with respect to the results obtained in this study.

Unwettable particles in the fluid are expected to cause rupture when the thickness of the sheet is reduced to the characteristic dimension of the particles. Based on the perforation growth rate data, holes are first formed when the sheet thickness is about 5-20 microns. As no attempt was made to protect the test fluid from airborne dust, particles in this size range may have been present in the system and could be the causative agent of rupture.

In addition to the presence of airborne contaminants, air bubbles may also be present. The test fluid was recirculated throughout each run and may have entrained micron-sized air bubbles. Larger bubbles were detected in several high-speed 16 mm films, but the flow loop and operating procedures were modified to eliminate them from other runs. In subsequent films, the number of visible air bubbles was significantly reduced, but the resolution of the images was not great enough to detect bubbles smaller than approximately 100 microns (0.1 mm).

While air bubbles are not unwettable particles, their presence may still be responsible for rupture. When the wave-thinned sheet thickness is reduced to the characteristic dimension of the bubble, the minimum local thickness will equal the thickness of the bubble film. This thickness will be significantly less than that of the surrounding liquid sheet and may be below the critical thickness for spontaneous rupture.

The process by which an entrained air bubble may result in rupture is sketched in Fig. 52. When the sheet thickness is much greater than the bubble dimension, the presence of entrained air has a minimal effect on the sheet (see Fig. 52 a). As radial expansion and waves thin the sheet, the thickness of the sheet will approach the characteristic dimension of the bubble (see Fig. 52 b). When the sheet thickness is less than or equal to the bubble diameter, a local thin spot will occur, where the thinnest dimension is equal to the bubble film thickness (see Fig. 52 c). If this thickness is less than the critical film thickness for spontaneous rupture,

the bubble film will burst creating a hole in the sheet with a radius equal to the radius of the bubble (see Fig. 52 d). Based on Taylor and Michael's[51] analysis, this hole will grow if the bubble radius is greater than the sheet thickness; however, this result was based on a balance of surface tension forces acting on a hole in a sheet at equilibrium. For the case of a hole formed from a bursting bubble, there are additional destabilizing effects associated with the inertia of the rupturing bubble. Thus, the local sheet thickness may be considered an upper bound for the minimum bubble radius needed to cause a growing perforation.

A sample of the glycerol/water solution was examined under an optical microscope at 200X magnification. Numerous air bubbles, ranging in size from approximately 5-100 microns, were observed, as shown in Fig. 53. Most of the bubbles shown are less than 20 microns in diameter, but a 90 μm bubble can also be seen. Although solid particles were also observed, the number of air bubbles seen was far greater.

The air bubbles observed are known to be entrained in the fluid during the spraying and recirculation processes. As the amount of air entrained became excessive, the liquid became opaque. Although all spray tests were completed before this condition was reached, the microscopic analysis results indicate that small air bubbles were still present.

The time required for an air bubble to rise out of a glycerol/water solution was calculated based on its terminal velocity. Bubbles in the size range of 1 to 20 microns were found to be in the Stoke's flow range ($Re << 1$). For a glycerol/water solution with a viscosity of 0.05 kg/m·s, bubbles 1 μm in diameter would require about 2100 hours to rise 10 centimeters, while 20 μm bubbles would rise the same distance in about 6 hours. (Because the bottom of the tank is sloped, the depth of fluid varies from 8 to 14 cm.) The time required for a 1 μm and a 20 μm bubble to rise 10 centimeters through a solution with a viscosity of 0.1 kg/m·s would be 4200 hours and 11 hours, respectively. Based on these results, it is

concluded that small air bubbles (less than 20 μm) were present in the spray experiments performed in this study.

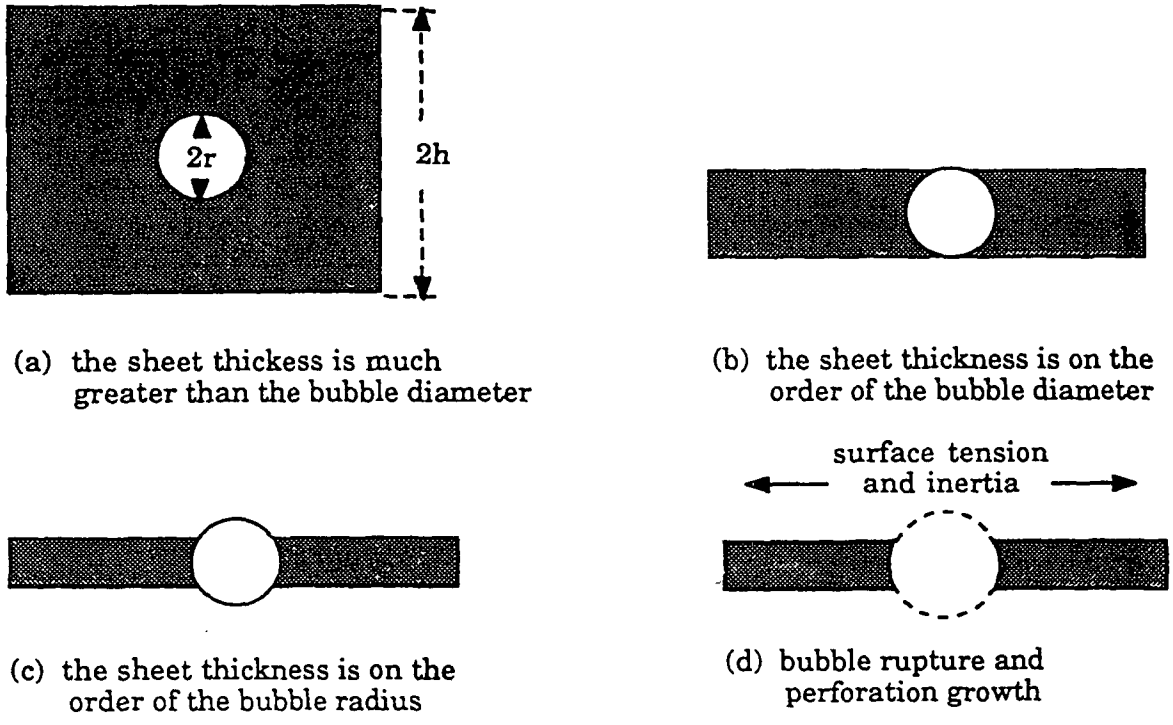

(a) the sheet thickess is much greater than the bubble diameter

(b) the sheet thickness is on the order of the bubble diameter

(c) the sheet thickness is on the order of the bubble radius

(d) bubble rupture and perforation growth

Figure 52. Perforation initiation by an air bubble rupture mechanism.

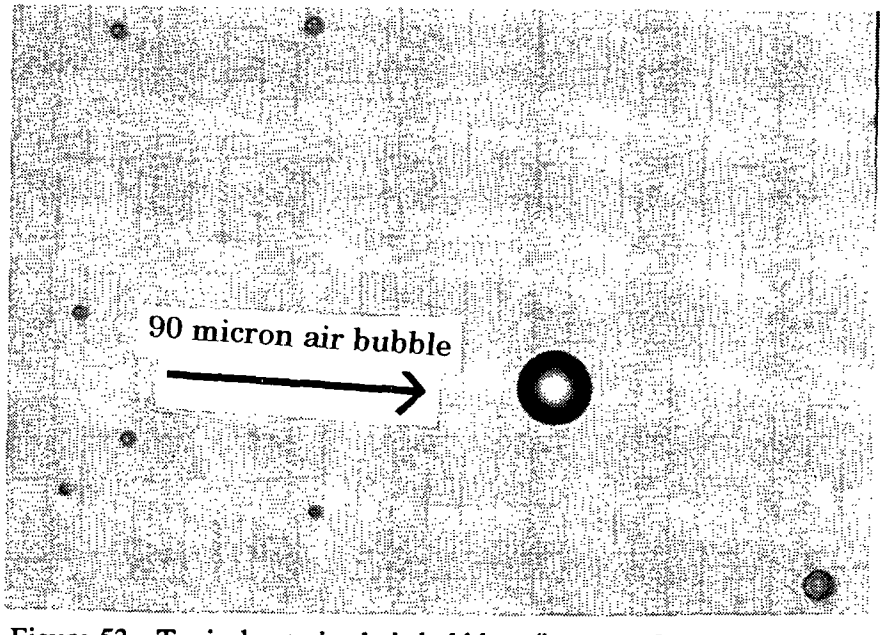

Figure 53. Typical entrained air bubbles (image at 200X magnification).

The impingement of drops on the sheet has also been cited as a cause of rupture. Although no drops forming at the nozzle or deflecting off the tank walls were observed striking the sheet, a fraction of the drops formed in the region of breakup appeared to have an upstream component of velocity. These drops might strike and puncture the sheet.

The wave-thinning analysis performed in this study was based on the growth of a single wave; however, as shown in the images of the rims formed by splitting the sheet, the wave shapes did not correspond to a single sine wave. This result could be used to infer that the sheet is perturbed by two or more interacting waves. This interaction may lead to sheet thickness variations in addition to the radial and single-wave thinning mechanisms.

At least two disturbance wavelengths are expected based on the vibration analysis and wavelength measurement results. The measured wavelength appears to follow the trends predicted by linear theory, while the FFT spectra suggest the presence of an additional wave with a frequency of about 354 Hz. The results of the perforation count experiments demonstrated that, when this wavelength of the disturbance resulting from this vibration was near the wavelength of optimum growth, the breakup length was reduced. Even when the vibration-induced wavelength is significantly different from the optimum wavelength, the two waves will interact to enhance the rate of wave thinning and, thus, reduce the breakup length.

In addition to the observed sinuous waves, dilational waves are also expected to be present. Although dilational waves were found to thin the sheet more slowly than sinuous waves, these dilational waves are still expected to contribute to the total rate of thinning.

Certain features are common to all of these mechanisms of rupture. First, each process is random, that is the location of the particle, bubble, or impinging drop causing each rupture cannot be predicted, and the initial amplitude and phase lag of vibration-induced waves relative

to the aerodynamically-induced waves is not known. Also, it is reasonable to expect that all mechanisms could be active in real spray systems and do not represent a feature particular to this study. Finally, each mechanism requires the prior thinning of the sheet by other processes. In the case of the airborne contaminants and air bubbles, this thickness is related to the dimension of the particles, while for impinging drops, it will be a function of the size and momentum of each drop.

No direct experimental evidence was obtained in this study to confirm any of these mechanisms of rupture, and each may contribute to the total rate of perforation formation. However, based on indirect evidence, the air bubble and wave interaction mechanisms are expected to dominate.

SIGNIFICANCE OF RESULTS

Previous investigations of the sheet breakup process have focussed on either a wave mechanism or a perforation mechanism of breakup. The perforation mechanism was generally attributed to the unique operating conditions of the spray being investigated, while discussions of the wave mechanism have focussed on growth rates and the wavelength of optimum growth, without a description of the process by which these waves result in sheet breakup.

The main result of this study is the description that waves in the sheet, regardless of their wavelength or growth rate, will cause thinning. When sufficient thinning has occurred, local rupture of the sheet will occur. Although the wave-thinned sheet thickness of the sheet appears to be too large for spontaneous thinning to cause the perforations, the presence of air bubbles in the system investigated will result in sufficient additional local thinning, such that spontaneous rupture may occur.

Although it is possible to control the approximate downstream position at which rapid perforation occurs by controlling the sheet thickness, velocity, and dominant waves, the spatial distribution of the holes and their histories as they collect fluid into clumps and strands will result in a drop size distribution. Therefore, for all sheet-producing nozzles, even if the mean drop size can be controlled by varying the location of rapid perforation, a distribution of drop sizes about this mean will still result.

One possible method for controlling the spatial distribution of perforations is to promote the development of dilational waves. The thinnest regions of a sheet perturbed by a dilational wave occur in concentric bands; therefore, perforations might be expected to occur only in these regions as well. Once formed, the perforations would grow more rapidly in the thin bands (the lateral direction) and less rapidly in the radial direction. This may result in the production of more uniform strands and, thus, a narrower drop size distribution.

The analysis of the relative growth rates of sinuous and dilational waves demonstrated that, in order to cause dilational waves to dominate the breakup of the sheet, the initial amplitude of the disturbance must be large relative to the sheet thickness. From this it can be inferred that vibratory assist (the external inducement of disturbances) may be a means of controlling drop size, provided the induced vibrations result in the formation of large amplitude dilational waves.

The radial and wave-thinning processes described in this study will be present in the sheets formed when spraying black liquor; however, the mechanism initiating perforations may not involve air bubbles. Despite this difference, the broad distribution of drop sizes resulting from a random distribution of sites for rupture in a sheet thinned by sinuous waves is still expected. Therefore, the inducement of dilational waves by external vibration appears to be the only method available for controlling drop size.

SUGGESTIONS FOR FUTURE WORK

This study has provided a description of the sheet breakup process; however, several features have not been confirmed experimentally. First, the downstream position at which a particular sinuous wave disturbance results in rapid thinning is dependent on the initial disturbance amplitude. Because the true disturbance amplitude was not determined experimentally, the effects of other system parameters on the breakup length of the sheet could only be determined qualitatively. If a splash plate spray system could be constructed such that disturbances of a fixed amplitude could be induced in the sheet, the resulting breakup lengths could be compared quantitatively to predicted values.

A second area for investigation is the amplitude and wavelength of disturbances in the breakup region. In this study, the optimum sinuous wave for a radially thinning, viscous sheet was used. This result was obtained from linear theory and is strictly valid only when the amplitude of the disturbance is less than the thickness of the sheet. The undisturbed sheet thickness at breakup was on the order of 50 μm, while the predicted disturbance amplitudes were on the order of 5 mm (5000 μm). At this amplitude, nonlinear effects may be important and could result in a modified wave shape, and exponential growth may not continue into this region. These effects are not expected to influence the mechanism of breakup, but will alter the rate of downstream wave-thinning. If accurate predictions of the breakup length are determined to be important, a higher order description of the wavelength and growth rate of wave disturbances will be required.

The drop size distribution resulting from the breakup of liquid sheets is the key to many processes. Previous attempts to predict the drop size distribution have focussed on the breakup of strands, assumed to be formed from the disintegration of the sheet. While some

strands will form from the merging of neighboring perforation rims, much of the fluid is collected into clumps of liquid. Also, the size distribution of the strands that form is a function of the distribution and histories of the holes. A third area for investigation might involve combining a statistical description of the fluid masses expected to result from the sheet breakup process described in this study, with a statistical prediction of the drop sizes expected to form from such clumps, in order to predict drop size distributions. A convenient starting point for such an analysis might involve a combination of Rayleigh's[52] theory for predicting drop sizes produced from the breakup of strands, with Sellens and Brzustowski's[72] maximum entropy theory approach to predicting the drop size distribution produced from the breakup of sheet segments.

A fourth area of interest might be a thorough investigation of the disturbance of optimum growth as a function of the operating conditions. A number of experimental techniques for determining frequency and wave shape appear viable including probes which contact the crests of successive waves,[71] laser probes which count waves by measuring the rate at which successive disturbances interrupt the path of a collimated beam of light,[73] piezoelectric films which would monitor the temporal and spatial distribution of spray impact on a pressure responsive medium,[74] and a noncontact optical probe which might be capable of detailing the shape of waves as they pass beneath a fixed point.[75]

The laser and simple probe methods provide information on the wave frequency only. The piezoelectric film technique might provide data related to both the amplitude and the frequency of the waves, but like the simple probe, it is intrusive, and its effect on the spray behavior would have to be investigated. The noncontact optical probe is used to measure the curvature of a sample by determining the angle at which an incident light beam is deflected off the surface.[75] The method has the benefit of being nonobtrusive and may provide wavelength, amplitude, and wave shape information.

A fifth area of potential investigation is the determination of the distribution of drop velocities in the region of breakup. The role of drop velocity in biasing the results of certain drop size distribution measurement techniques has been discussed.[76] Of particular importance is the preferential influence of air drag on smaller drops relative to larger drops and the resulting effects on the observed distribution of drop sizes. Groeneweg et al.[77] presented arguments for treating the drop velocity at the point of breakup as a statistical variable like drop diameter, rather than as a constant equal to the sheet velocity. Sellens and Brzustowski[72] attempted to predict this distribution with their maximum entropy model of sheet breakup, but were forced to introduce an arbitrary loss term in the momentum balance. Without the loss term, the drop velocity was predicted to be uniform.

The approach of Sellens and Brzustowski[72] relied on a simplified description of the sheet at breakup, specifically a sheet of uniform velocity and thickness. The results of this study suggest a physical source for the loss of momentum they required to obtain realistic results with the maximum entropy model. The sheet segments formed from the merging of holes have a momentum associated not only with the bulk flow of the sheet downstream, but also with the velocity of the perforation rims relative to the sheet. When these rims collide, a portion of the momentum will be lost due to the rapid mixing of the fluid. It may be possible to estimate the magnitude of these losses relative to the total momentum of the sheet segment and, thus, provide a physical explanation for the observed distribution of drop velocities.

Finally, the possibility of controlling the breakup process and the resulting drop size distribution by promoting the growth of dilational waves relative to sinuous waves should be investigated. The splash plate nozzle used in this study does not appear to be suited for such a process; however, it may be possible to pulse the flow to a fan spray nozzle and, thus, form sheets with a large amplitude dilational disturbance. The breakup length and uniformity of

drop sizes produced could then be investigated as a function of the magnitude of the induced pulsations.

ACKNOWLEDGMENTS

I would like to express my sincere gratitude to my advisor, Dr. Cyrus Aidun, for his advice and guidance throughout this thesis. His efforts and encouragement, particularly in the final stages of writing, will forever increase the confidence I have in my abilities and the expectations I will have for my work. I am also grateful to Dr. Jeff Lindsay for his suggestions and support, and to Dr. Terry Adams for his insight and for teaching me that fluid mechanics is more than just math.

I would like to thank the Institute faculty for their technical advice and the staff for their assistance. I would also like to thank John McKibben for all his computer help, even though "he doesn't work here." I am grateful for the financial support of the Institute of Paper Science and Technology, its member companies and alumni, and the U.S. Department of Energy (No. FC02-88CE40839). I also thank Smith Meter Inc. and Fluid Flow of Georgia, Inc. for donating a mass flowmeter.

I am very thankful for the friendships I have made during my years at the Institute. They have helped to make the low points more tolerable and the high points more memorable. I am particularly grateful for the friendship of Pat Medvecz and Laura Thompson.

Finally, I would like to thank my parents for their love and support during this thesis and throughout my life. I am also grateful to my sister Jane for her encouragement when I needed it most, and my sister Ann for listening whenever I needed to talk.

LITERATURE CITED

1. Lefebvre, A.H. Atomization and Sprays. Combustion: An International Series, N. Chigier ed., Hemisphere Publishing Corp., 1989.

2. Lefebvre, A.H. Fuel Atomization, Droplet Evaporation, and Spray Combustion. Chapter Nine in: Fossil Fuel Combustion. Ed. Bartok, W.; Sarofim, A.F., John Wiley and Sons Inc., 1991.

3. Williams, A. Combustion of Liquid Fuel Sprays. Butterworths & Co. Ltd., 1990.

4. Spalding, D.B. Combustion and Mass Transfer. Pergamon Press, 1979.

5. Williams, F.A. Combustion Theory. Addison-Wesley Publishing Company, Inc.,1965.

6. Walsh, P.M.; Zhang, M.; Farmayan, W.F.; Beer, J.M. Twentieth (International) Symposium on Combustion, The Combustion Institute, Pittsburgh, 1984. (as referenced in Williams[3]).

7. Gonzalez, M.A.; Reitz, R.D. Modeling Diesel Engine Spray Vaporization and Combustion. Proceedings Fifth International Conference on Liquid Atomization and Spray Systems. NIST, Gaithersburg, MD, July 15-18, 1991(291-98).

8. Choudhury, P.R.; Gerstein, M. Analysis of a Fuel Spray Subjected to Coupled Evaporation and Decomposition. Nineteenth Symposium (International) on Combustion, 1982(993-7).

9. Hough, G. ed. Chemical Recovery in the Alkaline Pulping Processes. TAPPI Press, 1985.

10. Adams, T.N.; Frederick, W.J. Kraft Recovery Boiler Physical and Chemical Processes. The American Paper Institute, Inc., New York, 1988.

11. Smoot, L.D. Coal and Char Combustion, Chapter 10 in: Fossil Fuel Combustion. Ed. Bartok, W.; Sarofim, A.F., John Wiley and Sons Inc., 1991.

12. Kulas, K. A. An Overall Model of the Combustion of a Single Droplet of Kraft Black Liquor. Doctoral Dissertation. Appleton, WI, The Institute Of Paper Chemistry, 1990.

13. Frederick, W.J. Combustion Processes in Black Liquor Recovery: Analysis and Interpretation of Combustion Rate Data and an Engineering Design Model. Report No. One, Dept. of Energy Contract No. AC02-83CE40637, (March 1990).

14. Miller, P.T. Swelling of Kraft Black Liquor. Doctoral Dissertation. Appleton, WI, The Institute of Paper Chemistry, 1986.

15. Harper, F.D. Sulfur Release During the Pyrolysis of Black Liquor. Doctoral Dissertation. Appleton, WI, The Institute of Paper Chemistry, 1989.

16. Walsh, A.R. A Computer Model for In-Flight Black Liquor Combustion in a Kraft Recovery Furnace. Doctoral Dissertation. Appleton, WI, The Institute of Paper Chemistry, 1989.

17. Jones, A.K. A Model of the Kraft Recovery Furnace. Doctoral Dissertation. Appleton, WI, The Institute of Paper Chemistry, 1989.

18. Mugele, R.A.; Evans, H.D. Droplet Size Distribution in Sprays. Industrial and Engineering Chemistry, 43(6):1317-24(June 1951).

19. Sowa, W.A. Interpreting Mean Drop Diameters Using Distribution Moments. Atomization and Sprays, 2(1):1-17(1992).

20. Masters, K. Spray Drying Handbook. George Goodwin Limited, London, 1985.

21. Nukiyama, S.; Tanasawa, Y. Experiments on the Atomization of Liquids in an Air Stream, Report 3, On the Droplet-Size Distribution in an Atomized Jet, Defense Research Board, Department of National Defense, Ottawa, Canada; translated from Trans. Soc. Mech. Eng. Japan., 5(18):62-7(1939). (as referenced in Lefebvre[1]).

22. Rosin, N.K.; Rammler, E. The Laws Governing the Fineness of Powdered Coal. J. Inst. Fuel, 7(31):29-36(1933).(as referenced in Lefebvre[1]).

23. Xu, T.H.; Durst, F.; Tropea, C. The Three-Parameter Log-Hyperbolic Distribution and its Applications to Particle Sizing. Proceeding of the Fifth International Conference on Liquid Atomization and Spray Systems, NIST Gaithersburg, MD, July 15-18, 1991(pp. 315-24).

24. Goering, C.E.; Smith, D.B. Equations for Droplet Size Distributions in Sprays. Trans. of the ASAE,209-16(1978).

25. ASTM Standard E 799-87, Standard Practice for Determining Data Criteria and Processing for Liquid Drop Size Analysis. (1987).

26. Dietrich, V.E. Dropsize Distributions for Various Types of Nozzles. Proceedings of the First International Conference on Liquid Atomization and Spray Systems, Tokyo, Japan, August 27-31, 1978(69-77).

27. Andreussi, P.; Romano, G.; Zanelli, S. Drop Size Distribution in Annular-Mis Flows. Proceedings of the First International Conference on Liquid Atomization and Spray Systems, Tokyo, Japan, August 27-31, 1978(333-40).

28. Chin, J.S.; Lefebvre, A.H. Some Comments on the Characterization of Drop-Size Distributions in Sprays. Proceedings of the Third International Conference on Liquid Atomization and Spray Systems, Imperial College, London, July 8-10, 1985(IVA/1/1-12).

29. Taylor, G.I. Oblique Impact of a Jet on a Plane Surface. Phil. Trans. Roy. Soc. London A(260):96-100(1966).

30. Simmons, H.C. The Correlation of Drop-Size Distributions in Fuel Nozzle Sprays, Part 1: The Drop-Size/Volume-Fraction Distribution. Trans. of the A.S.M.E., Journal of Engineering for Power,309-14(July 1977).

31. Taylor, G.I. Formation of Thin Flat Sheets of Water. Proc. Roy. Soc. London A(259):1-17(November 1960).

32. Taylor, G.I. The Dynamics of Thin Sheets of Fluid I. Water Bells. Proc. Roy. Soc. London A(253):289-95(December 1959).

33. Taylor, G.I. The Dynamics of Thin Sheets of Fluid III. Disintegration of Fluid Sheets. Proc. Roy. Soc. London A(253):313-21(December 1959).

34. Obuskovic, N.; Adams, T.N. Fluid Sheet Thickness and Velocity at the Tip of a Black Liquor Splashplate Nozzle. AIChE 1989 Annual Meeting, San Francisco, CA, November 5-10, 1989.

35. Watson, E.J. The Radial Spread of a Liquid Jet Over a Horizontal Plane. J. Fluid Mech., 20(Part 3):481-99(1964).

36. Dombrowski, N.; Fraser, R.P. A Photographic Investigation into the Disintegration of Liquid Sheets. Phil. Trans. Roy. Soc. London, 247A:101-30(September 1954).

37. Clark, C.J.; Dombrowski, N. The Dynamics of the Rim of a Fan Spray Sheet. Chem. Eng. Sci., 26:1949-52(1971).

38. Huang, J.C.P. The Breakup of Axisymmetric Liquid Sheets. J. Fluid Mech., 43(2):305-19(1970).

39. Fraser, R.P.; Eisenklam, P.; Dombrowski, N.; Hasson, D. Drop Formation from Rapidly Moving Liquid Sheets. A.I.Ch.E. J., 8(5):672-80(November 1962).

40. Dombrowski, N.; Johns, W.R. The Aerodynamic Instability and Disintegration of Viscous Liquid Sheets. Chem. Eng. Sci., 18:203-13(1963).

41. Xianguo Li; Tankin, R.S. On the Temporal Instability of a Two-Dimensional Viscous Liquid Sheet. J. Fluid Mech., 226:425-43(1991).

42. Squire, H.B. Investigation of the Instability of a Moving Liquid Film. Brit. J. of Apl. Physics, 4:167-9(June 1953).

43. York, J.L.; Stubbs, H.E.; Tek, M.R. The Mechanism of Disintegration of Liquid Sheets. Trans. ASME, 75:1279-86(October 1953).

44. Hagerty, W.W.; Shea, J.F. A Study of the Stability of Plane Fluid Sheets. J. Appl. Mech., 22:509-514(December 1955).

45. Crapper, G.D.; Dombrowski, N.; Pyott, G.A.D. Kelvin-Helmholtz Wave Growth on Cylindrical Sheets. J. Fluid Mech., 68(Part 3):497-502(1975).

46. Weihs, D. Stability of Thin, Radially Moving Liquid Sheets. J. Fluid Mech., 87(Part 2):289-98(1978).

47. Sheludko, A. Thin Liquid Films. Advan. Colloid Interface Sci., Elsevier Publishing Company, Amsterdam, 1:391-464(1967).

48. Patzer, J.F.; Homsey, G.M. Hydrodynamic Stability of Thin Spherically Concentric Fluid Shells. J. Colloid and Interface Science, 51(3):499-508(June 1975).

49. Pandit, A.B.; Davidson, J.F. Hydrodynamics of the Rupture of Thin Liquid Films. J. Fluid Mech., 212:11-24(1990).

50. Fisher, J.C. The Fracture of Liquids. J. Appl. Physics, 19:1062-7(November 1948).

51. Taylor, G.I.; Michael, D.H. On Making Holes in a Sheet of Fluid. J. Fluid Mech., 58(part4):625-39(1973).

52. Rayleigh, J.W.S. The Theory of Sound - 2nd Edition, Vol II., Macmillan Publications 1896, reprinted by Dover Publications, New York, 1945:351-7.

53. Abramowitz, M.; Stegun, I.A. Editors Handbook of Mathematical Functions with Formulas, Graphs, and Mathematical Tables. National Bureau of Standards, Applied Math Series - 55:374-379(December 1972).

54. Weber, C. Zum Zerfall eines Flüssigkeitsstrahles. Ztschr. f. angew. Math. und Mech., 11(2):136-54(April 1931).

55. Yuen, M. Non-Linear Capillary Instability of a Liquid Jet. J. Fluid Mech., 33(Part 1):151-63(1968).

56. Rutland, D.F.; Jameson, G.J. Theoretical Prediction of the Sizes of Drops Formed in the Breakup of Capillary Jets. Chem. Eng. Sci., 25(11):1689-98(1970).

57. Lafrance, P. Nonlinear Breakup of a Laminar Liquid Jet. The Physics of Fluids, 18(4):428-32(April 1975).

58. Chaudhary, K.C.; Redekopp, L.G. The Nonlinear Capillary Instability of a Liquid Jet. J. Fluid Mech.,96(Part 2):257-74(1980).

59. Weihs, D.; Frankel, I. Equilibrium Shape and Stability of a Liquid Cylinder in Cross Flow at Low Weber Numbers, J. Fluid Mech., 116:393-409(1982).

60. CRC Handbook of Chemistry and Physics - 61st Edition. Weast, R.C. ed., pp. D239-40(1981).

61. CRC Handbook of Chemistry and Physics - 72nd Edition. Lide, D.R. ed., pp. 6:117(1992).

62. Lange's Handbook of Chemistry - 13th Edition. Dean, J.A. ed., pp. 10:97(1985).

63. ASTM Standard E 178-80, Standard Practice for Dealing with Outlying Observation.(1989).

64. Tietjen, G.L.; Moore, R.H. Some Grubbs-Type Statistics for the Detection Of Several Outliers. Technometrics, 14(3):583-97(August 1972).

65. Beyer, W.H., ed., CRC Standard Mathematical Tables., CRC Press Inc., 429-32(1978).

66. Gaster, M. A Note on the Relation Between Temporally-Increasing and Spatially-Increasing Disturbances in Hydrodynamic Instability. J. Fluid Mech., 14:222-4(1962).

67. Asare, H.R.; Takahashi, R.K.; Hoffman, M.A. Liquid Sheet Jet Experiments: Comparison with Linear Theory. J. Fluids Engineering, 103:595-604(December 1981).

68. Morris, P.J. A note appended to Asare *et al.*[67]

69. Lin, S.P.; Lian, Z.W.; Creighton, B.J. Absolute and Convective Instability of a Liquid Sheet. J. Fluid Mech., 220:673-89(1990).

70. Schlichting, H. Boundary Layer Theory. McGraw Hill Book Co., Inc., pp. 23-24(1955).

71. Crapper, G.D.; Dombrowski, N. A Note on the Effect of Forced Disturbances on the Stability of Thin Liquid Sheets and on the Resulting Drop Size. Int. J. Multiphase Flow, 10(6):731-6(1984).

72. Sellens, R.W.; Brzustowski, T.A. A Simplified Prediction of Droplet Velocity Distributions in a Spray. Combustion and Flame, 65:273-9(1986).

73. Mansour, A.; Chigier, N. Dynamic Similarity Between Liquid Sheets and Hard Spring Systems. Proceeding of the Fifth International Conference on Liquid Atomization and Spray Systems, NIST Gaithersburg, MD, July 15-18, 1991(181-7).

74. Lindsay, J. Personal Communication, May 1992.

75. Brodeur, P.H.; Waterhouse, J.F. Automated Curvature Evaluation (ACE), PaperLink, (A publication of the Institute of Paper Science and Technology), 7(2)(1992).

76. Tate, R.W. Some Problems Associated with the Accurate Representation of Droplet Size Distributions. Proceedings of the Second International Conference on Liquid Atomization and Spray Systems, Madison, WI, USA, June 20-24, 1982(341-51).

77. Groeneweg, J.F.; El-Wakil, M.M.; Myers, P.S.; Uyehara, O.A. The Role of Drop Velocity in a Statistical Spray Description. Proceedings of the First International Conference on Liquid Atomization and Spray Systems, Tokyo, Japan, August 27-31, 1978(277-84).

APPENDIX A: SURFACE TREATMENT OF THE SPLASH PLATE

The splash plates used in this study were polished in an attempt to minimize disturbances to the sheet.

Polishing procedure.

- hand polish the top and sides surfaces of the plate with 80 grit sandpaper,
- hand polish the top and sides surfaces of the plate with 120 grit sandpaper,
- using the Buehelr Ecomet 5 grinder/polisher, polish the plate with 240 grit sandpaper,
- using the Buehelr Ecomet 5 grinder/polisher, polish the plate with 400 grit sandpaper,
- using the Buehelr Ecomet 5 grinder/polisher, polish the plate with 600 grit sandpaper.

Each polishing step is completed when no marks or scratches larger than those caused by the sandpaper are apparent. Following the polishing procedure, the plate was coated with a silicon-based release agent.

Coating procedure.

- clean the splash plate with Frekote mold cleaner,
- place in a 105 °C oven for 10 minutes,
- coat with Frekote B15 mold sealer and wait 30 minutes,
- apply a second coat of B15 mold sealer,
- place in a 105 °C oven for 60 minutes,
- apply 1st coat of Frekote 700-NC, wait 20 minutes,
- apply 2nd coat of Frekote 700-NC, wait overnight (8-10 hours),
- apply 3rd coat of Frekote 700-NC, wait 20 minutes,
- apply 4th coat of Frekote 700-NC,
- place in a 105 °C oven for 20 minutes,
- let cool,
- inspect the plate for scratches, nicks, or coating nonuniformities.

APPENDIX B: SURFACE TENSION MEASUREMENTS

The surface tension of the glycerol/water solution was determined using a DuNouy ring surface tensiometer. The apparatus was calibrated with water, and the relationship between the mass of fluid suspended from the wire and the tensiometer reading was found to be

$$M(mg) = 12.09 \times (\text{reading}) - 11.12. \qquad \text{(B1)}$$

The volume of fluid suspended is then the mass suspended divided by the fluid density. The surface tension correction factor was then obtained from tables provided with the instrument.

Four evaluations of the surface tension were performed throughout this study. The data and calculations are summarized in the following tables.

DATE: 11/1/90 T = 21.1 C

R = 0.95413 cm

dens = 1.220 gm/cc

reading	mass (mg)	V (cm3)	R3/V	F	surf	
69.6	830.34	0.6707	1.2990	0.916	63.8	
68.0	811.00	0.6551	1.3300	0.915	62.2	
67.3	802.54	0.6483	1.3440	0.914	61.5	
68.7	819.46	0.6619	1.3162	0.916	62.9	
69.7	831.55	0.6717	1.2971	0.917	63.9	
66.9	797.70	0.6443	1.3522	0.914	61.1	
69.2	825.51	0.6668	1.3066	0.917	63.5	
67.4	803.75	0.6492	1.3420	0.915	61.7	
67.7	807.37	0.6522	1.3360	0.915	61.9	
68.4	815.84	0.6590	1.3221	0.916	62.7	
					62.5	=avg
					1.0	=std
					10	= N

surface tension = avg +/- t(0.975,N-1)*std/sqrt(N)

surface tension = 62.5 +/- 0.7 dyne/cm

DATE: 4/3/91 T = 21.2 C

R = 0.9551 cm

dens = 1.232 gm/cc

reading	mass (mg)	V (cm3)	R3/V	F	surf	
68.3	814.63	0.6672	1.3059	0.9189	62.8	
67.7	807.37	0.6612	1.3176	0.9182	62.2	
69.2	825.51	0.6761	1.2887	0.9199	63.7	
68.4	815.84	0.6682	1.3039	0.9190	62.9	
67.8	808.58	0.6622	1.3156	0.9183	62.3	
68.4	815.84	0.6682	1.3039	0.9190	62.9	
68.7	819.46	0.6711	1.2982	0.9193	63.2	
68.3	814.63	0.6672	1.3059	0.9189	62.8	
68.3	814.63	0.6672	1.3059	0.9189	62.8	
69.0	823.09	0.6741	1.2925	0.9197	63.5	
68.6	818.25	0.6702	1.3001	0.9192	63.1	
67.7	807.37	0.6612	1.3176	0.9182	62.2	
68.7	819.46	0.6711	1.2982	0.9193	63.2	
68.7	819.46	0.6711	1.2982	0.9193	63.2	
67.9	809.79	0.6632	1.3137	0.9184	62.4	
					62.8	=avg
					0.4	=std
					15	= N

surface tension = avg +/- t(0.975,N-1)*std/sqrt(N)

surface tension = 62.8 +/- 0.2 dyne/cm

DATE: 8/4/91 T = 22.3 C

R = 0.9551 cm

dens = 1.238 gm/cc

reading	mass (mg)	V (cm3)	R3/V	F	surf	
67.2	801.33	0.6473	1.3460	0.9166	61.6	
67.3	802.54	0.6483	1.3440	0.9167	61.7	
67.6	806.16	0.6512	1.3380	0.9171	62.0	
67.7	807.37	0.6522	1.3360	0.9172	62.1	
67.4	803.75	0.6492	1.3420	0.9168	61.8	
67.5	804.96	0.6502	1.3400	0.9170	61.9	
67.5	804.96	0.6502	1.3400	0.9170	61.9	
67.3	802.54	0.6483	1.3440	0.9167	61.7	
67.0	798.91	0.6453	1.3501	0.9164	61.4	
67.6	806.16	0.6512	1.3380	0.9171	62.0	
					61.8	=avg
					0.2	=std

surface tension = avg +/- t(0.975,N-1)*std/sqrt(N)

surface tension = 61.8 +/- 0.1 dyne/cm

DATE: 11/23/91 T = 21.2 C

R = 0.9551 cm

dens = 1.221 gm/cc

reading	mass (mg)	V (cm3)	R3/V	F	surf	
68.5	817.05	0.6692	1.3020	0.9191	63.0	
68.4	815.84	0.6682	1.3039	0.9190	62.9	
69.2	825.51	0.6761	1.2887	0.9199	63.7	
68.9	821.88	0.6731	1.2944	0.9196	63.4	
68.9	821.88	0.6731	1.2944	0.9196	63.4	
69.0	823.09	0.6741	1.2925	0.9197	63.5	
69.3	826.72	0.6771	1.2868	0.9200	63.8	
69.0	823.09	0.6741	1.2925	0.9197	63.5	
69.4	827.93	0.6781	1.2849	0.9202	63.9	
69.0	823.09	0.6741	1.2925	0.9197	63.5	
					63.4	=avg
					0.3	=std
					10	= N

surface tension = avg +/- t(0.975,N-1)*std/sqrt(N)

surface tension = 63.4 +/- 0.2 dyne/cm

APPENDIX C: DATA FOR THE PERFORATION COUNT EXPERIMENTS

This appendix contains the raw and reduced data for the perforation count experiments. These data are presented in the following order. In the first table, the operating conditions, number of perforations observed, the dimensions imaging area, and the area corrected number of perforations are presented for the trials run with the NF-6000 nozzle. The second table includes the area corrected number of perforations and the perforation counts at each position adjusted to exclude perforations accounted for at upstream positions. In the third table, the jet Reynolds number; the sheet thickness, both at the plate edge and downstream; and the sheet velocity are presented.

Perforation count experiments (NF-6000)
nozzle orifice diameter = 4.83 mm

trial number	mass flow (kg/s)	density (kg/m^3)	viscosity (kg/ms)	perfs. obs.	Uo (m/s)	center x (cm)	span S (cm)	width W (cm)	area corr. perfs.
120590.1	0.33	1216	0.068	12	14.8	13	4.8	6.2	32.9
120590.2	0.38	1216	0.065	9	17.1	13	4.8	6.2	24.7
120590.3	0.44	1215	0.064	14	19.8	13	4.8	6.2	38.4
120590.4	0.49	1215	0.063	22	22.0	13	4.8	6.2	60.4
120590.5	0.33	1215	0.062	41	14.8	15	4.8	6.2	129.8
120590.6	0.38	1214	0.061	36	17.1	15	4.8	6.2	114.0
120590.7	0.44	1214	0.059	55	19.8	15	4.8	6.2	174.2
120590.8	0.49	1214	0.058	73	22.0	15	4.8	6.2	231.2
120590.9	0.33	1214	0.060	60	14.8	17	4.8	6.2	215.4
120590.10	0.38	1214	0.060	85	17.1	17	4.8	6.2	305.1
120590.11	0.43	1214	0.059	100	19.3	17	4.8	6.2	358.9
120590.12	0.49	1215	0.058	225	22.0	17	4.8	6.2	807.6
120590.13	0.33	1214	0.061	133	14.8	19	4.8	6.2	533.5
120590.14	0.38	1214	0.061	131	17.1	19	4.8	6.2	525.5
120590.15	0.44	1214	0.060	196	19.8	19	4.8	6.2	786.2
120590.16	0.49	1215	0.058	561	22.0	19	4.8	6.2	2250.4
120590.17	0.33	1215	0.059	203	14.8	19	4.8	6.2	814.3
120590.18	0.38	1215	0.059	166	17.1	19	4.8	6.2	665.9
120590.19	0.44	1215	0.058	225	19.8	19	4.8	6.2	902.6
120590.20	0.49	1215	0.058	breakup	22.0	19	4.8	6.2	breakup
120590.21	0.33	1214	0.058	318	14.8	21	4.8	6.2	1409.9
120590.22	0.38	1214	0.058	429	17.1	21	4.8	6.2	1902.1
120590.23	0.43	1214	0.058	816	19.3	21	4.8	6.2	3617.9
120590.24	0.49	1214	0.057	breakup	22.0	21	4.8	6.2	breakup

NF-6000 reported new perforations

trial number	Uo (m/s)	center x (cm)	area corr. perfs.	reported new perfs.
120590.1	14.8	13	32.9	32.9
120590.5	14.8	15	129.8	96.9
120590.9	14.8	17	215.4	85.6
120590.13	14.8	19*	533.5	318.1
120590.17	14.8	19*	814.3	598.9
120590.21	14.8	21	1409.9	736
120590.2	17.1	13	24.7	24.7
120590.6	17.1	15	114.0	89.3
120590.10	17.1	17	305.1	191.1
120590.14	17.1	19*	525.5	220.4
120590.18	17.1	19*	665.9	360.8
120590.22	17.1	21	1902.1	1306.4

trial number	Uo (m/s)	center x (cm)	area corr. perfs.	reported new perfs.
120590.3	19.8	13	38.4	38.4
120590.7	19.8	15	174.2	135.8
120590.11	19.3	17	358.9	184.7
120590.15	19.8	19*	786.2	427.3
120590.19	19.8	19*	902.6	543.7
120590.23	19.3	21	3617.9	2773.5
120590.4	22.0	13	60.4	60.4
120590.8	22.0	15	231.2	170.8
120590.12	22.0	17	807.6	576.4
120590.16	22.0	19*	2250.4	1442.8
120590.20	22.0	19*	breakup	breakup
120590.24	22.0	21	breakup	breakup

*values at 19 cm
were treated as duplicate runs

Perforation count experiments (NF-6000)

trial number	inviscid thick (um) 2h(xp)	Rejet	viscous thick* 2h(xp)	D.S. thick** 2h (um)	linear regr* Us(m/s)
120590.1	115	1300	704	138	2.4
120590.2	115	1500	613	120	3.2
120590.3	115	1800	548	107	4.2
120590.4	115	2000	506	99	5
120590.5	115	1400	658	111	2.6
120590.6	115	1600	587	99	3.3
120590.7	115	2000	520	88	4.4
120590.8	115	2200	481	81	5.3
120590.9	115	1400	643	96	2.6
120590.10	115	1700	581	87	3.4
120590.11	115	1900	529	79	4.2
120590.12	115	2200	480	72	5.3
120590.13	115	1400	651	87	2.6
120590.14	115	1600	587	78	3.3
120590.15	115	1900	526	70	4.3
120590.16	115	2200	480	64	5.3
120590.17	115	1500	635	85	2.7
120590.18	115	1700	574	77	3.4
120590.19	115	2000	514	69	4.4
120590.20	115	2400	461	62	5.9
120590.21	115	1500	628	76	2.7
120590.22	115	1700	567	69	3.5
120590.23	115	2000	523	63	4.2
120590.24	115	2400	457	55	5.9

(*) calculated from the two-term linear regression equation

(**) downstream sheet thickness at the center of the imaging area

Perforation count experiments (NF-8000) part 1 of 2
nozzle orifice diameter = 5.56 mm

trial number	mass flow (kg/s)	density (kg/m^3)	viscosity (kg/ms)	perfs. obs.	Uo (m/s)	center x (cm)	span S (cm)	width W (cm)	area corr. perfs.
100890.1	0.45	1217	0.067	133	15.2	19	6.4	8.8	281.9
100890.2	0.51	1217	0.064	195	17.3	19	8.2	11	258.1
100890.3	0.60	1218	0.063	436	20.3	19	8.2	11	577.0
100890.4	0.65	1217	0.062	breakup	22.0	19	8.2	11	breakup
100890.5	0.37	1217	0.064	235	12.5	19	8.2	11	311.0
100890.6	0.37	1216	0.063	85	12.5	16.5	8.5	11.2	92.6
100890.7	0.45	1217	0.061	82	15.2	16.5	8.5	11.2	89.3
100890.8	0.52	1216	0.059	81	17.6	16.5	8.5	11.2	88.2
100890.9	0.59	1216	0.059	258	20.0	16.5	8.5	11.2	281.0
100890.10	0.67	1217	0.059	574	22.7	16.5	8.5	11.2	625.1
101590.1	0.37	1217	0.067	1	12.5	8.3	4.9	6.4	1.7
101590.2	0.44	1217	0.066	0	14.9	8.3	4.9	6.4	0.0
101590.3	0.51	1217	0.065	0	17.3	8.3	4.9	6.4	0.0
101590.4	0.59	1217	0.064	0	20.0	8.3	4.9	6.4	0.0
101590.5	0.67	1217	0.064	7	22.7	8.3	4.9	6.4	11.6
101590.6	0.37	1216	0.066	9	12.5	12.3	4.8	6.2	23.4
101590.7	0.44	1216	0.065	9	14.9	12.3	4.8	6.2	23.4
101590.8	0.52	1216	0.063	7	17.6	12.3	4.8	6.2	18.2
101590.9	0.59	1216	0.063	23	20.0	12.3	4.8	6.2	59.7
101590.10	0.67	1216	0.062	46	22.7	12.3	4.8	6.2	119.5

Perforation count experiments (NF-8000) part 2 of 2
nozzle orifice diameter = 5.56 mm

trial number	mass flow (kg/s)	density (kg/m^3)	viscosity (kg/ms)	perfs. obs.	Uo (m/s)	center x (cm)	span S (cm)	width W (cm)	area corr. perfs.
101690.1		1216	0.063	1	12.5	9.5	4.8	6.2	2.0
101690.2		1216	0.063	0	15.0	9.5	4.8	6.2	0.0
101690.3		1216	0.063	3	17.5	9.5	4.8	6.2	6.0
101690.4		1216	0.063	5	20.0	9.5	4.8	6.2	10.0
101690.5		1216	0.063	10	22.5	9.5	4.8	6.2	20.1
101690.6		1216	0.063	14	12.5	13.6	4.8	6.2	40.2
101690.7		1216	0.063	17	15.0	13.6	4.8	6.2	48.8
101690.8		1216	0.063	22	17.5	13.6	4.8	6.2	63.2
101690.9		1216	0.063	42	20.0	13.6	4.8	6.2	120.6
101690.10		1216	0.063	109	22.5	13.6	4.8	6.2	313.0
101790.1	0.37	1219	0.072	26	12.5	16.7	4.9	6.3	88.4
101790.2	0.45	1218	0.070	20	15.2	16.7	4.9	6.3	68.0
101790.3	0.52	1218	0.067	47	17.6	16.7	4.9	6.3	159.8
101790.4	0.60	1218	0.064	83	20.3	16.7	4.9	6.3	282.1
101790.5	0.67	1218	0.062	243	22.7	16.7	4.9	6.3	826.0
101790.6	0.37	1216	0.061	237	12.5	20.7	4.8	6.2	1035.8
101790.7	0.45	1216	0.060	227	15.2	20.7	4.8	6.2	992.1
101790.8	0.52	1217	0.058	321	17.6	20.7	4.8	6.2	1402.9
101790.9	0.59	1216	0.056	breakup	20.0	20.7	4.8	6.2	breakup
101790.10	0.66	1216	0.055	breakup	22.4	20.7	4.8	6.2	breakup

Reported perforation counts - excludes perforations accounted for upstream

NF-8000 reported new perforations

trial number	Uo (m/s)	center x (cm)	area corr. perfs.	reported new perfs.
101590.1	12.5	8.3	1.7	1.7
101690.1	12.5	9.5	2.0	0.3
101590.6	12.5	12.3	23.4	21.4
101690.6	12.5	13.6	40.2	16.8
100890.6	12.5	16.5*	92.6	52.4
101790.1	12.5	16.7*	88.4	48.2
100890.5	12.5	19.0	311.0	220.5
101790.6	12.5	20.7	1035.8	724.8
101590.2	14.9	8.3	0.0	0.0
101690.2	15.0	9.5	0.0	0.0
101590.7	14.9	12.3	23.4	23.4
101690.7	15.0	13.6	48.8	25.4
100890.7	15.2	16.5*	89.3	40.5
101790.2	15.2	16.7*	68.0	19.2
100890.1	15.2	19.0	281.9	203.3
101790.7	15.2	20.7	992.1	710.2
101590.3	17.3	8.3	0.0	0.0
101690.3	17.5	9.5	6.0	6.0
101590.8	17.6	12.3	18.2	12.2
101690.8	17.5	13.6	63.2	45.0
100890.8	17.6	16.5*	88.2	25.0
101790.3	17.6	16.7*	159.8	96.6
100890.2	17.3	19.0	258.1	134.1
101790.8	17.6	20.7	1402.9	1144.8

trial number	Uo (m/s)	center x (cm)	area corr. perfs.	reported new perfs.
101590.4	20.0	8.3	0.0	0.0
101690.4	20.0	9.5	10.0	10.0
101590.9	20.0	12.3	59.7	49.7
101690.9	20.0	13.6	120.6	60.9
100890.9	20.0	16.5*	281.0	160.4
101790.4	20.3	16.7*	282.1	161.5
100890.3	20.3	19.0	577.0	295.5
101790.9	20.0	20.7	breakup	breakup
101590.5	22.7	8.3	11.6	11.6
101690.5	22.5	9.5	20.1	8.5
101590.10	22.7	12.3	119.5	99.4
101690.10	22.5	13.6	313.0	193.5
100890.10	22.7	16.5*	625.1	312.1
101790.5	22.7	16.7*	826.0	513.0
100890.4	22.0	19.0	breakup	breakup
101790.10	22.4	20.7	breakup	breakup

*values at 16.5 and 16.7 cm
were treated as duplicate runs

Perforation count experiments (NF-8000) part 1 of 2

trial number	inviscid thick (um) 2h(xp)	Rejet	viscous thick* 2h(xp)	D.S. thick** 2h (um)	linear regr* Us(m/s)
100890.1	152	1500	615	82	3.8
100890.2	152	1800	554	74	4.7
100890.3	152	2200	503	67	6.1
100890.4	152	2400	476	64	7.1
100890.5	152	1300	676	90	2.8
100890.6	152	1300	670	103	2.8
100890.7	152	1700	581	89	4
100890.8	152	2000	524	81	5.1
100890.9	152	2300	490	75	6.2
100890.10	152	2600	459	71	7.5
101590.1	152	1300	697	213	2.7
101590.2	152	1500	617	189	3.7
101590.3	152	1800	559	171	4.7
101590.4	152	2100	511	156	5.9
101590.5	152	2400	478	146	7.2
101590.6	152	1300	691	143	2.8
101590.7	152	1600	611	126	3.7
101590.8	152	1900	544	112	4.9
101590.9	152	2100	507	105	6
101590.10	152	2500	471	97	7.3

(*) calculated from the two-term linear regression equation

(**) downstream sheet thickness at the center of the imaging area

Perforation count experiments (NF-8000) part 2 of 2

trial number	inviscid thick (um) 2h(xp)	Rejet	viscous thick* 2h(xp)	D.S. thick** 2h (um)	linear regr* Us(m/s)
101690.1	152	1300	670	179	2.8
101690.2	152	1600	597	160	3.8
101690.3	152	1900	546	146	4.9
101690.4	152	2100	507	136	6
101690.5	152	2400	477	128	7.2
101690.6	152	1300	670	125	2.8
101690.7	152	1600	597	111	3.8
101690.8	152	1900	546	102	4.9
101690.9	152	2100	507	95	6
101690.10	152	2400	477	89	7.2
101790.1	152	1200	731	111	2.6
101790.2	152	1500	632	96	3.7
101790.3	152	1800	563	86	4.8
101790.4	152	2100	507	77	6.1
101790.5	152	2500	471	72	7.3
101790.6	152	1400	656	80	2.9
101790.7	152	1700	576	71	4
101790.8	152	2100	519	64	5.2
101790.9	152	2400	476	58	6.4
101790.10	152	2800	446	55	7.7

(*) calculated from the two-term linear regression equation

(**) downstream sheet thickness at the center of the imaging area

Perforation count experiments (NF-10000)
nozzle orifice diameter = 6.07 mm

trial number	mass flow (kg/s)	density (kg/m^3)	viscosity (kg/ms)	perfs. obs.	Uo (m/s)	center x (cm)	span S (cm)	width W (cm)	area corr. perfs.
103090.1	0.48	1217	0.077	0	13.6	10	4.8	6.2	0.0
103090.2	0.59	1218	0.074	0	16.7	10	4.8	6.2	0.0
103090.3	0.68	1217	0.072	0	19.3	10	4.8	6.2	0.0
103090.4	poor control of operating conditions, trial was repeated as #103090.6								
103090.5	0.87	1217	0.069	15	24.7	10	4.8	6.2	31.7
103090.6	0.77	1216	0.068	3	21.9	10	4.8	6.2	6.3
103090.7	0.48	1216	0.070	5	13.6	15.6	4.8	6.2	16.5
103090.8	0.58	1216	0.068	4	16.5	15.6	4.8	6.2	13.2
103090.9	0.68	1216	0.068	3	19.3	15.6	4.8	6.2	9.9
103090.10	0.77	1216	0.068	36	21.9	15.6	4.8	6.2	118.6
103090.11	0.87	1216	0.068	294	24.7	15.6	4.8	6.2	968.3
103090.12	0.48	1216	0.069	11	13.6	18.8	4.8	6.2	43.7
103090.13	0.58	1216	0.067	10	16.5	18.8	4.8	6.2	39.7
103090.14	0.67	1216	0.067	55	19.0	18.8	4.8	6.2	218.3
103090.15	0.77	1216	0.067	232	21.9	18.8	4.8	6.2	920.9
103090.16	0.87	1217	0.067	breakup	24.7	18.8	4.8	6.2	breakup

NF-10000 reported new perforations

trial number	Uo (m/s)	center x (cm)	area corr. perfs.	reported new perfs.
103090.1	13.6	10	0.0	0
103090.7	13.6	15.6	16.5	16.5
103090.12	13.6	18.8	43.7	27.2
103090.2	16.7	10	0.0	0
103090.8	16.5	15.6	13.2	13.2
103090.13	16.5	18.8	39.7	26.5
103090.3	19.3	10	0.0	0
103090.9	19.3	15.6	9.9	9.9
103090.14	19.0	18.8	218.3	208.4
103090.6	21.9	10	6.3	6.3
103090.10	21.9	15.6	118.6	112.3
103090.15	21.9	18.8	920.9	802.3
103090.5	24.7	10	31.7	31.7
103090.11	24.7	15.6	968.3	936.6
103090.16	24.7	18.8	breakup	breakup

Perforation count experiments (NF-10000)

trial number	inviscid thick (um) 2h(xp)	Rejet	viscous thick* 2h(xp)	D.S. thick** 2h (um)	linear regr* Us(m/s)
103090.1	181	1300	690	175	3.6
103090.2	181	1700	599	152	5.1
103090.3	181	2000	550	140	6.4
103090.4	no data				
103090.5	181	2600	482	122	9.3
103090.6	181	2400	505	128	7.8
103090.7	181	1400	653	106	3.8
103090.8	181	1800	579	94	5.2
103090.9	181	2100	535	87	6.5
103090.10	181	2400	505	82	7.8
103090.11	181	2700	480	78	9.3
103090.12	181	1500	648	88	3.8
103090.13	181	1800	574	78	5.2
103090.14	181	2100	534	72	6.5
103090.15	181	2400	502	68	7.9
103090.16	181	2500	496	67	8.2

(*) calculated from the two-term linear regression equation

(**) downstream sheet thickness at the center of the imaging area

APPENDIX D: DERIVATION OF BOUNDARY LAYER EQUATIONS

A boundary layer velocity was assumed in the development of several correlative equations. These expressions will be derived in this appendix.

Sheet thickness ratio in the developing boundary layer region ($x \leq x_t$).

The sheet thickness in the developing boundary layer region was given as

$$2h(x) = \frac{d_0^2}{8x} + \left(1 - \frac{2\pi}{3\sqrt{3}c^2}\right)\delta, \tag{D1}$$

where:

$$\delta^2 = \left(\frac{\pi\sqrt{3}c^3}{\pi - c\sqrt{3}}\right)\left(\frac{\upsilon_{liq}\, x d_0^2}{4Q\,\rho_{liq}}\right), \tag{D2}$$

with:

- c = constant = 1.402;
- d_0 = orifice diameter [m];
- $2h$ = sheet thickness [m];
- Q = volumetric flow rate [m^3/s];
- x = radial position downstream [m];
- d = boundary layer thickness [m];
- μ_{liq} = liquid viscosity [kg/m·s]; and
- ρ_{liq} = liquid density [kg/m3].

The sheet thickness expression is modified by dividing through by the inviscid sheet thickness,

$$2h_* = \frac{d_0^2}{8x}, \tag{D3}$$

and substituting in the definitions for the boundary layer thickness, δ, and the volumetric flow rate,

$$Q = \frac{\pi\, d_0^2 U_0}{4}, \tag{D4}$$

where U_0 is the average jet velocity in meters per second, that is

$$\frac{2h(x)}{2h_*} = 1.0 + \frac{8x}{d_0^2}\left(1 - \frac{2\pi}{3\sqrt{3}c^2}\right)\left(\frac{\pi\sqrt{3}c^3}{\pi - c\sqrt{3}}\right)^{1/2}\left(\frac{\upsilon_{liq}\, x}{\pi U_0\, \rho_{liq}}\right)^{1/2}. \tag{D5}$$

This expression is further reduced by combining all the constants, thus obtaining

$$\frac{2h(x)}{2h_*} = 1.0 + \left(\frac{7.964\, x}{d_0^2}\right)\left(\frac{\upsilon_{liq}\, x}{U_0\, \rho_{liq}}\right)^{1/2}. \tag{D6}$$

This expression can be simplified by substituting in the definition of the jet Reynolds number,

$$Re_{jet} = \frac{\rho_{liq}\, d_0 U_0}{\mu_{liq}}, \tag{D7}$$

thus obtaining the final form of the expression for the sheet thickness ratio in the developing boundary layer region

$$\frac{2h(x)}{2h_*(x)} = 1.0 + \left(\frac{7.964}{Re_{jet}^{1/2}}\right)\left(\frac{x}{d_0}\right)^{3/2}. \tag{D8}$$

<u>Sheet thickness ratio in the fully-developed boundary layer region</u> ($x > x_t$).

The sheet thickness in the fully-developed boundary layer region was given as

$$2h(x) = \left(\frac{2\pi^2}{3\sqrt{3}}\right)\left(\frac{\mu_{liq}(x^3 + \Gamma^3)}{\rho_{liq}\, Qx}\right), \tag{D9}$$

where the characteristic length scale, Γ, is given by

$$\Gamma = 0.567\frac{d_0}{2}Re_{Watson}^{1/3}. \tag{D10}$$

The Reynolds number in this expression is defined as

$$Re_{Watson} = \frac{Q\,\rho_{liq}}{\mu_{liq}(d_0/2)} = \frac{\pi}{2}\left(\frac{\rho_{liq}\,d_0U_0}{\mu_{liq}}\right),$$

$$Re_{Watson} = \left(\frac{\pi}{2}\right)Re_{jet}. \qquad (D11)$$

Upon making this substitution, the characteristic length scale is given by

$$\Gamma = 0.33d_0Re_{jet}^{1/3}, \qquad (D12)$$

and the sheet thickness equation becomes

$$2h(x) = \left(\frac{2\pi^2}{3\sqrt{3}}\right)\left(\frac{\mu_{liq}(x^3 + 0.036Re_{jet}d_0^3)}{\rho_{liq}\,Qx}\right). \qquad (D13)$$

Upon dividing this expression by the inviscid sheet thickness equation and substituting for the definition of the volumetric flow rate, an expression for the sheet thickness ratio is obtained, that is

$$\frac{2h(x)}{2h_*(x)} = 1.39 + \frac{38.7}{Re_{jet}}\left(\frac{x}{d_0}\right)^3. \qquad (D14)$$

Average velocity expressions for the fully-developed boundary layer region.

The velocity profile in the fully-developed boundary layer region is given by

$$U(x,z) = U_{max}(x)f(z/2h). \qquad (D15)$$

This expression can be substituted into the equation for the arithmetic mean velocity,

$$U_{s,avg} = \frac{\int_{z=0}^{z=2h} U(x_p,z)dz}{\int_{z=0}^{z=2h} dz}, \tag{D16}$$

to obtain

$$U_{s,avg}(x) = \frac{\int_{z=0}^{z=2h(x)} U_{max}(x)f(z/2h(x))dz}{\int_{z=0}^{z=2h(x)} dz}. \tag{D17}$$

Using the substitutions $\eta = z/2h(x)$ and $2h(x)d\eta = dz$, this expression reduces to

$$U_{s,avg}(x) = \frac{U_{max}(x)\int_{\eta=0}^{\eta=1} f(\eta)d\eta}{\int_{\eta=0}^{\eta=1} d\eta}. \tag{D18}$$

The integral appearing in the numerator of this expression was given by Watson[35] as

$$\int_{\eta=0}^{\eta=1} f(\eta)d\eta = \frac{2\pi}{3\sqrt{3}c^2} = 0.615; \tag{D19}$$

therefore, the expression for the arithmetic average sheet velocity becomes

$$U_{s,avg}(x) = 0.615U_{max}(x). \tag{D20}$$

The expression for the root mean square velocity was given as

$$U_{s,rms}(x) = \sqrt{\frac{\int_{z=0}^{z=2h} U^2(x_p,z)dz}{\int_{z=0}^{z=2h} dz}}. \tag{D21}$$

Substituting in the expression for the boundary layer velocity profile, the new independent variable,η, and rearranging, the root mean square velocity equation can be rewritten as

$$U_{s,rms}(x) = U_{max(}x) \sqrt{\frac{\left(\int_{\eta=0}^{\eta=1} d\eta\right)^2}{\int_{\eta=0}^{\eta=1} d\eta}}. \qquad \text{(D22)}$$

The integral appearing in the numerator was given by Watson[35] as

$$\int_{\eta=0}^{\eta=1} d\eta = \frac{2}{3c} = 0.47551; \qquad \text{(D23)}$$

therefore, the expression for the root mean square sheet velocity in the fully-developed boundary layer region is given by

$$U_{s,rms}(x) = 0.690U_{max}(x). \qquad \text{(D24)}$$

APPENDIX E: DATA FOR THE SHEET THICKNESS EXPERIMENTS

This appendix is used to summarize the raw and processed data for the sheet thickness experiments. These data are presented in the following order. Two tables are presented for each nozzle (the NF-6000, the sharp edge orifice, the QU-00120, and the QU-00200). The first table contains the operating conditions, average sheet thickness, jet Reynolds number, and the independent and dependent parameter for the linear regression. The independent parameter is $(1/Re)(x/d_0)^3$, and the dependent parameter is the sheet thickness ratio. The second table for each nozzle includes the reference and top surface positions measured by each micrometer, and the average, standard deviation, and normalized standard deviation of the probe measurements for each trial.

These tables are followed by the residual plots and the linear regression and F-test statistics.

sheet thickness experiments (nozzle NF-6000)
nozzle orifice diameter = 4.83 mm

IND = (1/Re)(x/do)^3
DEP = h/h*

trial number	mass flow (kg/s)	density (kg/m3)	viscosity (kg/ms)	2h (um)	Uo (m/s)	Reynolds number	DEP param	IND param
112191.16	0.18	1220	0.085	1111	8.6	590	8.8	0.146
112191.17	0.21	1220	0.084	863	10.3	720	6.8	0.120
112191.18	0.27	1221	0.083	737	12.8	910	5.8	0.095
112191.19	0.31	1220	0.082	652	15.1	1100	5.2	0.080
112191.20	0.36	1220	0.081	611	17.1	1200	4.8	0.070
112191.21	0.40	1220	0.080	619	19.3	1400	4.9	0.061
112191.22	0.44	1220	0.078	525	21.2	1600	4.2	0.054
112191.23	0.48	1221	0.077	484	23.1	1800	3.8	0.049
112191.24	0.52	1220	0.075	461	24.9	2000	3.6	0.044
112191.25	0.19	1219	0.073	932	9.1	730	7.4	0.119
112191.26	0.22	1219	0.073	752	10.6	860	5.3	0.101
112191.27	0.27	1219	0.073	638	13.1	1000	5.0	0.082
112191.28	0.32	1219	0.072	581	15.3	1200	4.6	0.070
112191.29	0.36	1219	0.072	538	17.3	1400	4.3	0.061
112191.30	0.40	1219	0.072	494	19.4	1600	3.9	0.055
112191.31	0.45	1219	0.071	459	21.5	1800	3.6	0.049
112191.32	0.49	1219	0.070	442	23.5	2000	3.5	0.044
112191.33	0.52	1219	0.069	433	25.2	2100	3.4	0.040

Sheet thickness measurements (nozzle NF-6000)

trial number	#1 ref. pos.	#1 top pos.	#1 2h (um)	#2 ref. pos.	#2 top pos.	#2 2h (um)	#3 ref. pos.	#3 top pos.	#3 2h (um)	avg 2h (um)	std dev (um)	norm std dev
112191.16	598.8	641.9	1094.7	128.3	175.2	1191.3	146.4	187.6	1046.5	1111	74	0.07
112191.17	598.9	633.7	883.9	138.2	170.6	823.0	126.1	160.7	878.8	862	34	0.04
112191.18	598.8	628.2	746.8	138.2	165.3	688.3	125.9	156.5	777.2	737	45	0.06
112191.19	597.2	623.9	678.2	136.5	161.2	627.4	127.3	152.9	650.2	652	25	0.04
112191.20	596.9	621.9	635.0	137.1	159.4	566.4	129.7	154.6	632.5	611	39	0.06
112191.21	597.0	620.2	589.3	136.0	156.7	525.8	136.1	165.3	741.7	619	111	0.18
112191.22	597.3	618.3	533.4	136.4	154.9	469.9	141.4	163.9	571.5	525	51	0.10
112191.23	597.8	617.0	487.7	136.8	154.3	444.5	141.5	162.0	520.7	484	38	0.08
112191.24	596.6	613.9	439.4	136.2	153.1	429.3	139.3	159.6	515.6	461	47	0.10
112191.25	595.7	634.4	983.0	139.6	173.2	853.4	121.3	159.1	960.1	932	69	0.07
112191.26	598.5	628.7	767.1	139.6	169.6	762.0	126.1	154.7	726.4	752	22	0.03
112191.27	598.2	623.7	647.7	141.2	166.2	635.0	127.0	151.9	632.5	638	8	0.01
112191.28	597.8	622.2	619.8	140.6	162.4	553.7	126.4	148.8	569.0	581	35	0.06
112191.29	597.7	619.7	558.8	138.8	160.2	543.6	126.5	146.7	513.1	538	23	0.04
112191.30	598.3	618.9	523.2	139.4	158.2	477.5	126.4	145.3	480.1	494	26	0.05
112191.31	597.6	616.2	472.4	140.2	157.1	429.3	126.9	145.6	475.0	459	26	0.06
112191.32	596.4	614.0	447.0	138.8	155.8	431.8	128.4	146.0	447.0	442	9	0.02
112191.33	594.1	612.1	457.2	137.6	154.3	424.2	143.5	159.9	416.6	433	22	0.05

note: thickness in microns is equal to 25.4*(top - ref)

sheet thickness experiments (sharp edge orifice)
nozzle orifice diameter = 6.36 mm

IND = (1/Re)(x/do)^3
DEP = h/h*

trial number	mass flow (kg/s)	density (kg/m3)	viscosity (kg/ms)	2h (um)	Uo (m/s)	Reynolds number	DEP param	IND param
61191.17	0.59	1214	0.062	534	15.4	1900	2.3	0.020
61191.18	0.66	1213	0.059	510	17.1	2200	2.2	0.017
61191.19	0.66	1212	0.057	464	17.2	2300	2.0	0.017
61191.20	0.73	1212	0.056	446	19.0	2600	1.9	0.015
61191.21	0.23	1211	0.053	765	5.9	860	3.2	0.044
61191.22	0.52	1212	0.054	592	13.5	1900	2.5	0.020
61191.23	0.44	1212	0.054	575	11.5	1600	2.4	0.024
61191.24	0.59	1212	0.053	522	15.4	2200	2.2	0.017
61191.25	0.37	1212	0.053	612	9.7	1400	2.6	0.027
61191.26	0.23	1211	0.051	757	5.9	880	3.2	0.043
61191.27	0.73	1211	0.053	513	19.2	2800	2.2	0.014
61191.28	0.44	1211	0.052	569	11.5	1700	2.4	0.022
61191.29	0.37	1212	0.052	602	9.7	1400	2.6	0.027
61191.30	0.30	1211	0.051	661	7.8	1200	2.8	0.032
61191.31	0.30	1212	0.051	652	7.8	1200	2.8	0.032
61191.32	0.52	1212	0.051	542	13.5	2000	2.3	0.019
61491.1	0.45	1215	0.067	645	11.7	1300	2.7	0.029
61491.2	0.59	1213	0.060	537	15.3	2000	2.3	0.019
61491.3	0.44	1213	0.058	593	11.4	1500	2.5	0.025
61491.4	0.60	1213	0.056	555	15.6	2100	2.3	0.018
61491.5	0.44	1212	0.055	584	11.4	1600	2.5	0.024

Sheet thickness measurements (sharp edge orifice nozzle)

trial number	ref. pos.	#1 top pos.	2h (um)	ref. pos.	#2 top pos.	2h (um)	ref. pos.	#3 top pos.	2h (um)	avg 2h (um)	std dev (um)	norm std dev
61191.17	-7.0	16.0	584.2	-3.6	15.8	492.8	-1.2	19.5	525.8	534	46	0.09
61191.18	-7.5	13.0	520.7	-6.2	15.8	558.8	-0.8	16.9	449.6	510	55	0.11
61191.19	-6.8	13.6	518.2	-5.5	12.3	452.1	-0.1	16.5	421.6	464	49	0.11
61191.20	-7.6	11.9	495.3	-7.6	8.9	419.1	-1.9	14.8	424.2	446	43	0.10
61191.21	-3.2	27.1	769.6	-3.1	29.5	828.0	2.5	29.9	696.0	765	66	0.09
61191.22	-5.5	16.9	569.0	-6.6	18.6	640.1	-1.1	21.2	566.4	592	42	0.07
61191.23	-4.1	18.3	569.0	-2.5	19.9	569.0	-0.3	22.8	586.7	575	10	0.02
61191.24	-6.5	14.4	530.9	-3.4	15.9	490.2	-1.7	19.7	543.6	522	28	0.05
61191.25	-4.0	19.5	596.9	-2.0	22.2	614.7	-0.7	23.9	624.8	612	14	0.02
61191.26	-2.3	26.7	736.6	-2.0	28.6	777.2	1.0	30.8	756.9	757	20	0.03
61191.27	-6.6	13.3	505.5	-6.4	14.4	528.3	-2.8	17.0	502.9	512	14	0.03
61191.28	-3.9	18.2	561.3	-3.2	18.2	543.6	0.5	24.2	602.0	569	30	0.05
61191.29	-2.9	21.4	617.2	-2.7	20.2	581.7	2.0	25.9	607.1	602	18	0.03
61191.30	-2.7	24.5	690.9	-2.3	23.1	645.2	0.5	26.0	647.7	661	26	0.04
61191.31	-2.8	23.8	675.6	-2.2	23.0	640.1	1.6	26.8	640.1	652	21	0.03
61191.32	-5.0	15.7	525.8	-3.6	17.0	523.2	-2.8	19.9	576.6	542	30	0.06

note: thickness in microns is equal to 25.4*(top - ref)

trial number	#1 ref. pos.	#1 top pos.	#1 2h (um)	#2 ref. pos.	#2 top pos.	#2 2h (um)	#3 ref. pos.	#3 top pos.	#3 2h (um)	avg 2h (um)	std dev (um)	cum. avg. (um)	cum. std. dev	cum. norm dev
61491.1-A	500.0	525.7	652.8	438.5	466.7	716.3	498.3	523.4	637.5	669	42	645	46	0.07
61491.1-B	500.8	524.1	591.8	438.1	464.7	675.6	499.3	522.8	596.9	621	47			
61491.2-A	499.0	520.0	533.4	438.1	459.4	541.0	498.1	517.8	500.4	525	22	537	23	0.04
61491.2-B	498.1	519.4	541.0	436.5	458.7	563.9	497.3	518.6	541.0	549	13			
61491.3-A	500.9	525.0	612.1	440.9	465.2	617.2	500.9	522.1	538.5	589	44	593	29	0.05
61491.3-B	500.4	524.2	604.5	440.0	463.5	596.9	498.0	521.1	586.7	596	9			
61491.4-A	499.0	520.0	533.4	439.1	463.0	607.1	497.6	519.1	546.1	562	39	555	33	0.06
61491.4-B	498.5	519.5	533.4	438.4	459.5	535.9	495.2	517.7	571.5	547	21			
61491.5-A	500.6	523.7	586.7	441.2	465.0	604.5	499.2	521.4	563.9	585	20	584	21	0.04
61491.5-B	499.0	522.4	594.4	440.7	464.2	596.9	500.3	522.3	558.8	583	21			

note: thickness in microns is equal to 25.4*(top - ref)

sheet thickness experiments (nozzle QU-00120)
nozzle orifice diameter = 6.556 mm

IND = (1/Re)(x/do)^3
DEP = h/h*

trial number	mass flow (kg/s)	density (kg/m3)	viscosity (kg/ms)	2h (um)	Uo (m/s)	Reynolds number	DEP param	IND param
112191.1	0.23	1223	0.102	1164	5.6	440	4.6	0.079
112191.2	0.32	1223	0.100	944	7.7	620	3.8	0.056
112191.3	0.45	1222	0.097	819	10.9	900	3.3	0.038
112191.4	0.54	1223	0.096	839	13.0	1100	3.3	0.032
112191.5	0.61	1222	0.094	735	14.9	1300	2.9	0.027
112191.6	0.69	1222	0.091	659	16.8	1500	2.6	0.024
112191.7	0.75	1221	0.090	630	18.1	1600	2.5	0.022
112191.8	0.75	1221	0.092	647	18.3	1600	2.6	0.022
112191.9	0.69	1221	0.090	754	16.8	1500	3.0	0.023
112191.10	0.62	1220	0.088	701	15.1	1400	2.8	0.025
112191.11	0.54	1220	0.087	708	13.0	1200	2.8	0.029
112191.12	0.45	1220	0.085	679	10.9	1000	2.7	0.034
112191.13	0.33	1219	0.082	860	8.0	780	3.4	0.045
112191.14	0.24	1219	0.079	1002	5.8	590	4.0	0.059

Sheet thickness measurements (nozzle QU-00120)

trial number	#1 ref. pos.	#1 top pos.	#1 2h (um)	#2 ref. pos.	#2 top pos.	#2 2h (um)	#3 ref. pos.	#3 top pos.	#3 2h (um)	avg 2h (um)	std dev (um)	norm std dev
112191.1	553.0	601.5	1231.9	101.2	146.2	1143.0	169.4	213.4	1117.6	1164	60	0.05
112191.2	556.0	594.5	977.9	104.0	138.6	878.8	167.0	205.4	975.4	944	56	0.06
112191.3	554.2	586.0	807.7	98.9	131.1	817.9	166.5	199.2	830.6	819	11	0.01
112191.4	550.0	583.0	838.2	97.1	128.0	784.9	160.5	195.7	894.1	839	55	0.07
112191.5	552.3	581.6	744.2	98.3	125.0	678.2	163.0	193.8	782.3	735	53	0.07
112191.6	549.5	578.5	736.6	99.6	121.5	556.3	143.2	170.1	683.3	659	93	0.14
112191.7	550.5	578.2	703.6	99.2	118.6	492.8	145.0	172.3	693.4	630	119	0.19
112191.8	550.0	577.2	690.9	93.0	115.0	558.8	164.0	191.2	690.9	647	76	0.12
112191.9	548.8	578.2	746.8	93.8	122.3	723.9	161.9	193.0	789.9	754	34	0.04
112191.10	554.8	580.5	652.8	99.8	124.2	619.8	166.3	199.0	830.6	701	113	0.16
112191.11	555.7	582.6	683.3	100.8	127.8	685.8	167.2	196.9	754.4	708	40	0.06
112191.12	557.7	586.4	729.0	102.0	131.5	749.3	169.2	191.2	558.8	679	105	0.15
112191.13	557.3	593.0	906.8	104.5	136.4	810.3	169.3	203.3	863.6	860	48	0.06
112191.14	557.4	596.9	1003.3	104.3	144.1	1010.9	169.8	208.9	993.1	1002	9	0.01

note: thickness in microns is equal to 25.4*(top - ref)

sheet thickness experiments (nozzle QU-00200)
nozzle orifice diameter = 8.448 mm

IND = (1/Re)(x/do)^3
DEP = h/h*

trial number	mass flow (kg/s)	density (kg/m3)	viscosity (kg/ms)	2h (um)	Uo (m/s)	Reynolds number	DEP param	IND param
121091.1	0.20	1222	0.095	1403	3.0	320	3.4	0.050
121091.2	0.27	1222	0.095	1216	4.0	440	2.9	0.037
121091.3	0.30	1220	0.090	1139	4.4	510	2.7	0.032
121091.4	0.42	1221	0.089	982	6.1	700	2.4	0.023
121091.5	0.48	1221	0.087	940	7.0	830	2.3	0.020
121091.6	0.58	1220	0.086	889	8.4	1000	2.1	0.016
121091.7	0.72	1220	0.086	876	10.6	1300	2.1	0.013
121191.1	0.24	1223	0.096	1322	3.6	380	3.2	0.042
121191.2	0.39	1222	0.095	1101	5.6	610	2.6	0.027
121191.3	0.53	1221	0.093	1017	7.8	860	2.4	0.019
121191.4	0.70	1221	0.092	941	10.3	1200	2.3	0.014
121191.5	0.83	1221	0.090	857	12.2	1400	2.1	0.012
121191.6	0.64	1221	0.090	932	9.3	1100	2.2	0.015
121191.7	0.71	1220	0.089	898	10.4	1200	2.2	0.013
121191.8	0.76	1221	0.087	854	11.1	1300	2.1	0.012
121191.9	0.81	1220	0.086	821	11.9	1400	2.0	0.011
121191.10	0.86	1219	0.085	816	12.6	1500	2.0	0.011

Sheet thickness measurements (nozzle QU-00200)

trial number	#1 ref. pos.	#1 top pos.	#1 2h (um)	#2 ref. pos.	#2 top pos.	#2 2h (um)	#3 ref. pos.	#3 top pos.	#3 2h (um)	avg 2h (um)	std dev (um)	norm std dev
121091.1	583.9	640.7	1442.7	25.6	80.3	1389.4	280.4	334.6	1376.7	1403	35	0.02
121091.2	585.4	632.9	1206.5	25.9	73.8	1216.7	279.7	327.9	1224.3	1216	9	0.01
121091.3	585.8	630.2	1127.8	25.9	71.5	1158.2	280.9	325.4	1130.3	1139	17	0.01
121091.4	585.5	624.5	990.6	26.3	64.8	977.9	281.8	320.3	977.9	982	7	0.01
121091.5	585.6	622.9	947.4	27.5	65.4	962.7	281.9	317.7	909.3	940	27	0.03
121091.6	585.0	618.8	858.5	28.6	65.8	944.9	281.3	315.3	863.6	889	48	0.05
121091.7	582.2	619.0	934.7	30.3	63.2	835.7	277.2	311.0	858.5	876	52	0.06
121191.1	582.4	635.7	1353.8	36.3	87.5	1300.5	279.2	330.9	1313.2	1322	28	0.02
121191.2	583.3	626.7	1102.4	36.7	79.3	1082.0	276.2	320.2	1117.6	1101	18	0.02
121191.3	582.2	622.8	1031.2	37.3	78.2	1038.9	276.7	315.3	980.4	1017	32	0.03
121191.4	580.4	619.3	988.1	41.7	75.3	853.4	272.3	311.0	983.0	941	76	0.08
121191.5	579.9	615.7	909.3	42.8	75.4	828.0	276.6	309.4	833.1	857	46	0.05
121191.6	580.4	620.4	1016.0	44.9	78.2	845.8	275.9	312.7	934.7	932	85	0.09
121191.7	581.6	619.4	960.1	42.9	77.3	873.8	277.4	311.3	861.1	898	54	0.06
121191.8	581.9	616.3	873.8	44.8	79.0	868.7	280.4	312.7	820.4	854	29	0.03
121191.9	580.7	614.8	866.1	48.2	79.4	792.5	280.6	312.3	805.2	821	39	0.05
121191.10	580.7	615.4	881.4	48.3	78.0	754.4	277.7	309.7	812.8	816	64	0.08

note: thickness in microns is equal to 25.4*(top - ref)

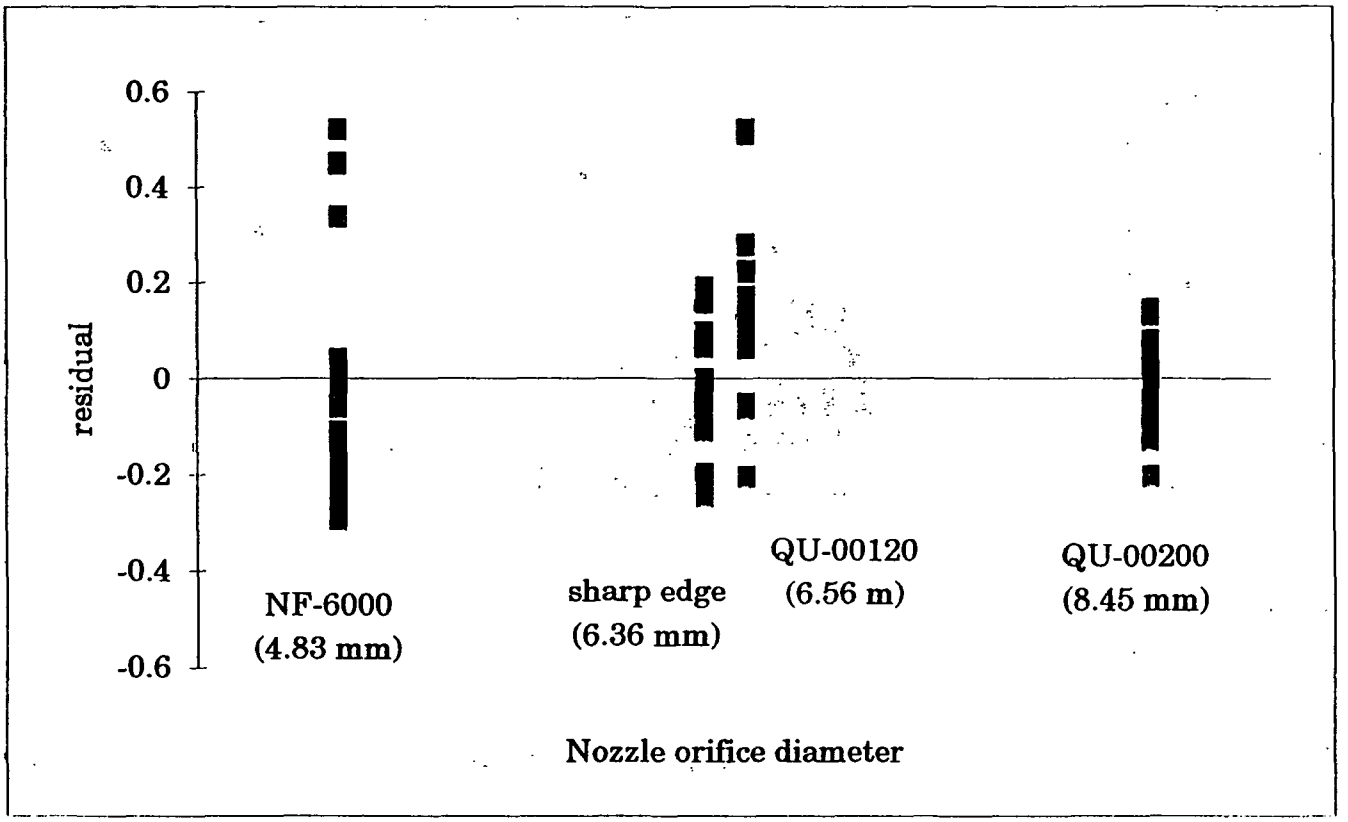
0.6
0.4
0.2
0
-0.2
-0.4
-0.6
residual
NF-6000
(4.83 mm)
sharp edge
(6.36 mm)
QU-00120
(6.56 m)
QU-00200
(8.45 mm)
Nozzle orifice diameter

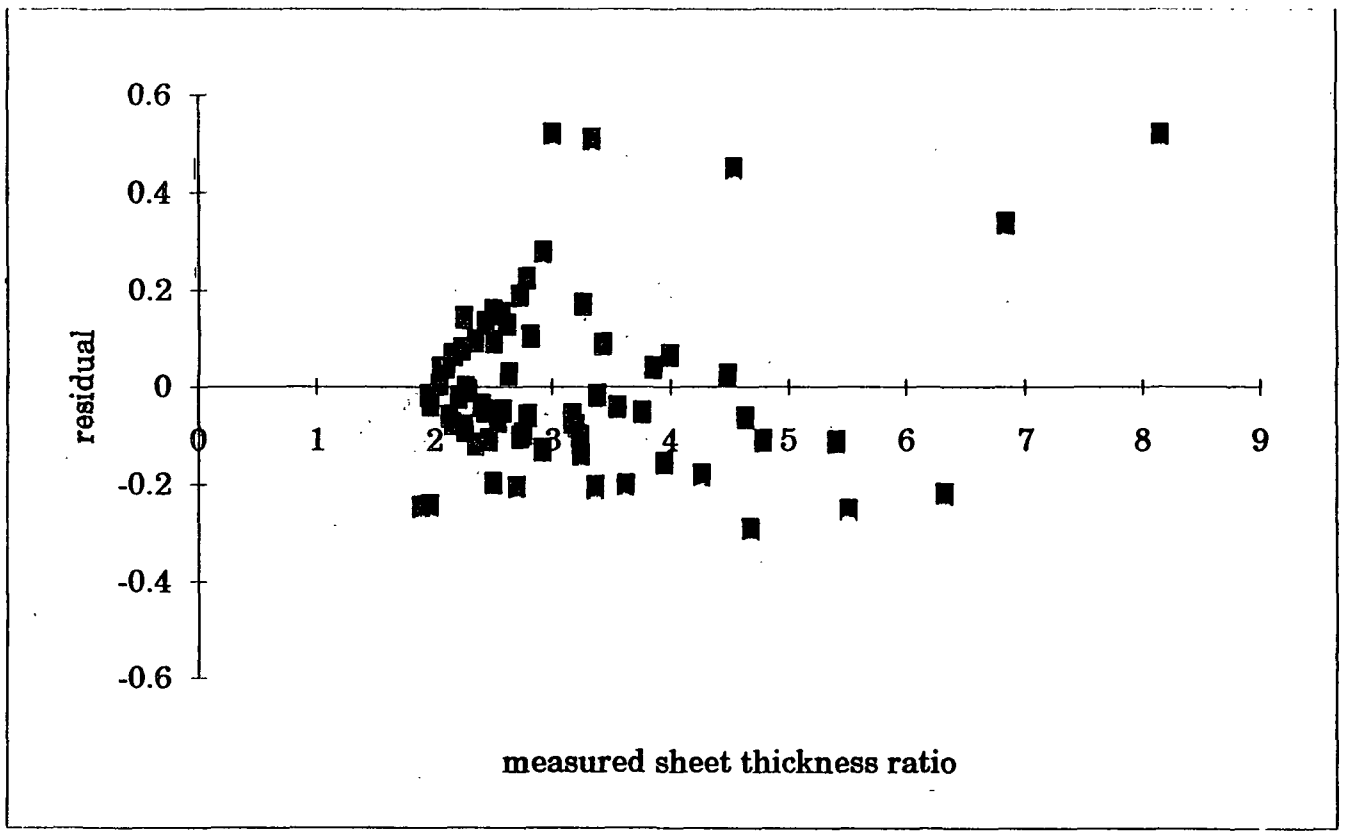
0.6
0.4
0.2
0
-0.2
-0.4
-0.6
residual
0
1
2
3
4
5
6
7
8
9
measured sheet thickness ratio

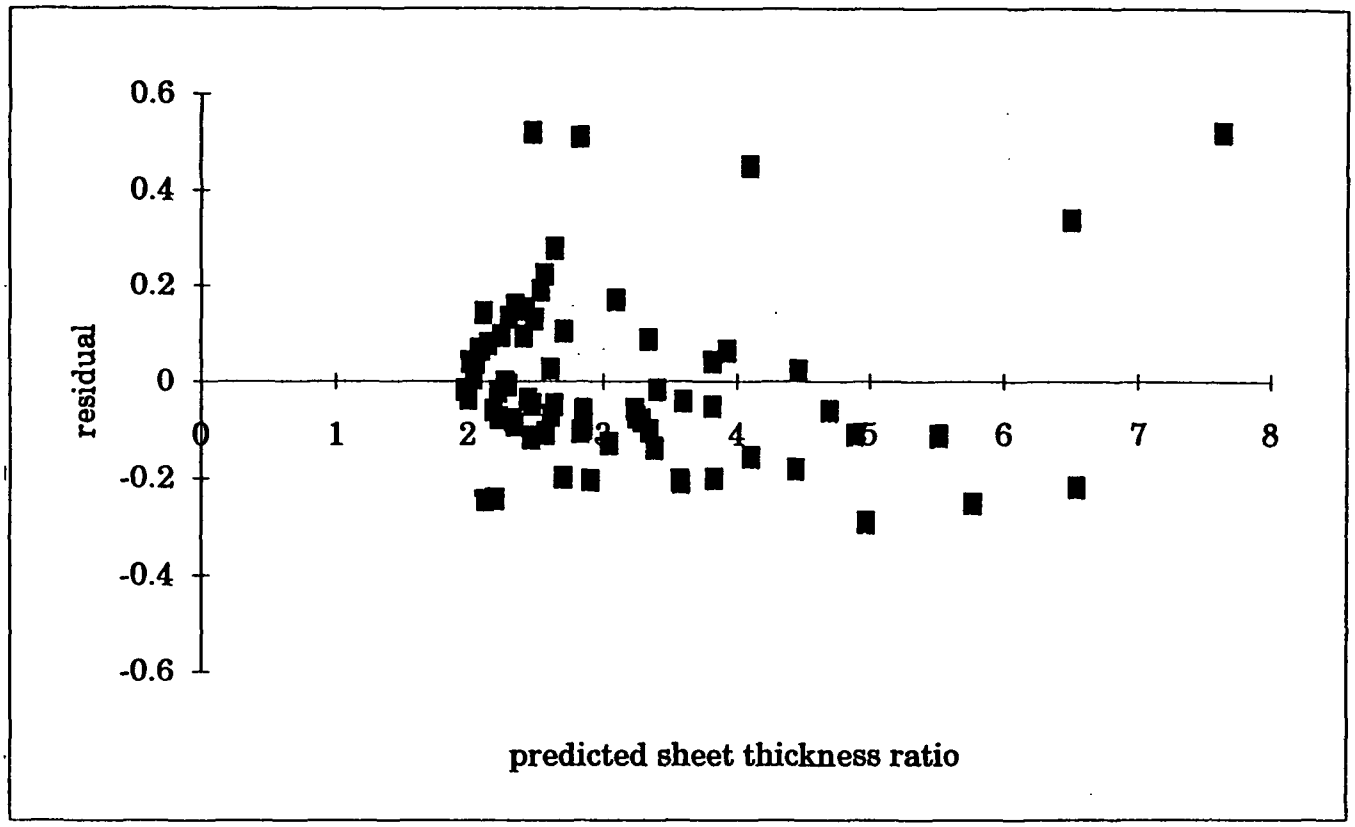
0.6
0.4
0.2
0
-0.2
-0.4
-0.6
residual
0
1
2
3
4
5
6
7
8
predicted sheet thickness ratio

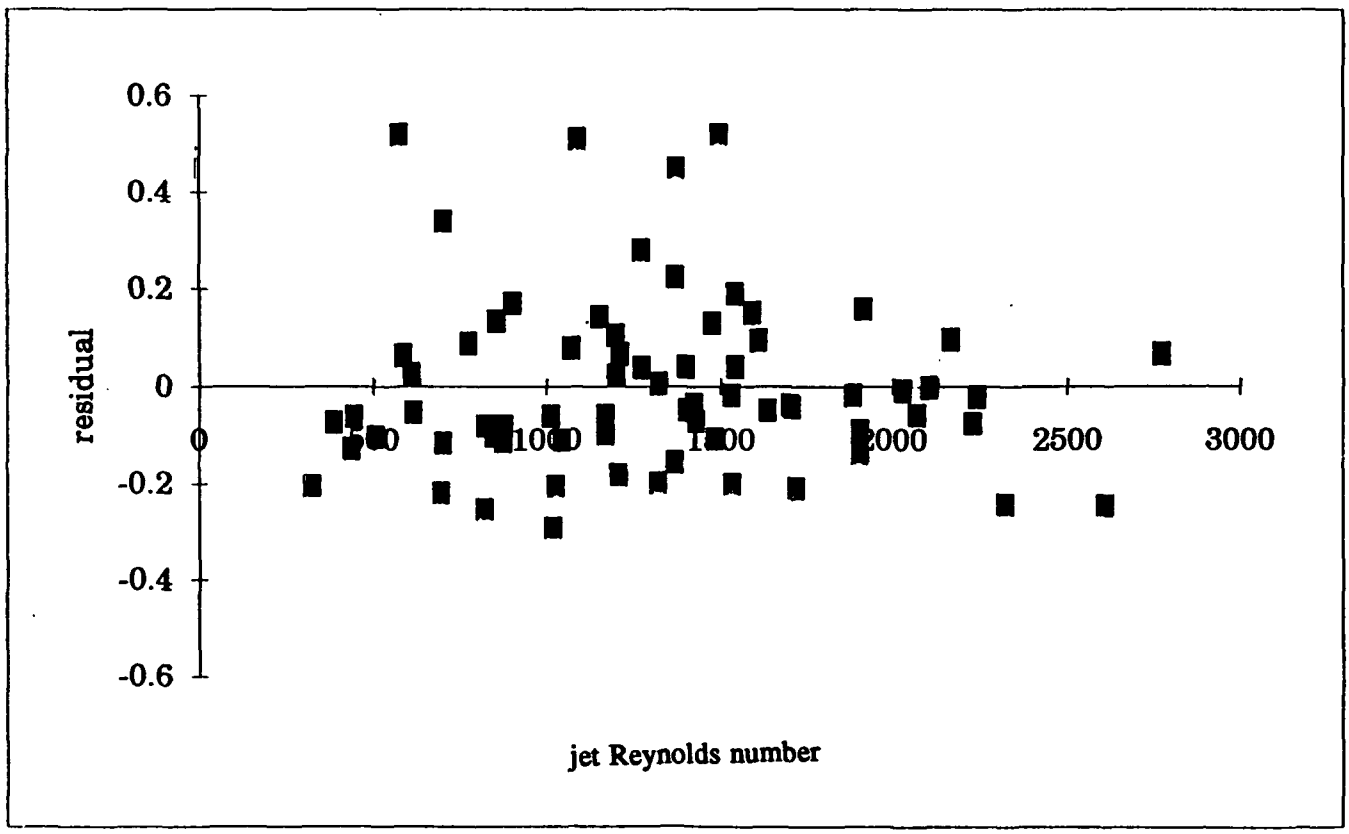
0.6
0.4
0.2
0
-0.2
-0.4
-0.6
residual
0
1000
2000
2500
3000
jet Reynolds number

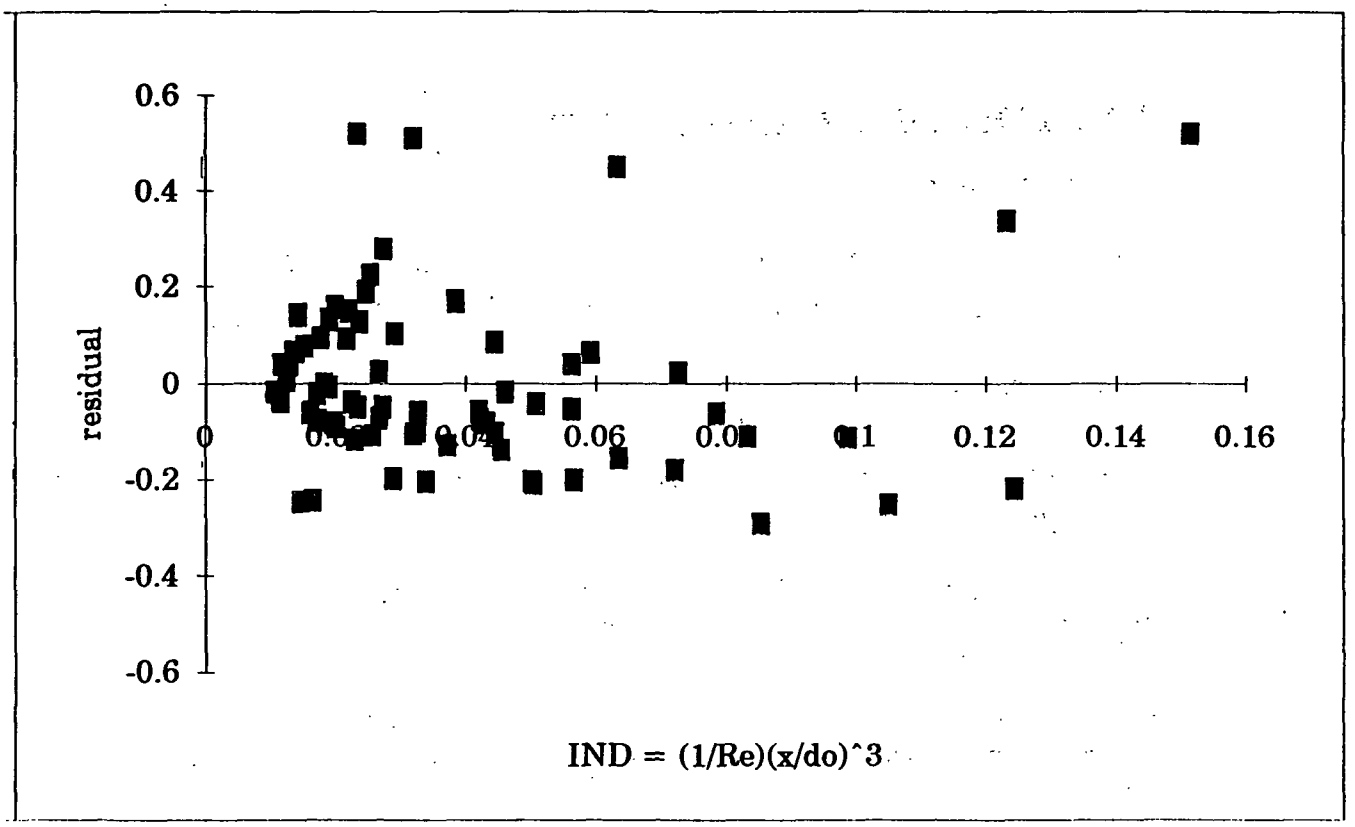
0.6
0.4
0.2
0
-0.2
-0.4
-0.6
residual
0
0.06
0.12
0.14
0.16
IND = (1/Re)(x/do)^3

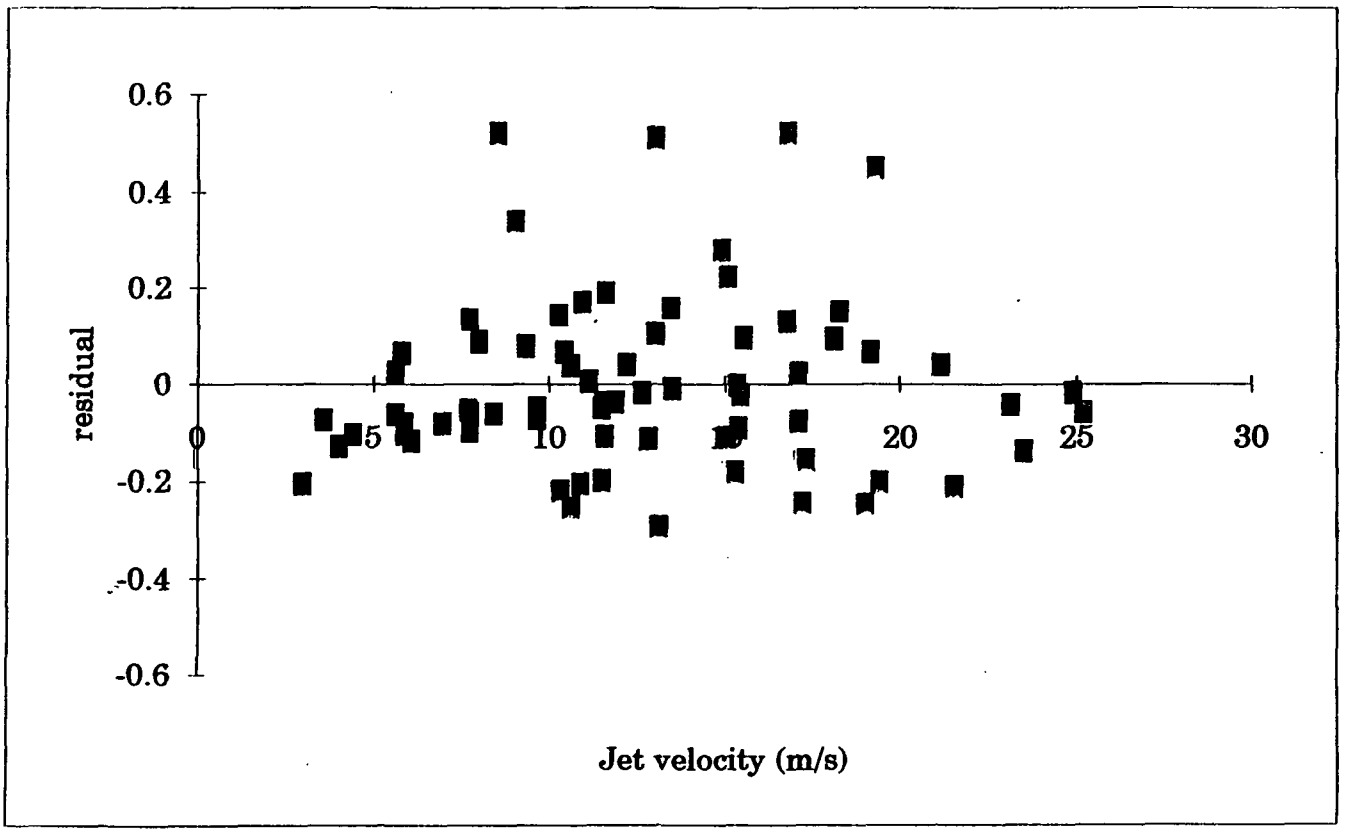
0.6
0.4
0.2
0
-0.2
-0.4
-0.6
residual
0
5
10
20
25
30
Jet velocity (m/s)

TEST OF THE LINEAR REGRESSION MODEL

N = 70 data points

$\alpha = 0.05$ (95% confidence level) $\quad t(1-\alpha/2,N) = t(0.975,70) = 2.0$

$k = 1$ for a two-term correlation $\quad F(1-\alpha,k,N-k-1]) = F(0.95,1,68) = 3.99$

regression equation: $\frac{h}{h^*} = C_0 + \frac{C_1}{Re_{jet}}\left(\frac{x}{d_0}\right)^3$

$C_0 = 1.55 \pm 0.08$ (95% confidence interval) $\quad C_1 = 40.2 \pm 1.4$

$r^2 = 0.978$

	SS	dF	MS	Fcalc
regression	98.46	1	98.46	2988
residual	2.24	68	0.033	

Because Fcalc is greater than F(0.95,1,68), a linear relationship between the sheet thickness ratio and $(1/Re_{jet})(x/d_0)^3$ cannot be rejected at the 95% confidence level.

TEST OF THE SIGNIFICANCE OF THE NOZZLE ORIFICE DIAMETER

k = 2 for a three-term model $F(1-\alpha,k,N-k-1]) = F(0.95,2,67) = 3.14$

regression equation: $\frac{h}{h^*} = \frac{U_0}{U_s} = C_0 + \frac{C_1}{Re_{jet}}\left(\frac{x}{d_0}\right)^\beta + C_2(d_0)$

$C_0 = 1.5 \pm 0.3$ (95% confidence interval) $C_1 = 40 \pm 2$
$C_2 = 10 \pm 40$ $r^2 = 0.978$

	SS	dF	MS	Fcalc
regression	98.47	2	49.23	1479
residual	2.23	67	0.033	

$SS_{reg}(C_2|C_1) = SS_{reg}(C_1 \text{ and } C_2) - SS_{reg}(C_1) = 0.01$
$F(C_2|C_1) = SS_{reg}(C_2|C_1)/ME_{res}(C_1 \text{ and } C_2) = 0.303$

Because $F(C_2|C_1)$ is less than $F_{crit}(0.95,2,67)$, the addition of a term linear in the nozzle orifice diameter can be rejected at the 95% confidence level. Also, the uncertainty limits applied to the coefficient on the d_0 term include the value $C_2 = 0.0$, thus a regression including the orifice diameter term can be rejected on this basis as well.

TEST OF SIGNIFICANCE OF THE JET VELOCITY

k = 2 for a three-term model $F(1-\alpha,k,N-k-1]) = F(0.95,2,67) = 3.14$

regression equation: $\frac{h}{h^*} = \frac{U_0}{U_s} = C_0 + \frac{C_1}{Re_{jet}}\left(\frac{x}{d_0}\right)^{\beta} + C_3(U_0)$

$C_0 = 1.5 \pm 0.1$ (95% confidence interval) $C_1 = 40 \pm 1$
$C_3 = 0.002 \pm 0.008$ $r^2 = 0.978$

	SS	dF	MS	Fcalc
regression	98.462	2	49.23	1476
residual	2.240	67	0.033	

$SS_{reg}(C_2|C_1) = SS_{reg}(C_1 \text{ and } C_2) - SS_{reg}(C_1) = 0.006$
$F(C_2|C_1) = SS_{reg}(C_2|C_1)/ME_{res}(C_1 \text{ and } C_2) = 0.18$

Because $F(C_2|C_1)$ is less than $F_{crit}(0.95,2,67)$, the addition of a term linear in the jet velocity can be rejected at the 95% confidence level. Also, the uncertainty limits applied to the coefficient on the U_0 term include the value $C_3 = 0.0$, thus a regression including the jet velocity term can be rejected on this basis as well.

APPENDIX F: DATA FOR THE DOWNSTREAM VELOCITY EXPERIMENTS

This appendix contains the raw and processed data for the downstream sheet velocity experiments. The operating conditions for each trial were presented in Table 10. Four tables are included here listing the measured distance traveled, the framing rate, and the calculated velocity for each air bubble tracked. The data are grouped by the experiment number.

The statistical analysis used to reject three points in trial #61491.2 as outliers is also presented here.

Film #61491.1

series	ref. frame number	bubble number	meas. dist. (mm)	true dist. (mm)	number of steps	framing rate (FPS)	calc. Us (m/s)
A	700	1	175.5	25.9	28	4375	4.1
A	751	2	172	25.4	26	4375	4.3
A	774	3	27	4.0	4	4286	4.3
A	779	4	81	12.0	13	4286	3.9
A	815	5	156	23.1	23	4000	4.0
A	826	6	134	19.8	19	3846	4.0
B	659	1	141	21.7	16	2885	3.9
B	665	2	56	8.6	7	3182	3.9
B	662	3	114	17.5	13	3043	4.1
B	713	4	126	19.4	21	4375	4.0
B	747	5	82	12.6	14	4412	4.0
B	660	6	78	12.0	9	2913	3.9
B	675	7	186	28.6	26	3611	4.0
B	691	8	133	20.5	22	4167	3.9
B	666	9	110	16.9	14	3214	3.9
B	695	10	26	4.0	4	4286	4.3

Film #61491.2

series	ref. frame number	bubble number	meas. dist. (mm)	true dist. (mm)	number of steps	framing rate (FPS)	calc. Us (m/s)
A	914	1*	162	24.0	13	2000	3.7
A	974	2*	214	31.7	13	4333	10.6
A	976	3*	234	34.7	18	4375	8.4
A	978	4	113	16.7	12	4375	6.1
A	980	5	207	30.7	20	4375	6.7
A	994	6	171	25.3	17	4412	6.6
A	1009	7	159	23.6	16	4412	6.5
B	921	1	109	16.1	6	2500	6.7
B	918	2	153	22.6	8	2292	6.5
B	924	3	114	16.8	7	2647	6.4
B	937	4	171	25.3	13	3333	6.5
B	947	5	74	10.9	6	3750	6.8
B	943	6	126	18.6	10	3571	6.6
B	922	7	223	33.0	13	2647	6.7
B	931	8	186	27.5	12	3000	6.9
B	944	9	144	21.3	11	3611	7.0
B	925	10	181	26.7	11	2727	6.6
B	932	11	146	21.6	11	3076	6.0
B	940	12	96	14.2	7	3438	7.0
B	944	13	132	19.5	10	3611	7.0
B	942	14	77	11.4	6	3529	6.7

* three data points tested as outliers and rejected
the method of Tietjen and Moore(63) was used
ASTM standard #E178-80 pp. 163-4

Film #61491.4

series	ref. frame number	bubble code	meas. dist. (mm)	true dist. (mm)	number of steps	framing rate (FPS)	calc. Us (m/s)
A	572	a	135	21.0	8	2333	6.1
A	567	b	135	21.0	7	2000	6.0
A	568	c	174	27.1	8	2059	7.0
A	567	d	45	7.0	2	2000	7.0
A	568	e	112	17.5	5	2059	7.2
A	574	f	177	27.6	10	2500	6.9
A	574	g	91	14.2	5	2500	7.1
B	606	1	222	32.8	19	3947	6.8
B	605	2	129	19.1	12	3889	6.2
B	577	3	170	25.1	10	2632	6.6
B	575	4	173	25.6	9	2500	7.1
B	592	5	148	21.9	11	3333	6.6
B	622	6	203	30.0	18	4285	7.1
B	576	7	182	26.9	10	2580	6.9
B	577	8	166	24.5	9	2632	7.2
B	594	9	128	18.9	10	3462	6.5
B	593	10	184	27.2	14	3412	6.6

Film #61491.5

series	ref. frame number	bubble number	meas. dist. (mm)	true dist. (mm)	number of steps	framing rate (FPS)	calc. Us (m/s)
A	921	1	240	35.1	27	3393	4.4
A	926	2	168	24.6	20	3611	4.4
A	928	3	142	20.8	17	3696	4.5
A	928	4	125	18.3	15	3696	4.5
B	893	1	234	34.2	13	1695	4.5
B	893	2	236	34.5	13	1695	4.5
B	893	3	117	17.1	6	1695	4.8
B	894	4	254	37.2	15	1754	4.3
B	894	5	254	37.2	15	1754	4.3
B	895	6	151	22.1	9	1863	4.6
C	896	1	127	18.6	8	1923	4.5
C	896	2	141	20.6	9	1923	4.4
C	896	3	229	33.5	15	1923	4.3
C	896	4	32	4.7	2	1923	4.5
C	897	5	218	31.9	14	1923	4.4
C	897	6	92	13.5	6	1923	4.3
C	897	7	123	18.0	8	2019	4.5
C	897	8	122	17.9	8	2019	4.5
C	898	9	209	30.6	14	2019	4.4
C	899	10	230	33.7	16	2167	4.6

Analysis of potential outliers in the sheet velocity data for film #61491.1.
Following the procedure presented by Tietjen and Moore(64), the absolute residual |Us(i) - Us(avg)| was calculated for each data point. The data were ranked in order of increasing residual. Then, the k data points with the highest residuals could be checked as outliers.

The test statistic, Ek, is defined as the ratio of the sum of squares of the N-k "good" data points about the mean of those N-k points, divided by the sum of squares of all the data points about the mean of the total sample.

check the three largest residuals

E3 = sum of squares(N-3)/sum(N) =	0.0460952
Ekcrit(k=3,N=20,5%) =	0.302
Ekcrit(k=3,N=20,1%) =	0.236

since Ek < Ekcrit
reject the three points

Similarly, only the two highest residual points were tested. In this case k=2.
As shown, the two points are rejected. The remaining suspected point was tested using the T statistic as described below.

check the two largest residuals

E2 = sum(N-2)/sum(N)=	0.15409148
Ekcrit(k=2,N=20,5%) =	0.416
Ekcrit(k=2,N=20,1%) =	0.339

since Ek < Ekcrit
reject the two points

Having rejected the highest and lowest points, use Tn statistic to check the remaining one-sided outlier.
Tn = (x-xavg)/s

x =	8.43	Tcrit(N=19, 5%) =	2.532
xavg =	6.72	Tcrit(N=19, 1%) =	2.854
s =	0.49	Tn > Tcrit	
N =	19	therefore, the point can be rejected	
Tn =	3.46		

APPENDIX G: DERIVATION OF SINUOUS WAVELENGTH EQUATIONS

SHEET THINNING

In several analyses performed in this study, it was necessary to calculate the length measured along a sine wave as a function of the distance projected on the x-axis. The derivation of the appropriate equations is presented here.

The sheet is assumed to be disturbed by a single sinuous wave of amplitude, A; thus, the position of the sheet centerline relative to the undisturbed centerline ($z=0$) is given by

$$z_c = A \sin\left(\frac{2\pi x}{\lambda}\right). \tag{G1}$$

The length of a differential element of the sheet, dL, can be calculated from the geometry of the sheet as,

$$dL \approx [(dx)^2 + (dz)^2]^{1/2}. \tag{G2}$$

Since z is a function of x, dz can be determined using the chain rule, that is

$$dz = \left(\frac{\partial z}{\partial x}\right) dx, \tag{G3}$$

where

$$\left(\frac{\partial z}{\partial x}\right) = \left(\frac{2\pi A}{\lambda}\right) \cos\left(\frac{2\pi x}{\lambda}\right); \tag{G4}$$

thus,

$$dz = \left(\frac{2\pi A}{\lambda}\right)\cos\left(\frac{2\pi x}{\lambda}\right)dx. \tag{G5}$$

Equation G2 can then be written as

$$dL = \left[(dx)^2 + \left(\frac{2\pi A}{\lambda}\right)^2 \cos^2\left(\frac{2\pi x}{\lambda}\right)(dx)^2\right]^{1/2}, \text{ or}$$

$$dL = dx \times \left[1 + \left(\frac{2\pi A}{\lambda}\right)^2 \cos^2\left(\frac{2\pi x}{\lambda}\right)\right]^{1/2}. \tag{G6}$$

The total length of the sheet segment, L, is determined by integrating Eq. G6 over one wavelength of the disturbance, $x = 0$ to $x = \lambda$,

$$L = \int_{x=0}^{x=\lambda} \left[1 + \left(\frac{2\pi A}{\lambda}\right)^2 \cos^2\left(\frac{2\pi x}{\lambda}\right)\right]^{1/2} dx \tag{G7}$$

As will be shown, the resulting integral is reducible to an elliptic integral of the second kind; however, a simple numerical integration,

$$L = \sum_{x=0}^{x=\lambda} \Delta x \cdot \left[1 + \left(\frac{2\pi A}{\lambda}\right)^2 \cos^2\left(\frac{2\pi x}{\lambda}\right)\right]^{1/2}, \tag{G8}$$

can also be used. Upon examination of Eq. G7, it can be seen that the length of the sheet segment is a function of both the wavelength and the amplitude of the disturbance; thus, the sheet thickness is affected by these parameters as well.

Equation G7 can be rearranged to obtain the complete elliptic integral of the second kind, for which tabulated values are available. First, because of the symmetric properties of the sine

function, the integral can be evaluated from x=0 to x=λ/4, and the total length of the disturbed sheet then taken to be four times this value,

$$L = 4 \int_{x=0}^{x=\lambda/4} \left[1 + \left(\frac{2\pi A}{\lambda}\right)^2 \cos^2\left(\frac{2\pi x}{\lambda}\right) \right]^{1/2} dx. \qquad \text{(G9)}$$

Next, the following definitions are used to simplify the notation:

$$p = \frac{2\pi A}{\lambda}, \qquad \text{(G10)}$$

$$\hat{x} = \frac{2\pi x}{\lambda}, \qquad \text{(G11)}$$

and

$$L = 4 \int_{\hat{x}=0}^{\hat{x}=\pi/2} [1 + p^2 \cos^2 \hat{x}]^{1/2} \left(\frac{\lambda}{2\pi}\right) d\hat{x}. \qquad \text{(G12)}$$

Using the following trigonometric identity

$$\cos^2 \hat{x} = 1 - \sin^2 \hat{x}, \qquad \text{(G13)}$$

and the definition,

$$\hat{p} = \sqrt{\frac{p^2}{1 + p^2}}, \qquad \text{(G14)}$$

an expression containing the complete elliptic integral of the second kind is obtained as

$$L = \frac{2\lambda\sqrt{1 + p^2}}{\pi} \int_{\hat{x}=0}^{\hat{x}=\pi/2} [1 - \hat{p}^2 \sin^2 \hat{x}]^{1/2} \, d\hat{x} \qquad \text{(G15)}$$

This expression is further simplified by rearranging terms and using the standard notation for the complete elliptic integral, $E(\pi/2;\hat{p})$, resulting in

$$\frac{L}{\lambda} = \frac{2\sqrt{1 + p^2}}{\pi} E(\pi/2;\hat{p}), \qquad \text{(G16)}$$

where: $$E(\pi/2;\hat{p}) = \int_{\hat{x}=0}^{\hat{x}=\pi/2} [1 - \hat{p}^2 \sin^2 \hat{x}]^{1/2} \, d\hat{x}.$$

RADIAL PERFORATION GROWTH RATE

Similar equations were needed to calculate the true radial perforation growth rate as a function of the measured radial and lateral perforation growth rates. Equation G6 is used as the starting point for this derivation.

$$dL = dx \times \left[1 + \left(\frac{2\pi A}{\lambda}\right)^2 \cos^2\left(\frac{2\pi x}{\lambda}\right)\right]^{1/2} \qquad \text{(G17)}$$

The true radial length of the perforation is obtained by integrating this expression. Because the perforation was assumed to be initiated at the crest of the wave, the lower limit of integration is $\lambda/4$. The upper limit of integration is then $\lambda/4 + R_{P,meas.}$

$$R_{P,true} = L = \int_{x=\lambda/4}^{x=\lambda/4 + R_{Pmeas}} \left[1 + \left(\frac{2\pi A}{\lambda}\right)^2 \cos^2\left(\frac{2\pi x}{\lambda}\right)\right]^{1/2} dx \qquad \text{(G18)}$$

Where: $R_{P,true}$ = true radial perforation radius; and
$R_{P,meas}$ = the measured radial perforation radius.

Using the definitions of p, $\hat{p}$, and $\hat{x}$ presented previously, Eq. G18 can be rewritten as

$$R_{P,true} = L = \frac{\lambda\sqrt{1 + p^2}}{2\pi} \int_{\hat{x}=\pi/2}^{\hat{x}=\pi/2 + 2\pi R_{Pmeas}/\lambda} [1 - \hat{p}^2 \sin^2 \hat{x}]^{1/2} \, d\hat{x}. \qquad \text{(G19)}$$

APPENDIX H: FORTRAN PROGRAMS

This appendix contains listings of the various FORTRAN programs used in this study. Each program begins with a brief description of its function.

Thu Jun 04 12:21:54 1992 perf_proj.f Page 1

```
C
C         PROGRAM TO CALULATE THE PROJECTED RADIUS
C         OF A PERFORATION GROWING IN THE RAIDAL
C         DIRECTION ON A SINUOUSLY DISTURBED SHEET
C
C         FOR EACH PERFORATION, CALCULATE THE AMPLITUDE
C         OF THE OPTIMUM SINUOUS WAVE THAT CAUSES THE
C         SHEET THICKNESS TO EQUAL THE SHEET THICKNESS
C         PREDICTED FROM THE LATERAL PERFORATION GROWTH
C         RATE.  USING THIS AMPLITUDE, CALCUALTE THE
C         ACTUAL (UNPROJECTED) RADIAL SEMIAXIS LENGTH
C         DIMENSION VARIABLES AND DEFINE PARAMETERS
C
        CHARACTER FILM*10, PERF*6
        LOGICAL FIND, FAIL, ENDFILM, ENDPERF, ENDRAD
        IMPLICIT REAL (K)
        PARAMETER (PI = 3.141592654)
C
C         OPEN FILE CONTAINING RAW DATA INCLUDING
C         OPERATING CONDITIONS AND MEASURED RADIAL
C         AND LATERAL,PERFOATION GROWTH RATES
C         NOTE 'end' SIGNALS END TO FILE
C
        OPEN (88, FILE='dat_proj_2')
        ENDFILM = .FALSE.
        READ (88,*) FILM
C
C         WHERE "FILM" = FILM #
C
C         READ PARAMETERS
C
        DO WHILE (.NOT. ENDFILM)
C           SHEET VELOCITY (M/S)
          READ (88,*) US
C           GAS DENSITY (KG/M^3)
          READ (88,*) DENSGAS
C           SURFACE TENSION (KG/S^2)
          READ (88,*) SURF
C           LENGTH SCALE (M/MM)
          READ (88,*) SCALE
C           BULK SHEET THICKNESS (MICRONS)
          READ (88,*) HB2
C
C           CALCULATE OPTIMUM WAVELENGTH
C           BASED ON HAGERTY AND SHEA RESULTS
C
          WAVE = 4.0*PI*SURF/(DENSGAS*US*US)
C
C           WRITE OUT FILE PARAMETERS
C
```

```
      WRITE (6,300) FILM
      WRITE (6,350) US, DENSGAS, SURF
      WRITE (6,370) SCALE, WAVE, HB2
C
C       READ RADIUS LOOP
C
      ENDPERF = .FALSE.
      READ (88,*) PERF
      READ (88,*) HTHIN1
C
C       WHERE "PERF" = PERFORATION NUMBER
C       AND HTHIN1 = SHEET THICKNESS CALCULATED FROM
C       THE LATERAL PERFORTAION GROWTH RATE.
C
      WRITE (6,100) PERF
C
C       BEGIN LOOP ON DISTURBANCE AMPLITUDE (M)
C       CALCULATE AMPLITUDE WHICH CAUSES THE WAVE-
C       THINNED SHEET THICKNESS TO EQUAL THE SHEET
C       THICKNESS DETERMINED FROM THE LATERAL
C       PERFORATION GROWTH RATE
C
      DO WHILE (.NOT. ENDPERF)
        AMP = 0.0
        FIND = .FALSE.
        FAIL = .FALSE.
        DO WHILE (.NOT.FIND)
          AMP = AMP + 0.000025
C
C             CALCULATE PARAMETERS
C             FOR ELLIPTIC INTEGRAL CALCULATION
C
          P = 2.0*PI*AMP/WAVE
          PP = SQRT(P*P/(1.0 + P*P))
          KC2 = 1.0 - PP*PP
          KC = SQRT(KC2)
          COMPELL = CEL(KC,1.0,1.0,KC2)
          CONST = SQRT(1.0 + P*P)*WAVE/(2.0*PI)
          SHTLEN = 4.0*CONST*COMPELL
          HTHIN2 = HB2*WAVE/SHTLEN
C
C           HTHIN2 = SHEET THICKNESS FOR AMPLITUDE, AMP
C           STOP LOOP WHEN HTIN2 <= HTHIN1
C
          IF (HTHIN2 .LE. HTHIN1) FIND = .TRUE.
        END DO
        WRITE (6,600) HTHIN1, HTHIN2, 100.*AMP
        ENDRAD = .FALSE.
C
C       IF METHOD = 1, USE THE ELLIPTIC INTEGRAL METHOD
```

```
C                          FOR CALCULATING PROJECTED LENGTH
C
C           IF METHOD = 2, USE THE NUMERICAL INTEGRATION METHOD
C                          FOR CALCUALTING PROJECTED LENGTH
C
            METHOD = 2
C
            DO WHILE (.NOT. ENDRAD)
              READ (88,*) R2, Y2
C
C               R2 = RADIAL AXIS LENGTH MEASURED FROM IMAGES
C               Y2 = LATERAL AXIS LENGTH MEASURED FROM IMAGES
C
              IF (R2 .NE. 0.) THEN
               RPROJ = SCALE*(R2/2000.0)
               RACT = SCALE*(Y2/2000.0)
C
C               RPROJ = ASSUMED PROJECTED LENGTH OF PERFORATION
C                 EQUAL TO RADIAL SEMIAXIS LENGTH IN (M)
C               RACT = ASSUMED TRUE SEMIAXIS LENGTH
C                 EQUAL LATERAL SEMIAXIS IN (M)
C
               IF (METHOD .EQ.1) THEN
C
C                  ELLIPTIC INTEGRAL METHOD
C
                IF (RPROJ .LT. WAVE/4.0) THEN
                  UL = TAN(PI/2.0 - 2.0*PI*RPROJ/WAVE)
                  ELLIP2 = EL2(UL,KC,1.0,KC2)
                  RCALC = CONST*(COMPELL - ELLIP2)
                ELSEIF (RPROJ .LT. WAVE/2.0) THEN
                  UL = TAN(2.0*PI*RPROJ/WAVE - PI/2.0)
                  ELLIP2 = EL2(UL,KC,1.0,KC2)
                  RCALC = CONST*(COMPELL + ELLIP2)
                ELSEIF (RPROJ .LT. 3.0*WAVE/4.0) THEN
                  UL = TAN(3.0*PI/2.0 - 2.0*PI*RPROJ/WAVE)
                  ELLIP2 = EL2(UL,KC,1.0,KC2)
                  RCALC = CONST*(3.0*COMPELL - ELLIP2)
                ELSEIF (RPROJ .LT. WAVE) THEN
                  UL = TAN(2.0*PI*RPROJ/WAVE -3.0*PI/2.0)
                  ELLIP2 = EL2(UL,KC,1.0,KC2)
                  RCALC = CONST*(3.0*COMPELL + ELLIP2)
                ELSE
                  WRITE (6,400)
                ENDIF
                WRITE (6,150) RPROJ*100., RACT*100., RCALC*100.
               ELSE
C
C                  NUMERICAL INTEGRATION METHOD
C
```

```
                SUM = 0.0
                NSTEPS = 5000
                XMIN = WAVE/4.0
                XMAX = WAVE/4.0 + RPROJ
                T1 = 2.*3.14159*AMP/WAVE
                T2 = 2.*3.14159/WAVE
                DX = (XMAX-XMIN)/FLOAT(NSTEPS)
                X = XMIN
                DO 11 II = 1, NSTEPS
                  SUM = SUM + SQRT(1.+(T1**2)*(COS(T2*X))**2)*DX
                  X = X+ DX
11              CONTINUE
                RCALC = SUM
                WRITE (6,150) RPROJ*100., RACT*100., RCALC*100.
               ENDIF
             ELSE
               ENDRAD = .TRUE.
             ENDIF
           END DO
           READ (88,*) PERF
           IF (PERF .EQ. 'end') THEN
             ENDPERF = .TRUE.
             READ (88,*) FILM
             IF (FILM .EQ. 'end') ENDFILM = .TRUE.
           ELSE
             WRITE (6,100) PERF
             READ (88,*) HTHIN1
           ENDIF
         END DO
       END DO
100    FORMAT(//'PERFORATION DESIGNATION:  ',A6,/,'ALL VALUES IN cm')
150    FORMAT(/'RPROJ =',F5.2,3X,'RACT =',F5.2,3X,'RCALC =',F5.2)
200    FORMAT(//'FOR PERFORATION ',A6,
     1  ' THE CALCULATED AMPLITUDE IS GREATER THAN ',F6.4,' m')
300    FORMAT('1'//'FILE NAME:  ',A10)
350    FORMAT(//'US = ',F6.2,' m/s  GAS DENSITY = ',F4.1,' kg/m^3',
     1  '  SURFACE TENSION = ',F5.4,' kg/s^2')
370    FORMAT(/'LENGTH SCALE = ',F6.4,3X,'OPT WAVE = ',F6.4,
     1  ' m   BULK THICKNESS = ',F5.1,' um')
400    FORMAT(////'*** WARNING:  RADIUS GREATER THAN LAMDA ***')
600    FORMAT(/' HTHIN1 = ',F6.2,'   HTHIN2 = ',F6.2,'  AMP = ',F6.2)
       END
```

```
C
C         PROGRAM TO CALULATE THE PROJECTED RADIUS
C         OF A PERFORATION GROWING IN THE RADIAL
C         DIRECTION ON A SINUOUSLY DISTURBED SHEET
C
C         FOR EACH MEASURED RADIAL PERFORATION RADIUS,
C         DETERMINE THE AMPLITUDE OF THE OPTIMUM SINE
C         WAVE WHICH CAUSES THE TRUE (UNPROJECTED)
C         RADIAL SEMIAXIS LENGTH TO EQUAL THE ACTUAL
C         (LATERAL) SEMIAXIS LENGTH
C
C         DIMENSION VARIABLES AND DEFINE PARAMETERS
C
      CHARACTER FILM*10, PERF*6
      LOGICAL FIND, FAIL, ENDFILE, ENDPERF
      IMPLICIT REAL (K)
      PARAMETER (PI = 3.141592654)
C
C         OPEN FILE CONTAINING FILM #, OPERATING CONDITIONS
C         PERFORATION NUMBERS AND RADIAL AND LATERAL SEMI-
C         AXIS LENGTH DATA
C
      OPEN (88, FILE='9_3_data')
      ENDFILE = .FALSE.
C
C         FILM = I.D. NUMBER OF THE FILM
C
      READ (88,*) FILM
C
C         READ PARAMETERS
C
      DO WHILE (.NOT. ENDFILE)
C           SHEET VELOCITY (M/S)
        READ (88,*) US
C           GAS DENSITY (KG/M^3)
        READ (88,*) DENSGAS
C           SURFACE TENSION (KG/S^2)
        READ (88,*) SURF
C           LENGTH SCALE (M/MM)
        READ (88,*) SCALE
C           BULK SHEET THICKNESS (MICRONS)
        READ (88,*) HB2
C
C           CALCULATE OPTIMUM WAVELENGTH
C           FOR AN INVISCID SHEET BASED ON
C           HAGERTY AND SHEA'S ANALYSIS
C
        WAVE = 4.0*PI*SURF/(DENSGAS*US*US)
C
C           WRITE OUT FILE PARAMETERS
```

```
C
      WRITE (6,300) FILM
      WRITE (6,350) US, DENSGAS, SURF
      WRITE (6,370) SCALE, WAVE, HB2
C
C       READ RADIUS LOOP
C
      ENDPERF = .FALSE.
C
C       PERF = I.D. NUMBER FOR THE PERFORATION
C
      READ (88,*) PERF
      WRITE (6,100) PERF
      DO WHILE (.NOT. ENDPERF)
C
C         R2 = RADIAL AXIS LENGTH
C         Y2 = LATERAL AXIS LENGTH
C         VALUES ARE IN METERS AS MEASURED FROM
C         THE PROJECTED IMAGES
C
        READ (88,*) R2, Y2
        IF (R2 .NE. 0.) THEN
C
C           SCALE CONVERTS FORM MEASURED UNITS
C           TO REAL LENGTH UNITS ACCOUNTING FOR
C           THE MAGNIFICATION OF THE IMAGES
C           DIVIDING BY 2000 YIELDS THE SEMIAXIS
C           LENGTH IN METERS
C
          RPROJ = SCALE*(R2/2000.0)
          RACT = SCALE*(Y2/2000.0)
C
C             BEGIN LOOP ON DISTURBANCE AMPLITUDE (M)
C             TO DETERMINE WHAT AMPLITUDE CAUSES THE PROJECTION
C             OF THE ACTUAL SEMIAXIS LENGTH (LATERAL) TO EQUAL
C             RADIAL SEMIAXIS LENGTH
C
          AMP = 0.0
          FIND = .FALSE.
          FAIL = .FALSE.
          DO WHILE (.NOT.FIND)
            AMP = AMP + 0.0001
C
C               CALCULATE PARAMETERS FOR ELLIPTIC INTEGRAL
C
            P = 2.0*PI*AMP/WAVE
            PP = SQRT(P*P/(1.0 + P*P))
            KC2 = 1.0 - PP*PP
            KC = SQRT(KC2)
C
```

```
C                 CALL SUBROUTINE "COMPELLP.F"
C
                  COMPELL = CEL(KC,1.0,1.0,KC2)
                  CONST = SQRT(1.0 + P*P)*WAVE/(2.0*PI)
C
C                   A DIFFERENT CALCUALTION IS NEEDED DEPENDING
C                   ON HOW MANY QUARTER WAVE-LENGTHS LONG THE
C                   SEMI-AXIS IS
C
                  IF (RPROJ .LT. WAVE/4.0) THEN
                    UL = TAN(PI/2.0 - 2.0*PI*RPROJ/WAVE)
                    ELLIP2 = EL2(UL,KC,1.0,KC2)
                    RCALC = CONST*(COMPELL - ELLIP2)
                  ELSEIF (RPROJ .LT. WAVE/2.0) THEN
                    UL = TAN(2.0*PI*RPROJ/WAVE - PI/2.0)
                    ELLIP2 = EL2(UL,KC,1.0,KC2)
                    RCALC = CONST*(COMPELL + ELLIP2)
                  ELSEIF (RPROJ .LT. 3.0*WAVE/4.0) THEN
                    UL = TAN(3.0*PI/2.0 - 2.0*PI*RPROJ/WAVE)
                    ELLIP2 = EL2(UL,KC,1.0,KC2)
                    RCALC = CONST*(3.0*COMPELL - ELLIP2)
                  ELSEIF (RPROJ .LT. WAVE) THEN
                    UL = TAN(2.0*PI*RPROJ/WAVE -3.0*PI/2.0)
                    ELLIP2 = EL2(UL,KC,1.0,KC2)
                    RCALC = CONST*(3.0*COMPELL + ELLIP2)
                  ELSE
                    WRITE (6,400)
                    FIND = .TRUE.
                    FAIL = .TRUE.
                  ENDIF
C
C                   WHEN THE CALCULATION OF THE TRUE RADIAL SEMI-
C                   AXIS LENGTH IS JUST GREATER THAN THE LATERAL
C                   SEMIAXIS LENGTH, THE LOOP IS STOPPED AND THE
C                   CALCULATED AMPLITUDE IS USED TO CALCULATE THE
C                   WAVE-THINNED SHEET THICKNESS
C
                  IF (RCALC .GT. RACT) THEN
                    FIND = .TRUE.
                    SHTLEN = 4.0*CONST*COMPELL
                    RATLEN = WAVE/SHTLEN
                    HTHIN2 = HB2*RATLEN
                  ELSEIF (AMP .GT. 1.0) THEN
                    FIND = .TRUE.
                    FAIL = .TRUE.
                  ENDIF
                END DO
                IF (.NOT.FAIL) THEN
                  WRITE (6,150) RPROJ*100., RACT*100., AMP*100.,
     1             RATLEN, HTHIN2
```

```
              ELSE
                WRITE (6,200) PERF, AMP
                WRITE (6,150) RPROJ, RACT, RCALC
              ENDIF
            ELSE
C
C             READ IN THE NEXT PERFORATION I.D. NUMBER
C             IF PERF = 'end' READ IN NEXT FILM I.D.
C             IF FILM = 'end' END PROGRAM
C
              READ (88,*) PERF
              IF (PERF .EQ. 'end') THEN
                ENDPERF = .TRUE.
                READ (88,*) FILM
                IF (FILM .EQ. 'end') ENDFILE = .TRUE.
              ELSE
                WRITE (6,100) PERF
              ENDIF
            ENDIF
          END DO
        END DO
100     FORMAT(//'PERFORATION DESIGNATION:  ',A6,/,'ALL VALUES IN cm')
150     FORMAT(/'RPROJ =',F5.2,2X,'RACT =',F5.2,2X,'AMP =',F5.2,
     1    3X,'LAM/LEN =',F6.4,2X,'THICK = ',F5.2,' um')
200     FORMAT(//'FOR PERFORATION ',A6,
     1   ' THE CALCULATED AMPLITUDE IS GREATER THAN ',F6.4,' m')
300     FORMAT('1'//'FILM NUMBER:  ',A10)
350     FORMAT(//'US = ',F6.2,' m/s  GAS DENSITY = ',F4.1,' kg/m^3',
     1   '  SURFACE TENSION = ',F5.4,' kg/s^2')
370     FORMAT(/'LENGTH SCALE = ',F6.4,3X,'OPT WAVE = ',F6.4,
     1   ' m   BULK THICKNESS = ',F5.1,' um')
400     FORMAT(////'*** WARNING:  RADIUS GREATER THAN LAMDA ***')
        END
```

Mon Jun 08 21:52:18 1992 omega2.f Page 1

```
C
C       CALCULATE OPTIMUM WAVE IN A VISCOUS SHEET
C       BASED ON WEIHS EQUATION
C
      CHARACTER FILM*10
      IMPLICIT REAL (K)
      PARAMETER (PI = 3.14159)
C
C       READ OPERATING CONDITIONS
C
      OPEN (88, FILE='omega_3')
      READ (88,*) NUMFILM
      DO 10 IFILM = 1, NUMFILM
        READ (88,*) FILM
        READ (88,*) D0
        READ (88,*) U0
        READ (88,*) DENSLIQ
        READ (88,*) DENSGAS
        READ (88,*) VISCLIQ
        READ (88,*) SURF
C
C         CALCUALTE PARAMETERS
C
        XP = 0.0254
        XF = 0.35
        RE = DENSLIQ*U0*D0/VISCLIQ
        VISCKIN = VISCLIQ/DENSLIQ
C
C         CALCULATE THICKNESS AND VELOCITY AT THE PLATE EDGE
C         USE CONSTANTS DETERMINED FROM LINEAR REGRESSION MODEL
C
        H2INV = D0**2/(8.*XP)
        H2XP = H2INV*(1.55+(40.2/RE)*(XP/D0)**3)
        US = 1.12*U0/(1.55+(40.2/RE)*(XP/D0)**3)
C
C         CALCULATE OPTIMUM INVISCID WAVE NUMBER
C
        KINV = US**2*DENSGAS/(2.*SURF)
        WAVE = 2.*3.14159/KINV
        WRITE (6,500) FILM
        WRITE (6,600) DENSLIQ, DENSGAS, VISCLIQ, SURF
        WRITE (6,200) D0*1000., U0, US
        WRITE (6,300) H2INV*1.E6,H2XP*1.E6,KINV,WAVE*100.
C
C         LOOP ON DOWNSTREAM POSITION
C         CALC W, KSTAR, KVISC, WAVEVISC
C
        X = XP
        DX = 0.025
        DO WHILE (X .LE. XF)
```

```
            H2 = H2XP*(XP/X)
            W = SURF**3*DENSLIQ/(VISCLIQ**2*(H2/2.0)*DENSGAS**2*US**4)
            K = 1.0
1           TEST = K**3-4.*W*K**2+8.*W*K-4.*W
            IF (TEST .LT. 0.) THEN
              KSTAR = K
            ELSE
              K = K - 0.001
              GOTO 1
            ENDIF
            KVIS = KSTAR*KINV
            WAVEVISC = 2.*3.14159/KVIS
            WRITE (6,100) X*100., KSTAR, W, WAVEVISC*100.0
C
C             CALCULATE GROWTH RATE
C
              C1 = VISCKIN/2.0
              C2 = 8.*(DENSGAS*US**2*KVIS-SURF*KVIS**2)
              C3 = H2*DENSLIQ*VISCKIN**2
              SIMAG = C1*(-(KVIS**2)+SQRT(KVIS**4+C2/C3))
              SRAT = SIMAG/US
              SINV = SQRT((KVIS**2*US**2*(DENSGAS/DENSLIQ)-
     1          KVIS**3*SURF/DENSLIQ)/(KVIS*(H2/2)))
              WRITE (6,400) SIMAG,SRAT,SINV
              X = X + DX
            END DO
10        CONTINUE
100       FORMAT (/' X (CM) = ',F5.1,'  KSTAR = ',F5.3,'  W = ',
     1     E8.2,'  WAVE (CM) = ',F6.2)
200       FORMAT (/' D0 (MM) = ',F4.2,'   U0 (M/S) = ',F5.2,
     1     '    US (M/S) = ',F5.2)
300       FORMAT (/' H2INV (um) = ',F7.2,'  H2VIS (um) = ',F7.2,
     1     /,' KINV = ',E8.2,'  WAVE (CM) = ',F6.3)
400       FORMAT (' SVIS = ',F7.2,'  SRAT = ',F6.2,'  SINV = ',F7.2)
500       FORMAT (' FILM ',A10)
600       FORMAT (/' DENSLIQ = ',F5.0,' kg/m^3   DENSGAS = ',F3.1,
     1     ' kg/m^3',/,' VISCLIQ = ',F5.3,' km/ms    SURF = ',F5.3,
     2     'kg/s^2')
          END
```

Wed May 20 14:11:48 1992 ellip.f Page 1

```
      FUNCTION EL2(X,QQC,AA,BB)
C
C       GENERAL ELLIPTIC INTEGRAL OF THE 2ND KIND
C
C       COPIED FROM:  Press, W.H.; Flannery, B.P.;
C       Teukolsky, S.A.; Vetterling, W.T.  "Numerical
C       Recipes:  The Art of Scientific Computing,"
C       Cambridge University Press, 1986 (pp.186-7)
C
C       X = x >= 0, QQC = KC, AA = a, BB = b
C       KC^2 = 1 - K^2
C
C       WHERE K IS THE PARAMETER IN THE ELLIPTIC INTEGRAL
C
C       FOR ELLIP INT OF FIRST KIND SEND (X,KC,1.0,1.0)
C       FOR ELLIP INT OF SECOND KIND SEND (X,KC,1.0,KC^2)
C
      PARAMETER(PI=3.14159265, CA = 0.00001, CB = 1.0E-12)
      IF (X .EQ. 0.) THEN
        EL2 = 0.0
      ELSE IF (QQC .NE. 0.) THEN
        QC = QQC
        A = AA
        B = BB
        C = X**2
        D = 1.0 + C
        P = SQRT((1.0 + QC**2*C)/D)
        D = X/D
        C = D/(2.0*P)
        Z = A - B
        EYE = A
        A = 0.5*(B + A)
        Y = ABS(1.0/X)
        F = 0.0
        L = 0
        EM = 1.0
        QC = ABS(QC)
1       B = EYE*QC + B
        E = EM*QC
        G = E/P
        D = F*G + D
        F = C
        EYE = A
        P = G + P
        C = 0.5*(D/P + C)
        G = EM
        EM = QC + EM
        A = 0.5*(B/EM + A)
        Y = -E/Y + Y
        IF (Y .EQ. 0.) Y=SQRT(E)*CB
```

```
      IF (ABS(G-QC) .GT. CA*G) THEN
        QC = SQRT(E)*2.0
        L = L + L
        IF (Y .LT. 0.) L = L + 1
        GO TO 1
      ENDIF
      IF (Y .LT. 0.) L = L + 1
      E = (ATAN(EM/Y) + PI*L)*A/EM
      IF (X .LT. 0.) E = -E
      EL2 = E + C*Z
    ELSE
      PAUSE 'FAILURE IN EL2'
    ENDIF
    RETURN
    END
```

Wed May 20 14:15:09 1992 compellp.f Page 1

```
C
C       COMPLETE ELLIPTIC INTEGERAL OF THE
C       SECOND KIND
C
C       COPIED FROM:  Press, W.H.; Flannery, B.P.;
C       Teukolsky, S.A.; Vetterling, W.T.  "Numerical
C       Recipes:  The Art of Scientific Computing,"
C       Cambridge University Press, 1986  (pp. 187-8)
C
C       FOR COMPLETE ELLIPTIC INTEGRAL
C       SEND:  QQC=KC, PP=1., AA=1., BB = KC^2
C       WHERE:  KC^2 = 1.-K^2
C
C       WHERE:  K^2 IS THE PARAMETER OF THE ELLIP INT
C
      FUNCTION CEL(QQC,PP,AA,BB)
      PARAMETER (CA=0.00001, PIO2=1.5707963268)
      IF(QQC .EQ. 0.) RETURN
      QC = ABS(QQC)
      A = AA
      B = BB
      P = PP
      E = QC
      EM = 1.0
      IF(P .GT. 0.) THEN
        P = SQRT(P)
        B = B/P
      ELSE
        F = QC*QC
        Q = 1.0 - F
        G = 1.0 - P
        F = F - P
        Q = Q*(B - A*P)
        P = SQRT(F/G)
        A = (A - B)/G
        B = -Q/(G*G*P) + A*P
      ENDIF
1     F = A
      A = A + B/P
      G = E/P
      B = B + F*G
      B = B + B
      P = G + P
      G = EM
      EM = QC + EM
      IF(ABS(G-QC) .GT. G*CA) THEN
        QC = SQRT(E)
        QC = QC + QC
        E = QC*EM
        GO TO 1
```

```
      ENDIF
      CEL = PIO2*(B + A*EM)/(EM*(EM + P))
      RETURN
      END
```

APPENDIX I: DATA FOR THE PERFORATION GROWTH EXPERIMENTS

This appendix contains the tables and plots of the experimental data collected in the perforation growth rate experiments. The data are grouped by the experiment (film I.D.) number. Each section begins with tables of the lateral and radial perforation axis lengths. The data in the columns labeled "measured Radial" are the experimental measurements of the radial perforation axis made from the projected images. The data are presented in units of millimeters. The adjacent column, "scaled Radial," is the true radial semiaxis length in meters. This value is obtained by multiplying the measured axis length by the ratio of the true distance to the distance measured off the projected images and dividing by 2000. (1 m = 1000 mm and semi-axis = 1/2 axis length). Similar columns are presented for the lateral axis and semi-axis. An additional column appears for the lateral axis called the "corrected lateral." This column shows the lateral semiaxis length corrected for the geometric spreading of the perforation independent of its surface tension driven growth.

A final column, titled "relative time," accompanies each list of radial and lateral semiaxis lengths. These times were calculated from the TLG marks on the 16 mm films. Time equal zero was taken as the frame at which the first measurement of a particular perforation was measured. Lateral and radial semiaxis measurements made from the same frame will have the same relative time.

Following the presentation of the data in tabular form, plots of the lateral and radial semiaxis length versus the relative time are shown. The best fit linear regression line is also included.

Film # 61491_2
Perf # 908
act/meas = 0.1435
dt = 0.00067

relative t (sec)	measured Radial	scaled Radial
0.00000	71.6	0.0051
0.00067	80.4	0.0058
0.00135	93.6	0.0067
0.00202	102.3	0.0073

Film # 61491_2
Perf # 920
act/meas = 0.1435
dt = 0.00029

relative t (sec)	measured Radial	scaled Radial
0.00000	166.5	0.0119
0.00029	175.1	0.0126
0.00058	181.8	0.0130
0.00086	187.3	0.0134
0.00115	195.2	0.0140

Film # 61491_2
Perf # 927
act/meas = 0.1435
dt = 0.00035

relative t (sec)	measured Radial	scaled Radial
0.00000	17.0	0.0012
0.00035	36.9	0.0026
0.00071	41.2	0.0030
0.00106	54.0	0.0039

relative t (sec)	measured lateral	scaled lateral	corrected lateral
0.00000	17.0	0.0012	0.0012201
0.00023	36.9	0.0026	0.00263214
0.00045	41.2	0.0030	0.0029218
0.00068	83.2	0.0060	0.00593206

Film # 61491_2
Perf # 962
act/meas = 0.1435
dt = 0.00023

relative t (sec)	measured Radial	scaled Radial
0.00000	37.3	0.0027
0.00023	41.2	0.0030
0.00045	46.4	0.0033
0.00068	53.2	0.0038
0.00090	58.1	0.0042

relative t (sec)	measured lateral	scaled lateral	corrected lateral
0.00000	-	-	-
0.00023	58.3	0.0042	0.00418421
0.00045	74.2	0.0053	0.00526985
0.00068	88.6	0.0064	0.0062882
0.00090	103.0	0.0074	0.00730799

Film # 61491_2
Perf # 976
act/meas = 0.1435
dt = 0.00023

relative t (sec)	measured Radial	scaled Radial	relative t (sec)	measured lateral	scaled lateral	corrected lateral
0.00000	60.2	0.0043	0.00000	57.8	0.0041	0.00414833
0.00023	66.3	0.0048	0.00023	75.4	0.0054	0.00535645
0.00046	70.3	0.0050	0.00046	92.2	0.0066	0.00654543
0.00069	75.2	0.0054	0.00069	106.4	0.0076	0.00754858
0.00091	80.4	0.0058	0.00091	124.5	0.0089	0.0088341
0.00114	86.2	0.0062	0.00114	140.0	0.0100	0.00992931
0.00137	89.0	0.0064	0.00137	159.0	0.0114	0.01127819
0.00160	93.3	0.0067	0.00160	174.0	0.0125	0.01233665
0.00183	94.6	0.0068	0.00183	-	-	-
0.00206	99.8	0.0072	0.00206	-	-	-
0.00229	101.4	0.0073	0.00229	-	-	-
0.00251	103.5	0.0074	0.00251	-	-	-
0.00274	106.4	0.0076	0.00274	-	-	-

Film # 61491_2
Perf # 1026
act/meas = 0.1435
dt = 0.00023

relative t (sec)	measured Radial	scaled Radial	relative t (sec)	measured lateral	scaled lateral	corrected lateral
0.00000	42.0	0.0030	0.00000	53.3	0.0038	0.00382536
0.00023	44.0	0.0032	0.00023	60.7	0.0044	0.00432373
0.00046	44.2	0.0032	0.00046	69.8	0.0050	0.00497229
0.00069	47.2	0.0034	0.00069	78.0	0.0056	0.00555522
0.00091	48.3	0.0035	0.00091	86.8	0.0062	0.00618176
0.00114	51.2	0.0037	0.00114	92.4	0.0066	0.00657827
0.00137	54.0	0.0039	0.00137	100.0	0.0072	0.00712029
0.00160	55.2	0.0040	0.00160	107.7	0.0077	0.00766825
0.00183	58.0	0.0042	0.00183	115.6	0.0083	0.00823051
0.00206	58.8	0.0042	0.00206	121.6	0.0087	0.00865628
0.00229	64.0	0.0046	0.00229	130.0	0.0093	0.00925546
0.00251	64.2	0.0046	0.00251	136.7	0.0098	0.00973117
0.00274	67.8	0.0049	0.00274	145.2	0.0104	0.0103371
0.00297	69.2	0.0050	0.00297	-	-	-
0.00320	72.2	0.0052	0.00320	-	-	-
0.00343	74.5	0.0053	0.00343	-	-	-
0.00366	74.6	0.0054	0.00366	-	-	-
0.00389	79.4	0.0057	0.00389	-	-	-
0.00412	83.3	0.0060	0.00412	-	-	-
0.00434	86.7	0.0062	0.00434	-	-	-
0.00457	89.8	0.0064	0.00457	-	-	-
0.00480	92.4	0.0066	0.00480	-	-	-
0.00503	95.4	0.0068	0.00503	-	-	-

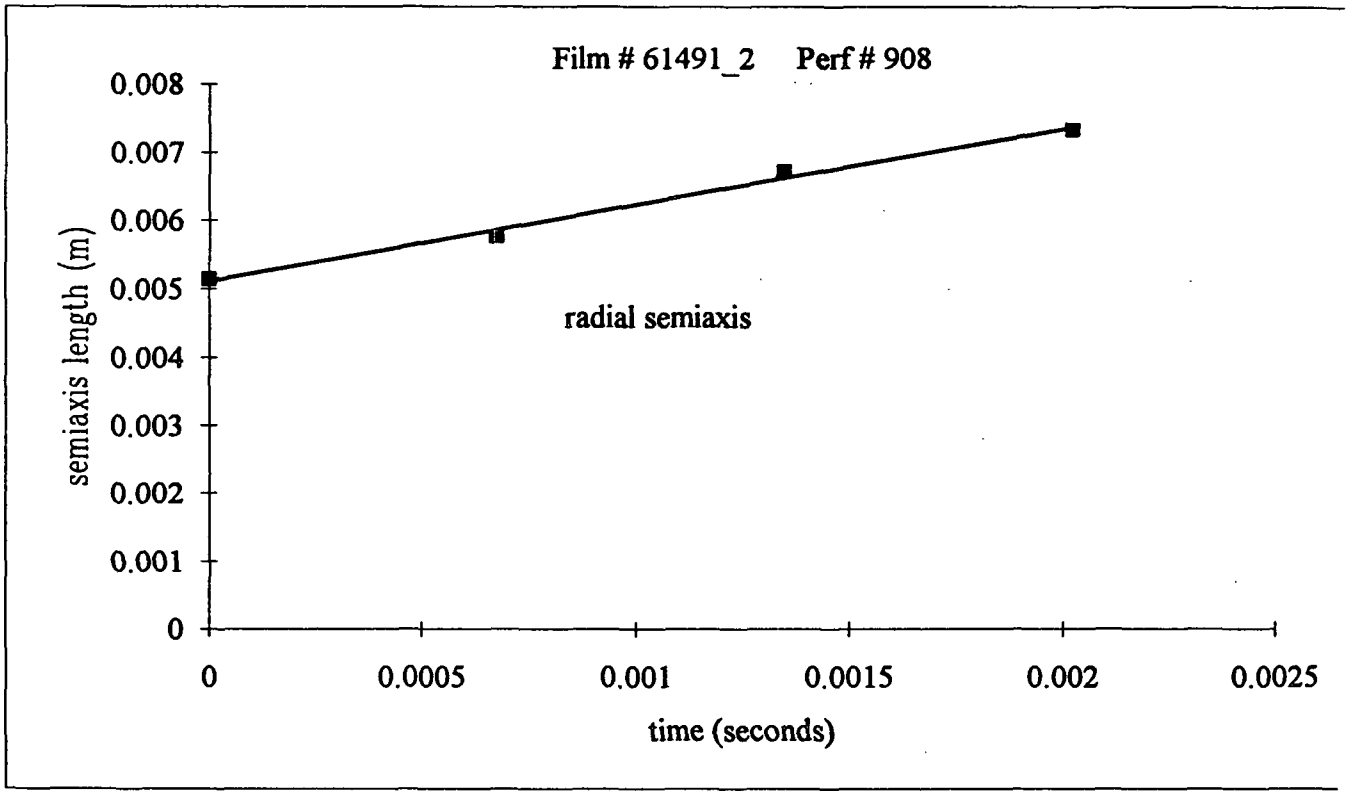
Film # 61491_2 Perf # 908
semiaxis length (m)
0.008
0.007
0.006
0.005
0.004
0.003
0.002
0.001
0
radial semiaxis
0
0.0005
0.001
0.0015
0.002
0.0025
time (seconds)

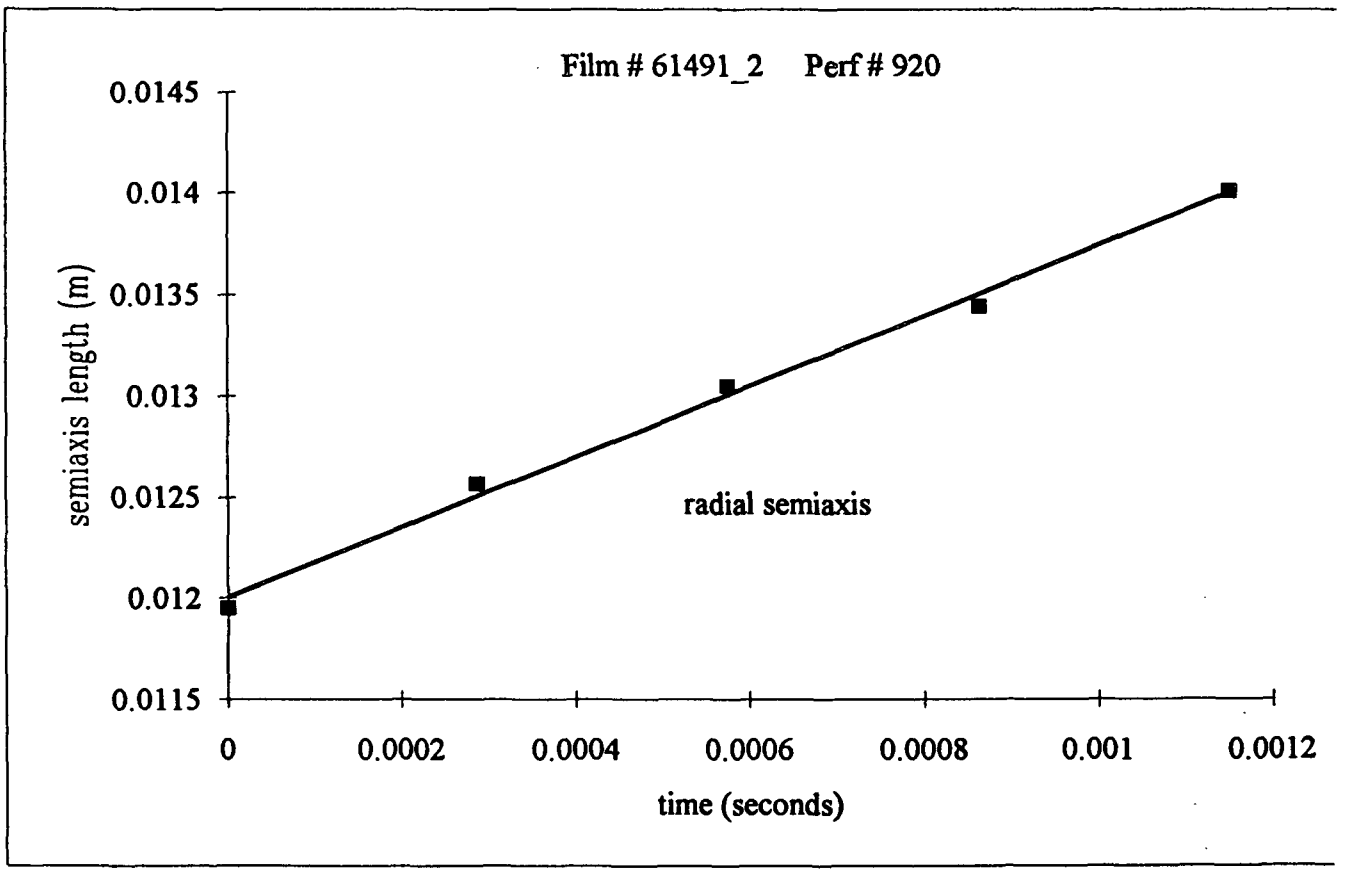
Film # 61491_2 Perf # 920
semiaxis length (m)
0.0145
0.014
0.0135
0.013
0.0125
0.012
0.0115
radial semiaxis
0
0.0002
0.0004
0.0006
0.0008
0.001
0.0012
time (seconds)

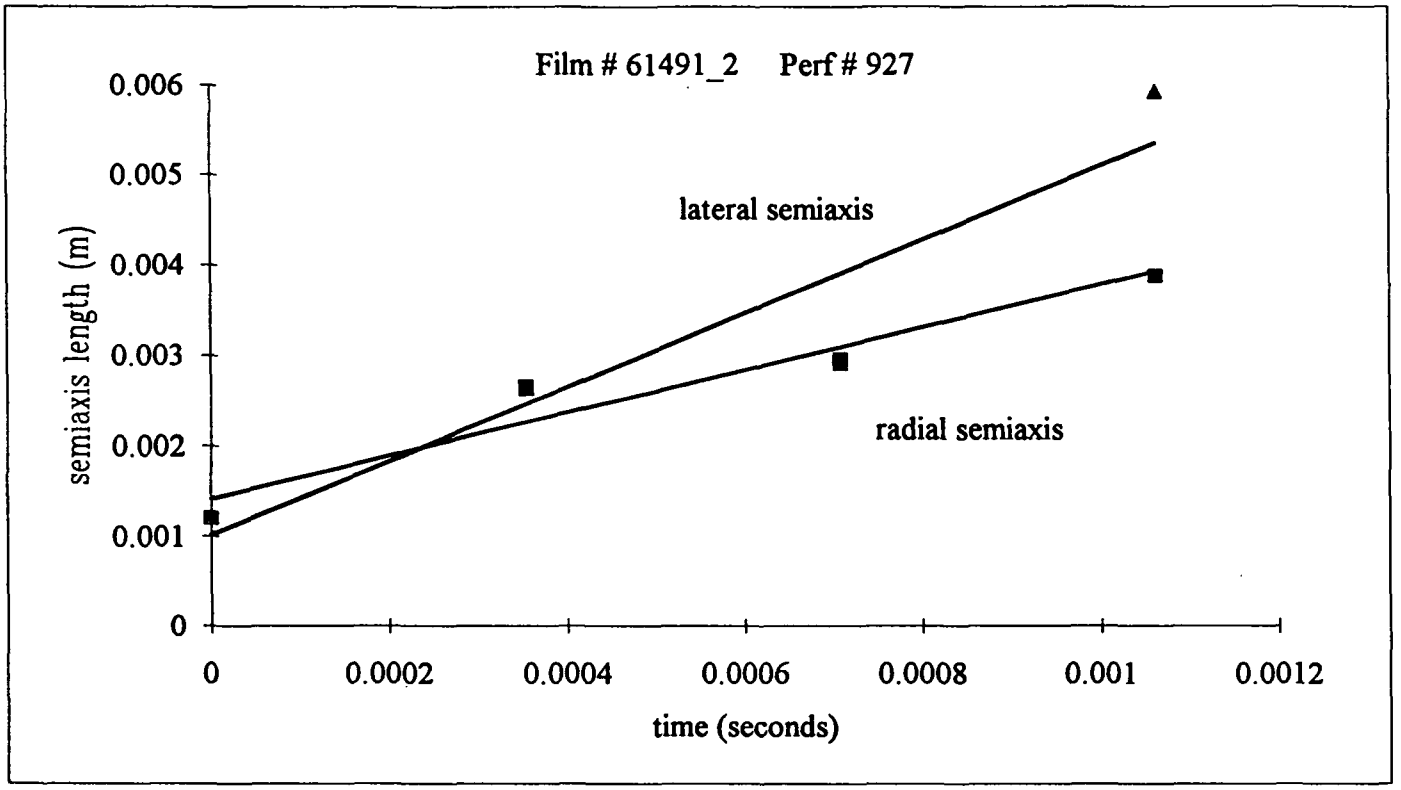
Film # 61491_2 Perf # 927
0.006
0.005
0.004
0.003
0.002
0.001
0
semiaxis length (m)
lateral semiaxis
radial semiaxis
0
0.0002
0.0004
0.0006
0.0008
0.001
0.0012
time (seconds)

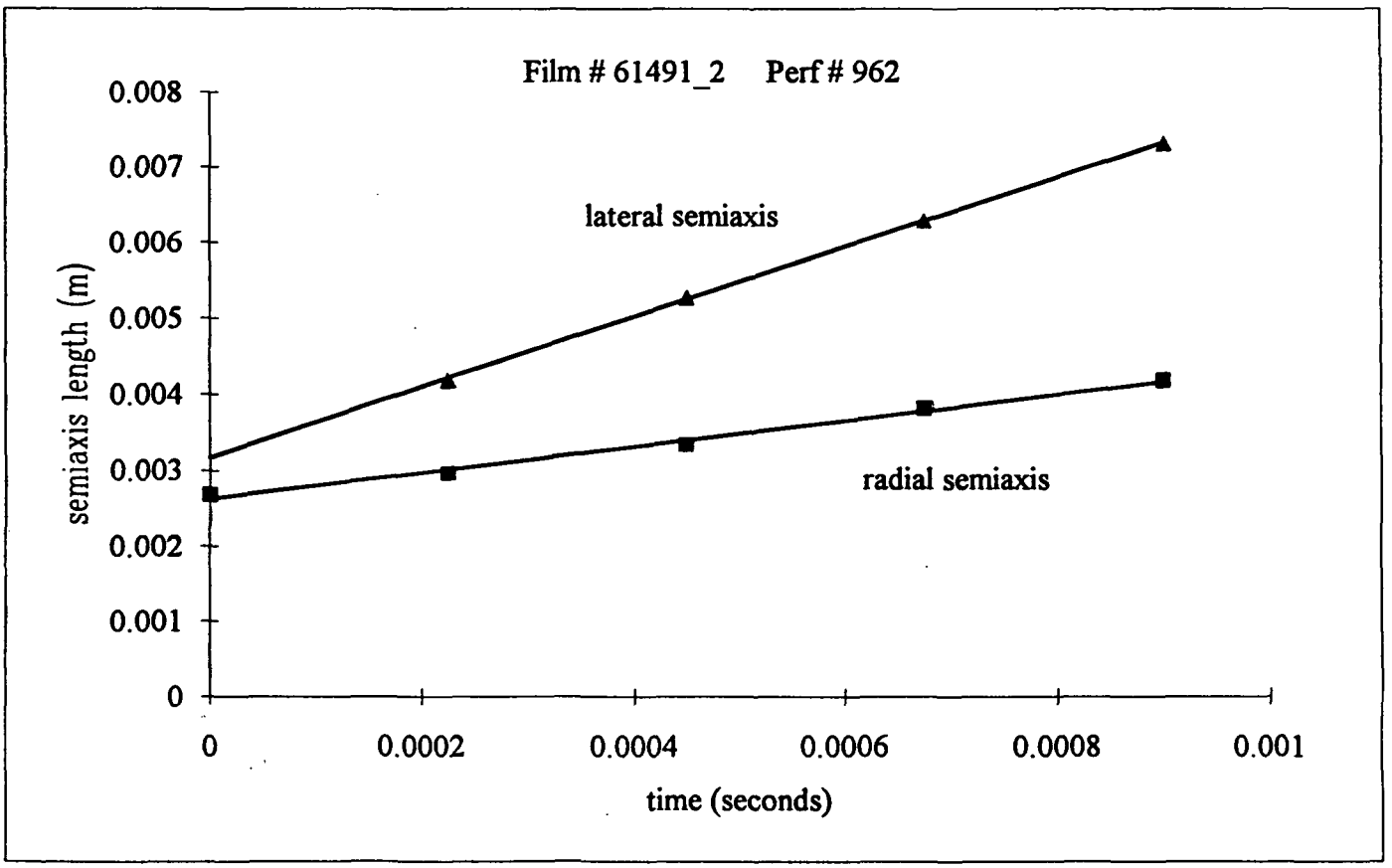
Film # 61491_2 Perf # 962
0.008
0.007
0.006
0.005
0.004
0.003
0.002
0.001
0
semiaxis length (m)
lateral semiaxis
radial semiaxis
0
0.0002
0.0004
0.0006
0.0008
0.001
time (seconds)

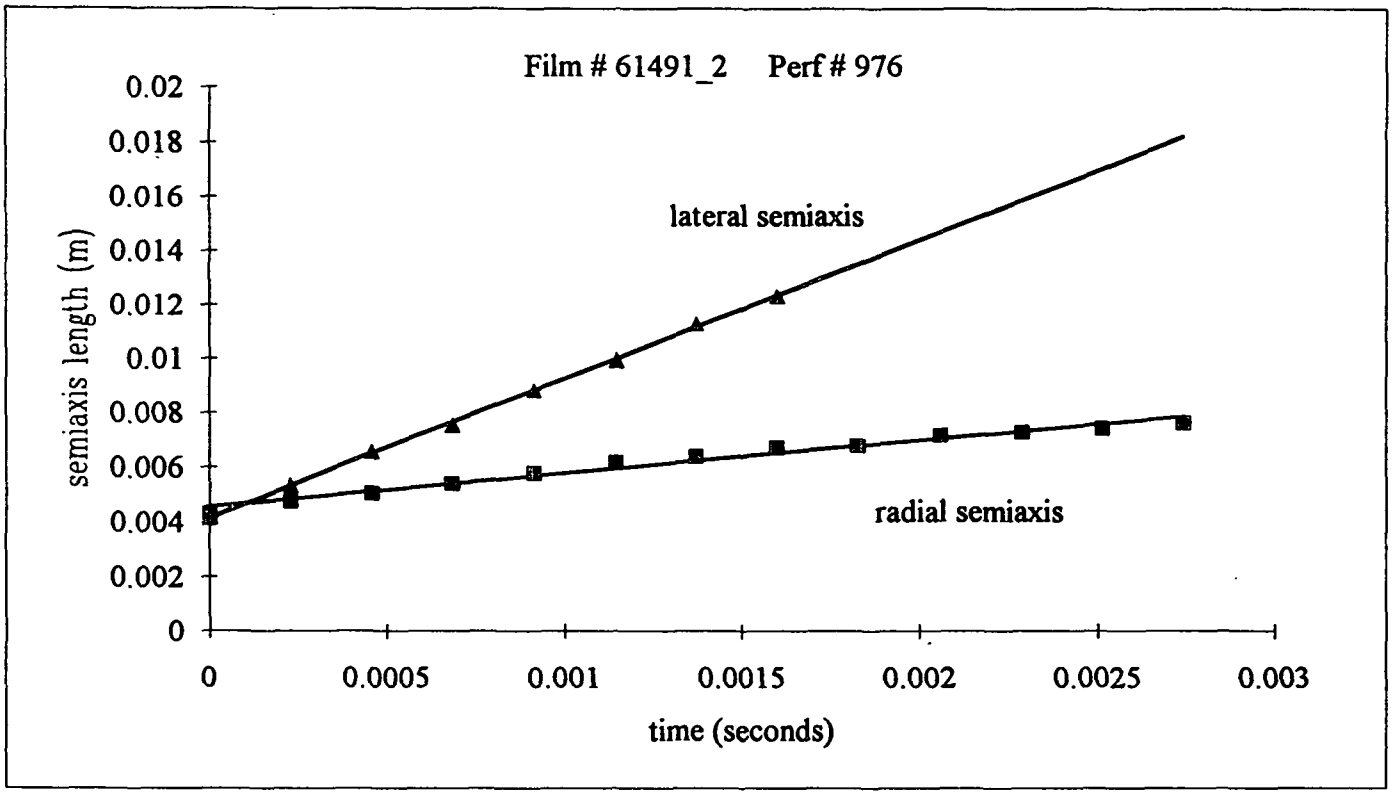
Film # 61491_2 Perf # 976
semiaxis length (m)
0.02
0.018
0.016
0.014
0.012
0.01
0.008
0.006
0.004
0.002
0
lateral semiaxis
radial semiaxis
0
0.0005
0.001
0.0015
0.002
0.0025
0.003
time (seconds)

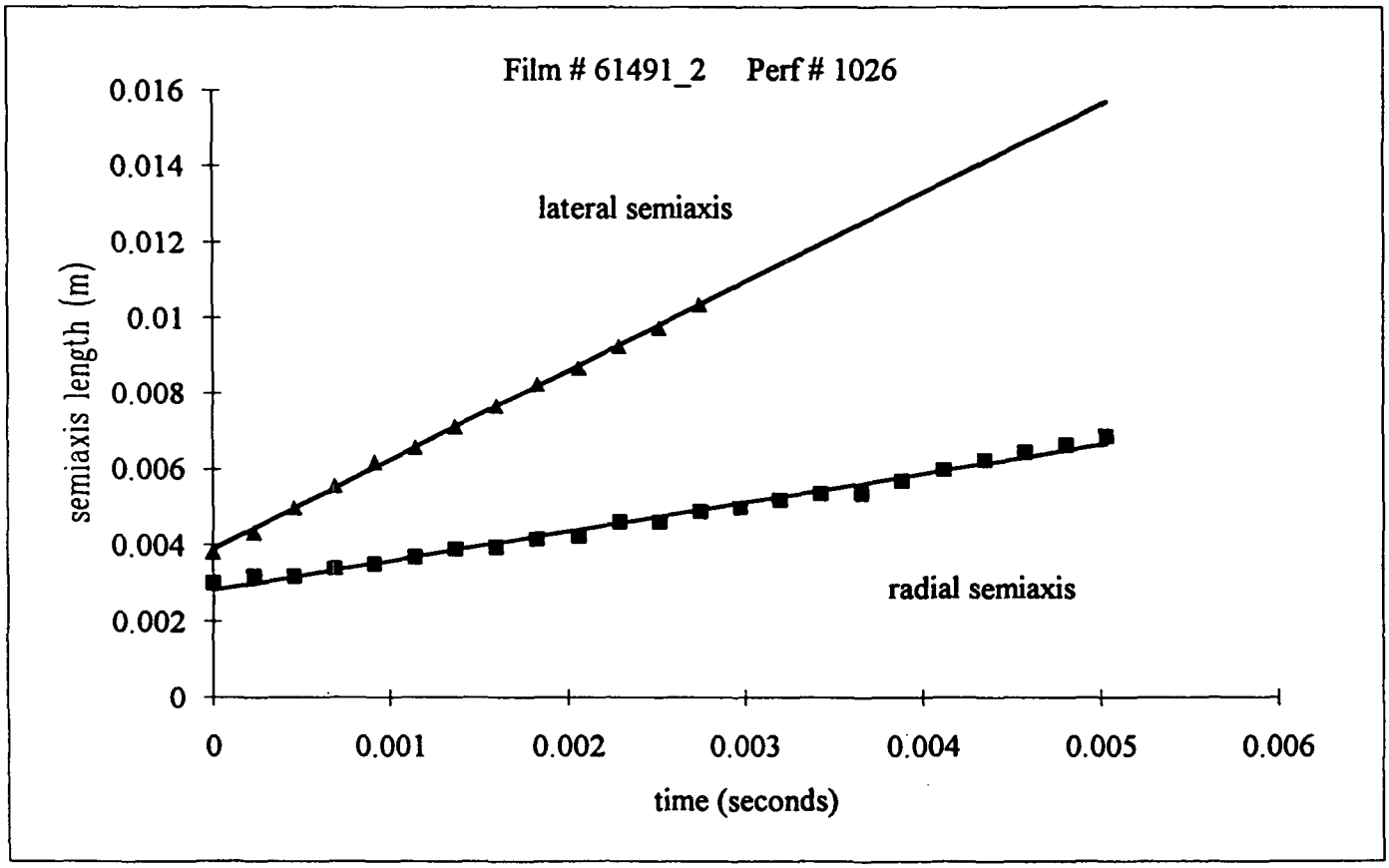
Film # 61491_2 Perf # 1026
semiaxis length (m)
0.016
0.014
0.012
0.01
0.008
0.006
0.004
0.002
0
lateral semiaxis
radial semiaxis
0
0.001
0.002
0.003
0.004
0.005
0.006
time (seconds)

Film # 61491_4
Perf # 580
act/meas = 0.1435
dt = 0.00036

relative t (sec)	measured Radial	scaled Radial
0.00000	81.9	0.0059
0.00036	97.5	0.0070
0.00071	112.3	0.0081
0.00107	121.0	0.0087
0.00143	130.2	0.0093

Film # 61491_4
Perf # 612
act/meas = 0.1435
dt = 0.00024

relative t (sec)	measured Radial	scaled Radial
0.00000	53.2	0.0038
0.00024	64.8	0.0047
0.00049	70.0	0.0050
0.00073	71.8	0.0052
0.00097	77.7	0.0056
0.00121	77.7	0.0056
0.00146	82.2	0.0059

relative t (sec)	measured lateral	scaled lateral	corrected lateral
0.00000	-	-	-
0.00024	122.0	0.0088	0.00875598
0.00049	137.4	0.0099	0.00979437
0.00073	150.0	0.0108	0.01069024
0.00097	164.2	0.0118	0.01170247
0.00121	-	-	-
0.00146	-	-	-

Film # 61491_4
Perf # 655
act/meas = 0.1435
dt = 0.00023

relative t (sec)	measured Radial	scaled Radial
0.00000	-	-
0.00023	43.2	0.0031
0.00045	55.2	0.0040
0.00068	67.8	0.0049
0.00091	76.5	0.0055

relative t (sec)	measured lateral	scaled lateral	corrected lateral
0.00000	15.5	0.0011	0.00111244
0.00023	43.0	0.0031	0.00307763
0.00045	59.5	0.0043	0.00424677
0.00068	-	-	-
0.00091	-	-	-

Film # 61491_4
Perf # 665
act/meas = 0.1435
dt = 0.00023

relative t (sec)	measured Radial	scaled Radial
0.00000	-	-
0.00023	-	-
0.00045	33.0	0.0024
0.00068	43.8	0.0031
0.00091	53.0	0.0038
0.00113	68.1	0.0049

relative t (sec)	measured lateral	scaled lateral	corrected lateral
0.00000	32.0	0.0023	0.00229665
0.00023	54.9	0.0039	0.00392265
0.00045	73.5	0.0053	0.00524503
0.00068	89.8	0.0064	0.00640469
0.00091	110.0	0.0079	0.00784552
0.00113	126.2	0.0091	0.00899712

Film # 61491_4
Perf # 716
act/meas = 0.1435
dt = 0.00023

relative t (sec)	measured Radial	scaled Radial
0.00000	135.8	0.0097
0.00023	138.4	0.0099
0.00045	144.1	0.0103
0.00068	147.6	0.0106
0.00090	149.9	0.0108
0.00113	153.6	0.0110
0.00135	160.0	0.0115
0.00158	161.5	0.0116
0.00180	166.6	0.0120
0.00203	168.7	0.0121

Film # 61491_4
Perf # 726
act/meas = 0.1435
dt = 0.00024

relative t (sec)	measured Radial	scaled Radial
0.00000	-	-
0.00024	73.2	0.0053
0.00049	88.4	0.0063
0.00073	100.9	0.0072
0.00097	109.8	0.0079
0.00121	118.1	0.0085
0.00146	122.6	0.0088
0.00170	128.7	0.0092
0.00194	133.0	0.0095

relative t (sec)	measured lateral	scaled lateral	corrected lateral
0.00000	69.9	0.0050	0.00501675
0.00024	109.2	0.0078	0.00779901
0.00049	141.0	0.0101	0.01005976
0.00073	164.8	0.0118	0.01175047
0.00097	-	-	-
0.00121	-	-	-
0.00146	-	-	-
0.00170	-	-	-
0.00194	-	-	-

Film # 61491_4
Perf # 746
act/meas = 0.1435
dt = 0.00026

relative t (sec)	measured Radial	scaled Radial
0.00000	119.9	0.0086
0.00025	124.5	0.0089
0.00051	125.8	0.0090
0.00076	127.2	0.0091
0.00102	127.8	0.0092
0.00127	127.2	0.0091
0.00153	128.8	0.0092
0.00178	126.7	0.0091
0.00204	-	-
0.00229	128.8	0.0092
0.00255	129.7	0.0093
0.00280	131.9	0.0095
0.00305	133.2	0.0096

Film # 61491_4
Perf # 752
act/meas = 0.1435
dt = 0.00026

relative t (sec)	measured Radial	scaled Radial
0.00000	62.8	0.0045
0.00026	61.5	0.0044
0.00051	68.6	0.0049
0.00077	70.6	0.0051
0.00103	78.5	0.0056
0.00129	79.9	0.0057
0.00154	82.8	0.0059
0.00180	88.7	0.0064
0.00206	90.2	0.0065
0.00231	92.8	0.0067
0.00257	93.1	0.0067
0.00283	97.5	0.0070
0.00309	100.2	0.0072
0.00334	101.9	0.0073
0.00360	105.7	0.0076
0.00386	110.2	0.0079

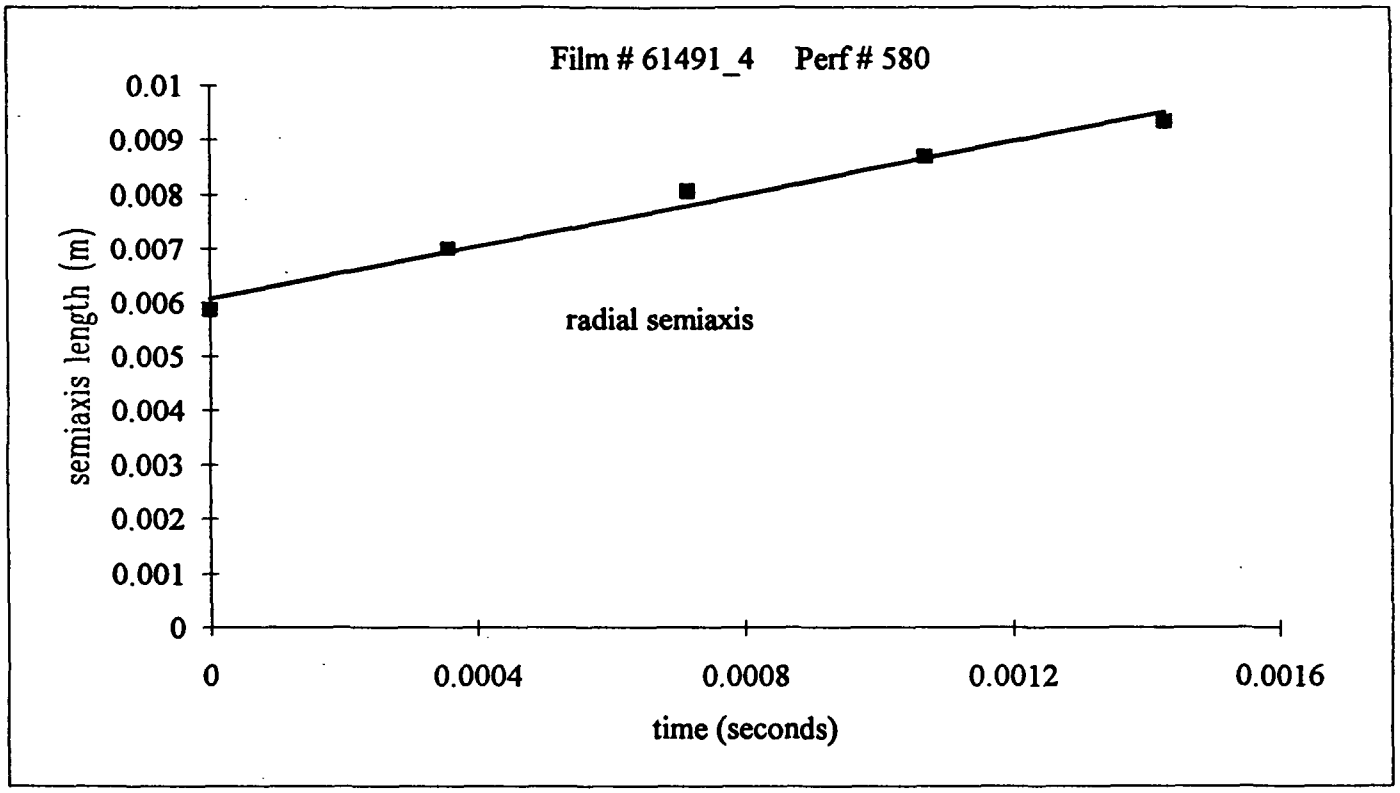
Film # 61491_4 Perf # 580
0.01
0.009
0.008
0.007
0.006
0.005
0.004
0.003
0.002
0.001
0
semiaxis length (m)
radial semiaxis
0
0.0004
0.0008
0.0012
0.0016
time (seconds)

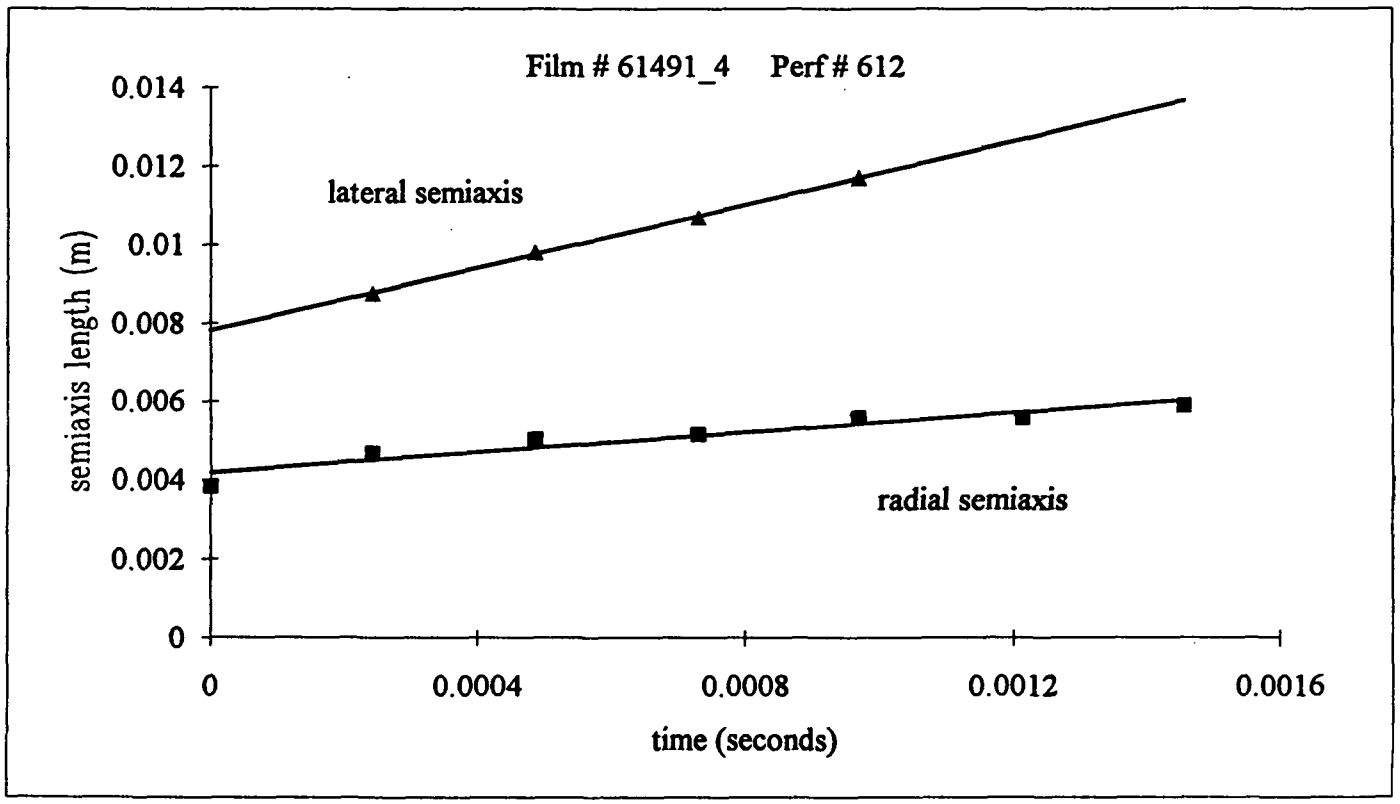
Film # 61491_4 Perf # 612
0.014
0.012
0.01
0.008
0.006
0.004
0.002
0
semiaxis length (m)
lateral semiaxis
radial semiaxis
0
0.0004
0.0008
0.0012
0.0016
time (seconds)

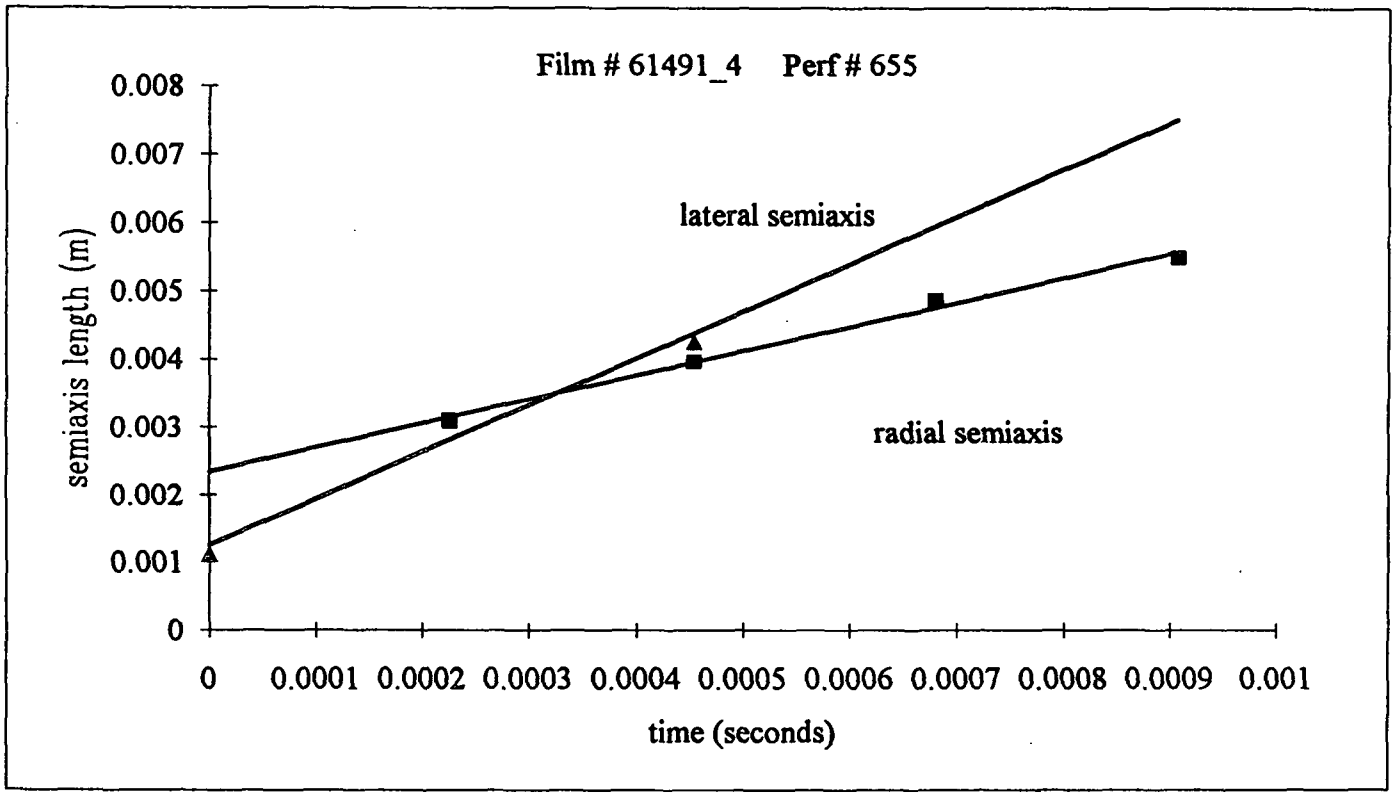
Film # 61491_4 Perf # 655
semiaxis length (m)
0.008
0.007
0.006
0.005
0.004
0.003
0.002
0.001
0
lateral semiaxis
radial semiaxis
0 0.0001 0.0002 0.0003 0.0004 0.0005 0.0006 0.0007 0.0008 0.0009 0.001
time (seconds)

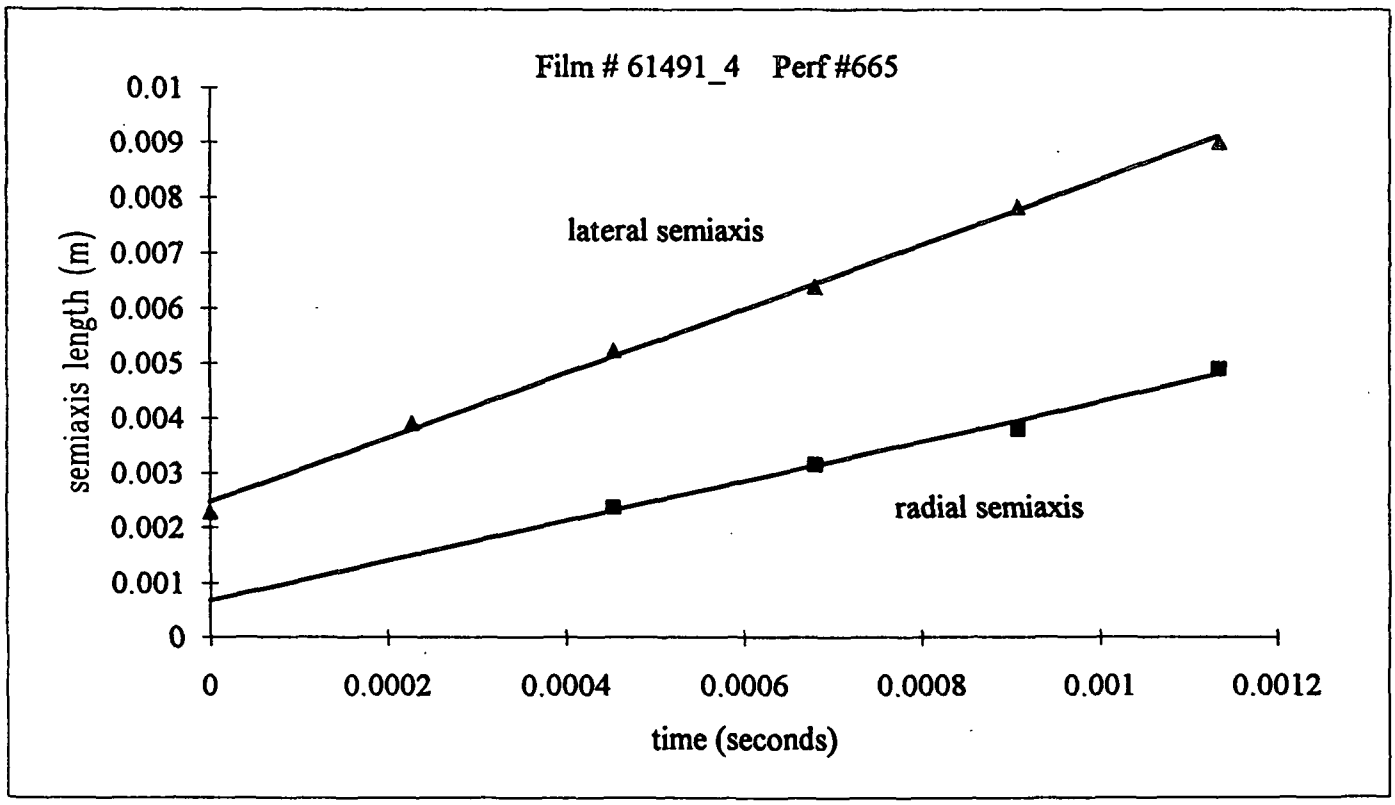
Film # 61491_4 Perf #665
semiaxis length (m)
0.01
0.009
0.008
0.007
0.006
0.005
0.004
0.003
0.002
0.001
0
lateral semiaxis
radial semiaxis
0 0.0002 0.0004 0.0006 0.0008 0.001 0.0012
time (seconds)

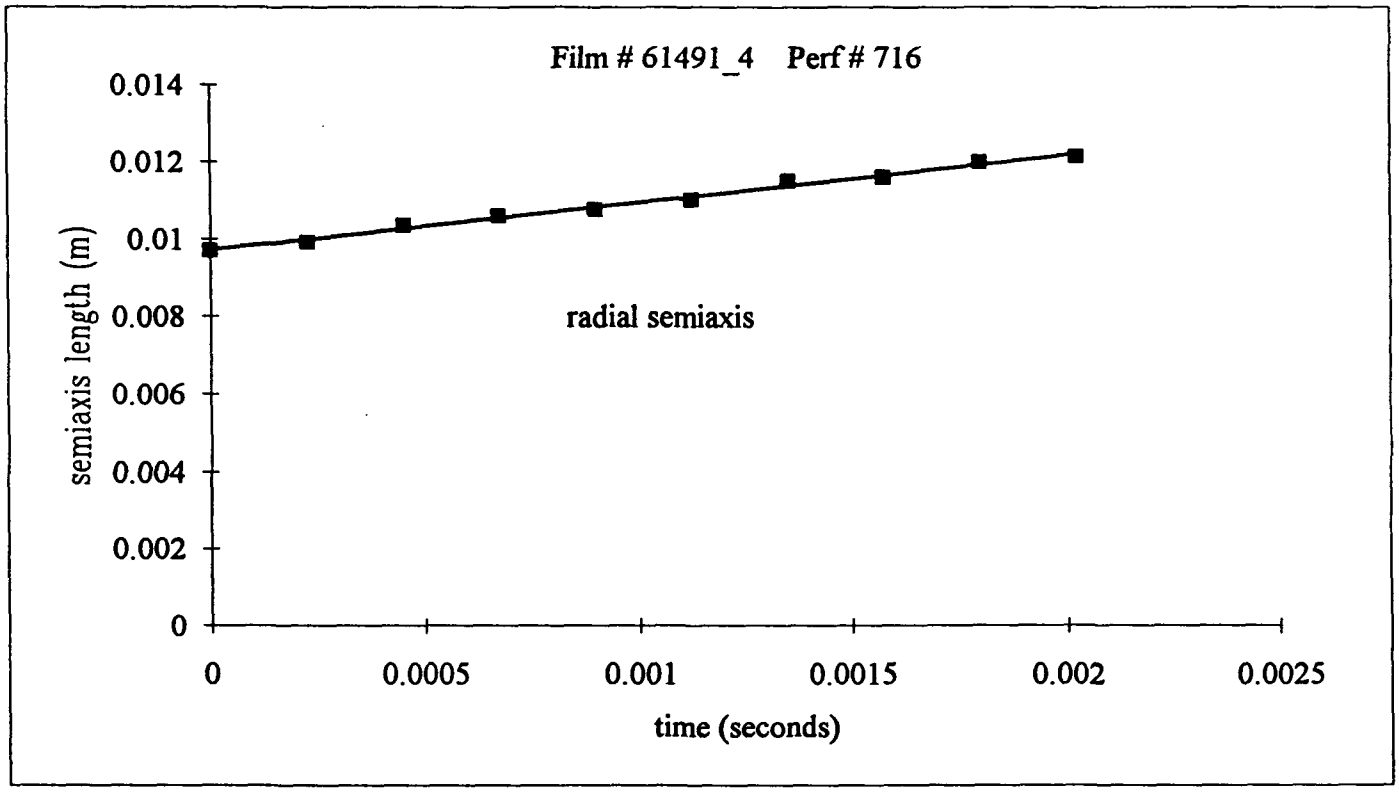
Film # 61491_4 Perf # 716
0.014
0.012
0.01
0.008
0.006
0.004
0.002
0
semiaxis length (m)
radial semiaxis
0
0.0005
0.001
0.0015
0.002
0.0025
time (seconds)

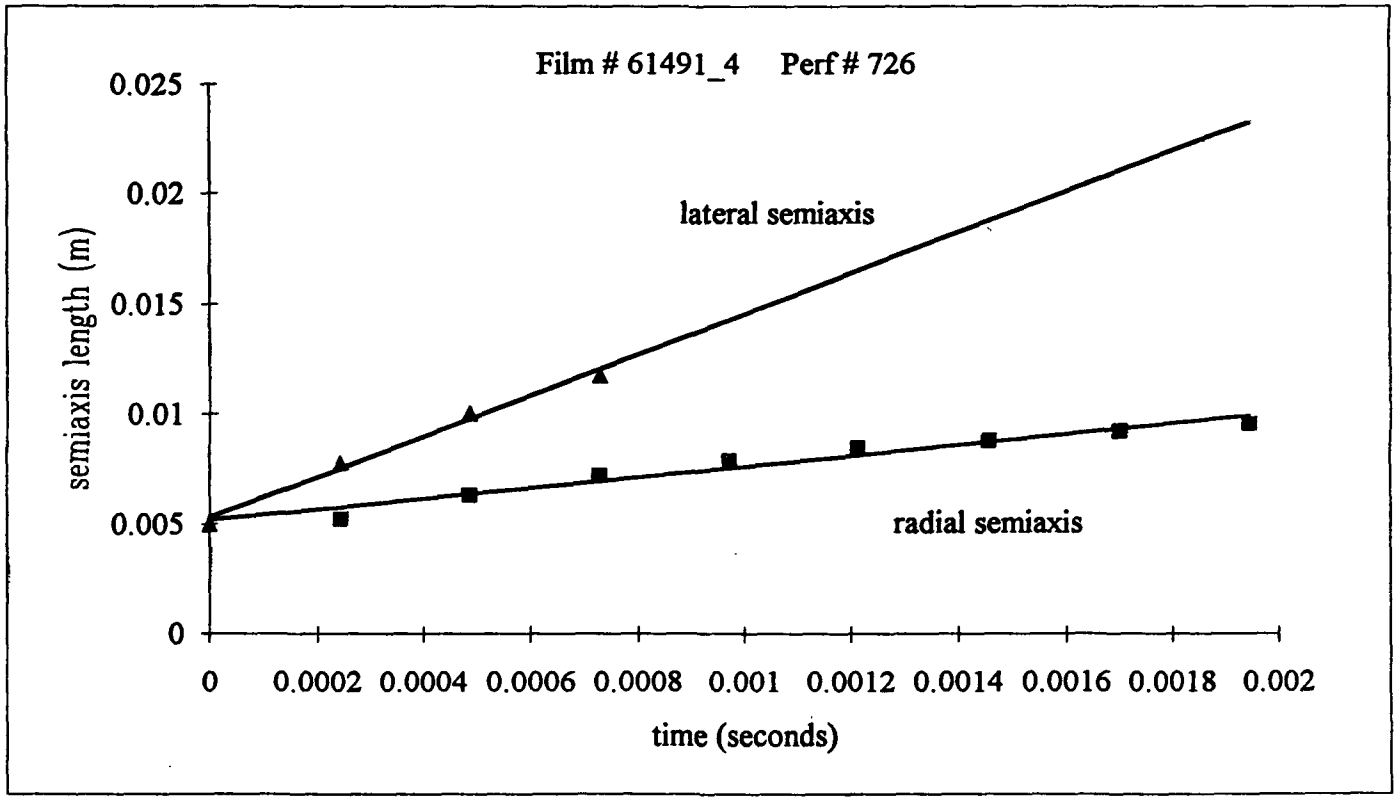
Film # 61491_4 Perf # 726
0.025
0.02
0.015
0.01
0.005
0
semiaxis length (m)
lateral semiaxis
radial semiaxis
0
0.0002
0.0004
0.0006
0.0008
0.001
0.0012
0.0014
0.0016
0.0018
0.002
time (seconds)

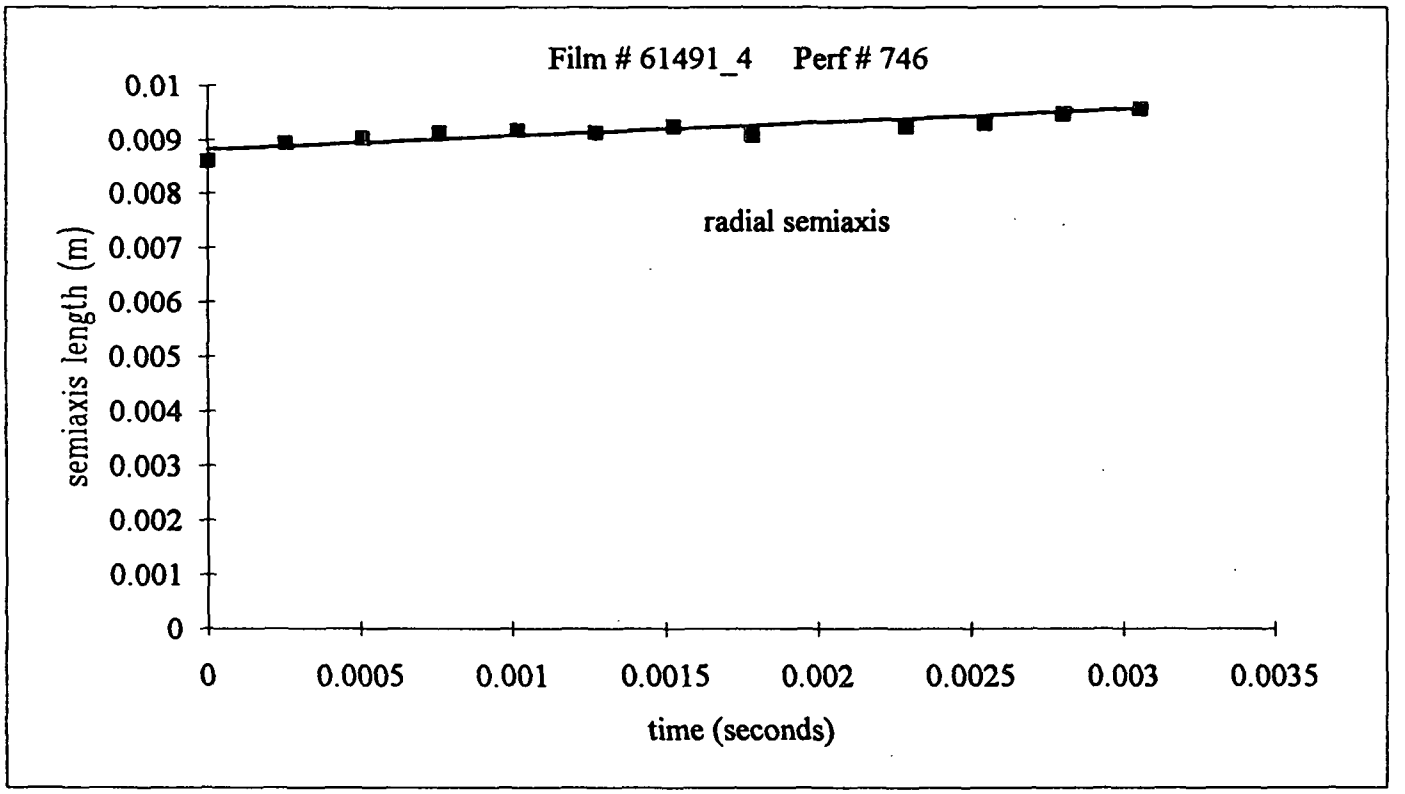
Film # 61491_4 Perf # 746
radial semiaxis
semiaxis length (m)
0.01
0.009
0.008
0.007
0.006
0.005
0.004
0.003
0.002
0.001
0
0
0.0005
0.001
0.0015
0.002
0.0025
0.003
0.0035
time (seconds)

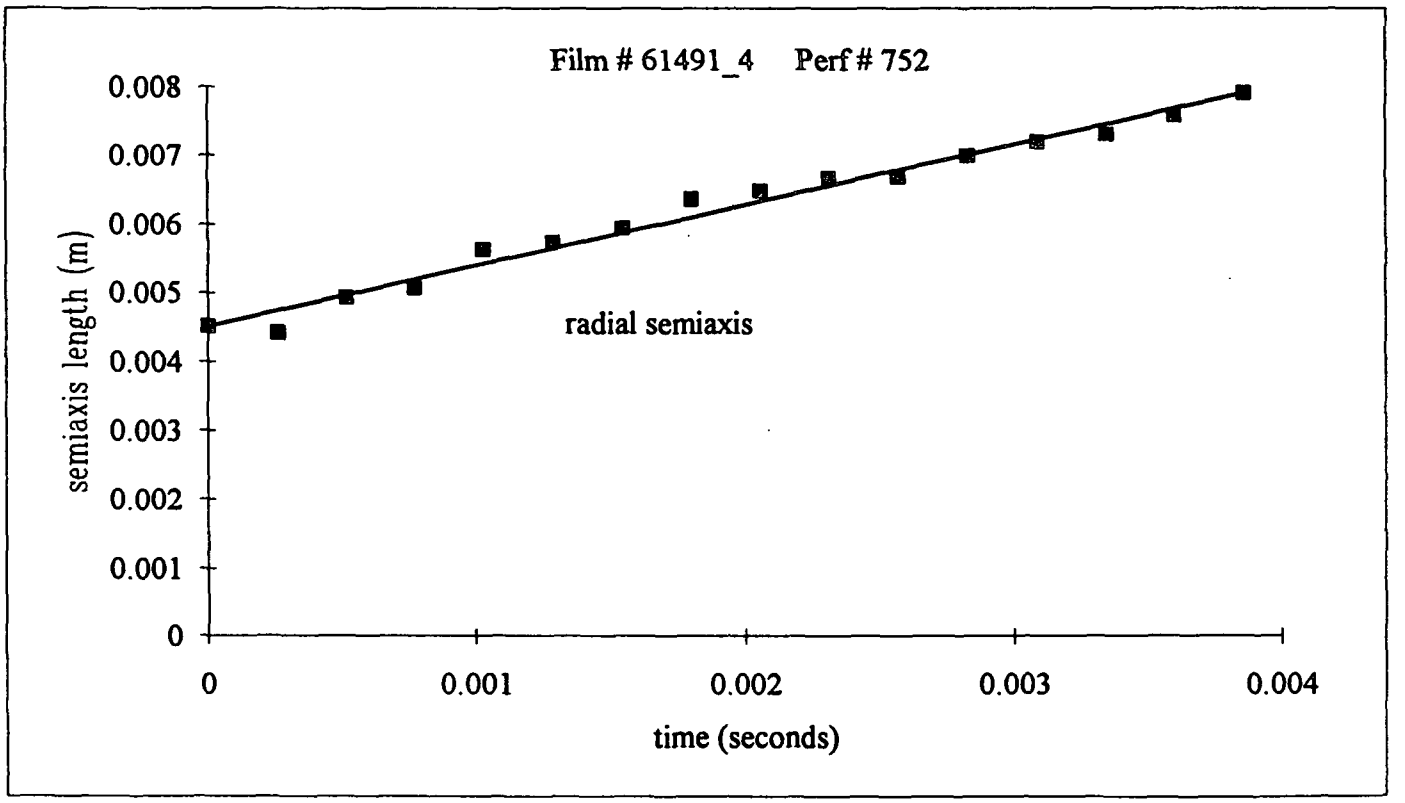
Film # 61491_4 Perf # 752
radial semiaxis
semiaxis length (m)
0.008
0.007
0.006
0.005
0.004
0.003
0.002
0.001
0
0
0.001
0.002
0.003
0.004
time (seconds)

Film # 93091_2
Perf # 9536
act/meas = 0. 0.471
dt = 0.00088

relative t (sec)	measured Radial	scaled Radial	relative t (sec)	measured lateral	scaled lateral	corrected lateral
0.00000	32.0	0.0075	0.00000	114.0	0.0268	0.026847
0.00088	38.0	0.0089	0.00088	118.0	0.0278	0.02751135
0.00176	41.0	0.0097	0.00176	129.0	0.0304	0.03009211
0.00264	45.0	0.0106	0.00264	133.0	0.0313	0.03100731
0.00351	48.0	0.0113	0.00351	139.0	0.0327	0.03241057
0.00439	51.0	0.0120	0.00439	146.0	0.0344	0.03404446

Film # 93091_2
Perf # 9570
act/meas = 0. 0.471
dt = 0.00095

relative t (sec)	measured Radial	scaled Radial	relative t (sec)	measured lateral	scaled lateral	corrected lateral
0.00000	13.0	0.0031	0.00000	15.0	0.0035	0.0035325
0.00095	19.0	0.0045	0.00095	21.0	0.0049	0.0049059
0.00190	25.0	0.0059	0.00190	31.0	0.0073	0.00724507
0.00286	31.0	0.0073	0.00286	40.0	0.0094	0.00933817
0.00381	35.0	0.0082	0.00381	49.0	0.0115	0.01143391
0.00476	42.0	0.0099	0.00476	57.0	0.0134	0.01329416
0.00571	48.0	0.0113	0.00571	67.0	0.0158	0.01562804
0.00667	54.0	0.0127	0.00667	76.0	0.0179	0.01772114
0.00762	61.0	0.0144	0.00762	85.0	0.0200	0.01981689
0.00857	66.0	0.0155	0.00857	93.0	0.0219	0.02167713

Film # 93091_2
Perf # 9584
act/meas = 0. 0.471
dt = 0.00095

relative t (sec)	measured Radial	scaled Radial
0.00000	7.0	0.0016
0.00095	9.0	0.0021
0.00190	20.0	0.0047
0.00285	27.0	0.0064
0.00380	31.0	0.0073
0.00475	37.0	0.0087
0.00570	44.0	0.0104
0.00665	48.0	0.0113
0.00760	51.0	0.0120
0.00855	52.0	0.0122

relative t (sec)	measured lateral	scaled lateral	corrected lateral
0.00000	6.0	0.0014	0.001413
0.00095	8.0	0.0019	0.00186821
0.00190	12.0	0.0028	0.00280494
0.00285	30.0	0.0071	0.00703341
0.00380	38.0	0.0089	0.00887004
0.00475	48.0	0.0113	0.01120398
0.00570	55.0	0.0130	0.01282616
0.00665	64.0	0.0151	0.01492723
0.00760	71.0	0.0167	0.01655204
0.00855	81.0	0.0191	0.01888862

Film # 93091_2
Perf # 9593
act/meas = 0. 0.471
dt = 0.00095

relative t (sec)	measured Radial	scaled Radial
0.00000	30.0	0.0071
0.00095	39.0	0.0092
0.00189	47.0	0.0111
0.00284	53.0	0.0125
0.00379	61.0	0.0144

relative t (sec)	measured lateral	scaled lateral	corrected lateral
0.00000	45.0	0.0106	0.0105975
0.00095	61.0	0.0144	0.01424739
0.00189	72.0	0.0170	0.01679589
0.00284	86.0	0.0203	0.02006402
0.00379	98.0	0.0231	0.02285328

Film # 93091_2
Perf # 9699
act/meas = 0. 0.471
dt = 0.00095

relative t (sec)	measured Radial	scaled Radial
0.00000	9.0	0.0021
0.00095	13.0	0.0031
0.00189	21.0	0.0049
0.00284	26.0	0.0061
0.00379	30.0	0.0071
0.00473	36.0	0.0085

relative t (sec)	measured lateral	scaled lateral	corrected lateral
0.00000	35.0	0.0082	0.0082425
0.00095	55.0	0.0130	0.01286064
0.00189	68.0	0.0160	0.01586964
0.00284	73.0	0.0172	0.01701302
0.00379	79.0	0.0186	0.0184129
0.00473	86.0	0.0203	0.02004565

Film #	93091_2
Perf #	9704
act/meas =	0. 0.471
dt =	0.00095

relative t (sec)	measured Radial	scaled Radial
0.00000	26.0	0.0061
0.00095	35.0	0.0082
0.00189	38.0	0.0089
0.00284	43.0	0.0101
0.00379	48.0	0.0113
0.00473	53.0	0.0125
0.00568	58.0	0.0137
0.00663	62.0	0.0146

relative t (sec)	measured lateral	scaled lateral	corrected lateral
0.00000	53.0	0.0125	0.0124815
0.00095	64.0	0.0151	0.01493289
0.00189	84.0	0.0198	0.01961402
0.00284	98.0	0.0231	0.02285853
0.00379	110.0	0.0259	0.02564778
0.00473	125.0	0.0294	0.02914879
0.00568	133.0	0.0313	0.03099342
0.00663	149.0	0.0351	0.03474042

Film # 93091_2
Perf # 9562
act/meas = 0.468
dt = 0.000937

relative t (sec)	measured Radial	scaled Radial
0.00000	33.2	0.0078
0.00094	40.0	0.0094
0.00187	44.4	0.0104
0.00281	50.5	0.0118
0.00375	54.0	0.0126
0.00469	55.3	0.0129
0.00562	65.0	0.0152
0.00656	70.2	0.0164
0.00750	76.0	0.0178
0.00843	82.1	0.0192
0.00937	84.9	0.0199
0.01031	89.8	0.0210
0.01125	92.2	0.0216
0.01218	94.2	0.0220
0.01312	98.2	0.0230
0.01406	101.7	0.0238
0.01500	105.1	0.0246
0.01593	108.9	0.0255
0.01687	113.3	0.0265
0.01781	116.0	0.0272
0.01874	118.7	0.0278

Film # 93091_2
Perf # 9669
act/meas = 0.468
dt = 0.00095

relative t (sec)	measured Radial	scaled Radial
0.00000	31.0	0.0073
0.00095	34.4	0.0081
0.00189	41.5	0.0097
0.00284	49.0	0.0115
0.00379	55.0	0.0129
0.00473	62.0	0.0145
0.00568	67.0	0.0157
0.00663	73.0	0.0171
0.00758	81.3	0.0190

Film # 93091_2
Perf # 9704
act/meas = 0.468
dt = 0.000947

relative t (sec)	measured Radial	scaled Radial
0.00000	32.5	0.0076
0.00095	43.0	0.0101
0.00189	45.5	0.0107
0.00284	46.0	0.0108
0.00379	52.2	0.0122
0.00473	56.2	0.0132
0.00568	60.2	0.0141
0.00663	67.3	0.0158
0.00758	72.8	0.0170
0.00852	78.2	0.0183
0.00947	83.3	0.0195
0.01042	86.8	0.0203
0.01136	91.0	0.0213
0.01231	96.5	0.0226

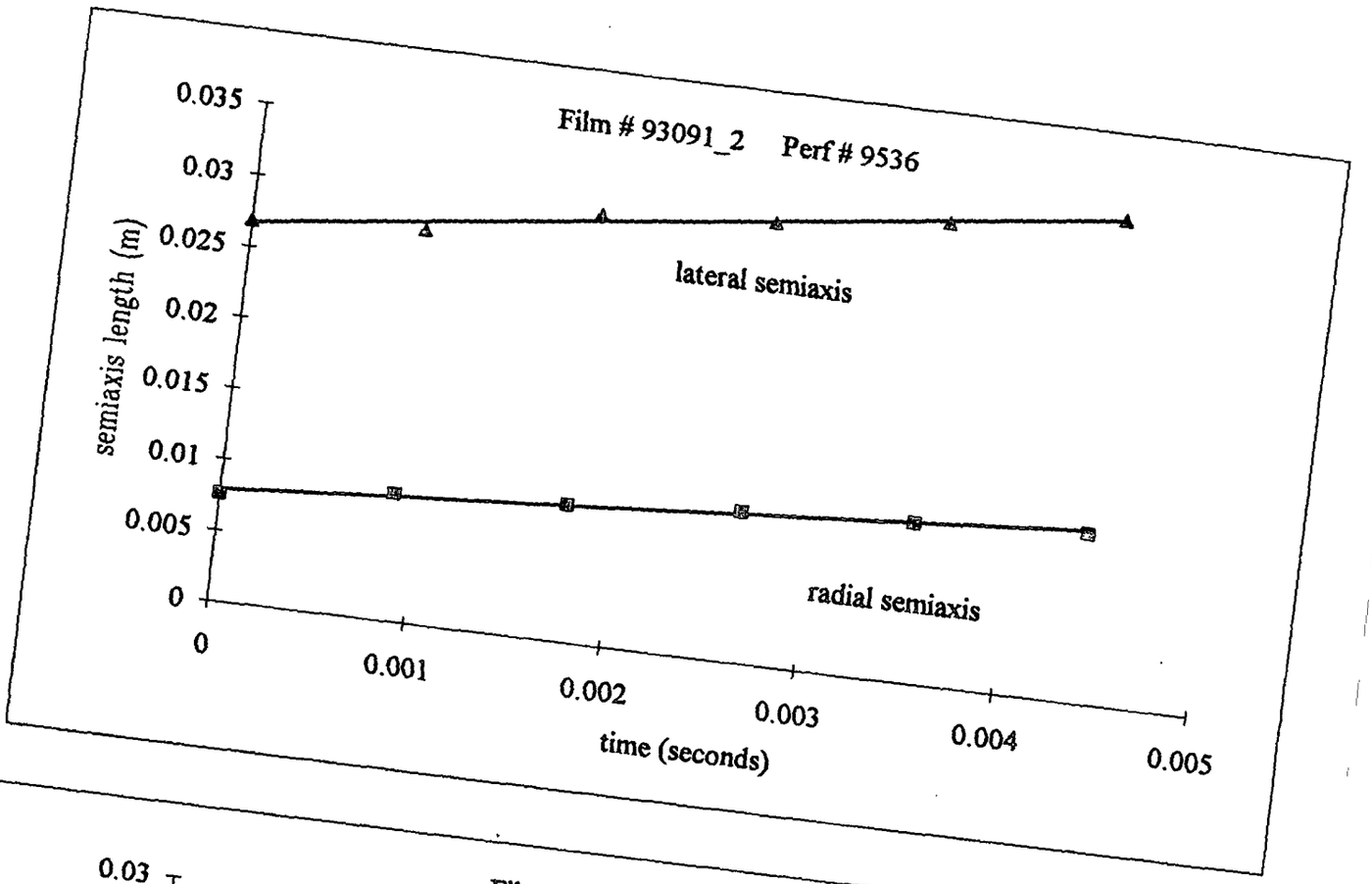
Film # 93091_2 Perf # 9536
lateral semiaxis
radial semiaxis
semiaxis length (m)
time (seconds)
0.035
0.03
0.025
0.02
0.015
0.01
0.005
0
0.001
0.002
0.003
0.004
0.005

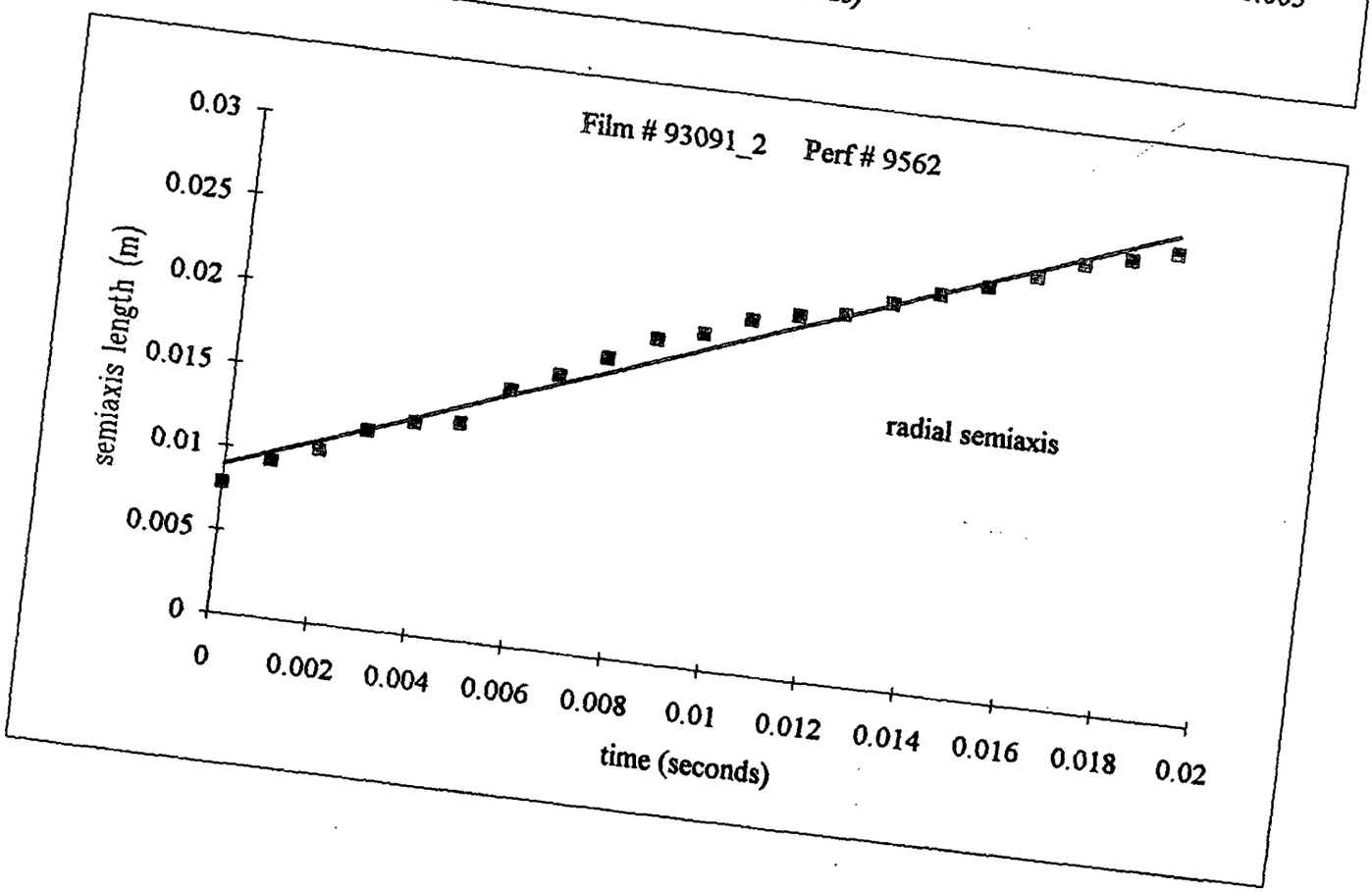
Film # 93091_2 Perf # 9562
radial semiaxis
semiaxis length (m)
time (seconds)
0.03
0.025
0.02
0.015
0.01
0.005
0
0.002
0.004
0.006
0.008
0.01
0.012
0.014
0.016
0.018
0.02

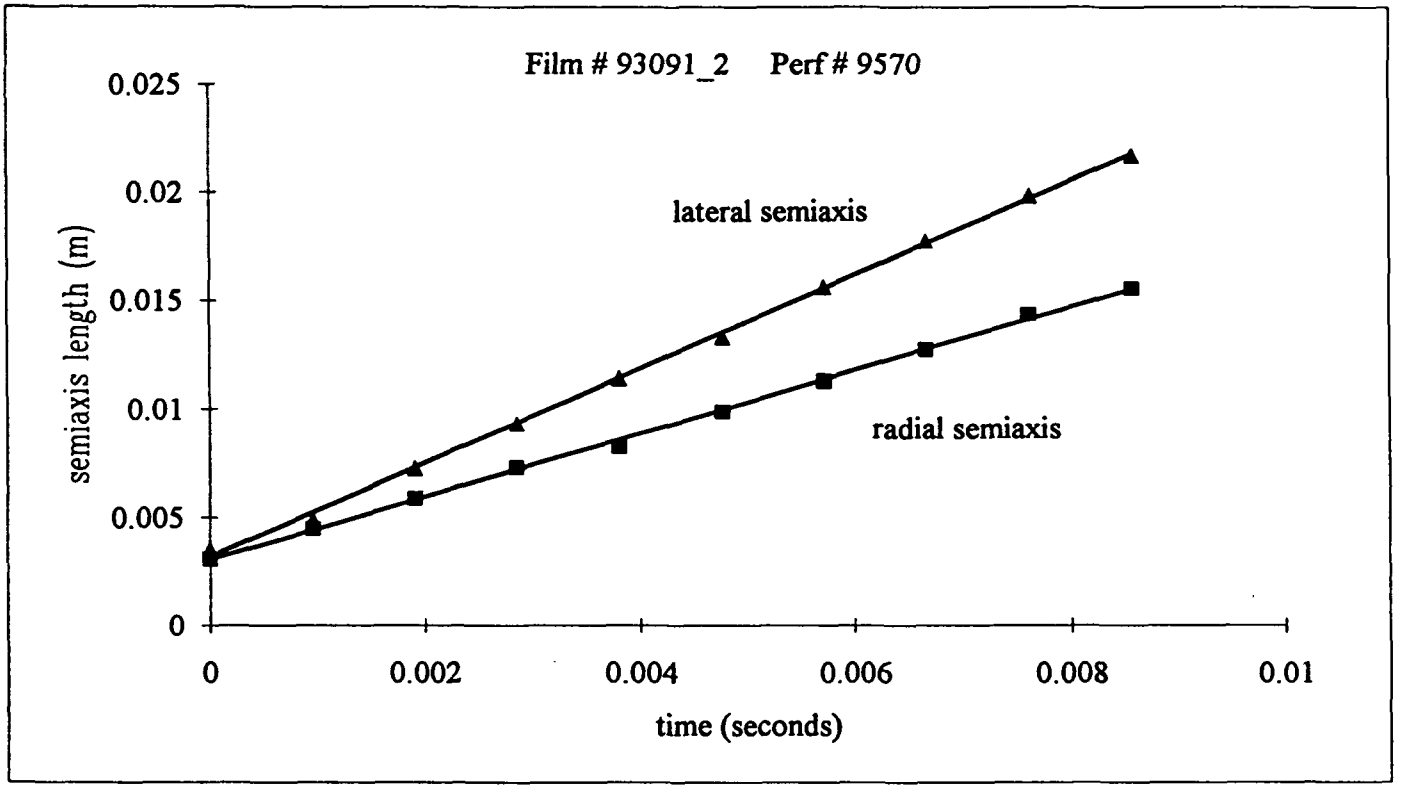
Film # 93091_2 Perf # 9570
0.025
0.02
0.015
0.01
0.005
0
semiaxis length (m)
lateral semiaxis
radial semiaxis
0
0.002
0.004
0.006
0.008
0.01
time (seconds)

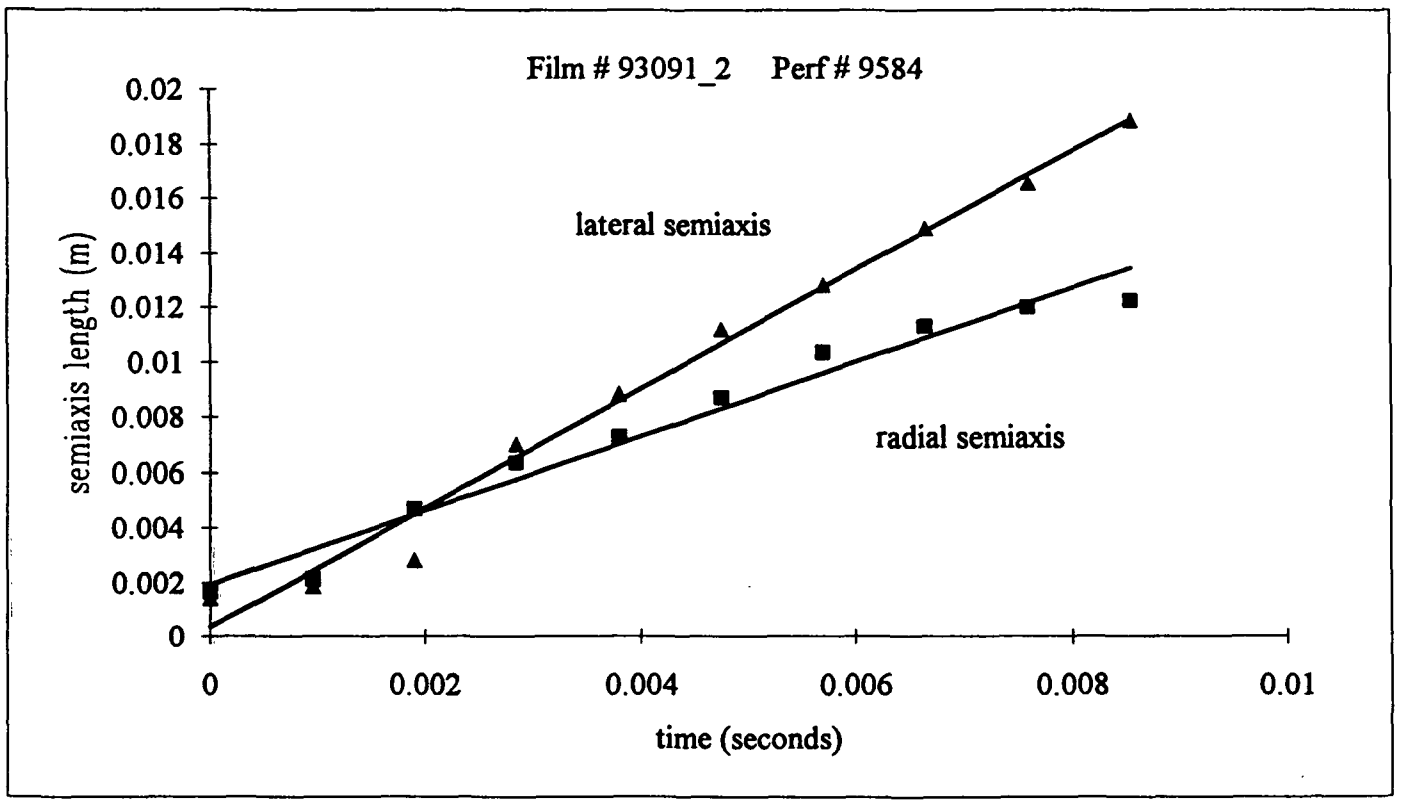
Film # 93091_2 Perf # 9584
0.02
0.018
0.016
0.014
0.012
0.01
0.008
0.006
0.004
0.002
0
semiaxis length (m)
lateral semiaxis
radial semiaxis
0
0.002
0.004
0.006
0.008
0.01
time (seconds)

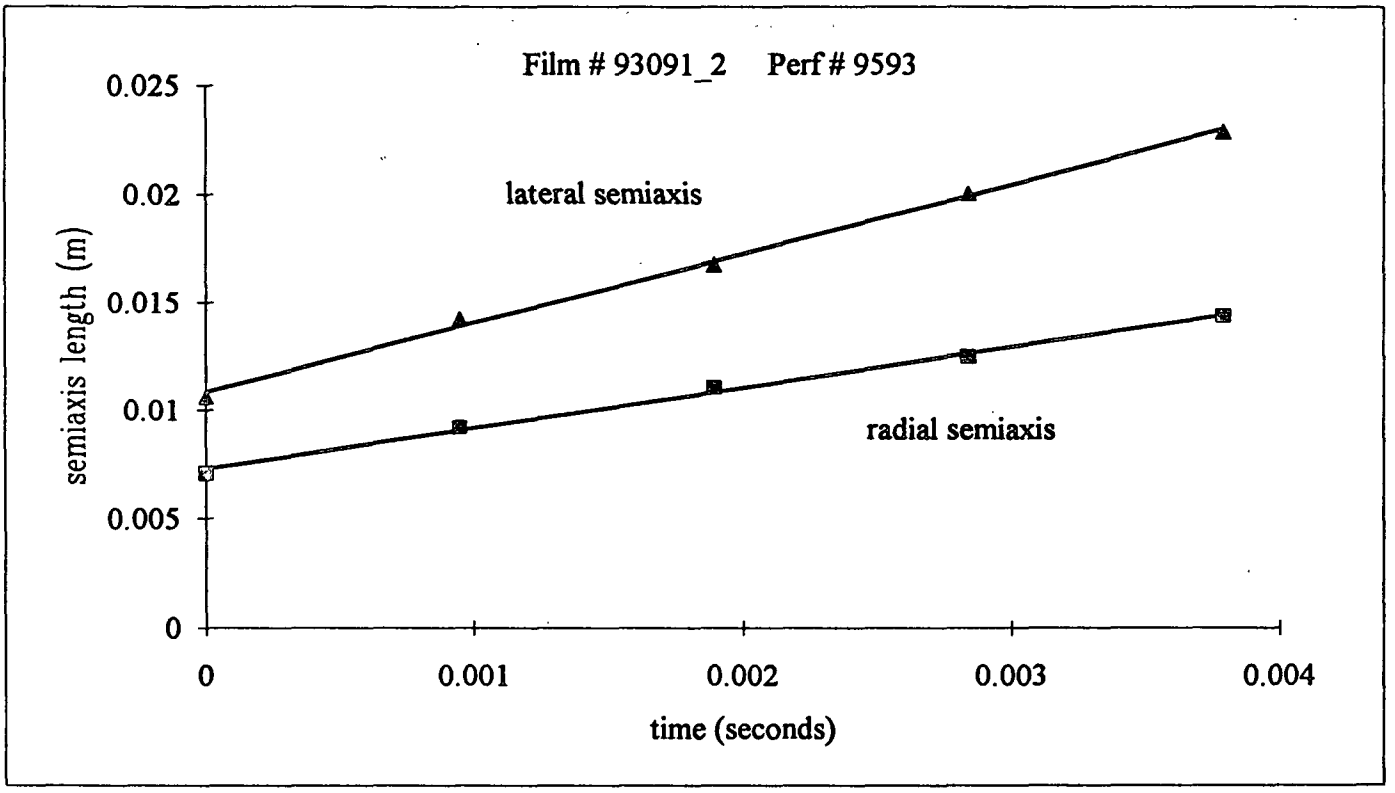
Film # 93091_2 Perf # 9593
lateral semiaxis
radial semiaxis
semiaxis length (m)
0.025
0.02
0.015
0.01
0.005
0
0
0.001
0.002
0.003
0.004
time (seconds)

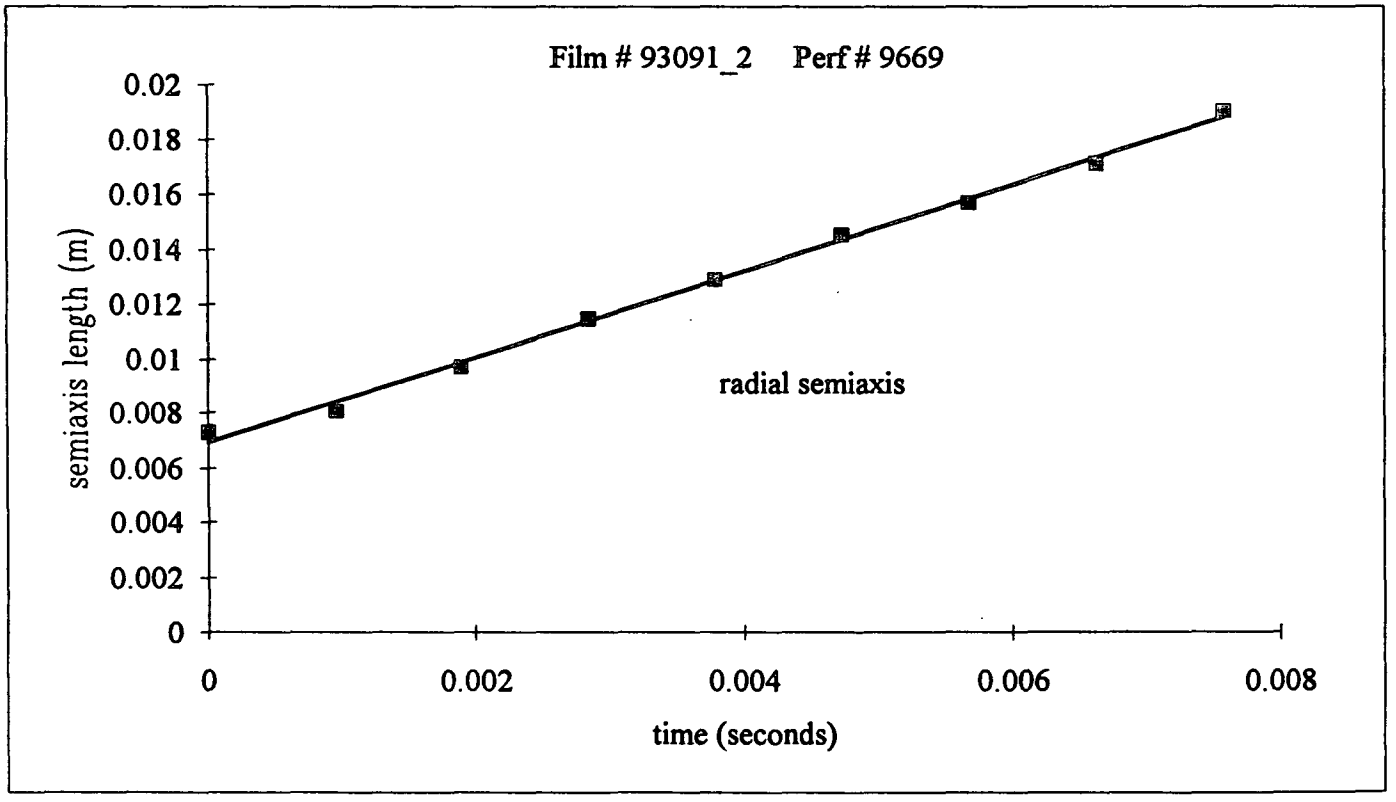
Film # 93091_2 Perf # 9669
radial semiaxis
semiaxis length (m)
0.02
0.018
0.016
0.014
0.012
0.01
0.008
0.006
0.004
0.002
0
0
0.002
0.004
0.006
0.008
time (seconds)

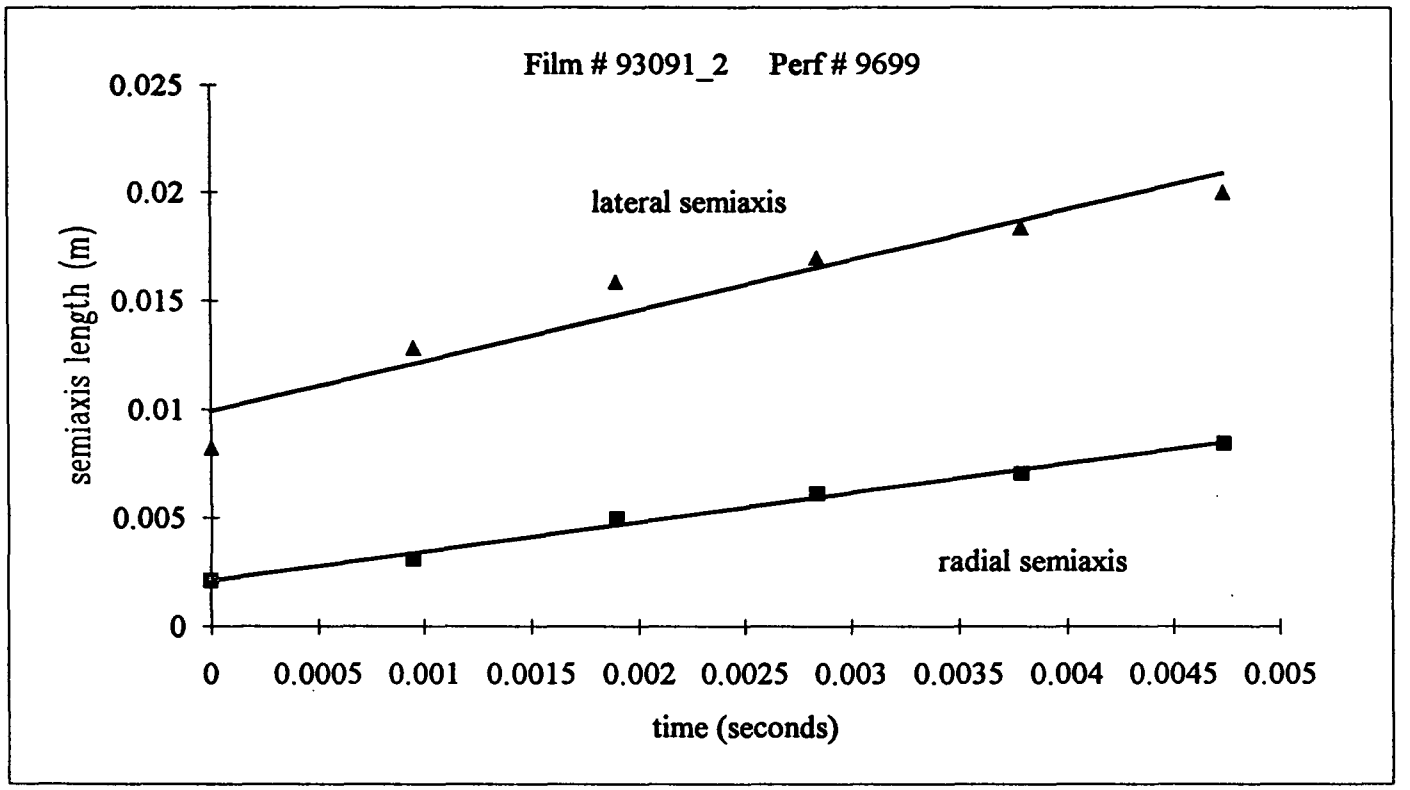
Film # 93091_2 Perf # 9699
lateral semiaxis
radial semiaxis
semiaxis length (m)
0.025
0.02
0.015
0.01
0.005
0
0 0.0005 0.001 0.0015 0.002 0.0025 0.003 0.0035 0.004 0.0045 0.005
time (seconds)

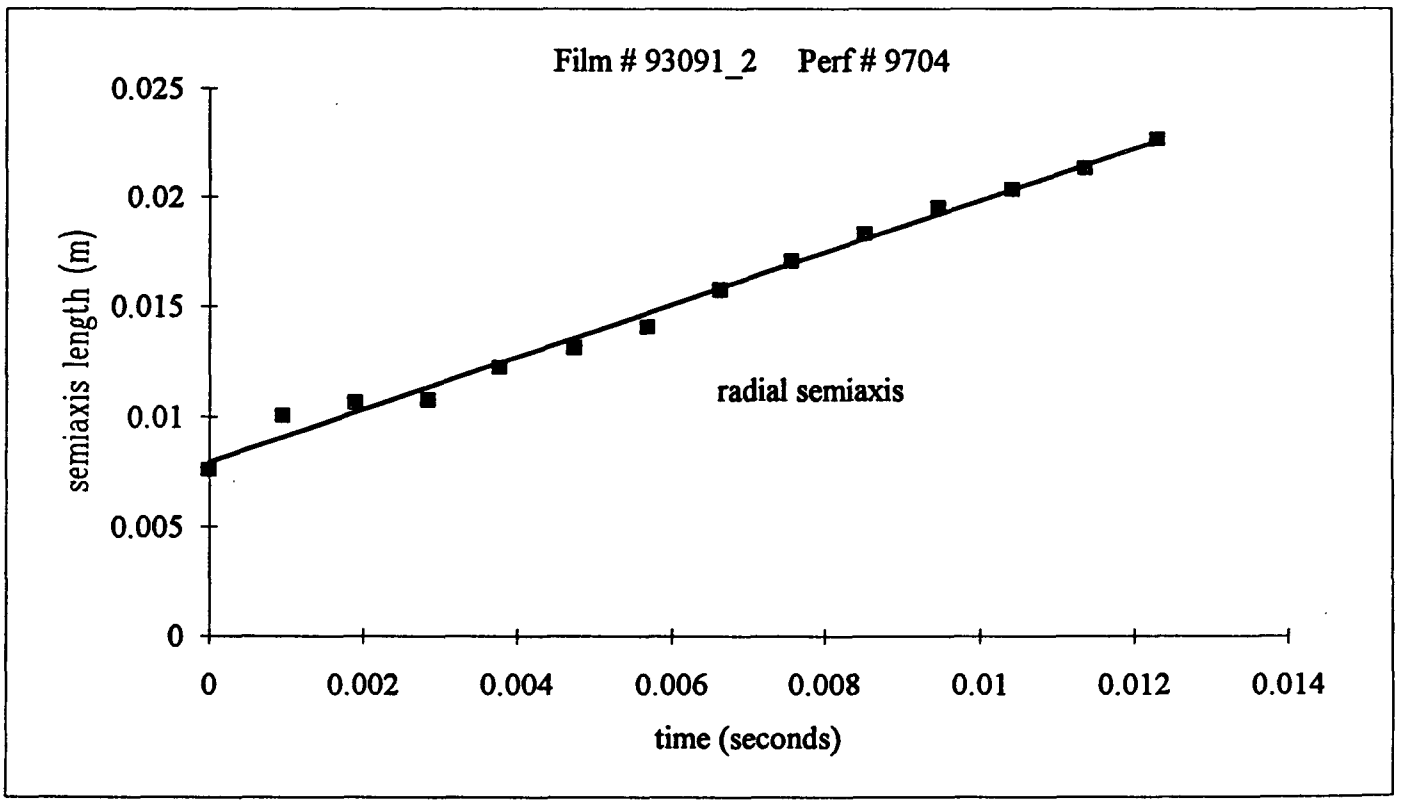
Film # 93091_2 Perf # 9704
radial semiaxis
semiaxis length (m)
0.025
0.02
0.015
0.01
0.005
0
0 0.002 0.004 0.006 0.008 0.01 0.012 0.014
time (seconds)

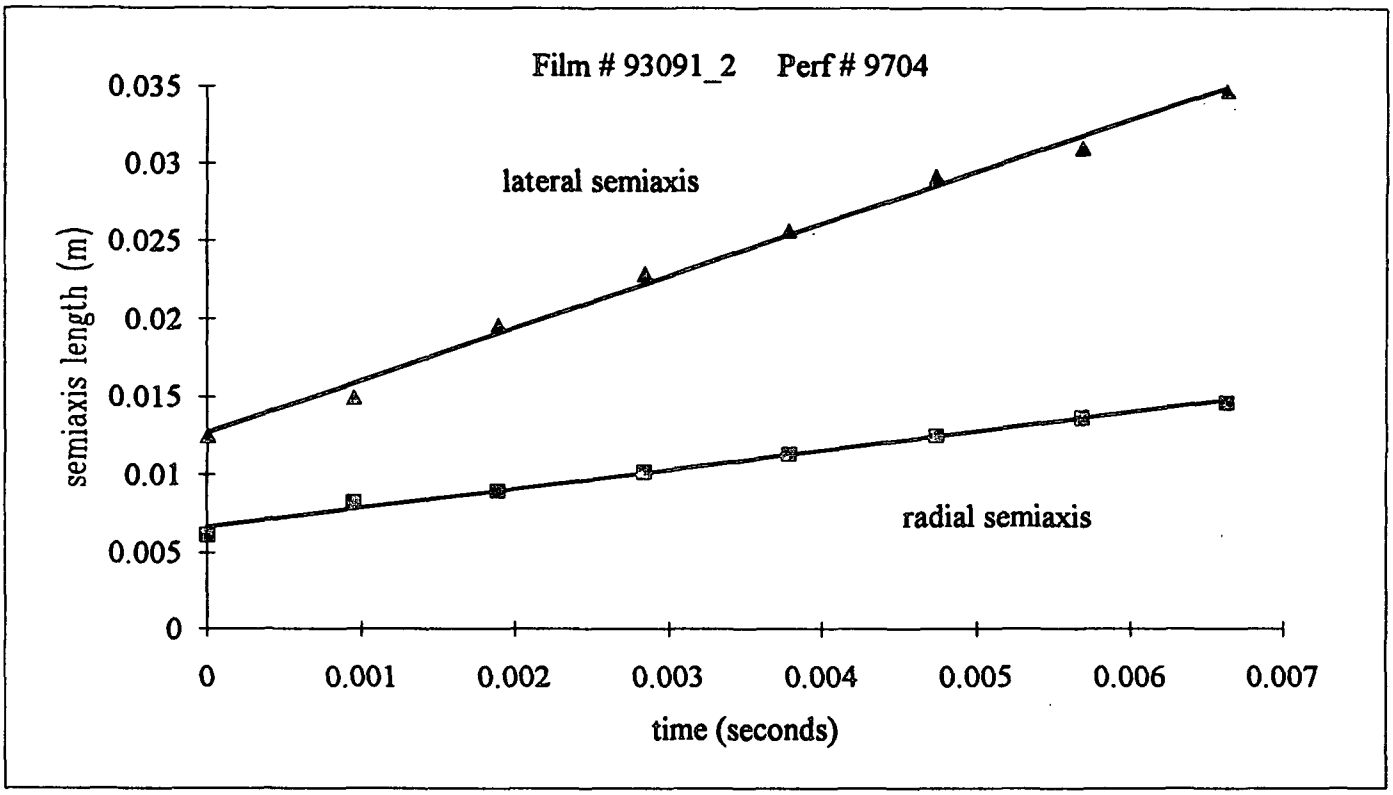
Film # 93091_2 Perf # 9704
lateral semiaxis
radial semiaxis
semiaxis length (m)
0.035
0.03
0.025
0.02
0.015
0.01
0.005
0
0
0.001
0.002
0.003
0.004
0.005
0.006
0.007
time (seconds)

Film # 93091_3
Perf # 3736
act/meas = 0.468
dt = 0.00088

relative t (sec)	measured Radial	scaled Radial	relative t (sec)	measured lateral	scaled lateral	corrected lateral
0.00000	20.3	0.0048	0.00000	23.5	0.0055	0.0055017
0.00088	27.8	0.0065	0.00088	35.7	0.0084	0.00829353
0.00177	35.0	0.0082	0.00177	49.0	0.0115	0.01137385
0.00265	38.7	0.0091	0.00265	64.0	0.0150	0.01484914
0.00353	43.5	0.0102	0.00353	70.5	0.0165	0.0163298
0.00441	44.0	0.0103	0.00441	81.0	0.0190	0.0187702
0.00530	51.0	0.0119	0.00530	92.0	0.0215	0.0213167

Film # 93091_3
Perf # 3735
act/meas = 0.468
dt = 0.00089

relative t (sec)	measured Radial	scaled Radial	relative t (sec)	measured lateral	scaled lateral	corrected lateral
0.00000	15.0	0.0035	0.00000	20.5	0.0048	0.00479936
0.00089	19.5	0.0046	0.00089	31.5	0.0074	0.00731847
0.00178	28.0	0.0066	0.00178	40.0	0.0094	0.00927831
0.00267	31.5	0.0074	0.00267	50.0	0.0117	0.01159618
0.00356	33.0	0.0077	0.00356	58.0	0.0136	0.01344171
0.00444	33.5	0.0078	0.00444	66.0	0.0155	0.01529272
0.00533	33.5	0.0078	0.00533	76.0	0.0178	0.01761195
0.00622	36.0	0.0084	0.00622	85.0	0.0199	0.0196916

Film # 93091_3
Perf # 3747
act/meas = 0.468
dt = 0.00096

relative t (sec)	measured Radial	scaled Radial	relative t (sec)	measured lateral	scaled lateral	corrected lateral
0.00000	9.0	0.0021	0.00000	13.5	0.0032	0.00316055
0.00097	19.5	0.0046	0.00097	32.0	0.0075	0.0074547
0.00193	24.0	0.0056	0.00193	40.0	0.0094	0.00927695
0.00290	29.5	0.0069	0.00290	51.0	0.0119	0.0118303
0.00386	30.5	0.0071	0.00386	62.0	0.0145	0.01437543
0.00483	29.0	0.0068	0.00483	72.0	0.0169	0.01668645
0.00579	30.0	0.0070	0.00579	81.0	0.0190	0.01876609
0.00676	30.0	0.0070	0.00676	88.0	0.0206	0.02038024

Film # 93091_3
Perf # 3755
act/meas = 0.468
dt = 0.001

relative t (sec)	measured Radial	scaled Radial	relative t (sec)	measured lateral	scaled lateral	corrected lateral
0.00000	10.5	0.0025	0.00000	13.5	0.0032	0.00316055
0.00100	22.0	0.0052	0.00100	28.0	0.0066	0.00651824
0.00200	29.5	0.0069	0.00200	36.0	0.0084	0.00835144
0.00300	34.5	0.0081	0.00300	49.0	0.0115	0.01137302
0.00400	41.0	0.0096	0.00400	57.5	0.0135	0.01332739
0.00500	46.0	0.0108	0.00500	68.0	0.0159	0.01576232
0.00600	51.5	0.0121	0.00600	77.0	0.0180	0.01784059
0.00700	56.0	0.0131	0.00700	89.0	0.0208	0.02062532
0.00800	60.0	0.0140	0.00800	96.0	0.0225	0.02223125

Film # 93091_3
Perf # 3758
act/meas = 0.468
dt = 0.00094

relative t (sec)	measured Radial	scaled Radial	relative t (sec)	measured lateral	scaled lateral	corrected lateral
0.00000	13.0	0.0030	0.00000	16.0	0.0037	0.00374584
0.00094	24.0	0.0056	0.00094	29.0	0.0068	0.00674551
0.00189	33.5	0.0078	0.00189	41.0	0.0096	0.00951928
0.00283	41.0	0.0096	0.00283	52.0	0.0122	0.01206167
0.00378	48.0	0.0112	0.00378	63.0	0.0147	0.01460681
0.00472	55.5	0.0130	0.00472	74.0	0.0173	0.01715194
0.00567	64.5	0.0151	0.00567	83.0	0.0194	0.01922884
0.00661	72.0	0.0169	0.00661	94.0	0.0220	0.02177946
0.00755	76.0	0.0178	0.00755	102.0	0.0239	0.02362224

Film # 93091_3
Perf # 3777
act/meas = 0.468
dt = 0.00094

relative t (sec)	measured Radial	scaled Radial	relative t (sec)	measured lateral	scaled lateral	corrected lateral
0.00000	8.0	0.0019	0.00000	13.0	0.0030	0.0030435
0.00094	12.0	0.0028	0.00094	20.0	0.0047	0.00464669
0.00189	19.5	0.0046	0.00189	32.0	0.0075	0.0074369
0.00283	24.5	0.0057	0.00283	42.0	0.0098	0.00974518
0.00378	32.0	0.0075	0.00378	51.0	0.0119	0.01182482
0.00472	35.0	0.0082	0.00472	59.0	0.0138	0.01367309
0.00567	41.0	0.0096	0.00567	67.0	0.0157	0.01552409
0.00661	44.0	0.0103	0.00661	76.0	0.0178	0.01760921
0.00755	49.0	0.0115	0.00755	85.0	0.0199	0.0196916

Film # 93091_3
Perf # 3779
act/meas = 0.468
dt = 0.00095

relative t (sec)	measured Radial	scaled Radial	relative t (sec)	measured lateral	scaled lateral	corrected lateral
0.00000	10.0	0.0023	0.00000	14.0	0.0033	0.00327761
0.00095	16.0	0.0037	0.00095	24.0	0.0056	0.00558041
0.00189	33.0	0.0077	0.00189	37.0	0.0087	0.00859651
0.00284	39.0	0.0091	0.00284	52.0	0.0122	0.01207263
0.00379	42.0	0.0098	0.00379	60.0	0.0140	0.01390446

Film # 93091_3
Perf # 3782
act/meas = 0.468
dt = 0.00095

relative t (sec)	measured Radial	scaled Radial	relative t (sec)	measured lateral	scaled lateral	corrected lateral
0.00000	13.0	0.0030	0.00000	13.0	0.0030	0.0030435
0.00095	24.5	0.0057	0.00095	25.0	0.0059	0.00581727
0.00189	33.0	0.0077	0.00189	36.5	0.0085	0.00847672
0.00284	42.0	0.0098	0.00284	48.0	0.0112	0.01113754
0.00379	53.0	0.0124	0.00379	59.0	0.0138	0.0136813
0.00473	64.0	0.0150	0.00473	71.0	0.0166	0.01646055

Film # 93091_3
Perf # 3785
act/meas = 0.468
dt = 0.00095

relative t (sec)	measured Radial	scaled Radial
0.00000	10.0	0.0023
0.00095	24.0	0.0056
0.00189	28.5	0.0067
0.00284	33.5	0.0078
0.00379	39.0	0.0091
0.00473	46.5	0.0109
0.00568	54.5	0.0128
0.00663	60.0	0.0140
0.00758	67.5	0.0158
0.00852	72.5	0.0170
0.00947	78.0	0.0183

relative t (sec)	measured lateral	scaled lateral	corrected lateral
0.00000	11.0	0.0026	0.00257527
0.00095	28.0	0.0066	0.00652509
0.00189	39.5	0.0092	0.00917084
0.00284	49.5	0.0116	0.01148049
0.00379	59.0	0.0138	0.01367719
0.00473	69.0	0.0162	0.01599232
0.00568	79.5	0.0186	0.01842314
0.00663	91.0	0.0213	0.0210867
0.00758	99.5	0.0233	0.02304517
0.00852	111.0	0.0260	0.02571421
0.00947	120.0	0.0281	0.02778975

Film # 93091_3
Perf # 3804
act/meas = 0.468
dt = 0.00095

relative t (sec)	measured Radial	scaled Radial	relative t (sec)	measured lateral	scaled lateral	corrected lateral
0.00000	8.0	0.0019	0.00000	7.5	0.0018	0.00175586
0.00095	13.5	0.0032	0.00095	13.0	0.0030	0.00302295
0.00189	23.5	0.0055	0.00189	25.0	0.0059	0.00581727
0.00284	30.0	0.0070	0.00284	36.0	0.0084	0.00835966
0.00379	39.0	0.0091	0.00379	46.5	0.0109	0.01078774
0.00473	46.5	0.0109	0.00473	55.5	0.0130	0.01286601
0.00568	51.0	0.0119	0.00568	64.0	0.0150	0.01483133
0.00663	58.5	0.0137	0.00663	74.0	0.0173	0.0171492
0.00758	65.5	0.0153	0.00758	85.5	0.0200	0.01981413
0.00852	73.0	0.0171	0.00852	94.0	0.0220	0.02177261
0.00947	77.0	0.0180	0.00947	104.5	0.0245	0.02420753
0.01042	76.0	0.0178	0.01042	116.0	0.0272	0.02687109
0.01136	76.0	0.0178	0.01136	127.0	0.0297	0.02941486
0.01231	77.5	0.0181	0.01231	138.5	0.0324	0.03207705

Film # 93091_3
Perf # 3834
act/meas = 0.468
dt = 0.00095

relative t (sec)	measured Radial	scaled Radial	relative t (sec)	measured lateral	scaled lateral	corrected lateral
0.00000	12.0	0.0028	0.00000	22.0	0.0052	0.00515053
0.00095	19.5	0.0046	0.00095	34.0	0.0080	0.00789965
0.00189	27.0	0.0063	0.00189	49.0	0.0115	0.0113785
0.00284	35.0	0.0082	0.00284	61.0	0.0143	0.01414679
0.00379	39.5	0.0092	0.00379	74.5	0.0174	0.01727448
0.00473	46.0	0.0108	0.00473	87.0	0.0204	0.02016393
0.00568	51.5	0.0121	0.00568	101.0	0.0236	0.0234073

Film # 93091_3
Perf # 3848
act/meas = 0.468
dt = 0.00095

relative t (sec)	measured Radial	scaled Radial	relative t (sec)	measured lateral	scaled lateral	corrected lateral
0.00000	13.5	0.0032	0.00000	19.5	0.0046	0.00456524
0.00095	19.0	0.0044	0.00095	28.0	0.0066	0.00650181
0.00189	26.0	0.0061	0.00189	39.0	0.0091	0.00905379
0.00284	32.0	0.0075	0.00284	50.0	0.0117	0.01159892
0.00379	40.0	0.0094	0.00379	58.0	0.0136	0.01344171
0.00473	54.0	0.0126	0.00473	70.0	0.0164	0.01622918
0.00568	62.0	0.0145	0.00568	79.0	0.0185	0.01830334
0.00663	72.0	0.0169	0.00663	93.0	0.0218	0.0215563

Film # 93091_3
Perf # 3851
act/meas = 0.468
dt = 0.00095

relative t (sec)	measured Radial	scaled Radial	relative t (sec)	measured lateral	scaled lateral	corrected lateral
0.00000	10.0	0.0023	0.00000	10.0	0.0023	0.00234115
0.00095	30.0	0.0070	0.00095	27.5	0.0064	0.00641077
0.00189	41.0	0.0096	0.00189	43.0	0.0101	0.00999162
0.00284	58.0	0.0136	0.00284	57.0	0.0133	0.01322677
0.00379	73.0	0.0171	0.00379	69.0	0.0162	0.0159978

Film # 93091_3
Perf # 3855
act/meas = 0.468
dt = 0.00095

relative t (sec)	measured Radial	scaled Radial	relative t (sec)	measured lateral	scaled lateral	corrected lateral
0.00000	28.0	0.0066	0.00000	44.0	0.0103	0.01030106
0.00095	24.1	0.0056	0.00095	59.5	0.0139	0.01380932
0.00189	51.0	0.0119	0.00189	73.0	0.0171	0.01692741

Film # 93091_3
Perf # 3902
act/meas = 0.468
dt = 0.00095

relative t (sec)	measured Radial	scaled Radial
0.00000	17.0	0.0040
0.00095	29.0	0.0068
0.00191	39.5	0.0092
0.00286	47.5	0.0111
0.00382	57.0	0.0133

relative t (sec)	measured lateral	scaled lateral	corrected lateral
0.00000	16.5	0.0039	0.0038629
0.00095	35.5	0.0083	0.00826589
0.00191	50.5	0.0118	0.01172557
0.00286	69.0	0.0162	0.0160156
0.00382	83.0	0.0194	0.01924254

Film # 93091_3
Perf # 3911
act/meas = 0.468
dt = 0.00095

relative t (sec)	measured Radial	scaled Radial
0.00000	18.0	0.0042
0.00095	24.0	0.0056
0.00190	31.5	0.0074
0.00285	38.5	0.0090
0.00380	47.5	0.0111
0.00475	53.0	0.0124
0.00570	58.5	0.0137
0.00665	58.0	0.0136

relative t (sec)	measured lateral	scaled lateral	corrected lateral
0.00000	22.0	0.0052	0.00515053
0.00095	46.5	0.0109	0.01082608
0.00190	62.5	0.0146	0.01450481
0.00285	78.0	0.0183	0.01808977
0.00380	89.0	0.0208	0.02062258
0.00475	101.0	0.0236	0.02340183
0.00570	110.0	0.0258	0.02547599
0.00665	123.0	0.0288	0.02849483

Film # 93091_3
Perf # 3912
act/meas = 0.468
dt = 0.00094

relative t (sec)	measured Radial	scaled Radial
0.00000	13.0	0.0030
0.00094	17.0	0.0040
0.00187	21.0	0.0049
0.00281	28.0	0.0066
0.00375	34.0	0.0080

relative t (sec)	measured lateral	scaled lateral	corrected lateral
0.00000	24.0	0.0056	0.00561876
0.00094	31.5	0.0074	0.00730888
0.00187	36.5	0.0085	0.00845891
0.00281	47.0	0.0110	0.01090342
0.00375	55.5	0.0130	0.01286464

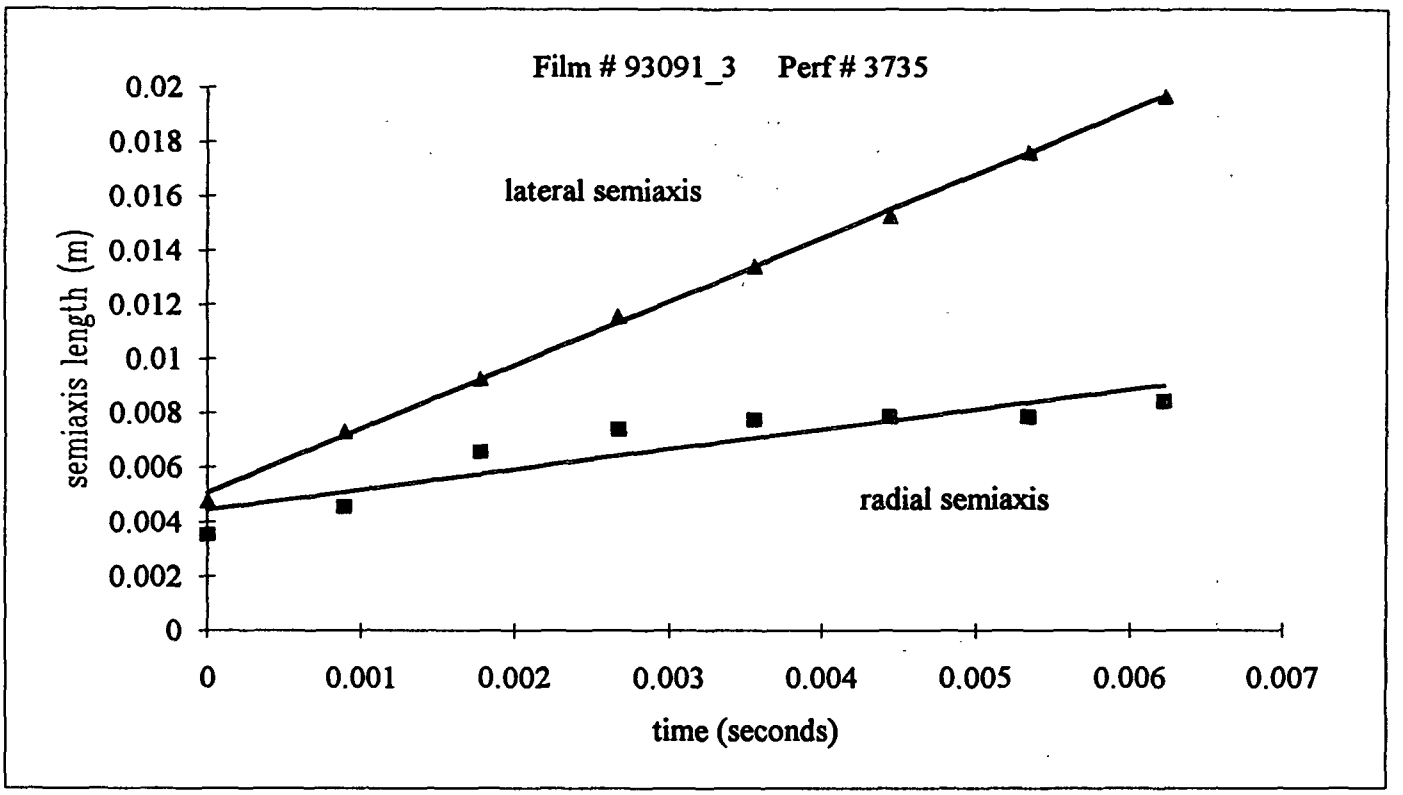
Film # 93091_3 Perf # 3735
lateral semiaxis
radial semiaxis
semiaxis length (m)
time (seconds)
0.02
0.018
0.016
0.014
0.012
0.01
0.008
0.006
0.004
0.002
0
0.001
0.002
0.003
0.004
0.005
0.006
0.007

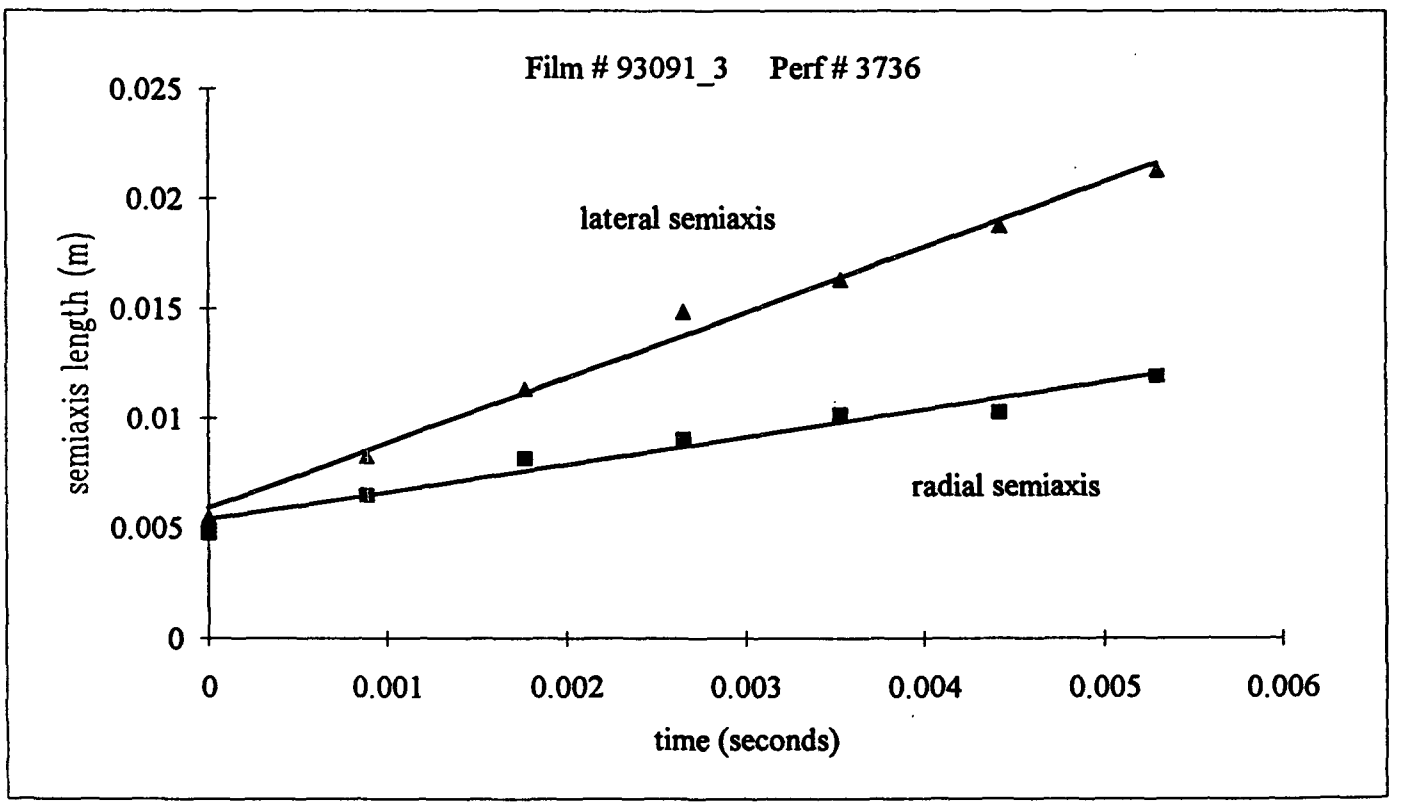
Film # 93091_3 Perf # 3736
lateral semiaxis
radial semiaxis
semiaxis length (m)
time (seconds)
0.025
0.02
0.015
0.01
0.005
0
0.001
0.002
0.003
0.004
0.005
0.006

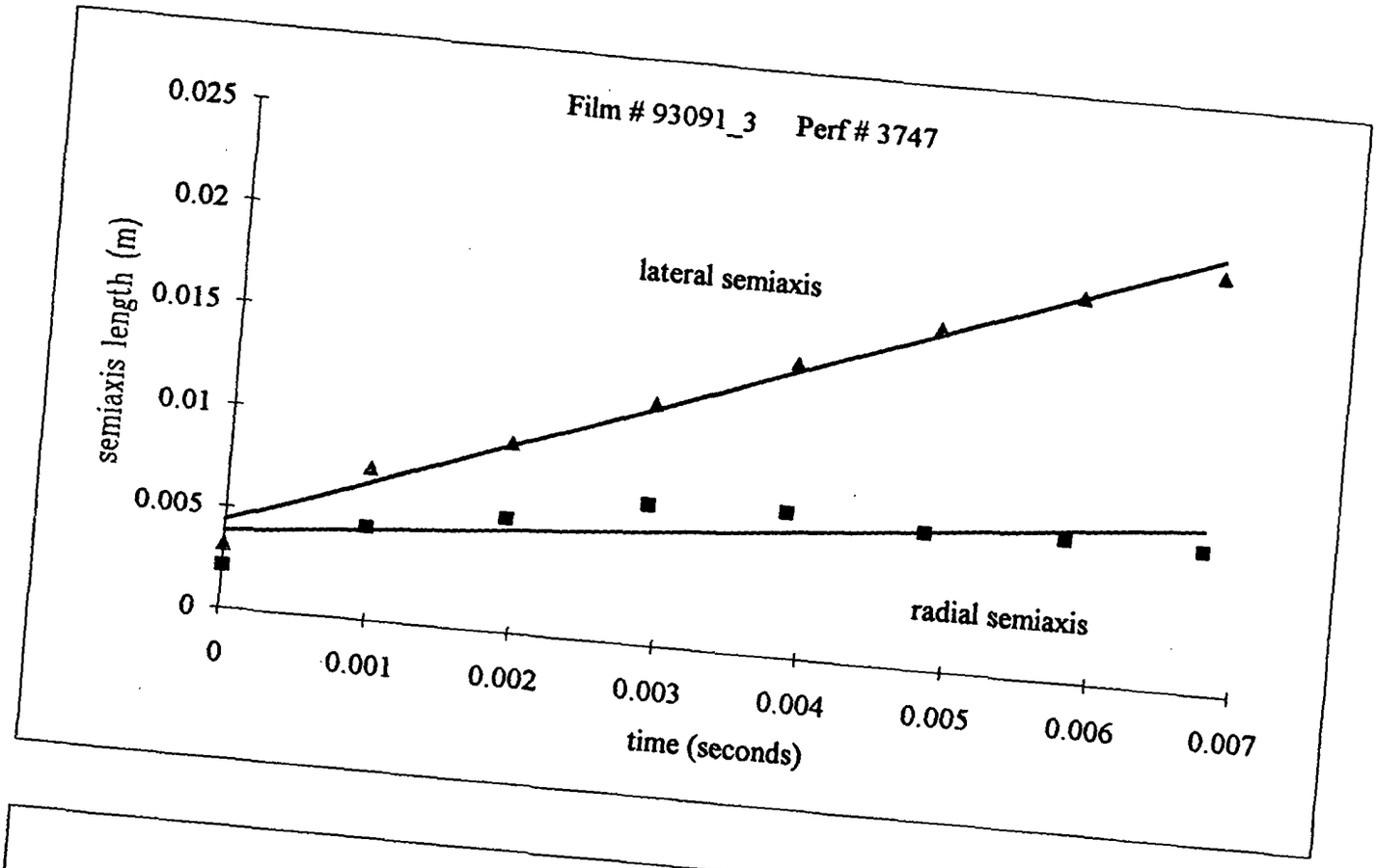
Film # 93091_3 Perf # 3747
semiaxis length (m)
0.025
0.02
0.015
0.01
0.005
0
lateral semiaxis
radial semiaxis
0
0.001
0.002
0.003
0.004
0.005
0.006
0.007
time (seconds)

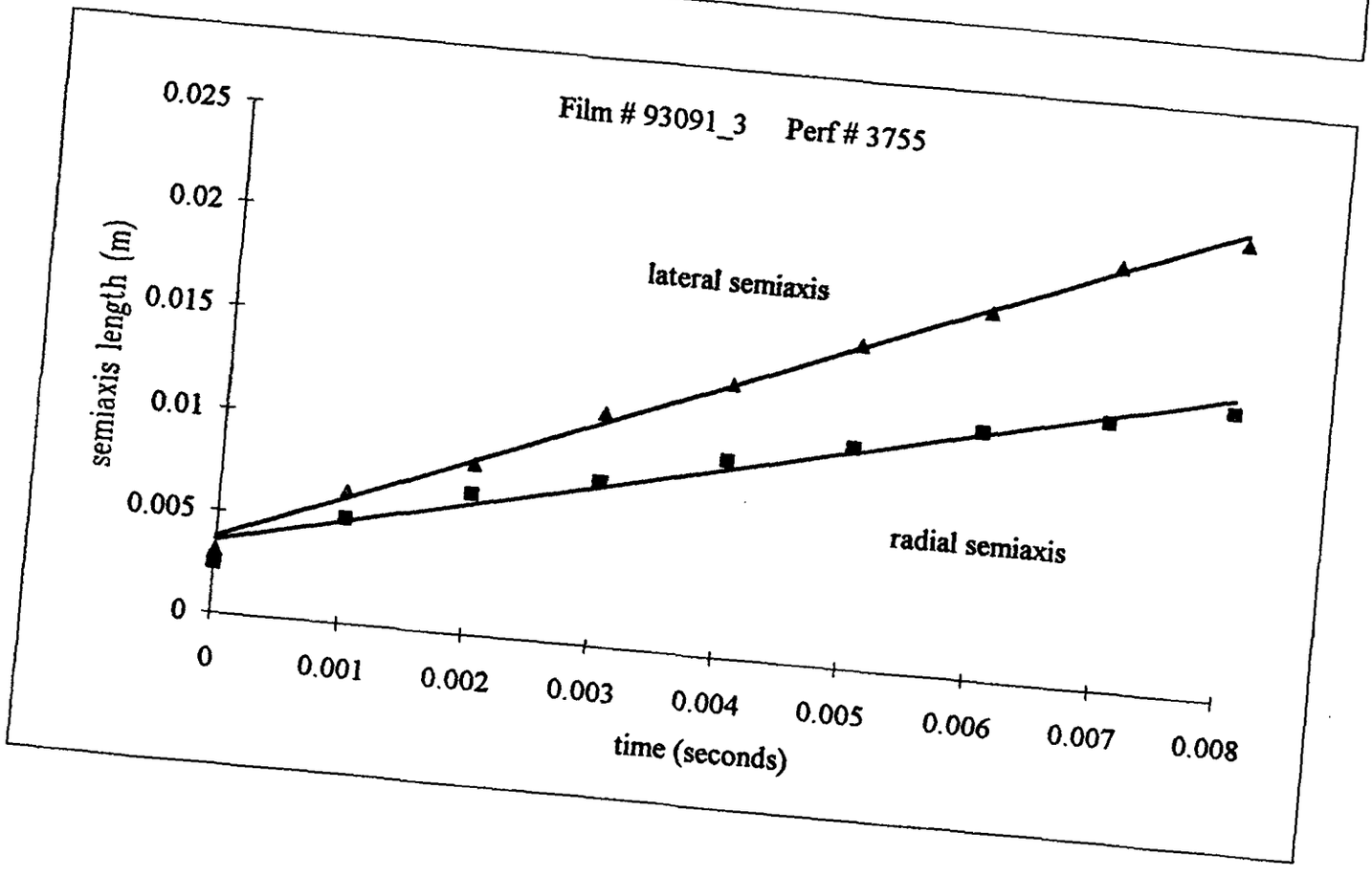
Film # 93091_3 Perf # 3755
semiaxis length (m)
0.025
0.02
0.015
0.01
0.005
0
lateral semiaxis
radial semiaxis
0
0.001
0.002
0.003
0.004
0.005
0.006
0.007
0.008
time (seconds)

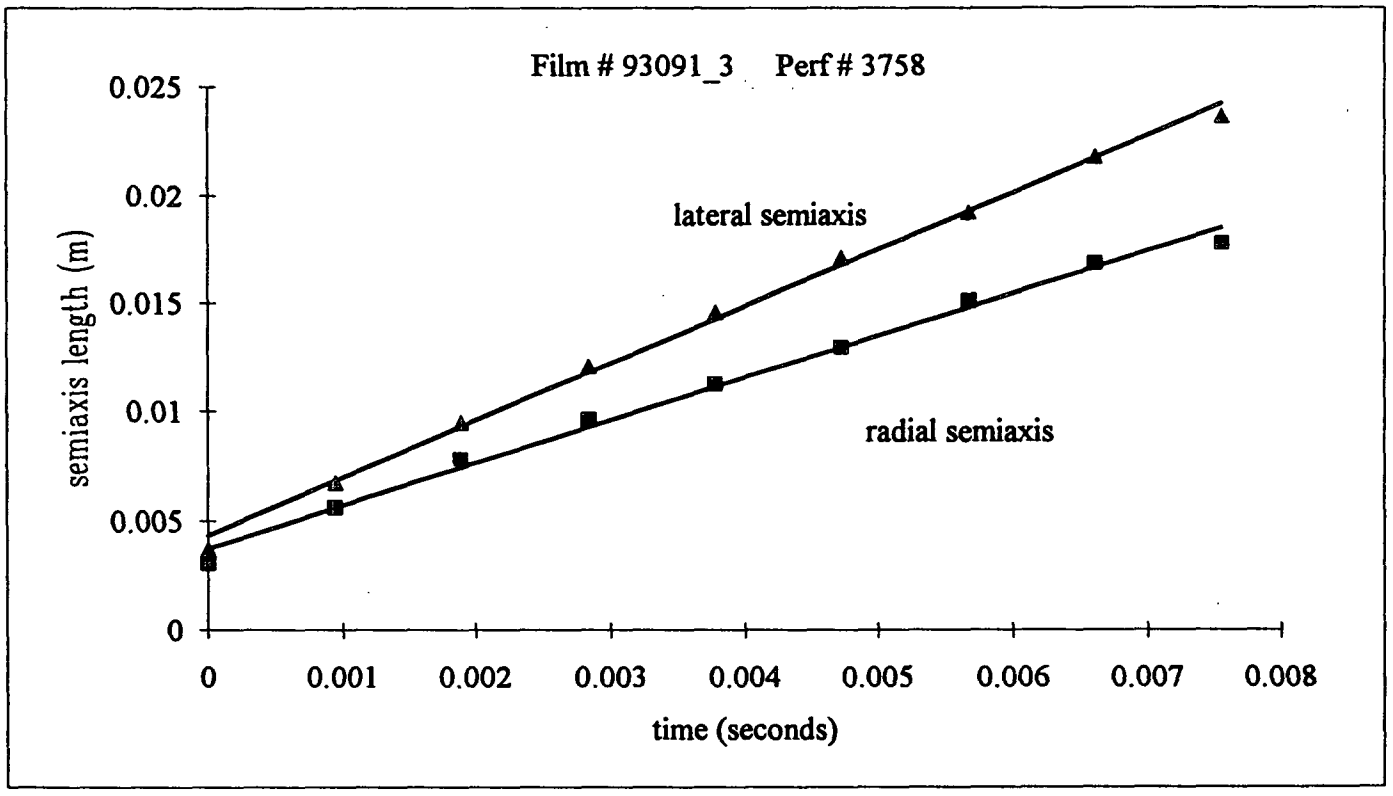
Film # 93091_3 Perf # 3758
0.025
0.02
0.015
0.01
0.005
0
semiaxis length (m)
lateral semiaxis
radial semiaxis
0
0.001
0.002
0.003
0.004
0.005
0.006
0.007
0.008
time (seconds)

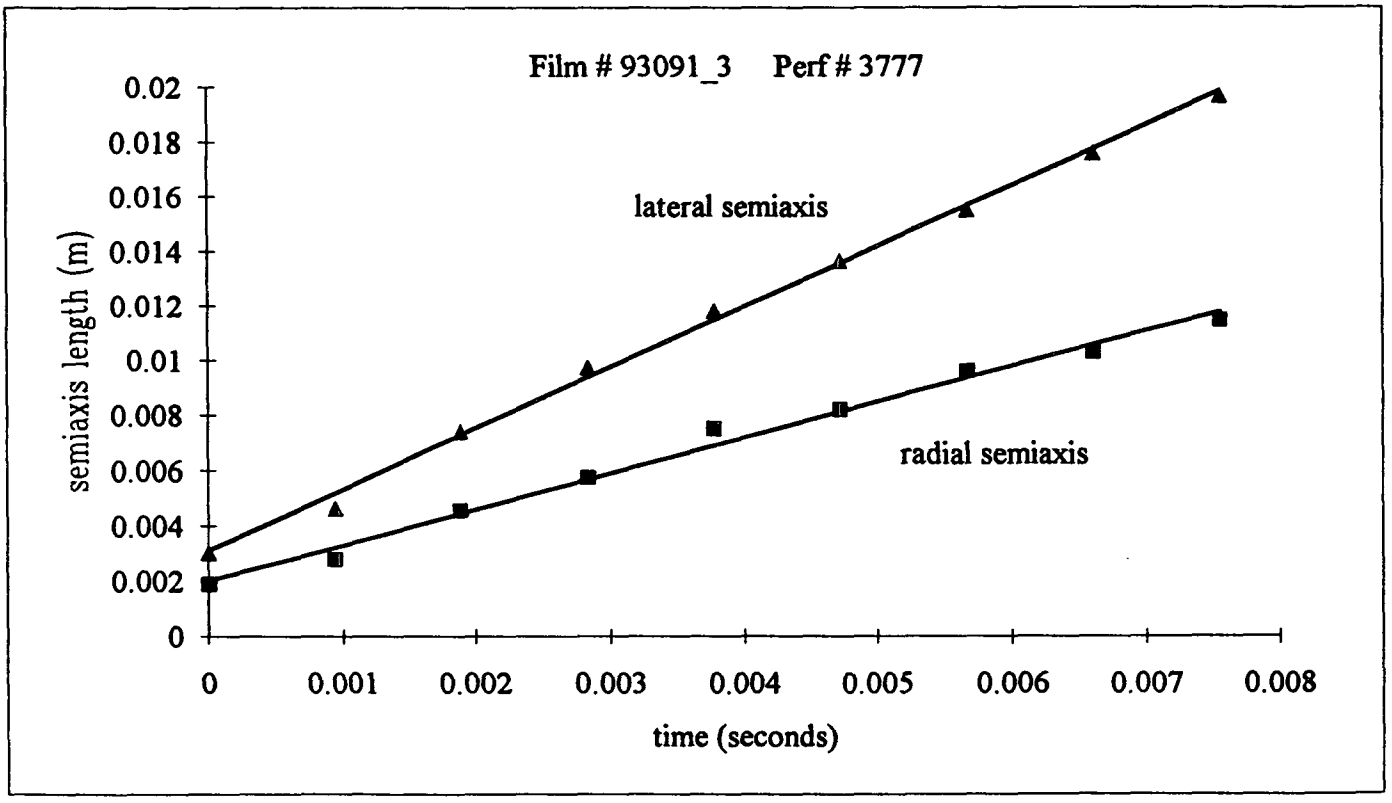
Film # 93091_3 Perf # 3777
0.02
0.018
0.016
0.014
0.012
0.01
0.008
0.006
0.004
0.002
0
semiaxis length (m)
lateral semiaxis
radial semiaxis
0
0.001
0.002
0.003
0.004
0.005
0.006
0.007
0.008
time (seconds)

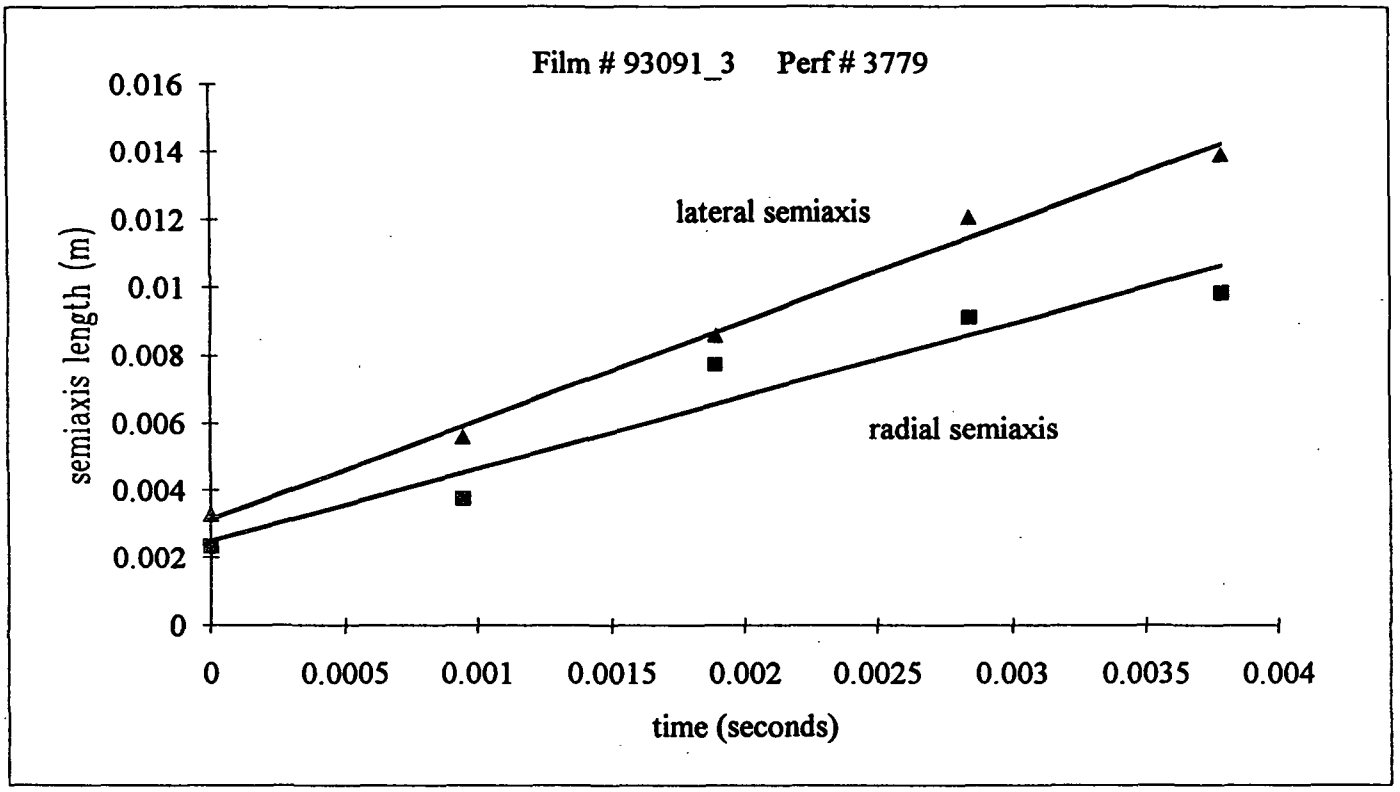
Film # 93091_3 Perf # 3779
semiaxis length (m)
0.016
0.014
0.012
0.01
0.008
0.006
0.004
0.002
0
lateral semiaxis
radial semiaxis
0
0.0005
0.001
0.0015
0.002
0.0025
0.003
0.0035
0.004
time (seconds)

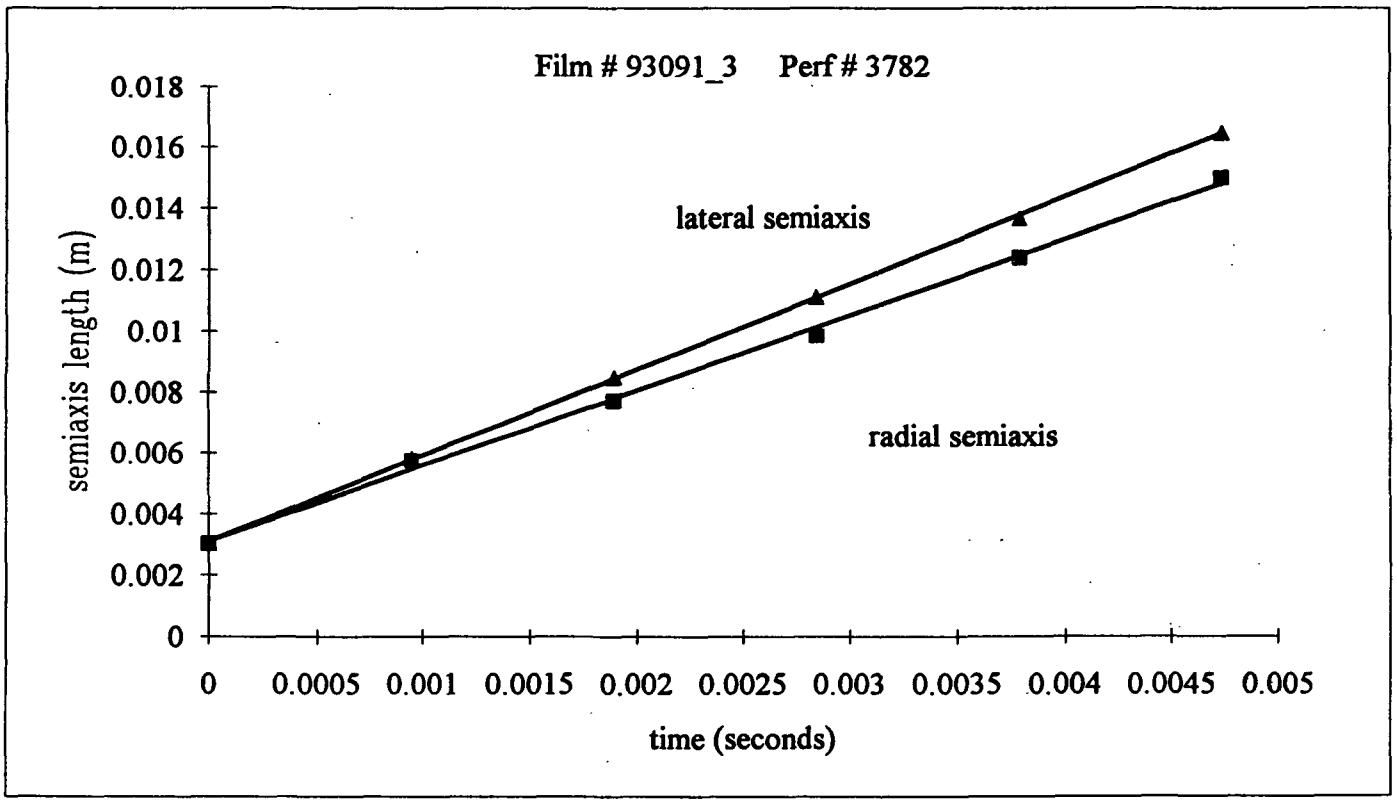
Film # 93091_3 Perf # 3782
semiaxis length (m)
0.018
0.016
0.014
0.012
0.01
0.008
0.006
0.004
0.002
0
lateral semiaxis
radial semiaxis
0
0.0005
0.001
0.0015
0.002
0.0025
0.003
0.0035
0.004
0.0045
0.005
time (seconds)

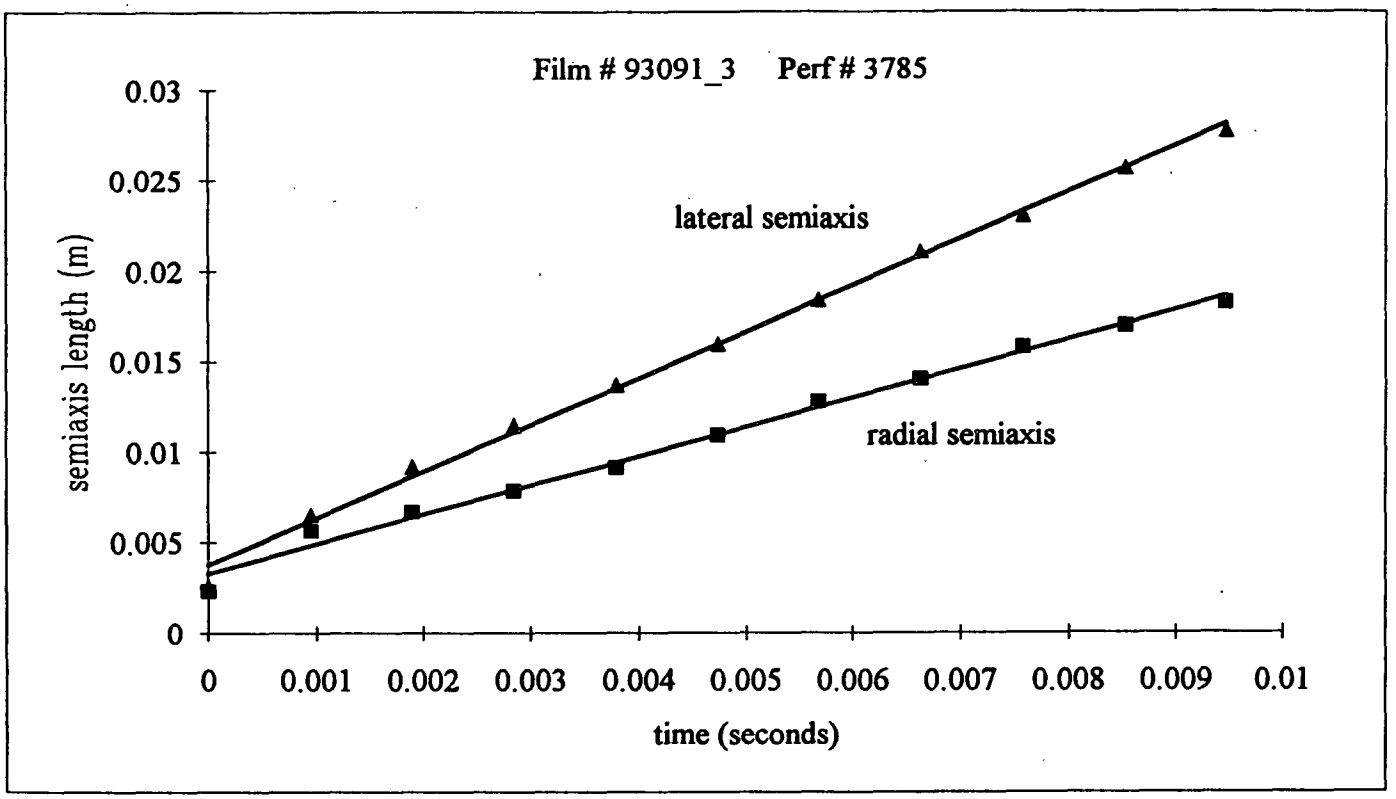
Film # 93091_3 Perf # 3785
semiaxis length (m)
0.03
0.025
0.02
0.015
0.01
0.005
0
lateral semiaxis
radial semiaxis
0
0.001
0.002
0.003
0.004
0.005
0.006
0.007
0.008
0.009
0.01
time (seconds)

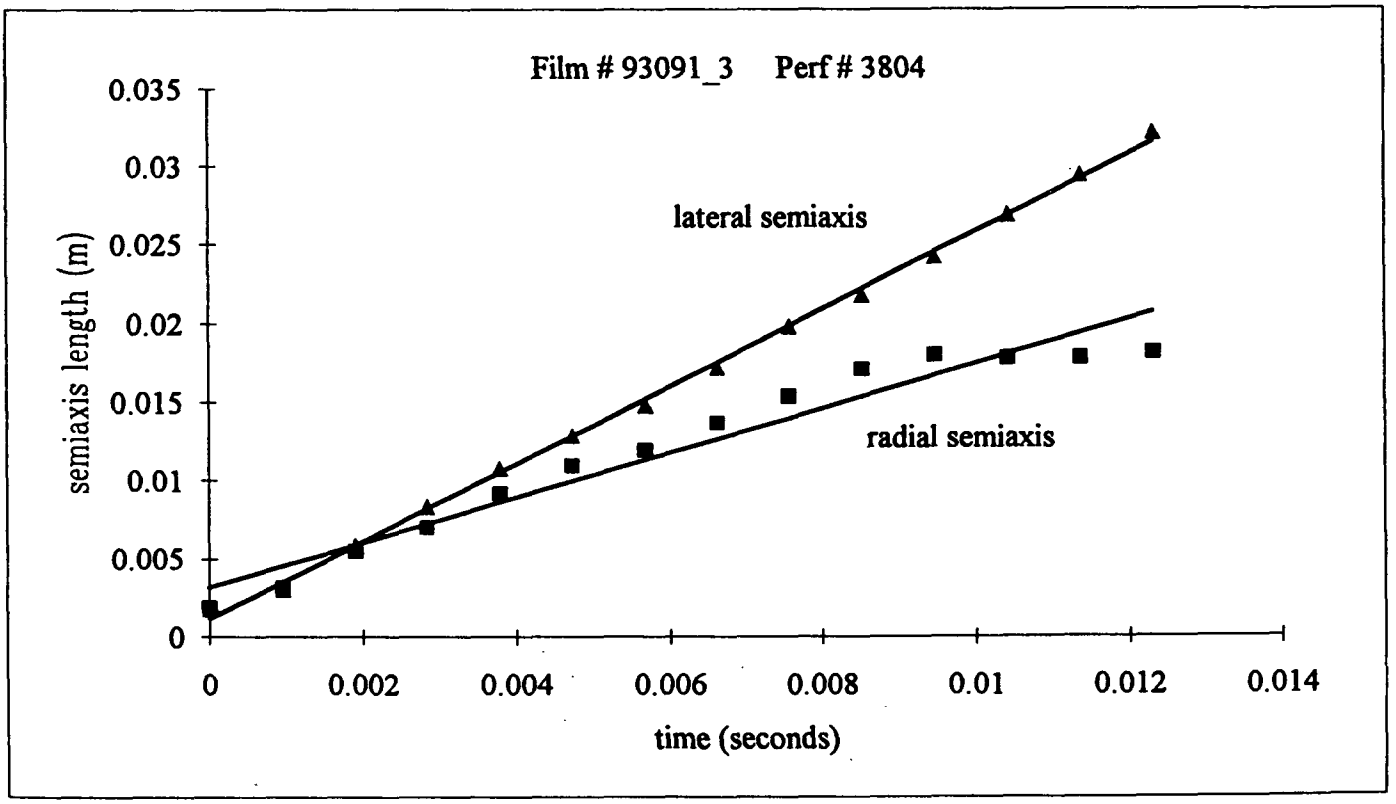
Film # 93091_3 Perf # 3804
semiaxis length (m)
0.035
0.03
0.025
0.02
0.015
0.01
0.005
0
lateral semiaxis
radial semiaxis
0
0.002
0.004
0.006
0.008
0.01
0.012
0.014
time (seconds)

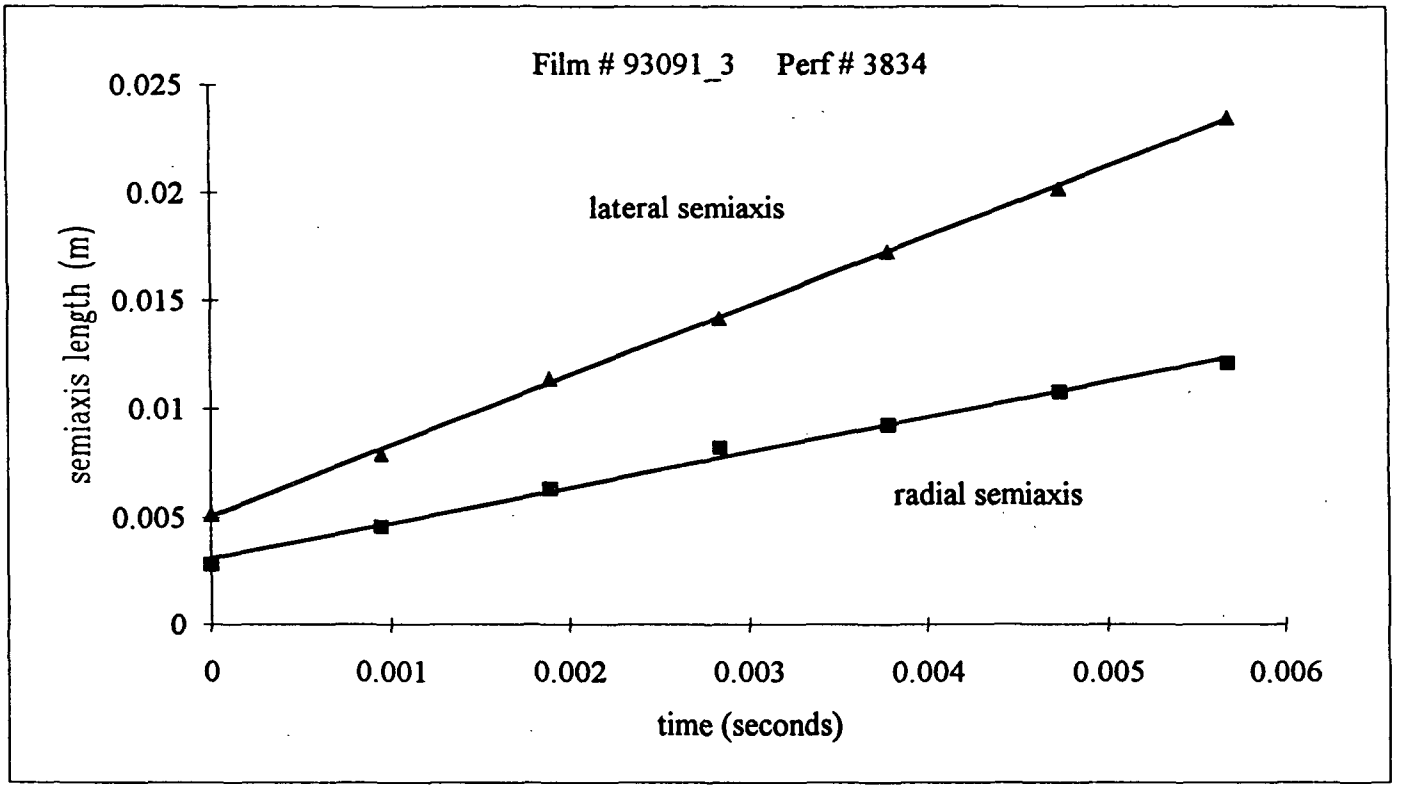
Film # 93091_3 Perf # 3834
lateral semiaxis
radial semiaxis
semiaxis length (m)
time (seconds)
0.025
0.02
0.015
0.01
0.005
0
0
0.001
0.002
0.003
0.004
0.005
0.006

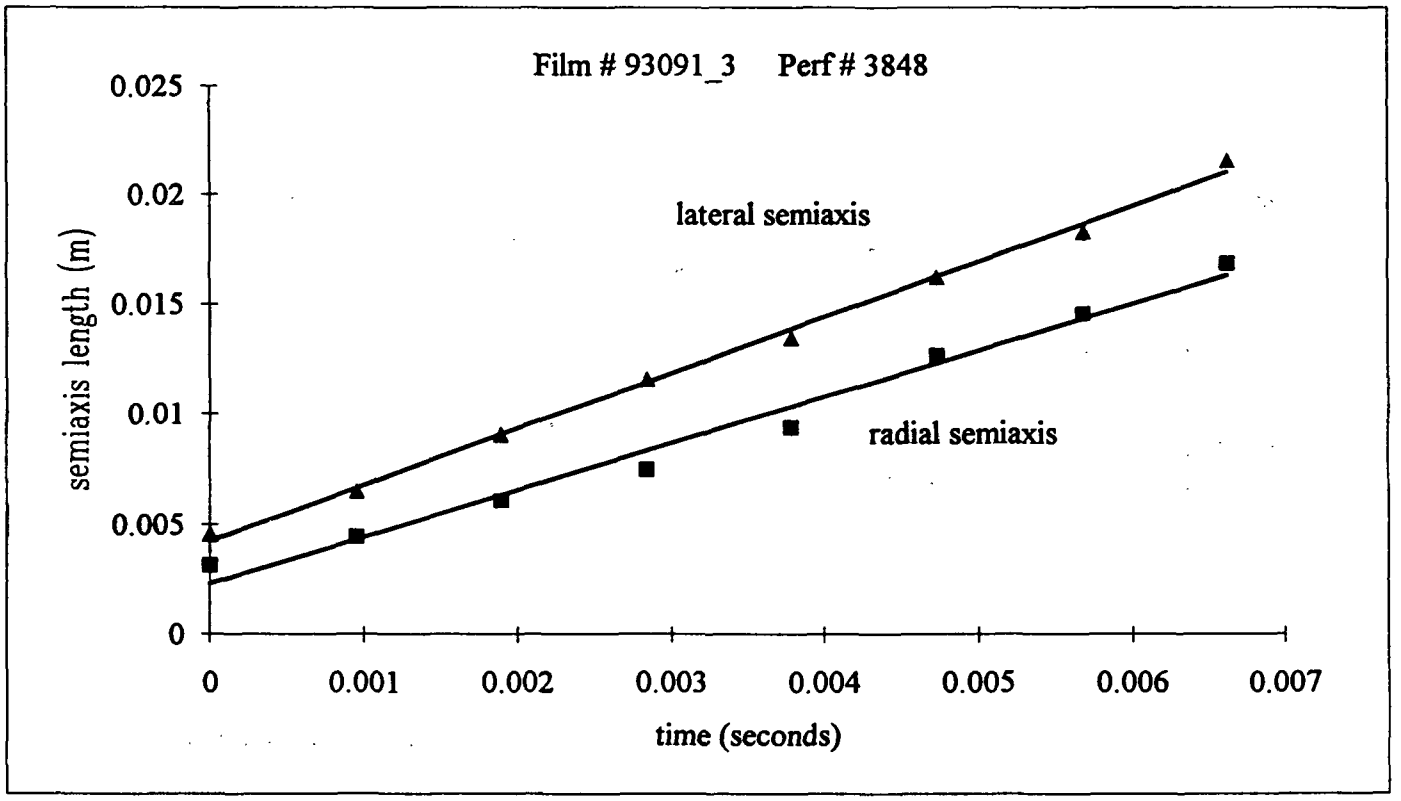
Film # 93091_3 Perf # 3848
lateral semiaxis
radial semiaxis
semiaxis length (m)
time (seconds)
0.025
0.02
0.015
0.01
0.005
0
0
0.001
0.002
0.003
0.004
0.005
0.006
0.007

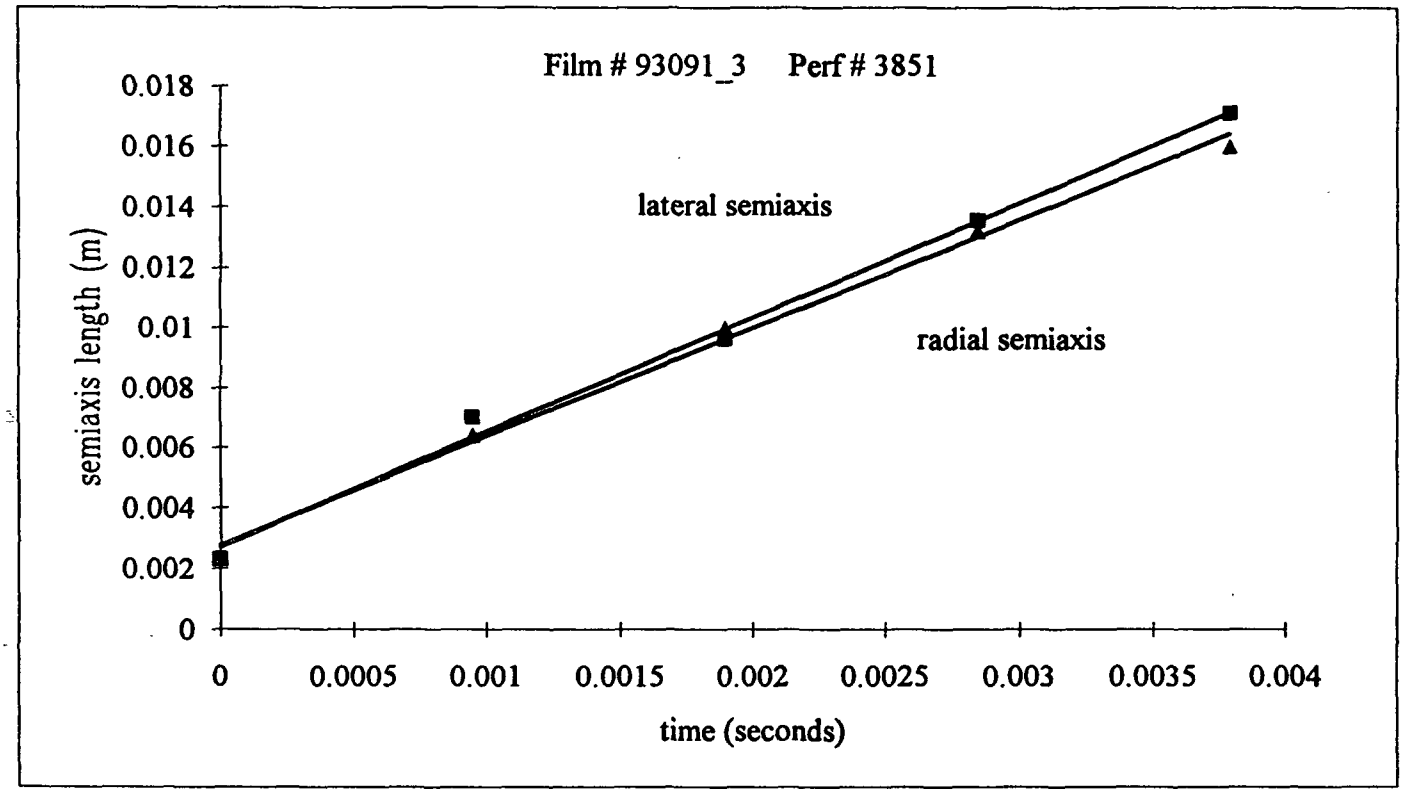
Film # 93091_3 Perf # 3851
lateral semiaxis
radial semiaxis
semiaxis length (m)
0.018
0.016
0.014
0.012
0.01
0.008
0.006
0.004
0.002
0
0 0.0005 0.001 0.0015 0.002 0.0025 0.003 0.0035 0.004
time (seconds)

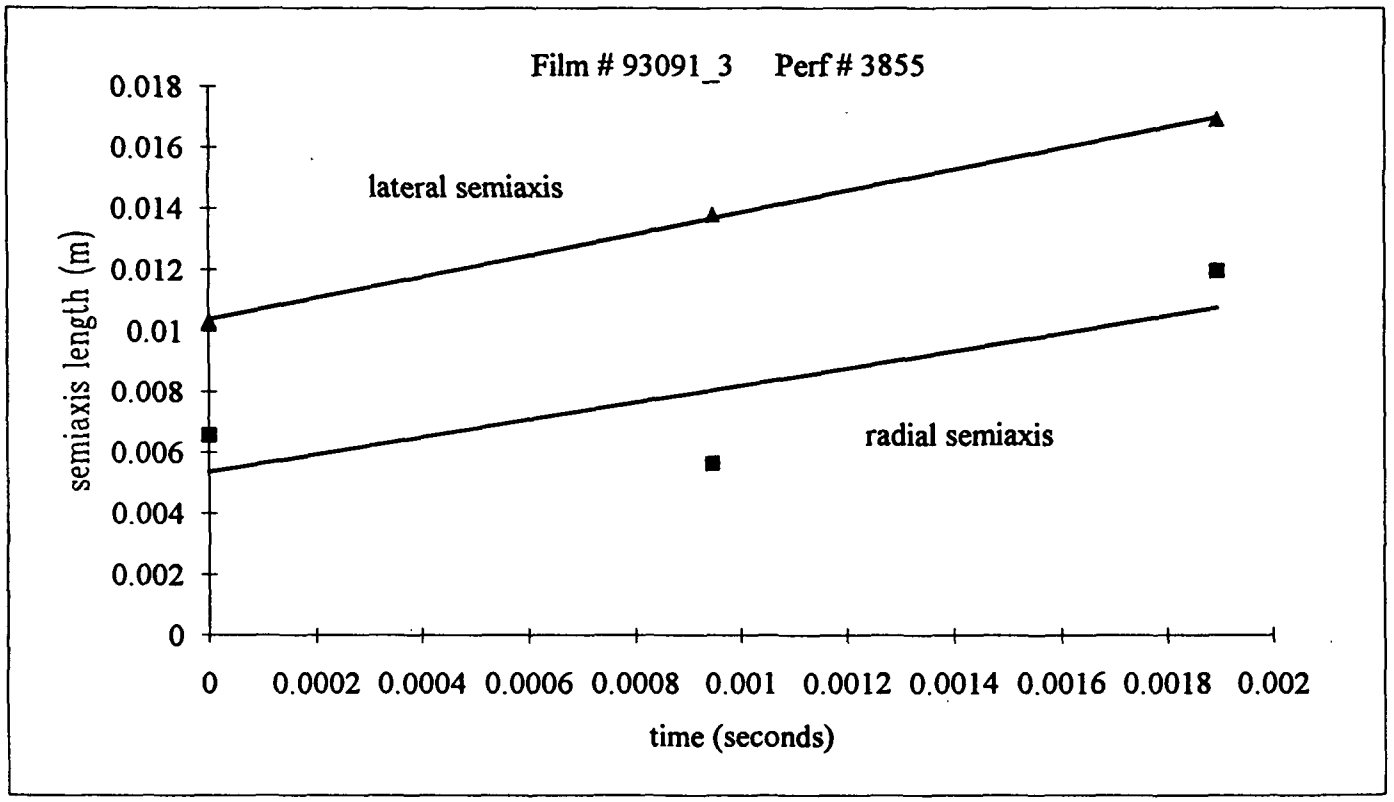
Film # 93091_3 Perf # 3855
lateral semiaxis
radial semiaxis
semiaxis length (m)
0.018
0.016
0.014
0.012
0.01
0.008
0.006
0.004
0.002
0
0 0.0002 0.0004 0.0006 0.0008 0.001 0.0012 0.0014 0.0016 0.0018 0.002
time (seconds)

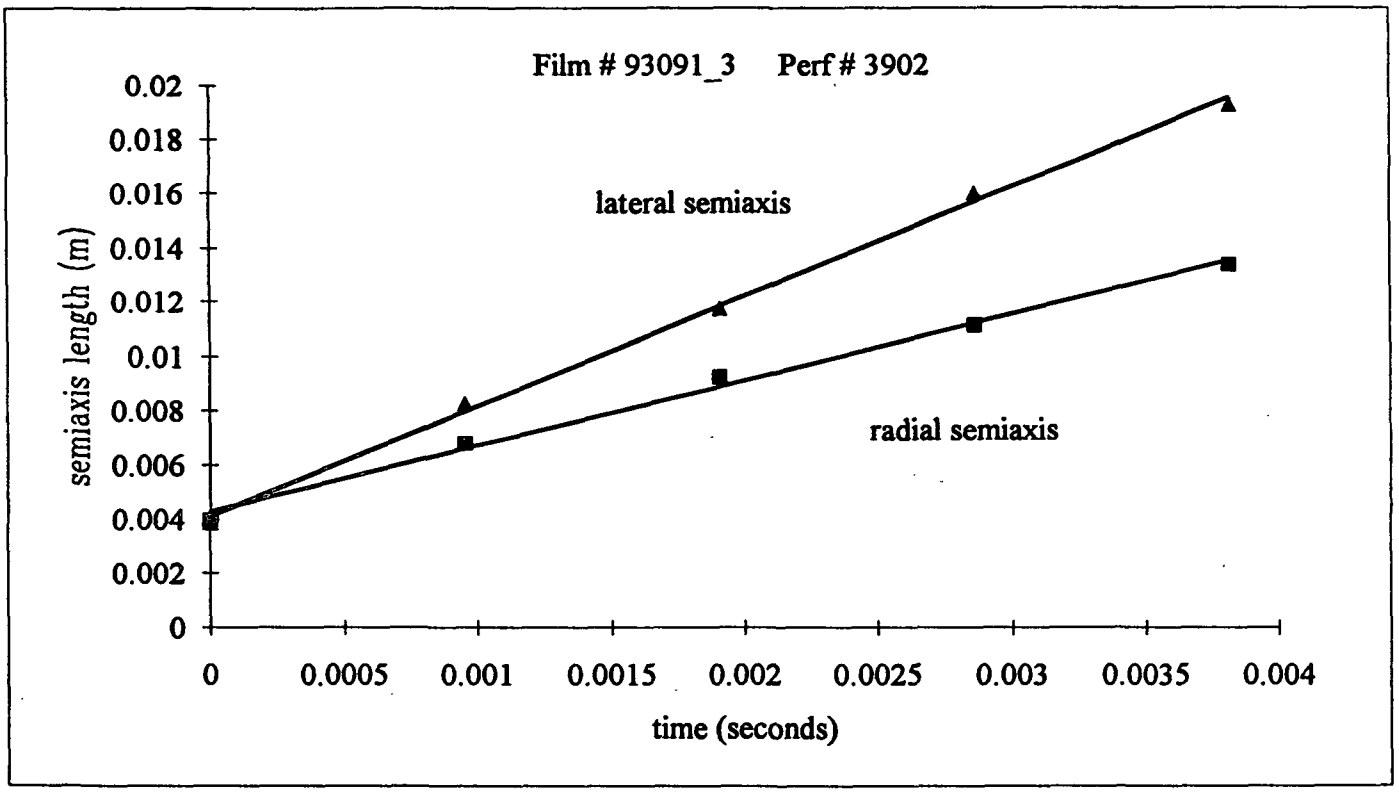
Film # 93091_3 Perf # 3902
lateral semiaxis
radial semiaxis
semiaxis length (m)
time (seconds)
0.02
0.018
0.016
0.014
0.012
0.01
0.008
0.006
0.004
0.002
0
0
0.0005
0.001
0.0015
0.002
0.0025
0.003
0.0035
0.004

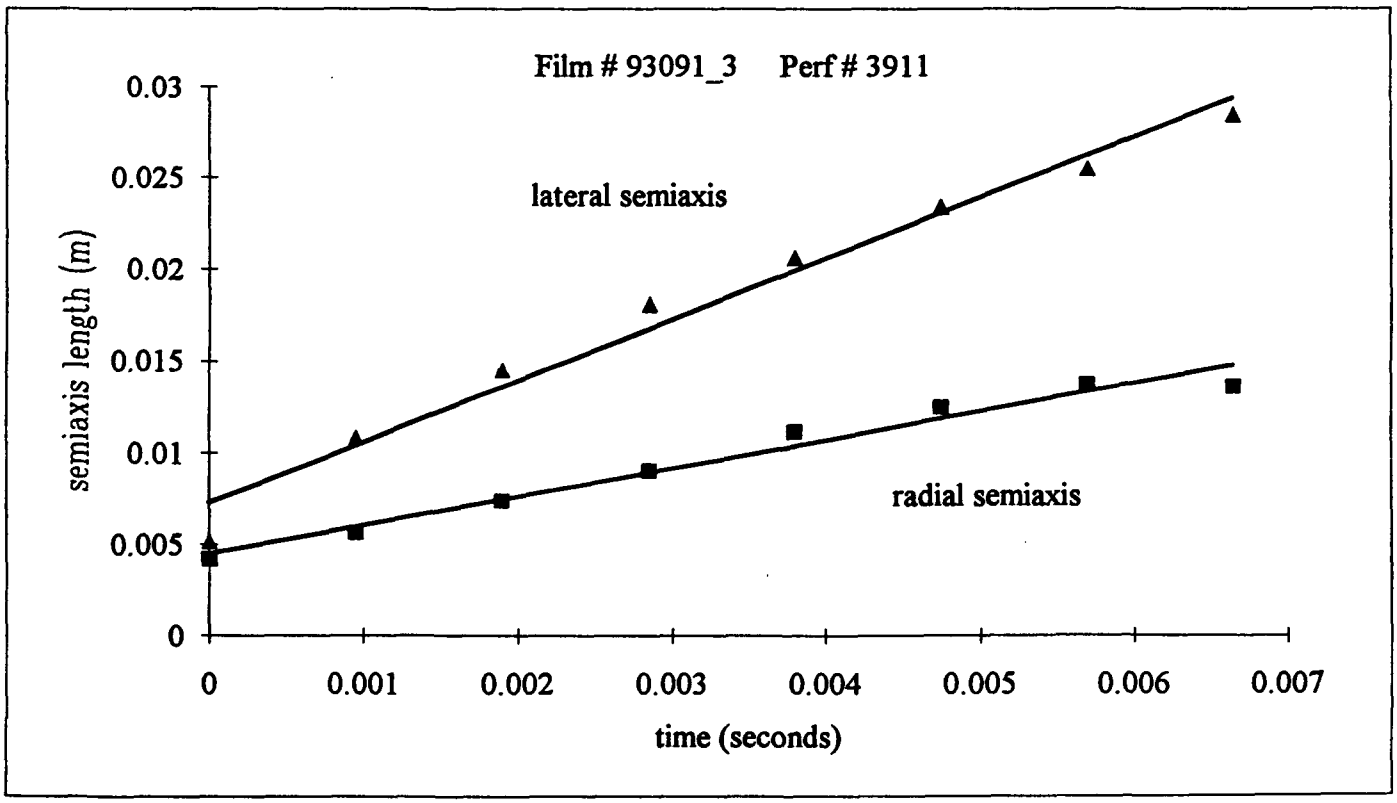
Film # 93091_3 Perf # 3911
lateral semiaxis
radial semiaxis
semiaxis length (m)
time (seconds)
0.03
0.025
0.02
0.015
0.01
0.005
0
0
0.001
0.002
0.003
0.004
0.005
0.006
0.007

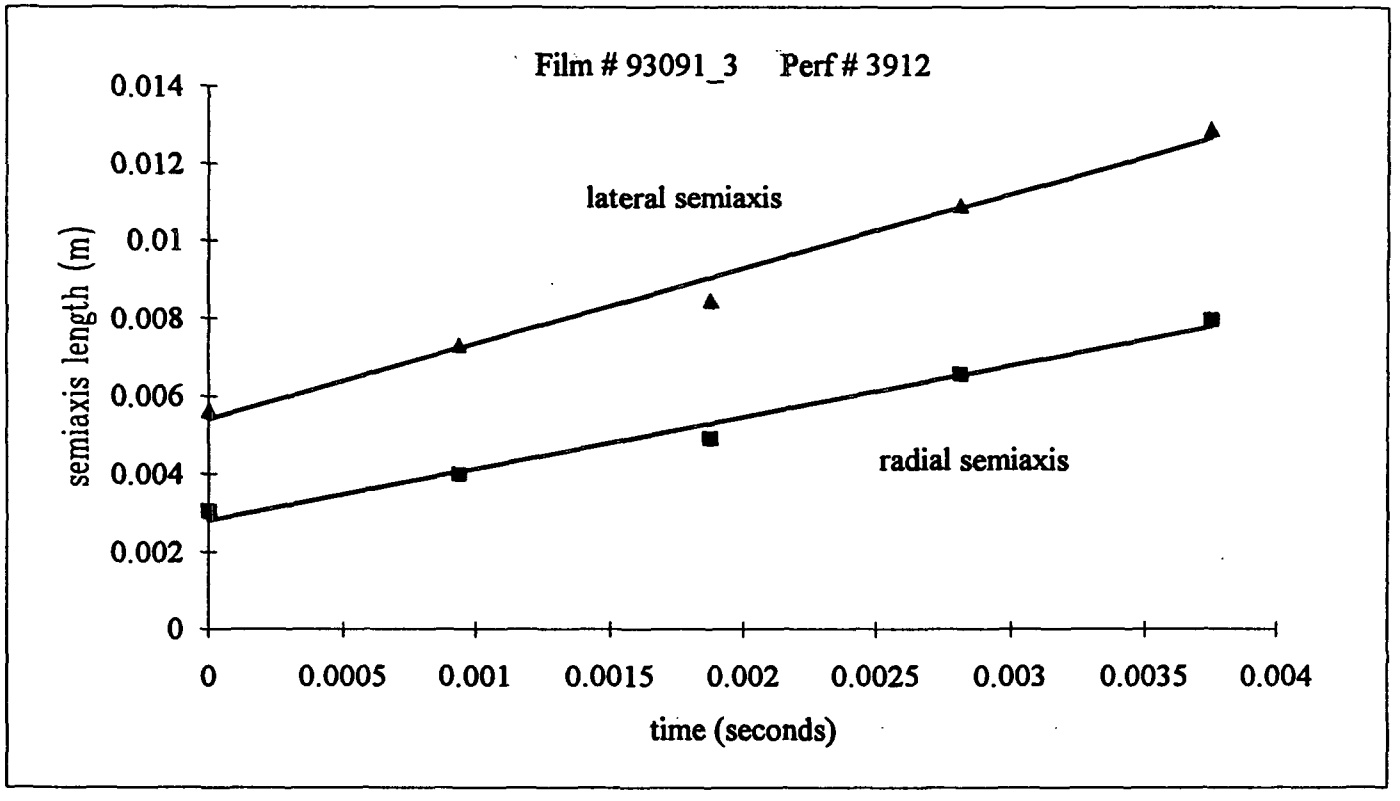
Film # 93091_3 Perf # 3912
lateral semiaxis
radial semiaxis
semiaxis length (m)
0.014
0.012
0.01
0.008
0.006
0.004
0.002
0
0
0.0005
0.001
0.0015
0.002
0.0025
0.003
0.0035
0.004
time (seconds)

Film # 93091_4
Perf # 1379
act/meas = 0.476
dt = 0.00087

relative t (sec)	measured Radial	scaled Radial	relative t (sec)	measured lateral	scaled lateral	corrected lateral
0.00000	14.0	0.0033	0.00000	13.0	0.0031	0.00309465
0.00087	24.0	0.0057	0.00095	25.0	0.0060	0.00590848
0.00173	35.0	0.0083	0.00189	39.0	0.0093	0.0092017
0.00260	44.0	0.0105	0.00284	50.0	0.0119	0.01177419
0.00347	47.0	0.0112	0.00379	61.0	0.0145	0.01435655
0.00433	54.0	0.0129	0.00473	73.0	0.0174	0.01717696
0.00520	59.0	0.0140	0.00568	86.0	0.0205	0.02023213
0.00607	62.0	0.0148	0.00663	102.0	0.0243	0.02399817

Film # 93091_4
Perf # 1382
act/meas = 0.476
dt = 0.00088

relative t (sec)	measured Radial	scaled Radial	relative t (sec)	measured lateral	scaled lateral	corrected lateral
0.00000	22.0	0.0052	0.00000	23.0	0.0055	0.00547515
0.00088	38.0	0.0090	0.00088	37.0	0.0088	0.00873078

Film # 93091_4
Perf # 1388
act/meas = 0.476
dt = 0.00089

relative t (sec)	measured Radial	scaled Radial	relative t (sec)	measured lateral	scaled lateral	corrected lateral
0.00000	28.0	0.0067	0.00000	29.0	0.0069	0.00690345
0.00089	36.0	0.0086	0.00089	45.0	0.0107	0.01061377
0.00179	50.0	0.0119	0.00179	65.0	0.0155	0.01532044
0.00268	60.0	0.0143	0.00268	79.0	0.0188	0.01858522

Film # 93091_4
Perf # 1396
act/meas = 0.476
dt = 0.00098

relative t (sec)	measured Radial	scaled Radial	relative t (sec)	measured lateral	scaled lateral	corrected lateral
0.00000	18.0	0.0043	0.00000	48.0	0.0114	0.0114264
0.00098	22.0	0.0052	0.00098	64.0	0.0152	0.01505654
0.00196	30.0	0.0071	0.00196	78.0	0.0186	0.01832968
0.00294	39.0	0.0093	0.00294	87.0	0.0207	0.02042002
0.00392	46.0	0.0110	0.00392	101.0	0.0240	0.02371922
0.00490	54.0	0.0129	0.00490	110.0	0.0262	0.02580956

Film # 93091_4
Perf # 1407
act/meas = 0.476
dt = 0.00095

relative t (sec)	measured Radial	scaled Radial	relative t (sec)	measured lateral	scaled lateral	corrected lateral
0.00000	20.0	0.0048	0.00000	21.0	0.0050	0.00499905
0.00095	37.0	0.0088	0.00095	42.0	0.0100	0.00992217
0.00190	55.0	0.0131	0.00190	59.0	0.0140	0.01389309
0.00286	63.0	0.0150	0.00286	70.0	0.0167	0.01645017

Film # 93091_4
Perf # 1421
act/meas = 0.476
dt = 0.00095

relative t (sec)	measured Radial	scaled Radial	relative t (sec)	measured lateral	scaled lateral	corrected lateral
0.00000	16.0	0.0038	0.00000	14.0	0.0033	0.0033327
0.00095	25.0	0.0060	0.00095	22.0	0.0052	0.00518648
0.00190	36.0	0.0086	0.00190	27.0	0.0064	0.0063478
0.00286	41.0	0.0098	0.00286	32.0	0.0076	0.00751997
0.00381	52.0	0.0124	0.00381	38.0	0.0090	0.00893019
0.00476	57.0	0.0136	0.00476	48.0	0.0114	0.011289
0.00571	67.0	0.0159	0.00571	58.0	0.0138	0.01363334
0.00667	72.0	0.0171	0.00667	70.0	0.0167	0.01645378
0.00762	86.0	0.0205	0.00762	82.0	0.0195	0.01926699
0.00857	102.0	0.0243	0.00857	95.0	0.0226	0.02231825

Film # 93091_4
Perf # 1423-A
act/meas = 0.476
dt = 0.00096

relative t (sec)	measured Radial	scaled Radial	relative t (sec)	measured lateral	scaled lateral	corrected lateral
0.00000	23.0	0.0055	0.00000	29.0	0.0069	0.00690345
0.00096	45.0	0.0107	0.00096	34.0	0.0081	0.00798834
0.00191	57.0	0.0136	0.00191	45.0	0.0107	0.01058872
0.00287	68.0	0.0162	0.00287	56.0	0.0133	0.01316731
0.00383	74.0	0.0176	0.00383	69.0	0.0164	0.016222

Film # 93091_4
Perf # 1423-B
act/meas = 0.476
dt = 0.00096

relative t (sec)	measured Radial	scaled Radial
0.00000	12.0	0.0029
0.00096	24.0	0.0057
0.00191	32.0	0.0076
0.00287	39.0	0.0093
0.00383	43.0	0.0102
0.00478	53.0	0.0126
0.00574	59.0	0.0140

relative t (sec)	measured lateral	scaled lateral	corrected lateral
0.00000	12.0	0.0029	0.0028566
0.00096	22.0	0.0052	0.0051935
0.00191	31.0	0.0074	0.00729962
0.00287	41.0	0.0098	0.00964742
0.00383	47.0	0.0112	0.01103939
0.00478	56.0	0.0133	0.01316004
0.00574	65.0	0.0155	0.0152698

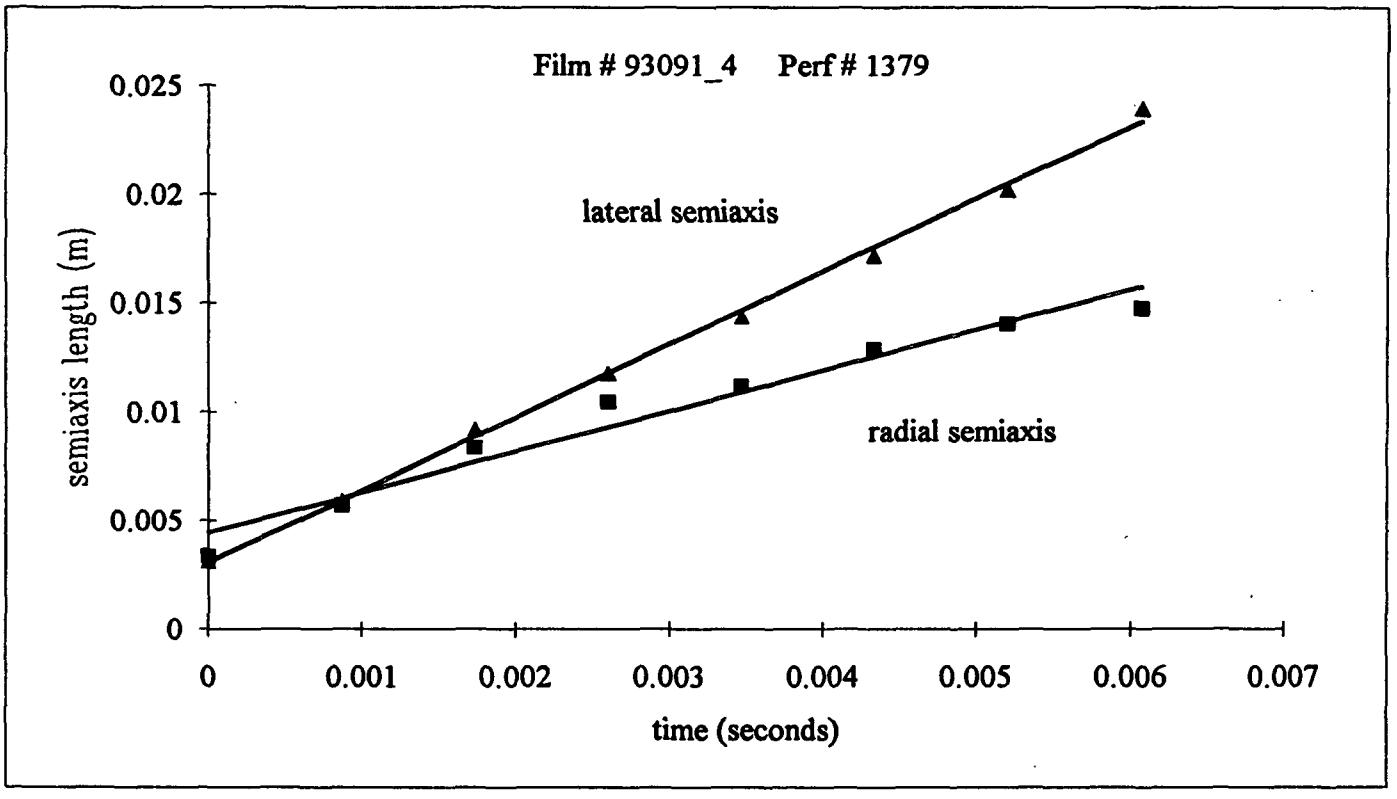
Film # 93091_4 Perf # 1379
lateral semiaxis
radial semiaxis
semiaxis length (m)
0.025
0.02
0.015
0.01
0.005
0
0
0.001
0.002
0.003
0.004
0.005
0.006
0.007
time (seconds)

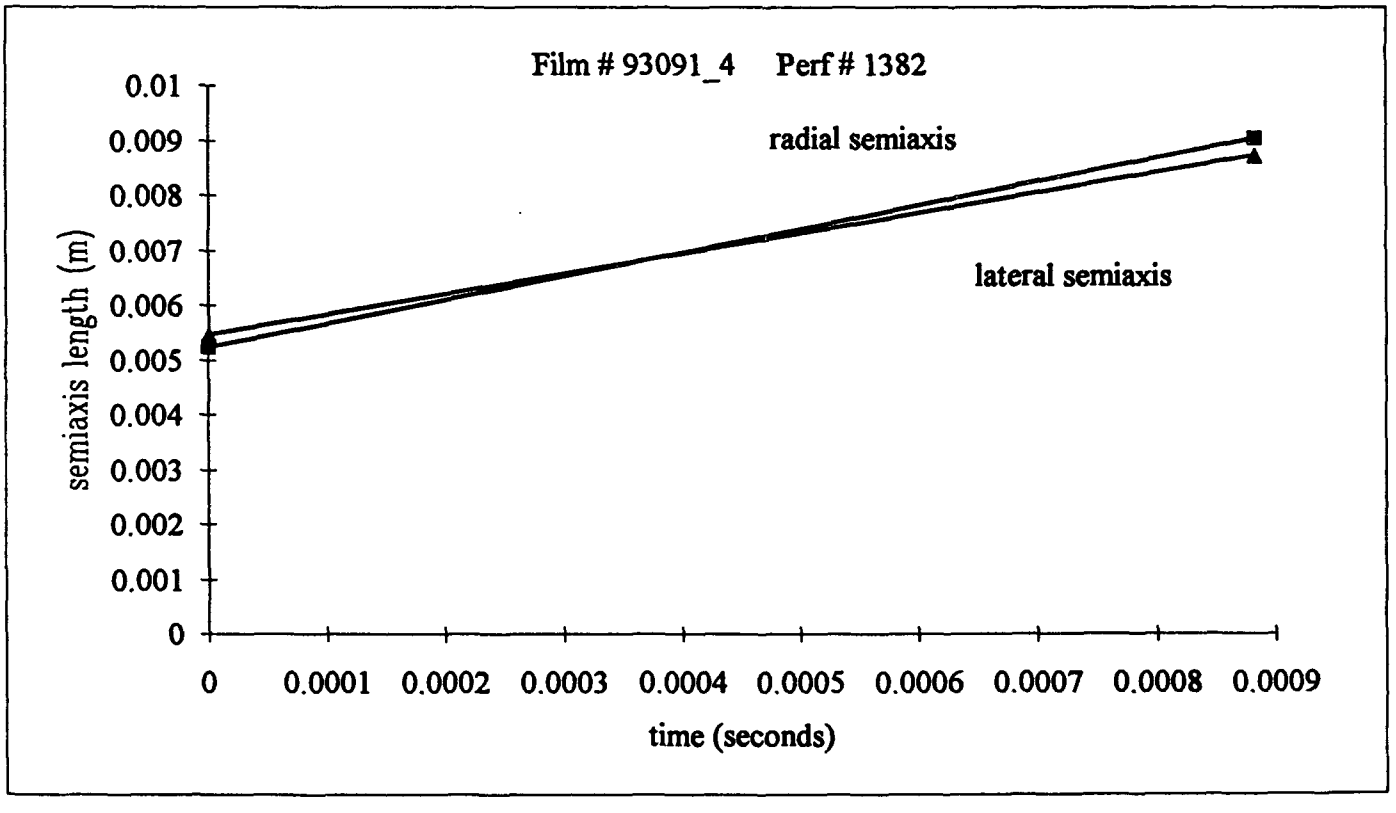
Film # 93091_4 Perf # 1382
radial semiaxis
lateral semiaxis
semiaxis length (m)
0.01
0.009
0.008
0.007
0.006
0.005
0.004
0.003
0.002
0.001
0
0
0.0001
0.0002
0.0003
0.0004
0.0005
0.0006
0.0007
0.0008
0.0009
time (seconds)

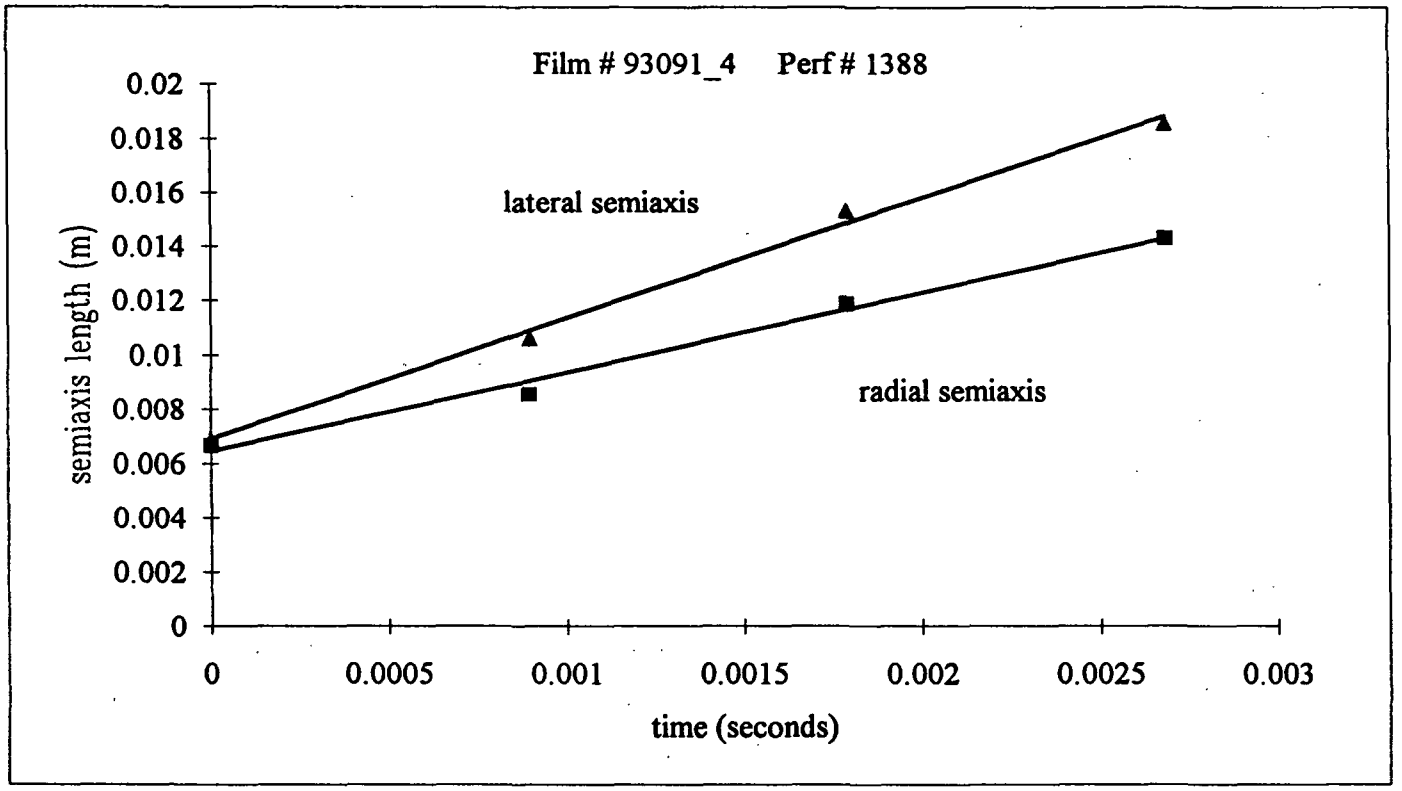
Film # 93091_4 Perf # 1388
0.02
0.018
0.016
0.014
0.012
0.01
0.008
0.006
0.004
0.002
0
semiaxis length (m)
lateral semiaxis
radial semiaxis
0
0.0005
0.001
0.0015
0.002
0.0025
0.003
time (seconds)

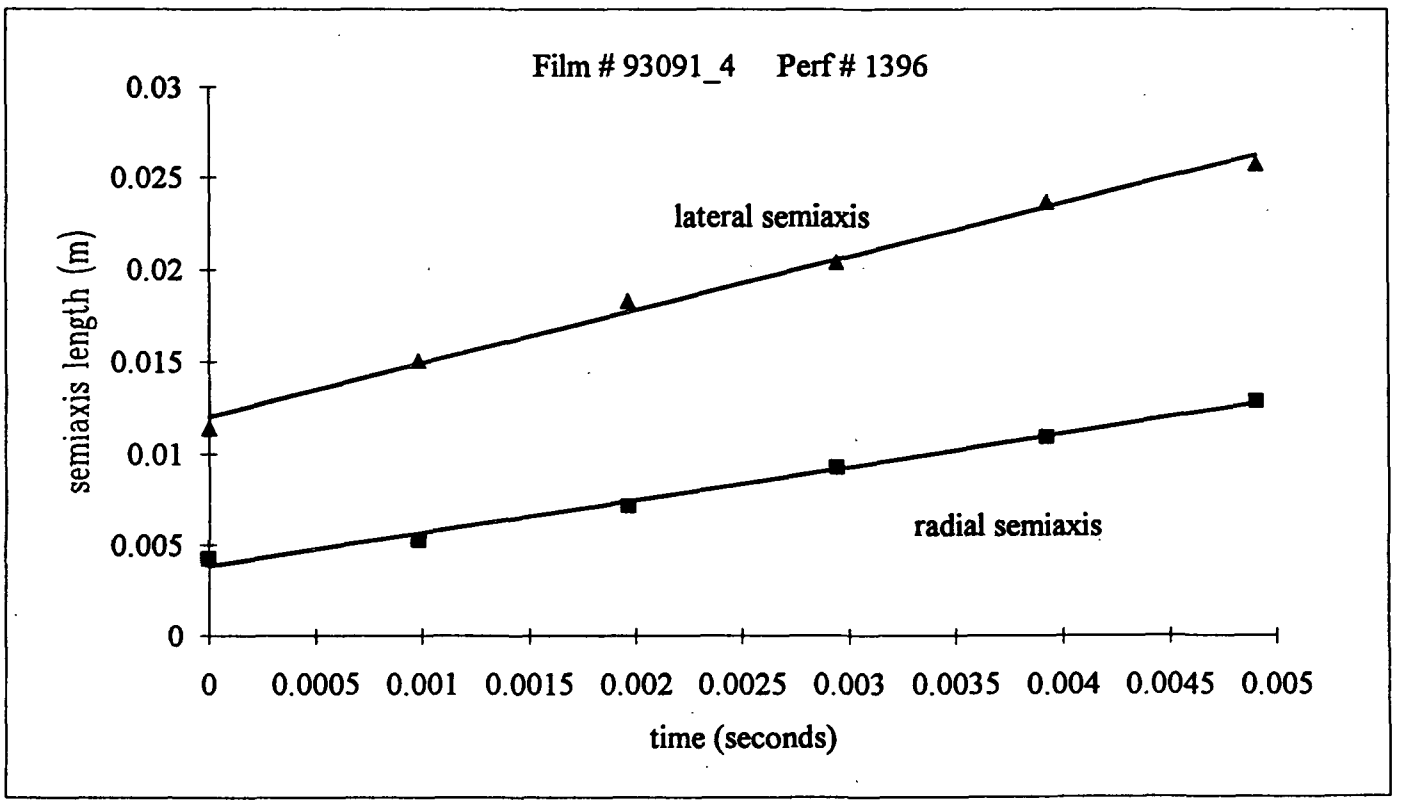
Film # 93091_4 Perf # 1396
0.03
0.025
0.02
0.015
0.01
0.005
0
semiaxis length (m)
lateral semiaxis
radial semiaxis
0
0.0005
0.001
0.0015
0.002
0.0025
0.003
0.0035
0.004
0.0045
0.005
time (seconds)

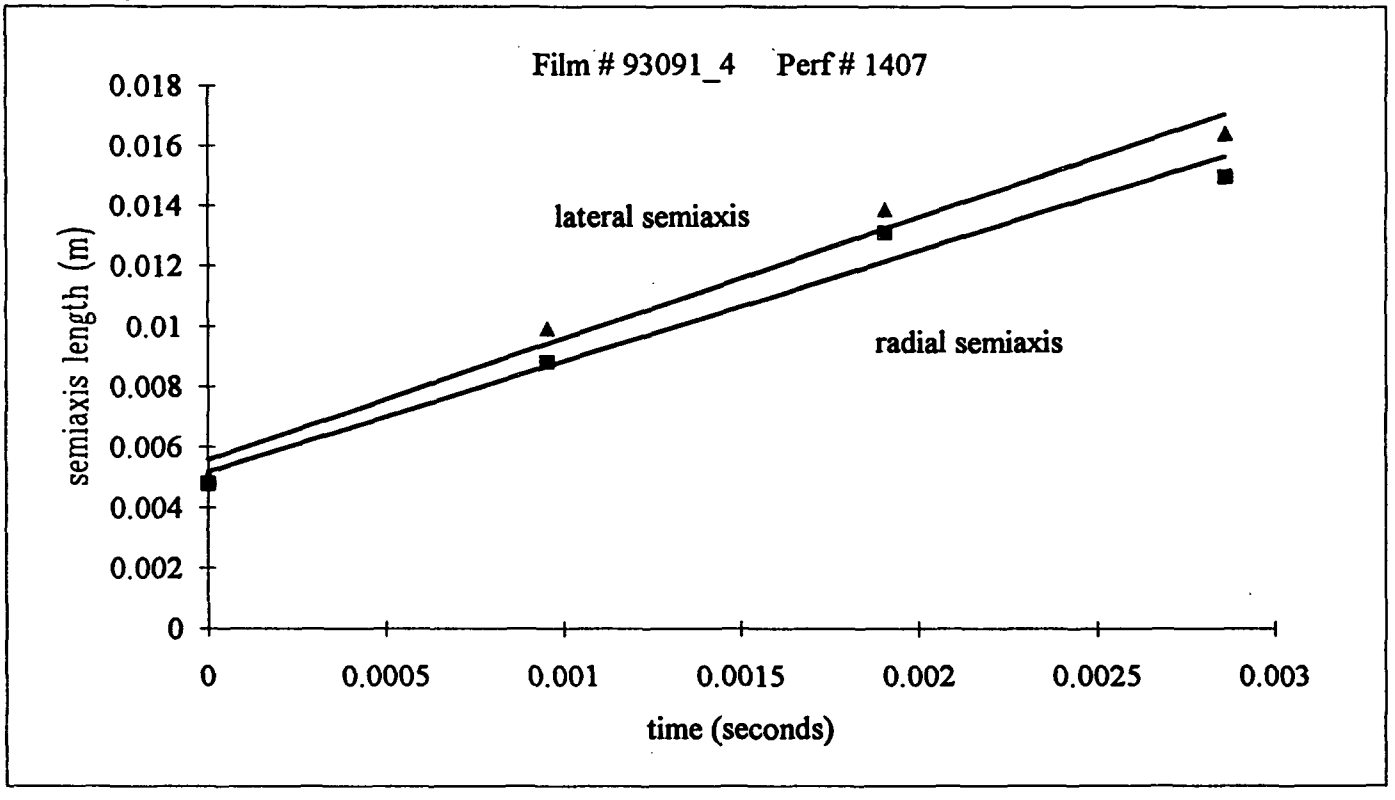
Film # 93091_4 Perf # 1407
lateral semiaxis
radial semiaxis
semiaxis length (m)
0.018
0.016
0.014
0.012
0.01
0.008
0.006
0.004
0.002
0
0
0.0005
0.001
0.0015
0.002
0.0025
0.003
time (seconds)

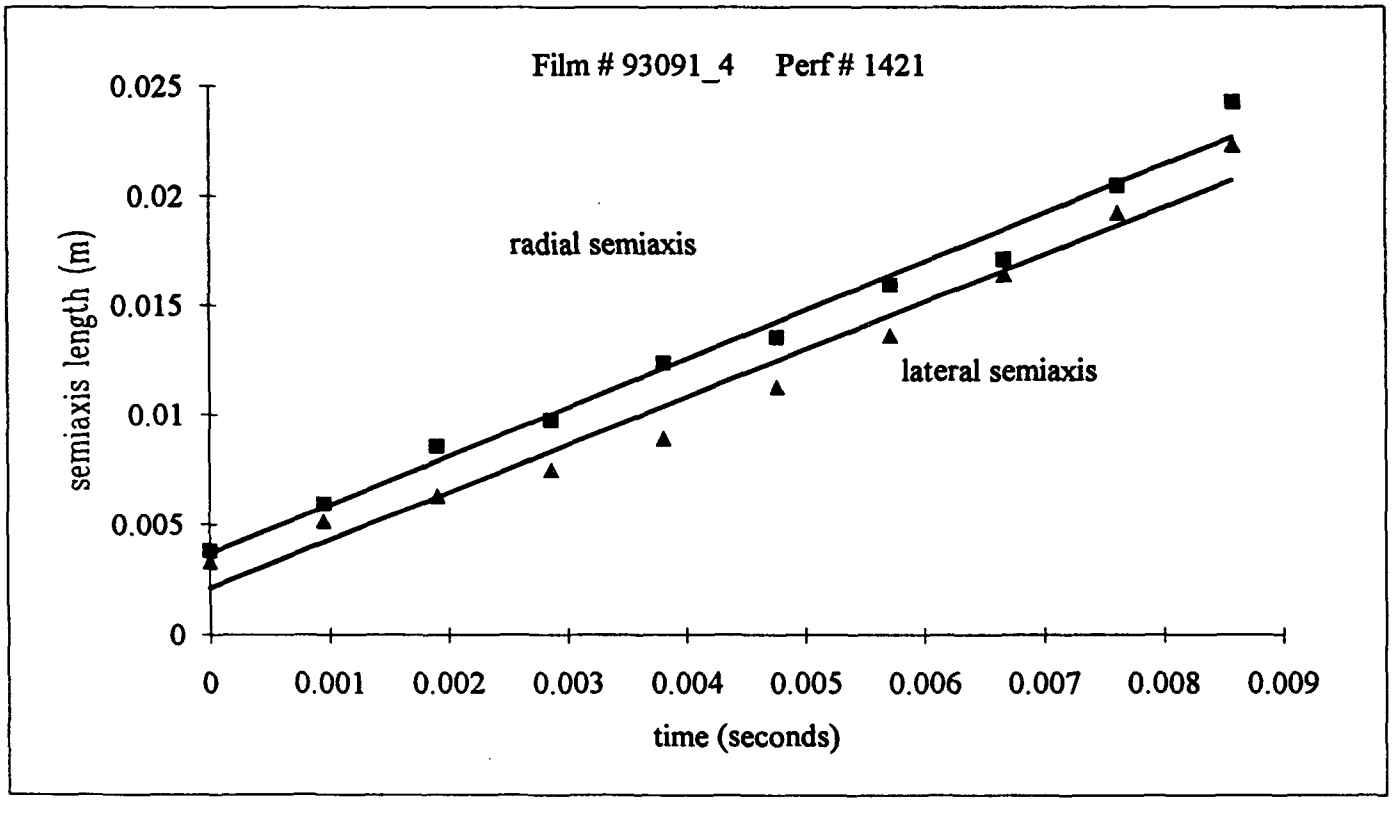
Film # 93091_4 Perf # 1421
radial semiaxis
lateral semiaxis
semiaxis length (m)
0.025
0.02
0.015
0.01
0.005
0
0
0.001
0.002
0.003
0.004
0.005
0.006
0.007
0.008
0.009
time (seconds)

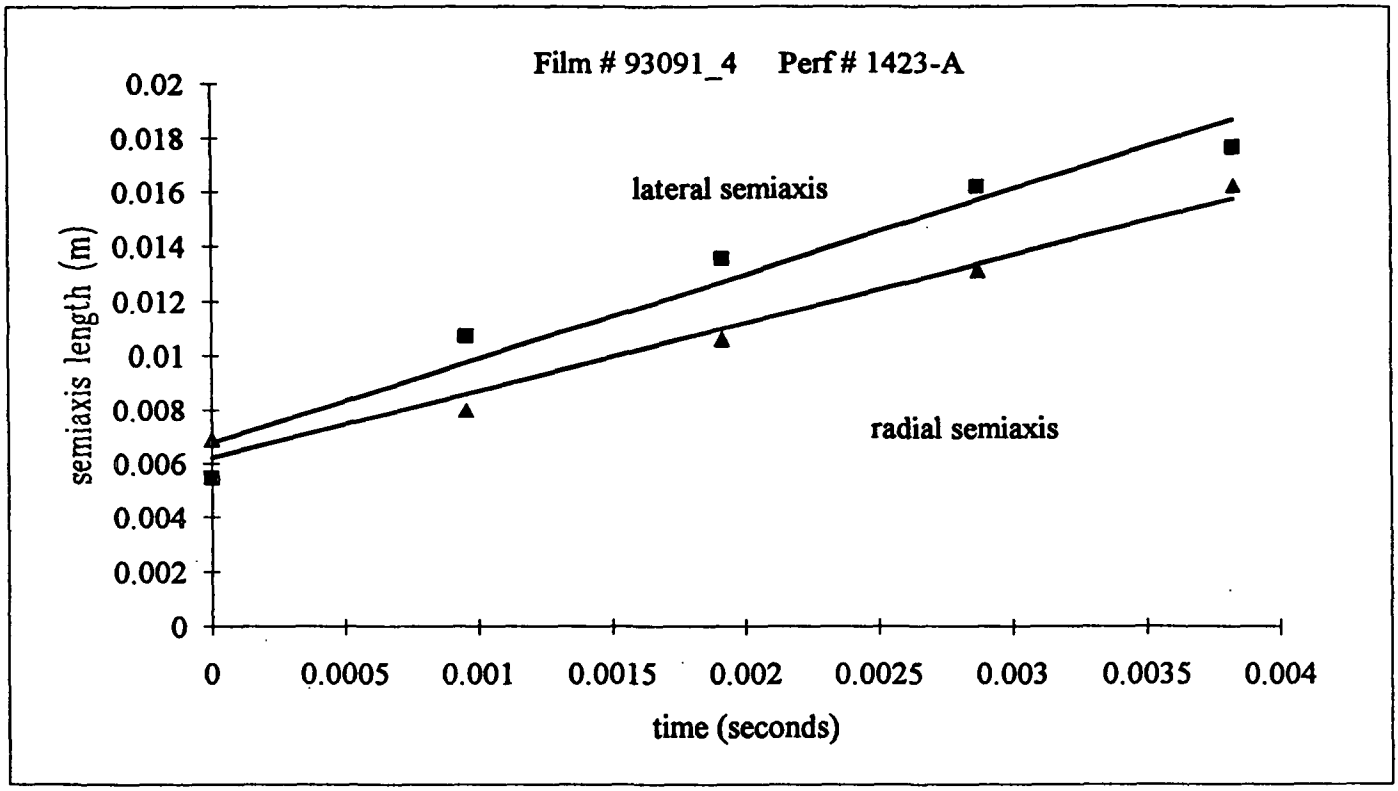
Film # 93091_4 Perf # 1423-A
lateral semiaxis
radial semiaxis
semiaxis length (m)
time (seconds)
0.02
0.018
0.016
0.014
0.012
0.01
0.008
0.006
0.004
0.002
0
0
0.0005
0.001
0.0015
0.002
0.0025
0.003
0.0035
0.004

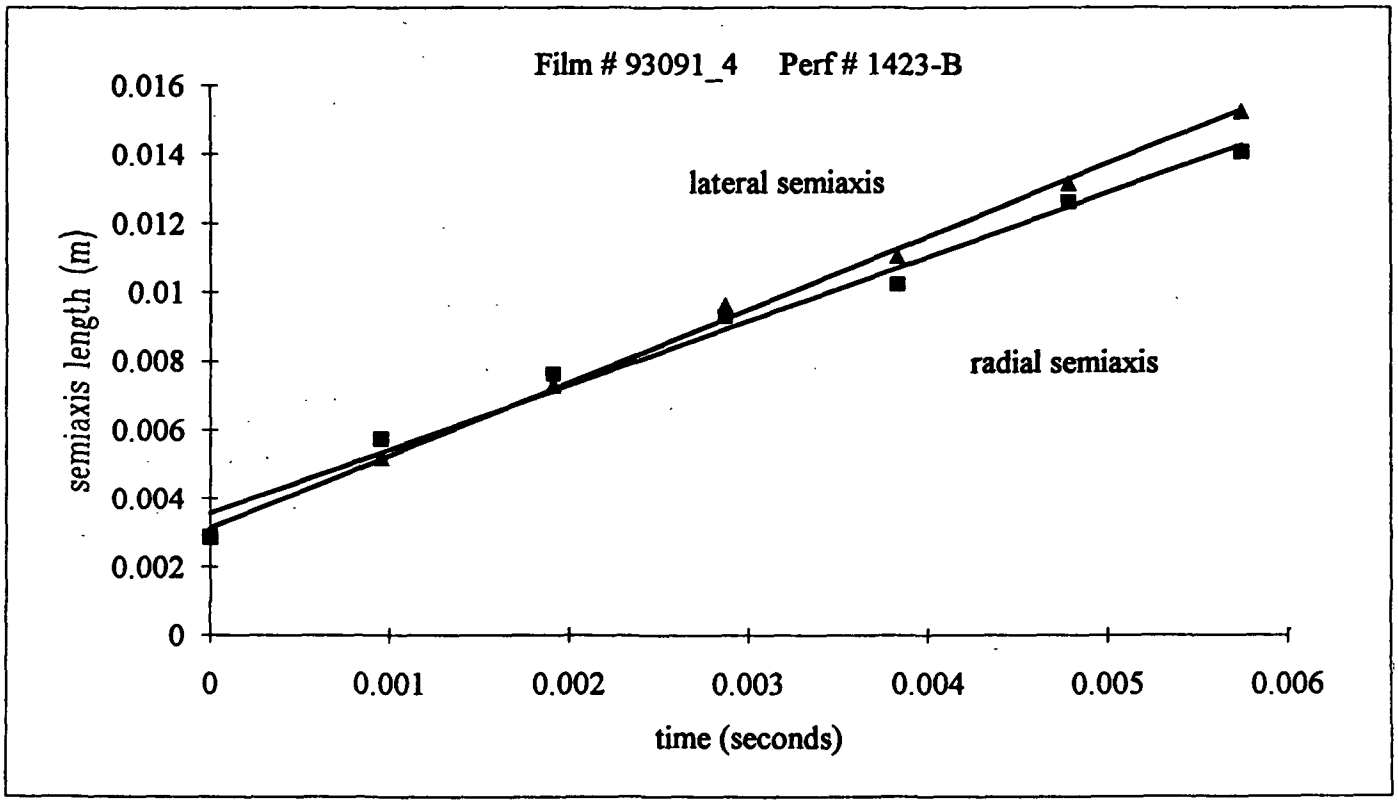
Film # 93091_4 Perf # 1423-B
lateral semiaxis
radial semiaxis
semiaxis length (m)
time (seconds)
0.016
0.014
0.012
0.01
0.008
0.006
0.004
0.002
0
0
0.001
0.002
0.003
0.004
0.005
0.006

APPENDIX J: VIBRATION ANALYSIS - FFT SPECTRA

The operating conditions for each of the FFT spectra collected in this appendix are summarized in the following tables.

title of spectrum	location of accelerometer	notes
Flowmeter	face plate of flowmeter	hand held
Viscometer	near rotor of viscometer	hand held
Motor	housing of motor	hand held
Pump	outlet port of pump	hand held
Inlet Pipe	below elbow	hand held
Nozzle	near connecting collar	hand held
Plate / All Off	below plate	screw mounted
Plate / Pump On, No Flow	below plate	screw mounted
Plate / Flow 1 - 52992.6	below plate	screw mounted
Plate / Flow 2 - 52992.7	below plate	screw mounted
Plate / Flow 3 - 52992.8	below plate	screw mounted
Plate / Flow 4 - 52992.9	below plate	screw mounted
Nozzle / Flow 5 - 52992.10	near connecting collar	hand held
Nozzle / Flow 6 - 52992.11	near connecting collar	hand held
No Excitation	---	isolated

trial number	probe location	pressure (psia)	viscosity (kg/m·s)	mass flow (lb/min)	density (kg/m^3)	jet velocity (m/s)
52292.6	plate	31.76	0.073	63.4	1216	11.7
52292.7	plate	35.56	0.072	70.8	1217	13.0
52292.8	plate	53.4	0.073	98.6	1217	18.2
52292.9	plate	70.0	0.074	119.0	1217	21.9
52292.10	nozzle	23.16	0.071	43.1	1216	7.9
52292.11	nozzle	49.95	0.072	94.0	1217	17.3

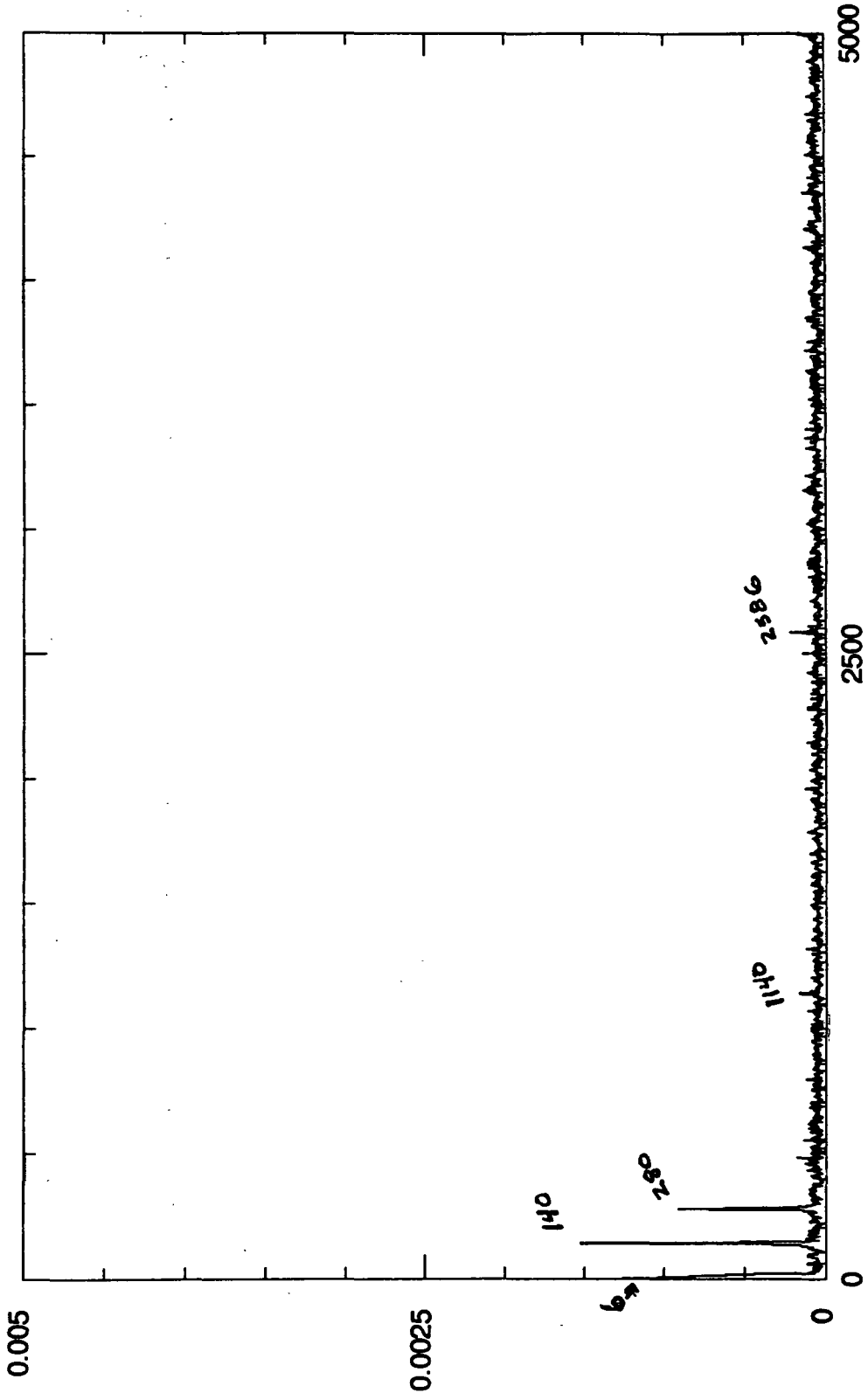
Flowmeter
FFT Magnitude of Accelerometer Output
0.005
0.0025
0
0
2500
5000
Hertz
69
140
282
1110
2586

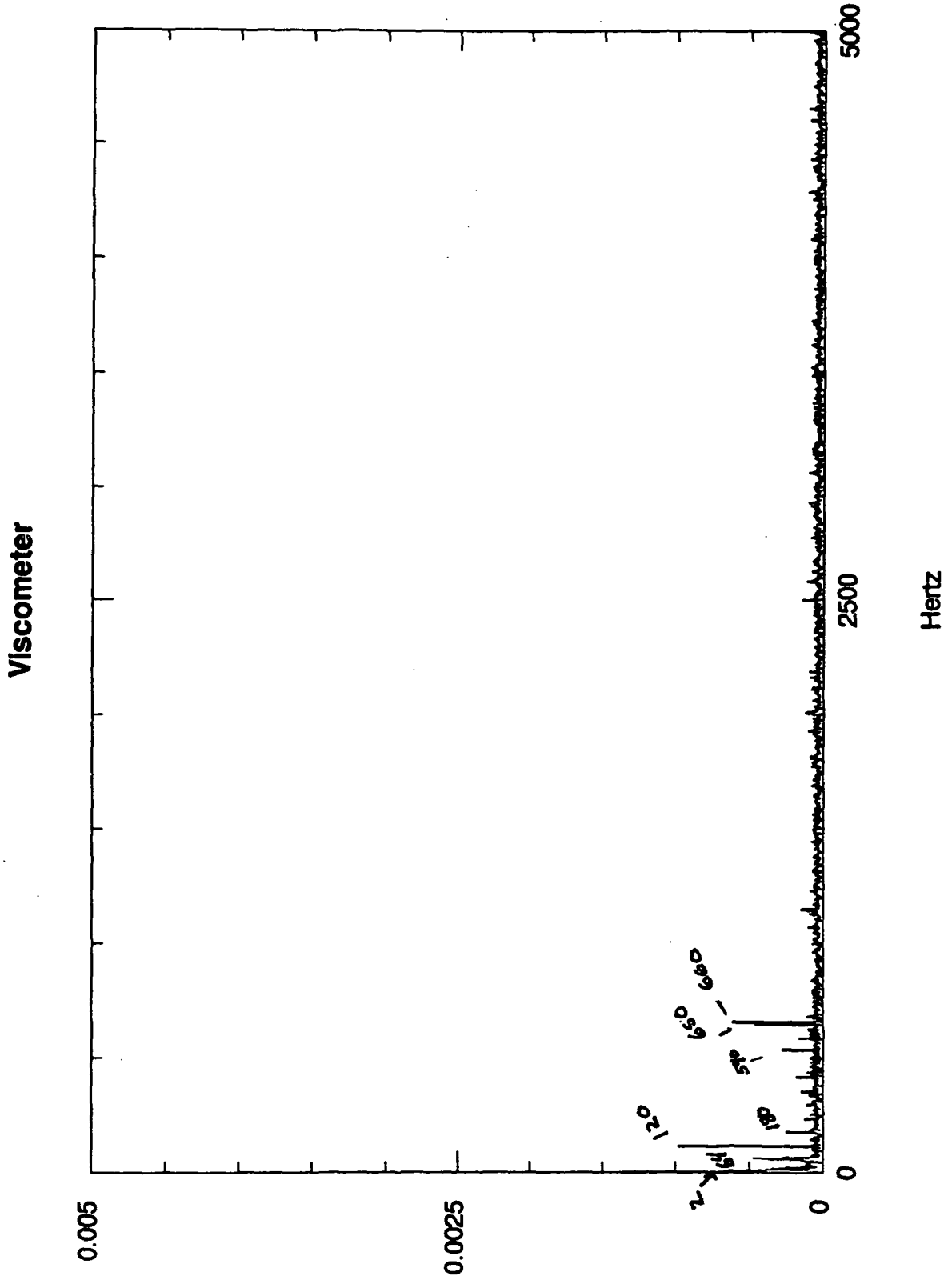
Viscometer
0.005
0.0025
0
0
2500
5000
Hertz
FFT Magnitude of Accelerometer Output

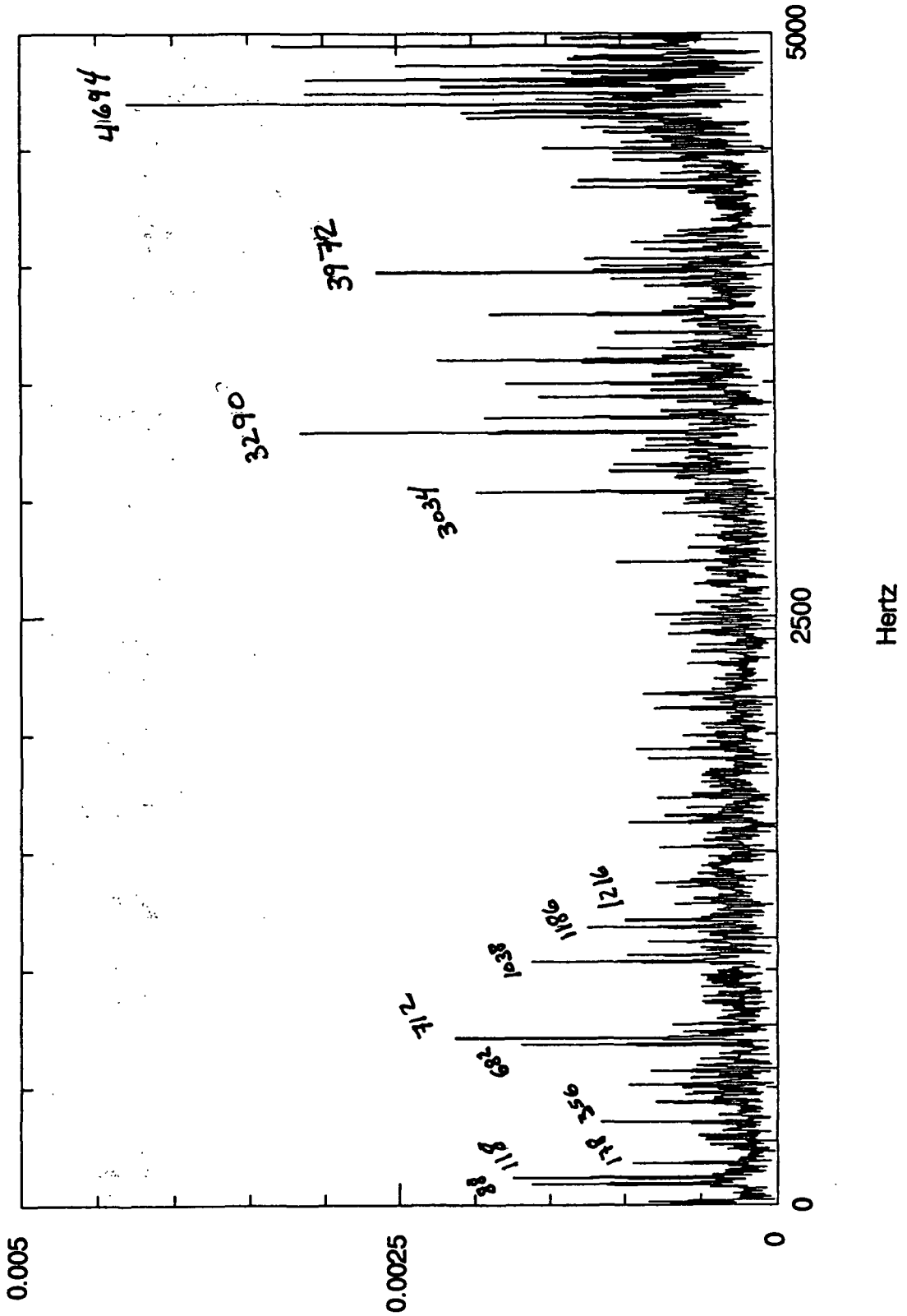
FFT Magnitude of Accelerometer Output
Motor
0.005
0.0025
0
0
2500
5000
Hertz
98
119
178
356
682
717
1038
1189
1424
3234
3290
3972
4694

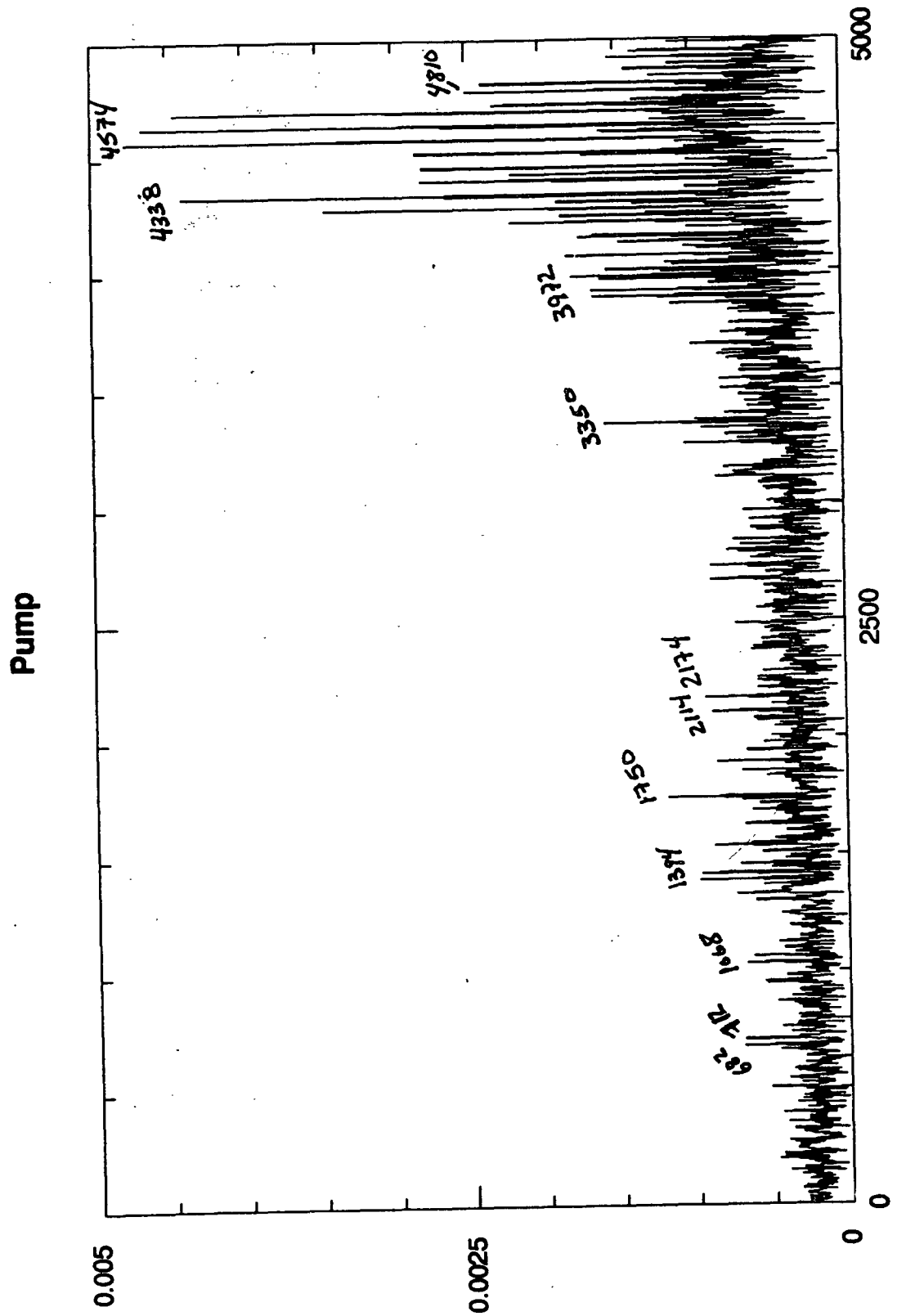
Pump
FFT Magnitude of Accelerometer Output
0.005
0.0025
0
0
2500
5000
Hertz
4574
4838
4810
3792
3350
2174
1950
1514
1068
782

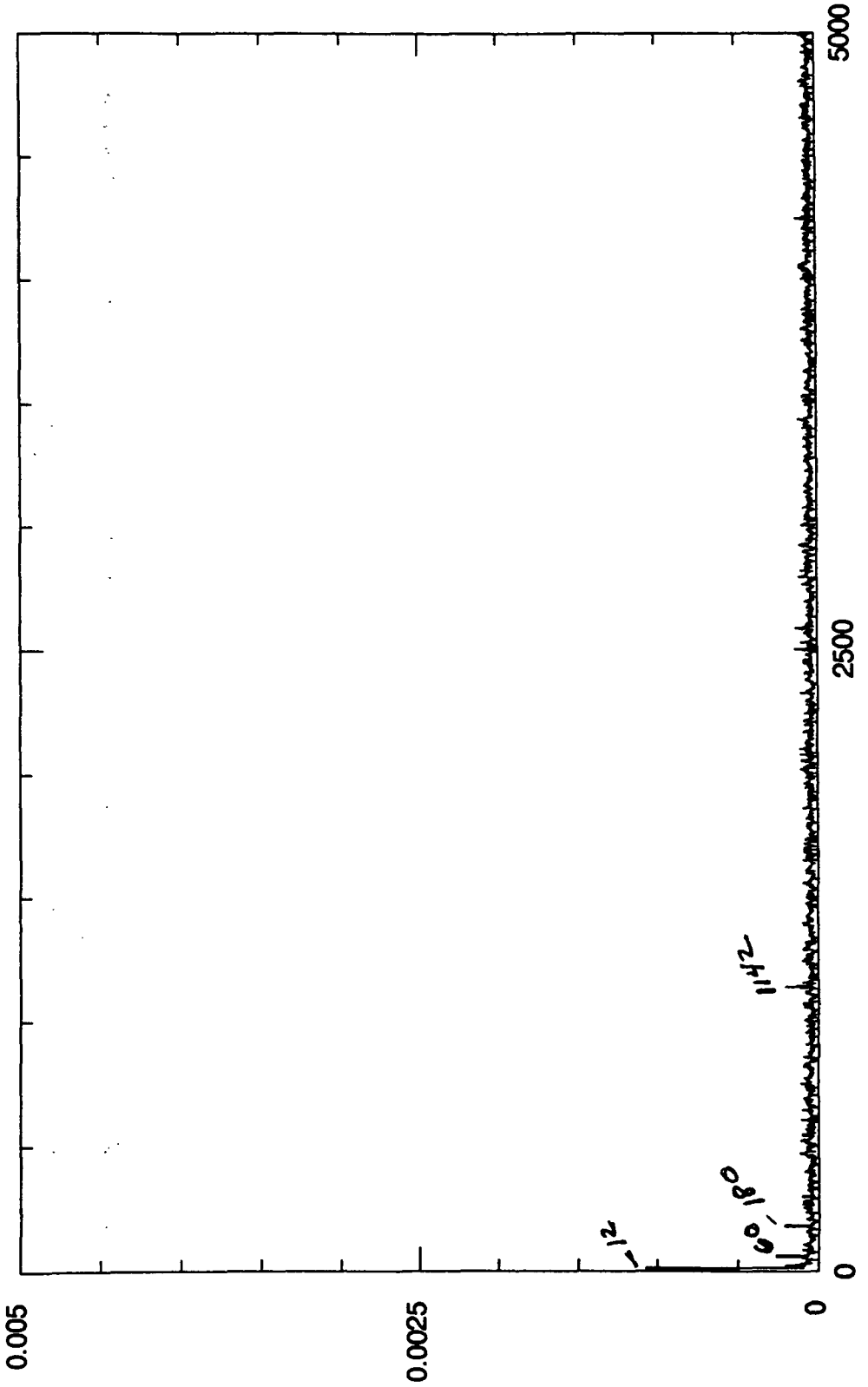
Inlet Pipe
FFT Magnitude of Accelerometer Output
0.005
0.0025
0
0
2500
5000
Hertz
12
60, 180
114.2

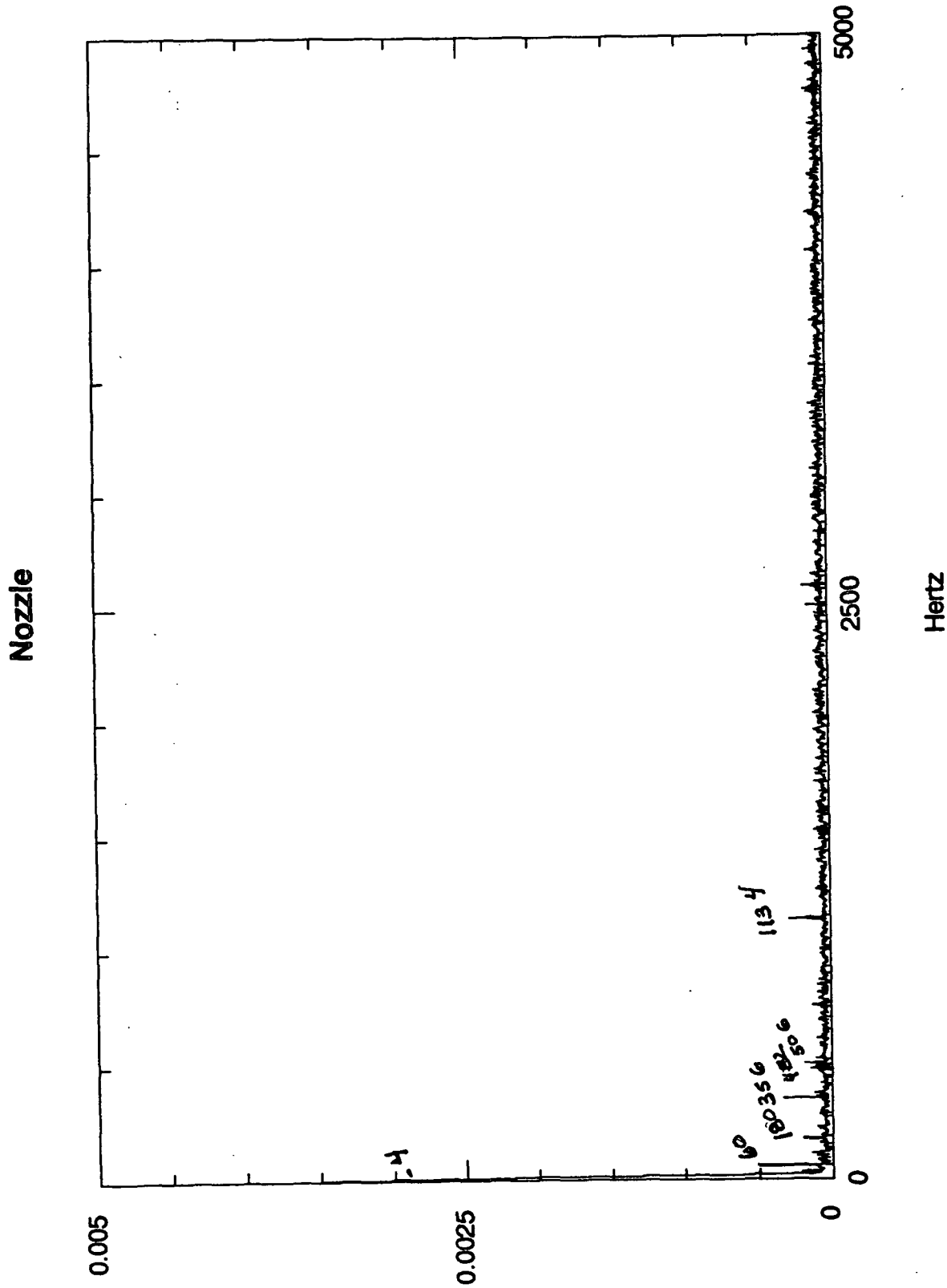
Nozzle
FFT Magnitude of Accelerometer Output
0.005
0.0025
0
0
2500
5000
Hertz
1134
1803
1506

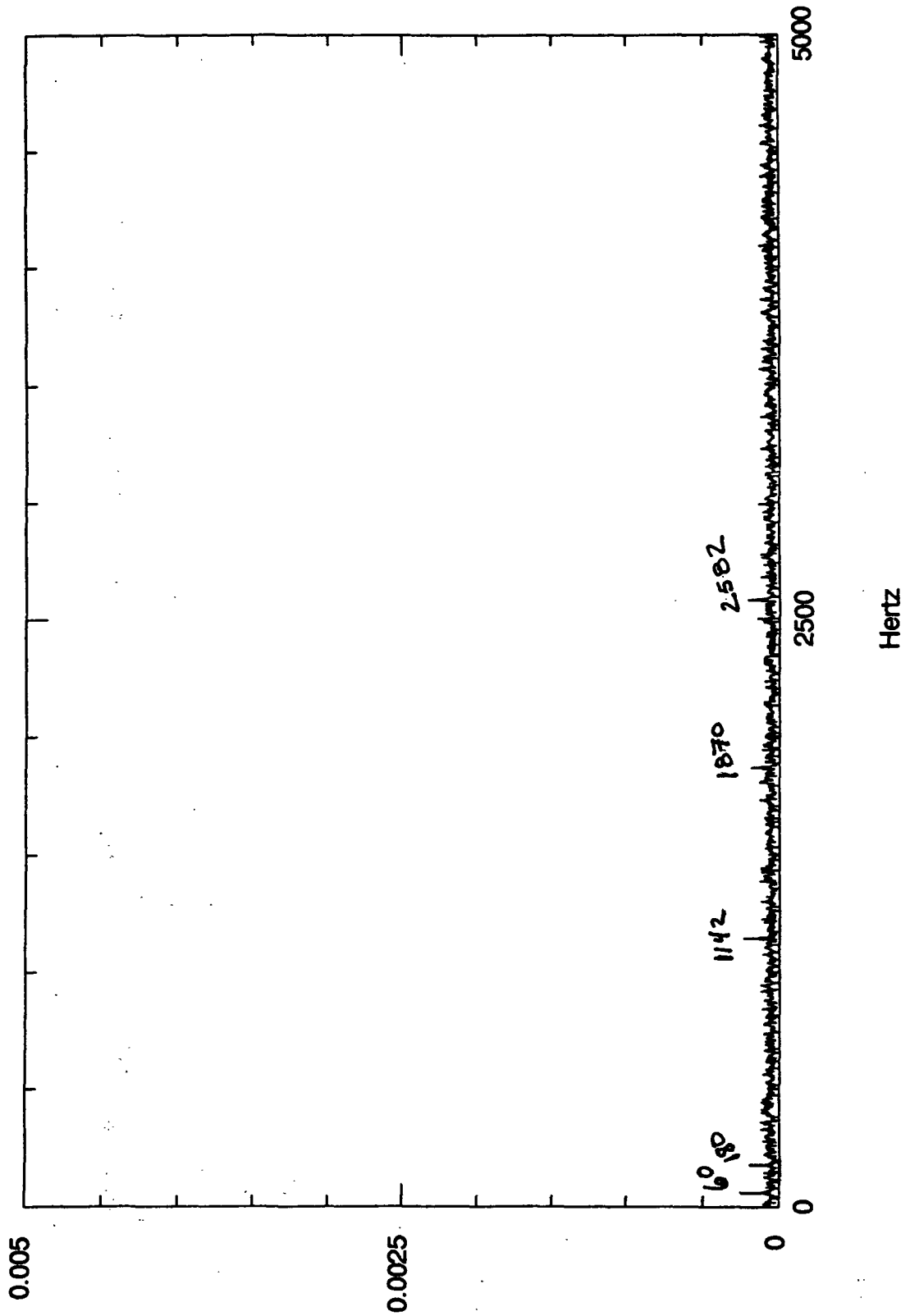
Plate/All Off
FFT Magnitude of Accelerometer Output
0.005
0.0025
0
0
2500
5000
Hertz
180
1142
1870
2582

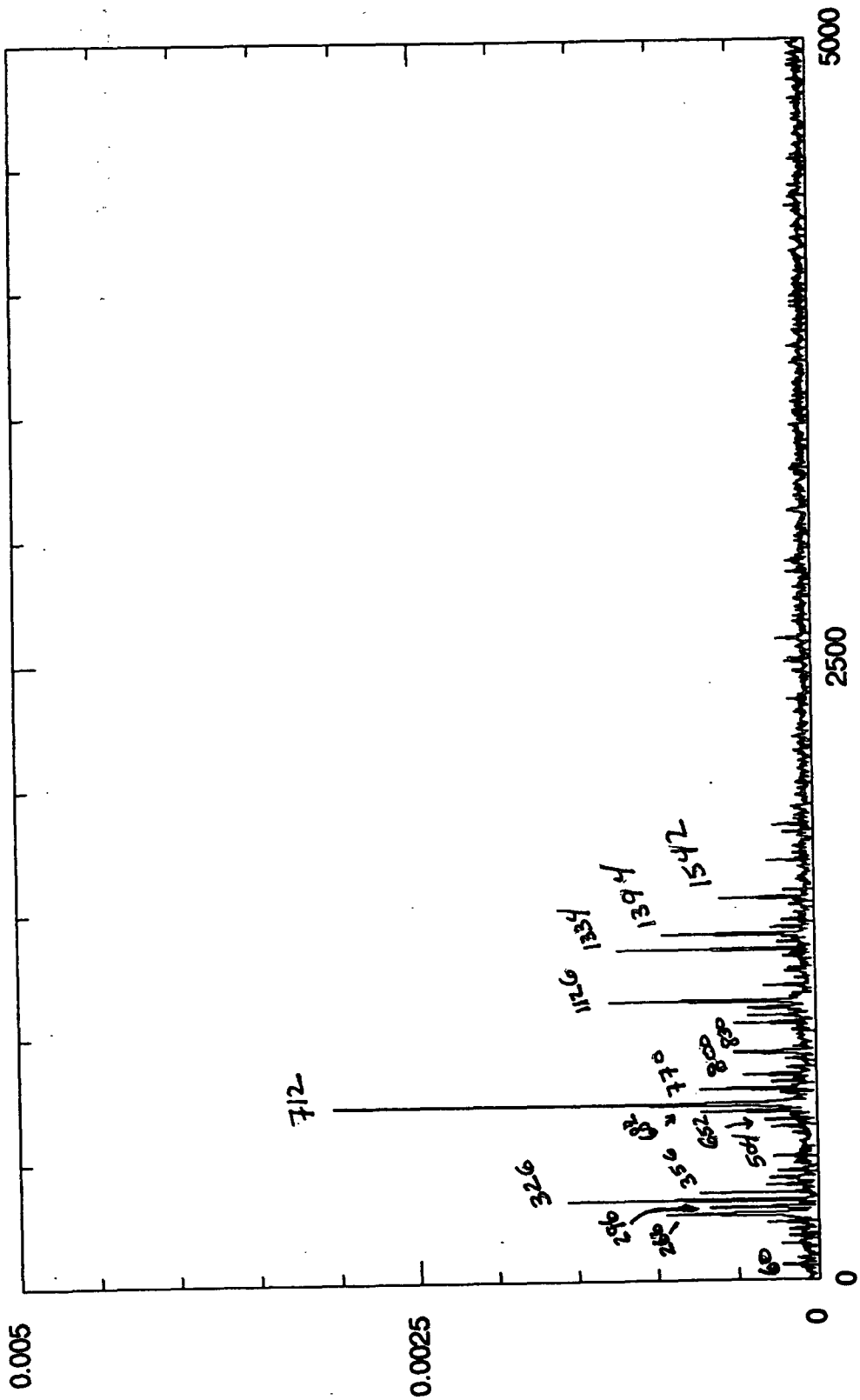
Plate/Pump On, No Flow
FFT Magnitude of Accelerometer Output
0.005
0.0025
0
0
2500
5000
Hertz
712
326
1176
1341
1504
1547

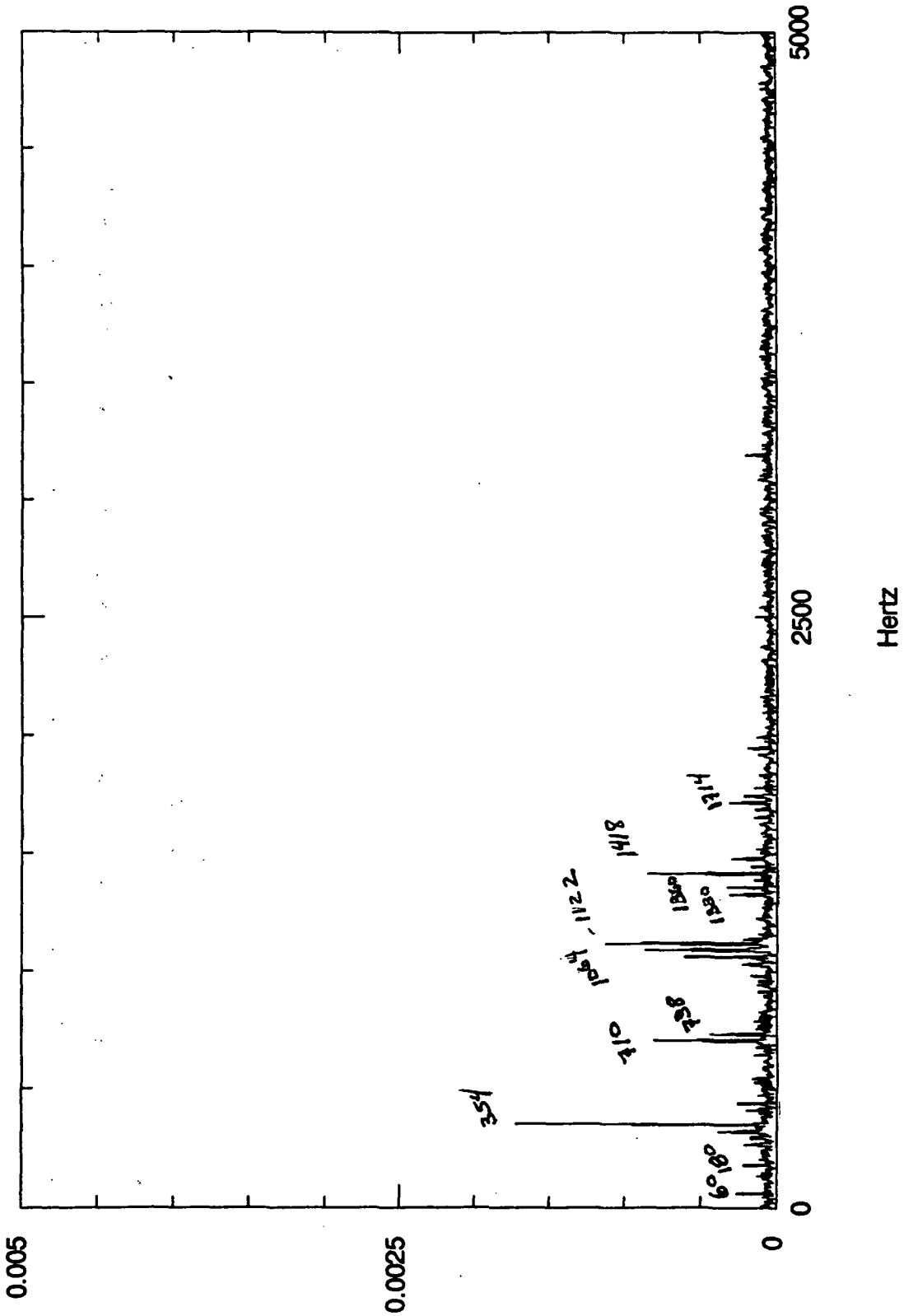
Plate/Flow 1 - 52992.6
FFT Magnitude of Accelerometer Output
0.005
0.0025
0
0
2500
5000
Hertz
354
410
738
1122
1418
1614
1800
1880
6080

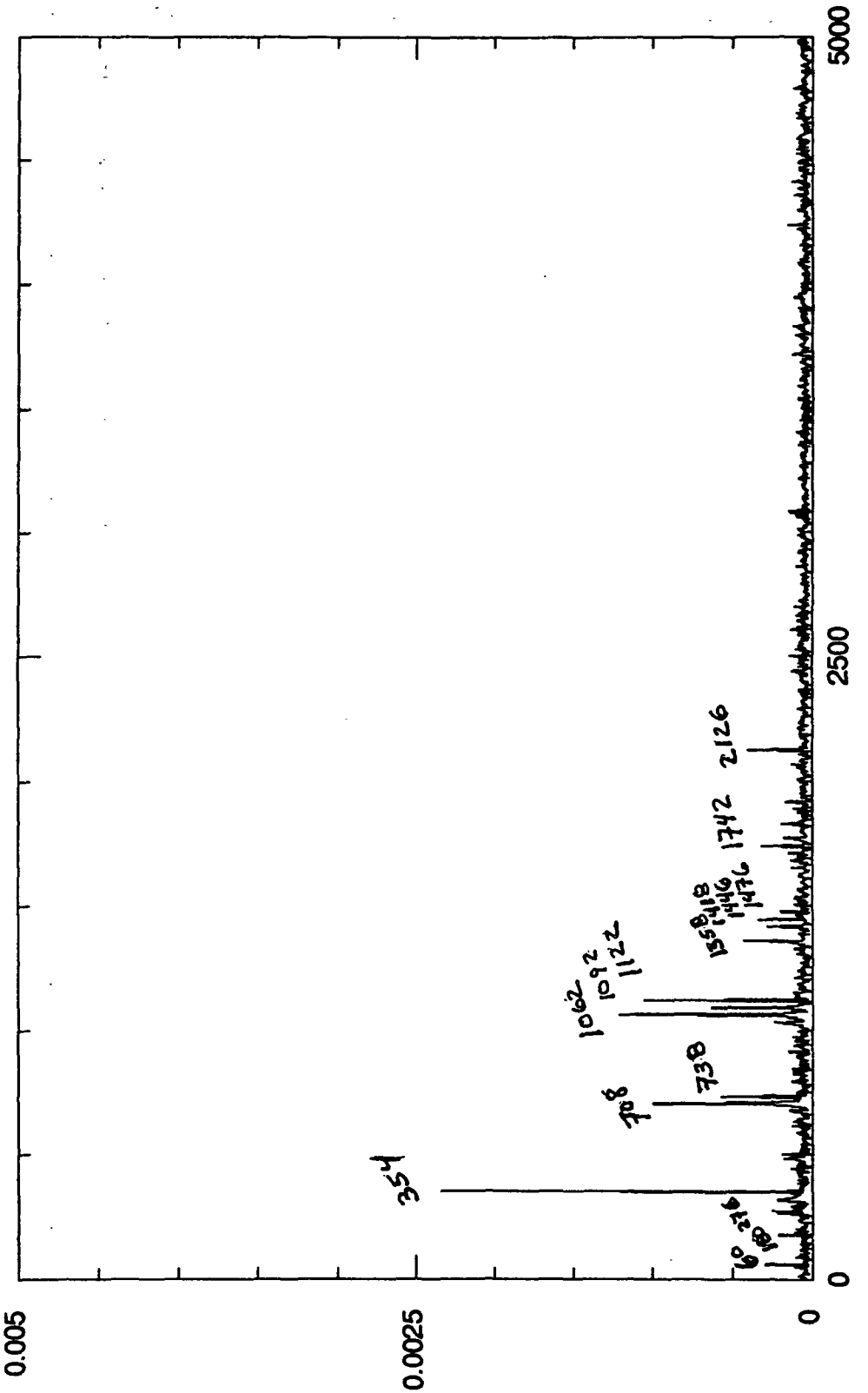
Plate/Flow 2 - 52992.7
FFT Magnitude of Accelerometer Output
0.005
0.0025
0
0
2500
5000
Hertz
354
738
1062
1092
1122
1742
2126

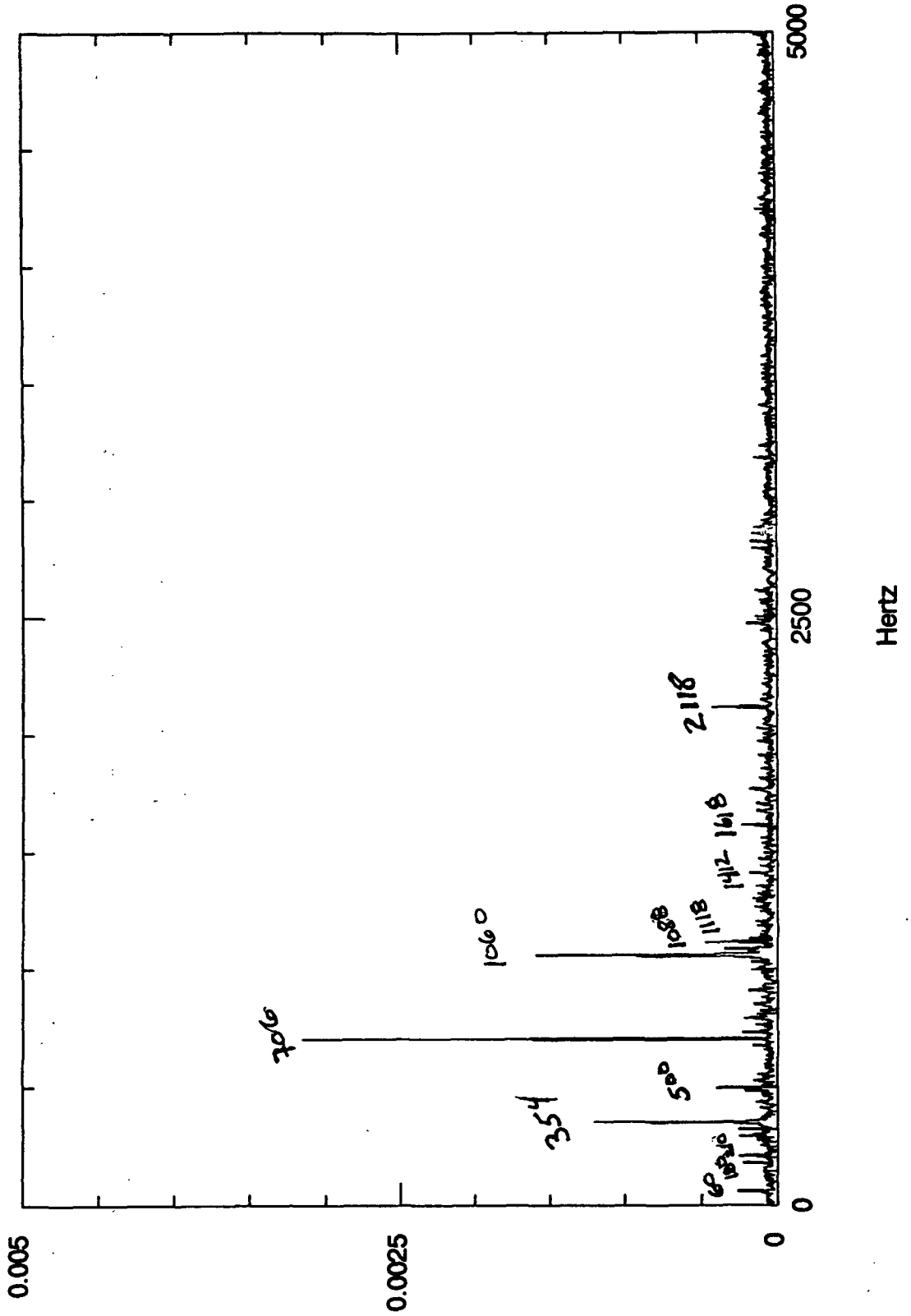
Plate/Flow 3 - 52992.8
FFT Magnitude of Accelerometer Output
0.005
0.0025
0
0
2500
5000
Hertz
706
354
106
58
108
118
161
218

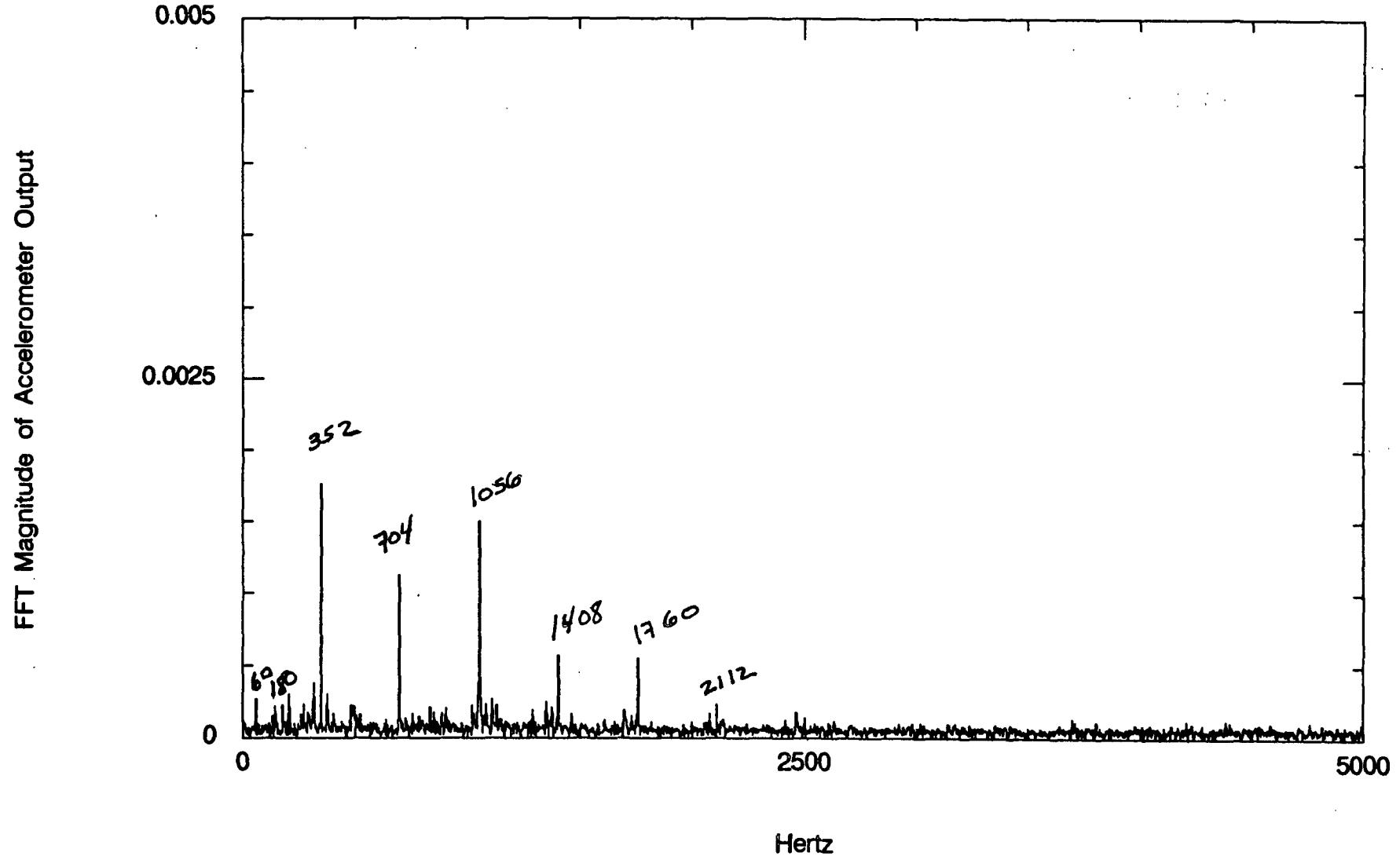
Plate/Flow 4 - 52992.9
0.005
0.0025
0
FFT Magnitude of Accelerometer Output
352
704
1056
1408
1760
2112
60
180
0
2500
5000
Hertz

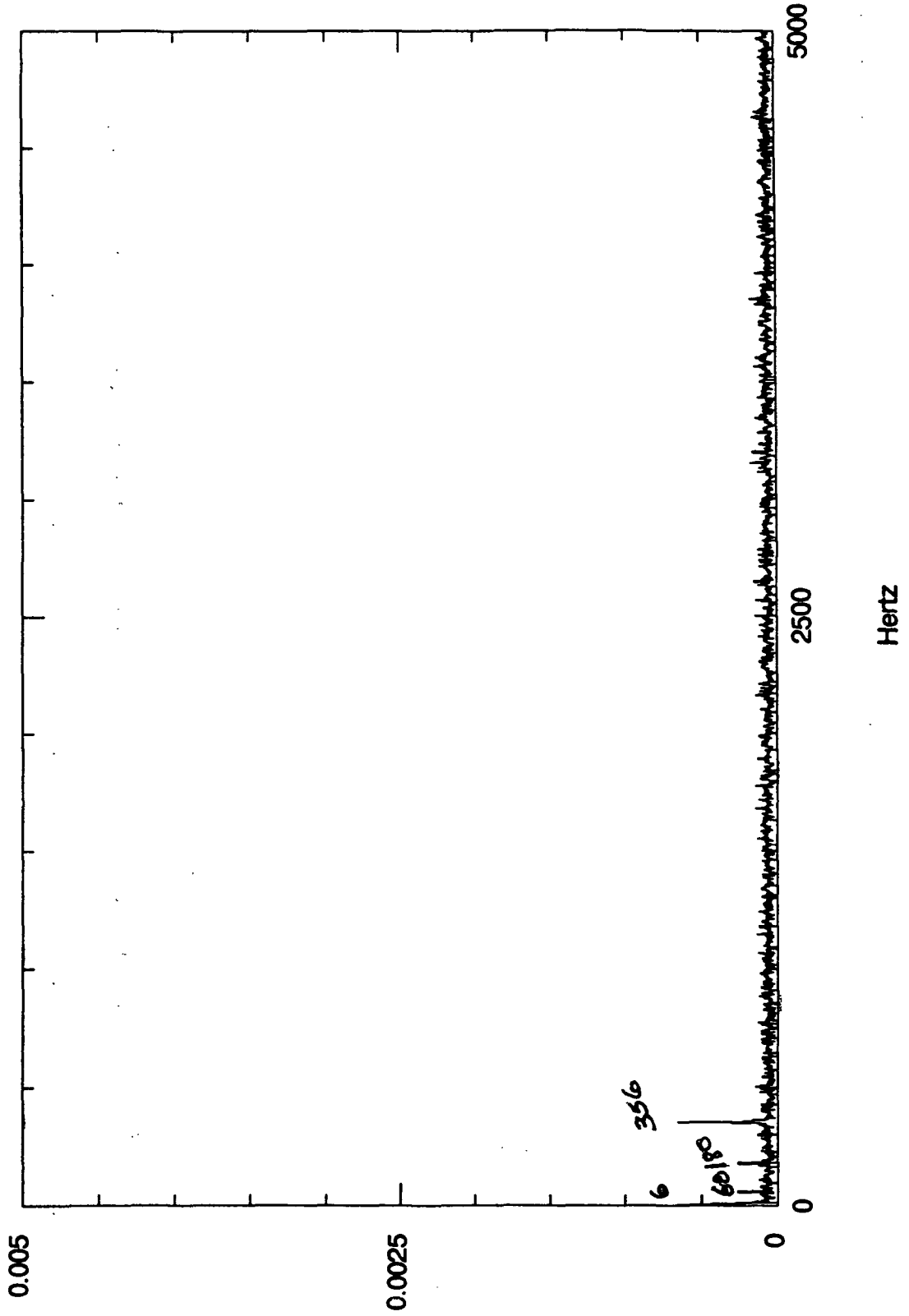
Nozzle/Flow 5 - 52992.10
FFT Magnitude of Accelerometer Output
0.005
0.0025
0
0
2500
5000
Hertz
6
356
6@180

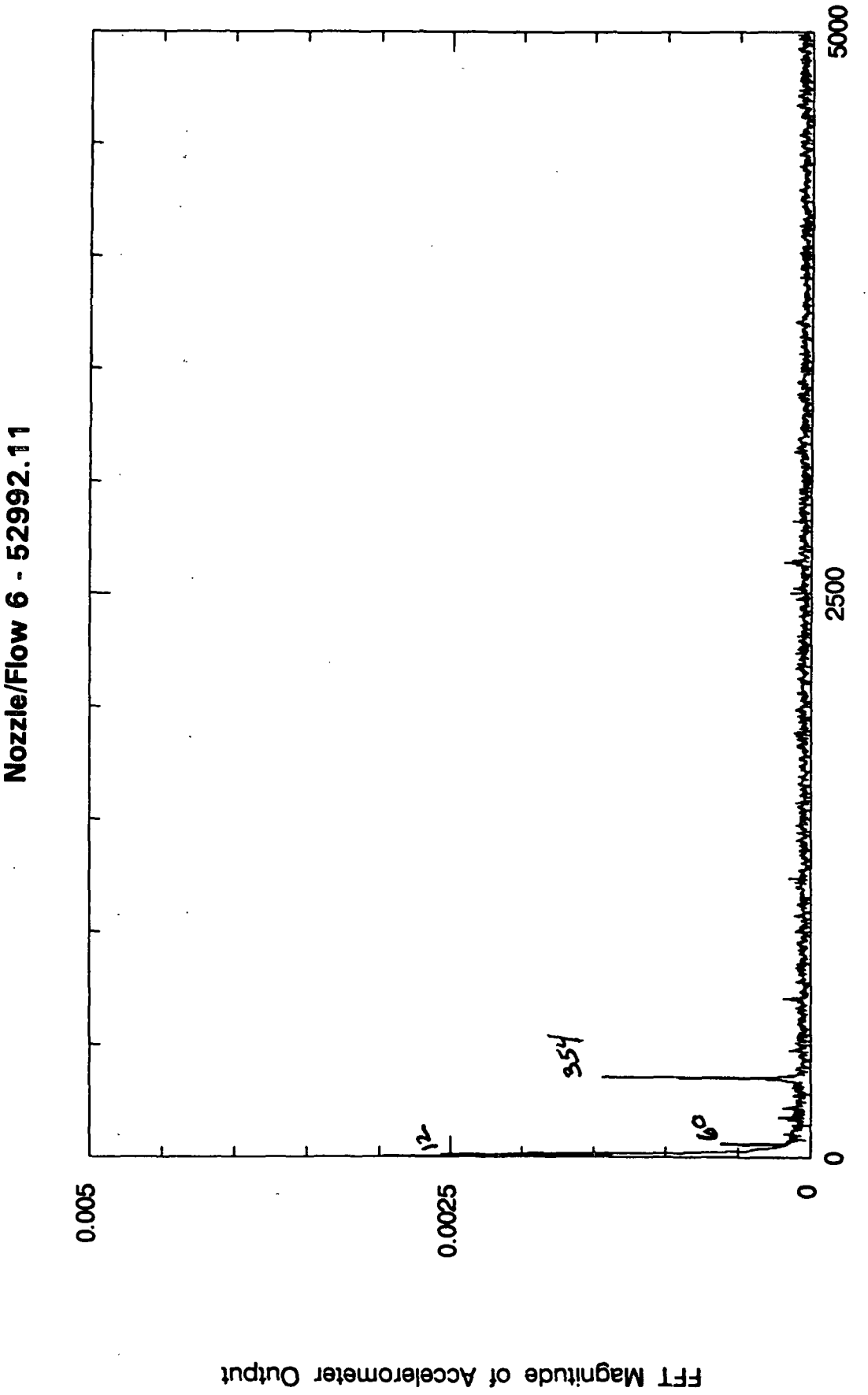
Nozzle/Flow 6 - 52992.11
FFT Magnitude of Accelerometer Output
0.005
0.0025
0
0
2500
5000
Hertz
12
60
354

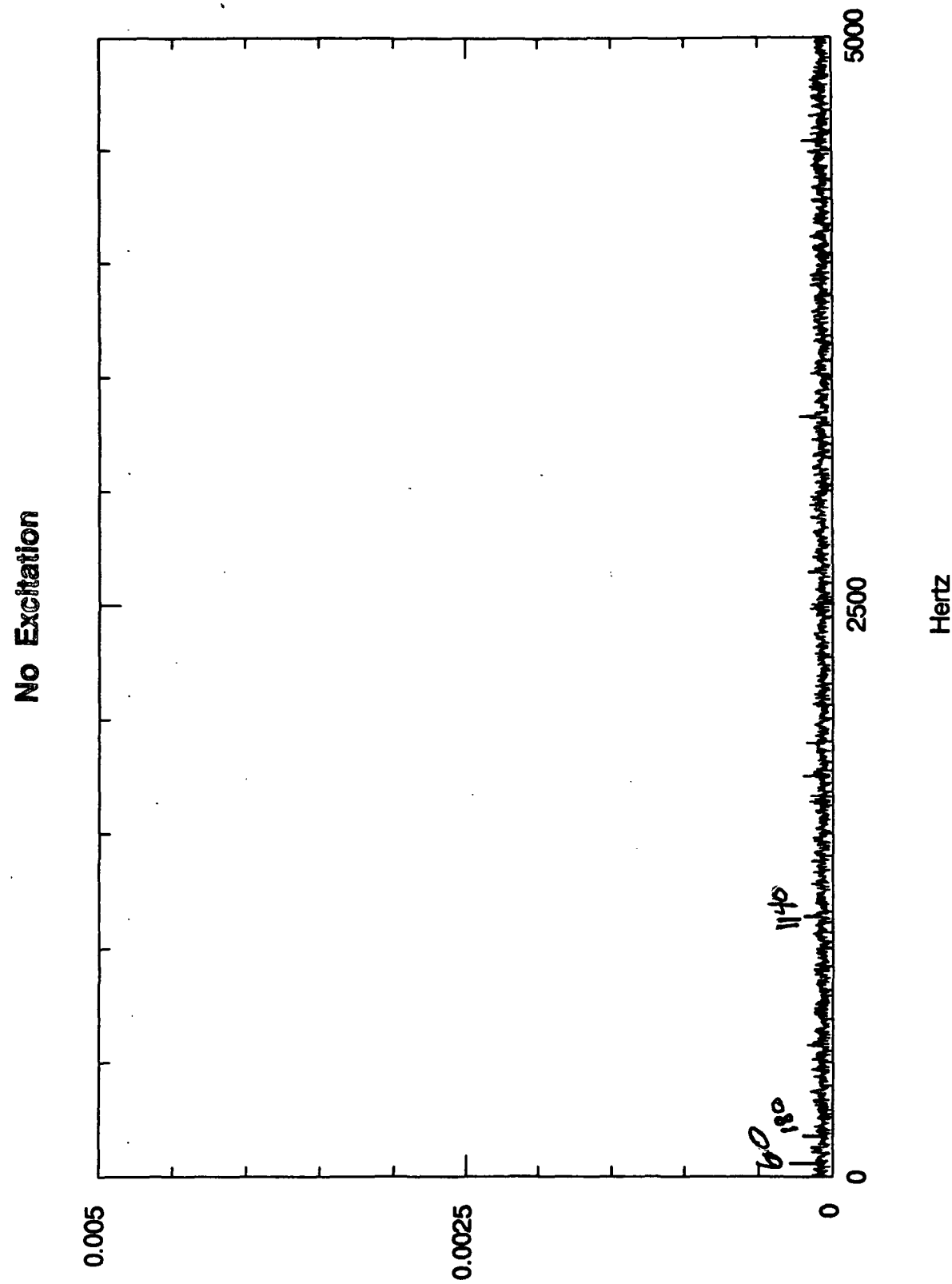
No Excitation
FFT Magnitude of Accelerometer Output
0.005
0.0025
0
0
2500
5000
Hertz